UNIVERSITY OF PISA
UNIVERSITY OF ADELAIDE

DOCTORAL THESIS

Optimal Space Time Adaptive Processing for Multichannel Inverse Synthetic Aperture Radar Imaging

Supervisors:
Prof. Marco MARTORELLA

Author:
Alessio BACCI

Prof. Douglas GRAY

Prof. Fabrizio BERIZZI

*A thesis submitted in fulfilment of the requirements
for the degree of Doctor of Philosophy*

Dottorato di Ricerca in Telerilevamento
Scuola di Dottorato in Ingegneria "Leonardo da Vinci"
The School of Electrical & Electronic Engineering
SSD ING-INF/03

July 2014

Declaration of Authorship

I, Alessio BACCI, declare that this thesis titled, 'Optimal Space Time Adaptive Processing for Multichannel Inverse Synthetic Aperture Radar Imaging ' and the work presented in it are my own. I confirm that:

- This work was done wholly or mainly while in candidature for a research degree at this University.

- Where any part of this thesis has previously been submitted for a degree or any other qualification at this University or any other institution, this has been clearly stated.

- Where I have consulted the published work of others, this is always clearly attributed.

- Where I have quoted from the work of others, the source is always given. With the exception of such quotations, this thesis is entirely my own work.

- I have acknowledged all main sources of help.

- Where the thesis is based on work done by myself jointly with others, I have made clear exactly what was done by others and what I have contributed myself.

Signed:

_____

Date:

_____

Abstract

Optimal Space Time Adaptive Processing for Multichannel Inverse Synthetic Aperture Radar Imaging

by Alessio Bacci

The thesis deals with the application of ISAR processing to obtain high resolution imaging of non-cooperative moving targets within a SAR scene. The research topic is of great interest nowadays. Modern SAR system can provide high resolution radar images of wide areas with reduced revisiting time. These features make them particularly suited for surveillance application. It is obvious that for these kind of applications the capability of imaging non-cooperative moving targets becomes fundamental. Since conventional SAR processing is unable to focus moving targets because of the lack of knowledge of the target motion a solution based on ISAR processing is proposed. In fact, ISAR systems, do not make any assumption about the target motion, but they exploit it to form the synthetic aperture and to obtain high resolution in the cross-range dimension. Since the ISAR processing must be applied to each target separately a detection step is fundamental. Although this detection step is not a problem when dealing with maritime targets, as the sea clutter return is usually much lower than the target return, it can a be a challenge when dealing with ground target. Multichannel information provided by SAR systems with multiple receivers can be exploited to mitigate the return of the static scene. STAP processing is then combined with ISAR technique to produce high resolution images of non-cooperative moving targets after detection within SAR images. The multichannel version of Range Doppler image formation algorithm is derived and analyzed. Then, it is used to define a Space Doppler Adaptive processing to mitigate the strong clutter before the application of ISAR autofocus. Performance are evaluated on simulated data. Results on real data prove the effectiveness of the proposed processing and its applicability on actual systems.

Contents

List of Figures

List of Tables

Abbreviations

ACE	**A**daptive **C**oherent **E**stimator
AMF	**A**daptive **M**atched **F**ilter
ATI	**A**long **T**rack Interferometry
CFAR	**C**onstant **F**alse **A**larm **R**ate
CPI	**C**oherent **P**rocessing Interval
CSK	**C**osmo **SK**yMed
DPCA	**Displaced Phase Centre Array**
DoF	**D**egree **of F**reedom
DoA	**D**irection **of A**rrival
FFT	**F**ast **F**ourier **T**ransform
FT	**F**ourier **T**ransform
GRLT	**G**eneralized **L**ikelihood **R**atio **T**est
IFFT	**I**nverse **F**ast **F**ourier **T**ransform
IFT	**I**nverse **F**ourier **T**ransform
IOK	**I**nverse **O**mega **K**ey
IRD	**I**nverse **R**ange **D**oppler
ISAR	**I**nverse **S**ynthetic **A**perture **R**adar
LCMV	**L**inearly **C**onstrained **M**inimum **V**ariance
LoS	**L**ine **of S**ight
LSE	**L**east **S**quare **E**rror
MTD	**M**oving **T**arget **D**etection
MTI	**M**oving **T**arget **I**ndication
NCTI	**N**on **C**ooperaive **T**arget **I**maging
PRF	**P**ulse **R**epetition **F**requency
PRI	**P**ulse **R**epetition Intervall
RD	**R**ange **D**oppler
SAR	**S**ynthetic **A**perture **R**adar
SDAP	**S**pace **D**oppler **A**daptive **P**rocessing

SMI   **S**ample **M**atrix **I**nversion

STAP   **S**pace **T**ime **A**daptive **P**rocessing

TFT   **T**ime **F**requency **T**ransform

TDC   **T**ime **D**omain **C**orrelation

WVD   **W**igner **V**ille **D**istribution

Symbols

_A_

A	Constraint matrix

_B_

B	Signal Bandwidth
B_D	Doppler Bandwidth
b	Constraint value

_D_

D_{y_1}/D_{y_2}	Non-ambiguity region in cross-range/range
D_{array}	Array size
D_{y_1}	Cross-range non-ambiguity region
D_{y_2}	Range non-ambiguity region

_E_

$\mathbf{e}_s(\theta)$	Spatial Steering Vector
$\mathbf{e}_t(F_D)$	Temporal Steering Vector
$\mathbf{e}(\theta, F_D)$	Spatial-Temporal Steering Vector

_F_

f	Range frequency
f_0	Carrier frequency
F_S	Spatial Frequency (beamforming)
F_D	Normalized Doppler Frequency

_G_

$\mathbf{G}(n,m)$	Reference signal vector
$\mathbf{G}_i(n,m)$	Reference signal vector (i^{th} window)
$\tilde{\mathbf{G}}(n,m)$	Reference signal vector
$\tilde{\mathbf{G}}_i(n,m)$	Post-Doppler Reference signal vector (i^{th} window)
$\mathbf{G}_D(n,m_\nu)$	Space Doppler Reference signal vector
$\mathbf{G}_{D,i}(n,m_\nu)$	Space Doppler Reference signal vector (i^{th} window)

$$\boldsymbol{I}$$

$\mathbf{i}_{LoS}$	LoS unit vector
$\mathbf{i}_{LoS_{Tx}}/\mathbf{i}_{LoS_{Rx}}$	LoS unit vector TX/RX
$\mathbf{i}_{LoS_{BI}}$	LoS unit vector (bistatic)
$\mathbf{i}_{LoS_x}^{(p,q)}$	LoS unit vector of the element (p,q) with respect T_x
$\mathbf{i}_{LoS_\xi}^{(p,q)}$	LoS unit vector of the element (p,q) with respect T_ξ
$I(\bullet,\bullet)$	ISAR image
i	Window index

$$\boldsymbol{K}$$

$K_{BI}(t)$	Phase modulation term (bistatic geometry)
$K_{BI_0}(t)$	Phase modulation term $t=0$ (bistatic geometry)
(k_{y_1}, k_{y_2})	Spatial frequencies

$$\boldsymbol{L}$$

L	Window length
L_f	Considered Doppler bins

$$\boldsymbol{M}$$

m	Pulse index
m_ν	Doppler frequency index
M	Slow time samples
M_ν	Doppler frequency samples
$\mathbf{M}_{\xi\mathbf{x}}$	Rotation matrix from T_ξ to T_x

$$\boldsymbol{N}$$

n	Range frequency index
n_τ	Delay time index
N	Frequency samples
N_τ	Delay time samples
$\mathbf{n}$	Guassian random vector with zero mean and Identity covariance matrix
N_d	Discarded pulses

$$\boldsymbol{P}$$

p	Array element index along ξ_1
P	Number of array element index along ξ_1
P_c	Clutter power

$$\boldsymbol{Q}$$

q	Array element index along ξ_3
Q	Number of array element index along ξ_3

$$\boldsymbol{R}$$

$R_0(t)$	Radar-target distance
R_0	Radar-target distance at $t = 0$
R_{Tx}/R_{Rx}	Distance between the target and the Tx/Rx
$\mathbf{R}_c$	Clutter space-slow time covariance matrix
$\mathbf{R}_{c,i}$	Clutter space-slow time covariance matrix (i^{th} window)
$\mathbf{R}_{D,c}$	Clutter cross-power spectral matrix
	_S_
$s_T(t_f)$	Transmitted signal
$s_R(t_f, t)$	Received signal
$S_R(f, t)$	Received signal in the frequency/slow time domain
$S_{R_C}(f, t)$	Motion compensated received signal
$S_0(\bullet, \bullet)$	Reference signal
$S_p(f, t)$	Received signal at p^{th} receiver
$S_{t,p}(f, t)$	Received signal at p^{th} receiver (target contribution)
$S_{c,p}(f, t)$	Received signal at p^{th} receiver (clutter contribution)
$\mathbf{s}_s$	data received in the nth frequency bin and the mth pulse
$\mathbf{s}(n)$	stacked signal vector
$\mathbf{s}_T$	stacked signal vector point like target (beamforming)
$S_{ref}(\bullet, \bullet)$	Reference Signal
$\mathbf{S}(n)$	Signal vector
$\mathbf{S}_i(n)$	Signal vector (i^{th} window)
$\tilde{\mathbf{S}}(n)$	Post-Doppler Signal vector
$\tilde{\mathbf{S}}_i(n)$	Post-Doppler Signal vector (i^{th} window)
	_T_
T_ξ	Reference system embedded on the radar
T_x	Reference system embedded on the target
T_y	Reference system embedded on the target (fixed)
t	Slow time
t_f	Fast time
T_R	Pulse Repetition Interval
T_{obs}	Observation time
T_{win}	Window length
T_{step}	Window step
$\mathbf{T}$	Unitary transformation matrix
$\mathbf{T}_t$	Fourier Matrix
$\mathbf{T}_w$	Unitary windowed transformation matrix

$\mathbf{T}_{w,t}$	Windowed Fourier Matrix
$\tilde{\mathbf{T}}_{w,t}$	Reduced Windowed Fourier Matrix
$\tilde{\mathbf{T}}_w$	Reduced windowed transformation matrix

$\underline{U}$

u	Platform position on the trajectory
U	Eigenvectors matrix
$u(\bullet, \bullet)$	Matched Filter Output
$u_i(\bullet, \bullet)$	Matched Filter Output (i^{th} window)
$u_w(\bullet, \bullet)$	Matched Filter Output (windowed)
$\tilde{u}(n, m_\nu$	Post-Doppler filtering output
$\tilde{u}_i(\bullet, \bullet)$	Post-Doppler Matched Filter Output (i^{th} window)
$\tilde{u}_w(\bullet, \bullet)$	Post-Doppler Matched Filter Output (windowed)
$u(\bullet, \bullet)_D$	Space Doppler Processing Output

$\underline{V}$

V	Volume where the target reflectivity is defined
v_p	Platform velocity
$\mathbf{V}$	Eigenvalues matrix
v_{t,y_1}, v_{t,y_1}	Target velocity along cross-range/range direction

$\underline{W}$

$W(f,t)$	Frequency/slow time domain where the signal is defined
$W(f,t)$	Spatial Frequencies domain time domain where the signal is defined
$\mathbf{w}(\theta, F_D)$	weightvector
$\mathbf{W}(n,m)$	Optimum weightvector
$\mathbf{W}_i(n,m)$	Optimum weightvector (i^{th} window)
$\tilde{\mathbf{W}}(n,m_\nu)$	Post-Doppler Optimum weightvector
$\tilde{\mathbf{W}}_i(n,m)$	Post-Doppler Optimum weightvector (i^{th} window)
$\tilde{\mathbf{W}}_D(n,m_\nu)$	Space Doppler Optimum weightvector
$\tilde{\mathbf{W}}_{D,i}(n,m_\nu)$	Space Doppler Optimum weightvector (i^{th} window)

$\underline{W}$

$\mathbf{x}$	Stacked received signal vector

$\underline{Y}$

(Y_1, Y_2)	Spatial frequencies
$y_s(\theta, n, m)$	Steered output in the direction θ
$y_{t,p}(F_D, n)$	Focused output at F_D
$y(\theta, F_D, n)$	Focused output at θ, F_D
$y^{(u)}$	useful output

$y^{(c)}$	clutter (disturbance) output
Z	
$\mathbf{Z}(n_r)$	Target-free data in the n_r^{th} range cell
α	
α	Angle between ξ_3 and x_3
β	
$\beta(t)$	Bistatic angle variation
Δ	
Δ_τ	Delay time resolution
Δ_ν	Doppler frequency resolution
$\Delta_{y_1}/\Delta_{y_2}$	Cross-range/range resolution
$\Delta Y_1/\Delta Y_1$	Spacial frequencies spacing
$\Delta\Theta$	Aspect angle variation
Θ	
θ_{in}	Incidence angle
θ	DoA
θ_{az}	Azimuth aperture
ν	
ν	Doppler frequency
ρ	
$\rho_s(\Delta_d)$	space correlation
$\rho_t(\Delta_t)$	time correlation
σ	
$\sigma(\mathbf{y})$	Reflectivity of the scatterer placed in **y**
σ_k	Reflectivity of the kth scatterer
σ_T	Reflectivity of a point like target (beamforming)
τ	
$\tau(\mathbf{y},t)$	Delay time of the scatterer placed in **y** at time t
Φ	
$\phi(\mathbf{y},f,t)$	Phase term (monostatic case)
$\phi_{BI}(\mathbf{y},f,t)$	Phase term (bistatic case)
Ω	
$\Omega_T(t)$	Total rotation vector
$\Omega_{eff}(t)$	Effective rotation vector

Chapter 1

Introduction

1.1 Background and Motivation

Developed in the 1950s, Synthetic Aperture Radar is a well know technology that exploits the relative motion between a radar mounted on a moving platform and a target area. In this way a long synthetic array antenna can be synthesize and can be exploited to obtain finer spatial resolution with respect to conventional beam scanning. SAR systems play a fundamental role in the Earth observation application because of their capability to operate in any weather and day night condition.

Airborne SAR systems are mainly used for the imaging of large areas with ad-hoc mission while spaceborne SAR system allow for the continuous monitoring of vast areas at global scale and, in case of modern system, reduced revisiting time.

These characteristics make SAR system specially suited for surveillance and homeland security applications.

It is quite obvious that in such a scenario moving targets are of particular interest. Notwithstanding, moving targets set a limitation for the applicability of conventional SAR techniques since conventional SAR image formation algorithms are unable to produce well focused images of non-cooperative moving targets. This is due to the lack of knowledge of the unpredictable target own motion that does not allow for coherent processing of the received echoes. As a consequence, moving targets within SAR images appear defocussed e misplaced. Imaging of moving targets within SAR images is an current research field.

Inverse Synthetic Aperture Radar (ISAR) has been suggested as an alternative way to look at the problem of forming a synthetic aperture for high resolution images of non-cooperative targets [1],[2]. ISAR techniques rely on the knowledge of the relative radar-target motion, but exploit the unknown motion to form the synthetic aperture. ISAR and SAR are strictly related and the only difference relies on the knowledge of the target motion. These characteristics make ISAR processing especially suited for imaging of non-cooperative target detected in SAR images.

In this scenario target detection is a critical step. In fact, in order to apply ISAR processing each target must be detected first. Detection is a complex process since the target energy is spread over a wide region because of the defocusing effect due to the non-coherent processing. In particular, detection is very hard in case of ground targets. In this case from a detection perspective ground clutter is focused since its echoes are coherently processed and this can cause a masking effect that prevents the detection of moving targets.

A number of moving target detection techniques from SAR have been studied in the last few decades. It has been demonstrated that better detection performance can be obtained with multichannel systems with respect to the conventional single channel radar. In fact, the processing of data collected by different antennas, i.e., channels, is an effective mean for ground clutter suppression.

A number of multichannel SAR system have been recently developed. Some of them are:

- INGARA: 'Integrated Airborne Imaging Radar' system is DSTO Australia's dual channel polarimetric SAR capable of interferometry. It operates at X-band with up to 600 MHz bandwidth [3].

- AMSAR: 'Advanced Multichannel Synthetic Aperture Radar' is a system developed by France, Germany and England with the aim to improve the 'Euroradar' [4].

- AER-II: 'Airborne Experimental Radar' is FGAN's first experimental MSAR equipped with an X-band system with 1m x 1m resolution. It has a fully polarimetric phased array for electronic azimuth beam-steering and four received channels [5].

- PAMIR: 'Phased Array Multifunctional Imaging Radar' is FGAN's follow up system to the AER-II. It is designed to be an experimental X-band system which can image at very high resolution. It has 256 receiver antennas which are grouped into five channels [6].

- RADARSAT-2: It is the Canada's latest fully polarimetric spaceborne SAR. It is launched in early 2006 and it is used for scientific purposes such as interferometry and ground mapping from 3m resolution [7].

- TERRASAR-X: It is a German system. It is an X-band fully polarimetric spaceborne SAR. Its purpose is to create digital elevation maps down to a resolution of 1 m [8].

- DRA C-band: It is an experimental C-Band MSAR built by the Swedish Defence Reserach Agency. It uses three antennas aligned along the track dimension to test different MTI techniques [9]

- AN/APG-76: It is a Ku band multimode radar system produced by Northrop-Grummen Aerospace and used in Israel's F-4 fighters [10]. It was the first system in the world to simultaneously produce high resolution radar imagery and perform MTI.

- APY-6: It is a MSAR produced by Northrop-Grummen Aerospace. The antenna is subdivided into a large panel for transmit and SAR receiver, and three smaller panel for MTI receiver.

The aim of this work is to develop a processing chain that exploit multichannel information provided by a MSAR system to obtain high resolution images of non-cooperative moving target within SAR images.

Two are the steps of the proposed processing chain. Clutter suppression an platform motion compensation is performed first exploiting the multichannel information in order to improve target detection capability within SAR image. At this point, ISAR autofocusing is required in order to compensate the residual target own-motion and to reduced the defocusing effect due to that unknown motion component. The study of the applicability of ISAR processing to refocus moving target detected within SAR images (obtained with conventional single channel SAR system) is the first objective of this work. Then the study of MTD/MTI techniques and the development of clutter mitigation algorithms is the second aim of this work. The integration of the proposed algorithms with ISAR techniques

leads to the final processing chain. All the developed techniques are tested on simulated and real dataset.

1.2 Thesis outline and contributions

This thesis is organized as follows. In the first part an exhaustive review of the ISAR and SAR signal modelling is provided. The monostatic case is treated as well as the bistatic and the multistatic case. Also a statistical description of clutter and some details about the simulator set up are provided. Special attention is given to the formulation of the multichannel version of the Range Doppler image formation technique with the analysis of its characteristics and limitations. The application of ISAR processing to refocus moving target detected in SAR images with single channel SAR system is then introduced and analysed. The detection issue is then introduced especially in case of ground clutter. A review of the MTI/MTD techniques for SAR is provided with special attention to the Space Time Adaptive Processing techniques. An integrated STAP ISAR processing is then developed and tested on simulated data. Finally a Space Doppler Adaptive Processing (SDAP) is derived starting from the multichannel Range Doppler and tested on simulated data. A comparison between STAP-ISAR and SDAP-ISAR is performed. In the last part of the thesis the real data analysis is performed. Specifically the multichannel Range Doppler is tested as well as the SDAP ISAR processing proving the effectiveness of the proposed processing chain.

The main contribution of this thesis are:

- Provide a multichannel signal model for ISAR and derive and analyse a multichannel version of the Range Doppler technique for image formation.

- Develop an ISAR based technique for imaging of non-cooperative moving targets detected within SAR images.

- Develop a joint STAP ISAR processing for the detection and imaging of non-cooperative moving target within SAR images.

- Developed a Space Doppler Adaptive Processing for clutter mitigation integration this with the ISAR techniques for non-cooperative target imaging.

- Demonstrate the effectiveness of the proposed processing on simulated and real dataset.

The following papers have been published during the research activities:

- Martorella, M.; Giusti, E.; Berizzi, F.; **Bacci, A.**; Dalle Mese, E.; , "ISAR based techniques for refocusing non-cooperative targets in SAR images," Radar, Sonar & Navigation, IET , vol.6, no.5, pp.332-340, June 2012

- Martorella, M.; Berizzi, F.; Giusti, E.; **Bacci, A.**; , "Refocussing of moving targets in SAR images based on inversion mapping and ISAR processing," Radar Conference (RADAR), 2011 IEEE , vol., no., pp.068-072, 23-27 May 2011

- Martorella, Marco; Giusti, Elisa; **Bacci, Alessio**; Berizzi, Fabrizio; Meta, Adriano; , "Non-cooperative maritime target imaging with an FMCW SAR system," Synthetic Aperture Radar, 2012. EUSAR. 9th European Conference on , vol., no., pp.127-130, 23-26 April 2012

- M. Martorella, E. Giusti, F. Berizzi, **A. Bacci**, E. Dalle Mese, "An ISAR Technique for Refocusing Moving Targets in SAR Images", chapter 14th of the book "Signal and Image Processing for Remote Sensing", Second edition CRC Press (Taylor and Francis Group), Edited by C.H. Chen, 2012

- **Bacci, A.**; Gray, D.; Martorella, M.; Berizzi, F., "Joint STAP-ISAR for non-cooperative target imaging in strong clutter," Radar Conference (RADAR), 2013 IEEE , vol., no., pp.1,5, April 29 2013-May 3 2013

- **Bacci, A.**; Gray, D.; Martorella, M.; Berizzi, F., "Space-Doppler processing for multichannel ISAR imaging of non-cooperative targets embedded in strong clutter," Radar (Radar), 2013 International Conference on , vol., no., pp.43,47, 9-12 Sept. 2013

- **Bacci, A.**; Martorella, M.; Gray, D.; Berizzi, F., "High Resolution Imaging of Moving Ground Targets via Clutter Mitigation and ISAR Processing," (accepted for poster presentation) 2014 Radar Conference, (Lille, France) 2014

- **Bacci, A.**; Martorella, M.; Gray, D.; Berizzi, F., "Space-Doppler Adaptive Processing for Radar Imaging of Moving Targets in Strong Clutter," Radar, Sonar & Navigation, IET (under review)

1.2.1 Chapter summary

Chapter 2

This chapter focuses on the definition of the signal model exploited in the thesis. The ISAR case is treated first with an exhaustive review of the ISAR theory. The bistatic and the multistatic cases are also treated leading to the formulation of a multichannel version of the Range Doppler image formation technique.

Then a brief review of the SAR theory is provided. In particular, the differences between ISAR and SAR scenarios will be highlighted.

ISAR and SAR signal models are used to define the scenario in which a multichannel SAR system illuminates a ground/sea spot where non-cooperative moving targets are present.

Since the aim of this work is to produce high resolution images of non-cooperative targets, the static scene is associated to clutter and a statistical description is provided.

Finally a brief description of the multichannel simulator set up is provided.

Chapter 3

High resolution ISAR imaging of non-cooperative moving targets in single channel SAR images is the core idea of this chapter.

A solution based on the application of ISAR processing is described. A comprehensive description of the ISAR image formation process is given. Results of the application of the proposed processing to two real datasets will be provided.

Chapter 4

In this chapter a review of the moving target indication/detection techniques in SAR images is presented. In particular, techniques that make use of multichannel information are introduced. These techniques are more effective in case of strong ground clutter in particular for the detection of slow moving targets. A special attention is given to the Space Time Adaptive Processing because of its characteristics that make it suitable for the purposes of this thesis.

Chapter 5

In this chapter a technique that combines clutter suppression and ISAR processing in order to obtain well focused images of extended moving targets is investigated. The problem is addressed from an imaging point of view. Two principal issues are addressed. The applicability of ISAR processing after clutter mitigation first, and then the need of sub-optimal approach due to the difficulties in the estimation of the clutter space-time covariance matrix is investigated. The optimum processing and two sub-optimum processing schemes are derived and tested on simulated data.

Chapter 6

In this chapter the Space Doppler Adaptive Processing (SDAP) is presented. It is a modified version of the classical STAP described in the previous chapter that is based on the multichannel Range Doppler image formation algorithm. The theoretical formulation is derived both for the optimum and the sub-optimum approach. It is combined with the ISAR processing in order to obtain well focused images of non-cooperative moving targets embedded in strong clutter environments. The effectiveness of the proposed processing is proved on simulated data. A comparison with the STAP-ISAR processing is also presented.

Chapter 7

In this chapter the results of the application of the proposed SDAP processing are presented. The multichannel range Doppler processing to obtain the SAR image is tested and some conclusions are drawn.

The SDAP-ISAR processing will be applied exploiting the two available channels. Since the system set up is not optimal for the application of the proposed algorithms some preliminary operations are needed to arrange the data in a manner that allows for the proposed processing to be applied.

Finally, a method to synthesize three virtual channels is presented. The SDAP-ISAR processing is applied to the three virtual channels data and compared to the results obtained with the two real channels data.

Chapter 2

Signal Modeling

2.1 Introduction

The objective of this chapter is to define the signal model used in the present work and define the multichannel version of the Range Doppler image formation algorithm.

First, the ISAR case will be considered with a brief review of ISAR theory and the Range Doppler (RD) algorithm for image formation.

The model for the single channel scenario for the monostatic configuration will be presented and then extended to the bistatic case. Then the multichannel case will be treated leading to the formulation of the multichannel Range Doppler (MRD) image formation algorithm.

Secondly, the SAR case will be considered and the SAR signal model derived in a different way with respect to the classical SAR theory. In fact, SAR systems can be seen as a special case of ISAR in which the relative motion between radar and target is known. Also the differences between SAR and ISAR will be investigated from a signal processing point of view. The multichannel SAR signal model will be presented as well.

All the above mentioned models will be used to describe the scenario in which a multichannel SAR systems illuminates a ground/sea spot where non-cooperative moving targets are present. Since the aim of this work is to produce high resolution images of non-cooperative targets, the static scene can be associated to clutter. For this reason, a statistical description of the clutter will be provided.

Finally a brief description of the multichannel simulator set up for this work will be provided.

2.2 ISAR Signal Model

In this section the ISAR signal model will be presented. Monostatic (single channel) and bistatic configurations will be treated and then the multichannel case will be presented.

2.2.1 Monostatic ISAR

Consider the typical ISAR geometry shown in Fig. 2.1 in which the transmitter/receiver is indicated as TX/RX. The Cartesian reference system T_ξ (ξ_1, ξ_2, ξ_3) is embedded on the radar while the reference system T_x (x_1, x_2, x_3) is embedded on the target with the origin in the target reference point. $R_0(t)$ denotes the time varying distance between the radar and the reference point on the target.

By considering the target as a rigid body the relative radar target motion can be considered as the superimposition of two contributions: a translational motion and a rotation motion.
The translational motion is the motion of the reference point with respect to the radar while the rotation motion is described by the vector $\mathbf{\Omega}_T(t)$ that takes into account the aspect angle variation due to both the translational motion and the own rotational motion of the target. The projection of $\mathbf{\Omega}_T(t)$ onto the plane orthogonal to the Line of Sight (LoS) is defined as the effective rotation vector $\mathbf{\Omega}_{eff}(t)$ that produces the effective aspect angle variation seen by the radar.
To define the reflectivity function of the target a new reference system $T_y = (y_1, y_2, y_3)$ embedded on the target is defined where its origin is the same reference point on the target. Its orientation does not change during the observation time (T_{obs}) and coincides with T_x at time $t = 0$. As it will be clear in the following the plane (y_1, y_2) defines the image plane and its axes correspond with the cross-range and range coordinates respectively.
The radar transmits a series of pulses called *pulse train* separated by a Pulse Repetition Interval (PRI), denoted by T_R and defined as $T_R = \frac{1}{PRF}$, where PRF is the *Pulse Repetition Frequency*. Using the *start and stop* approximation, the
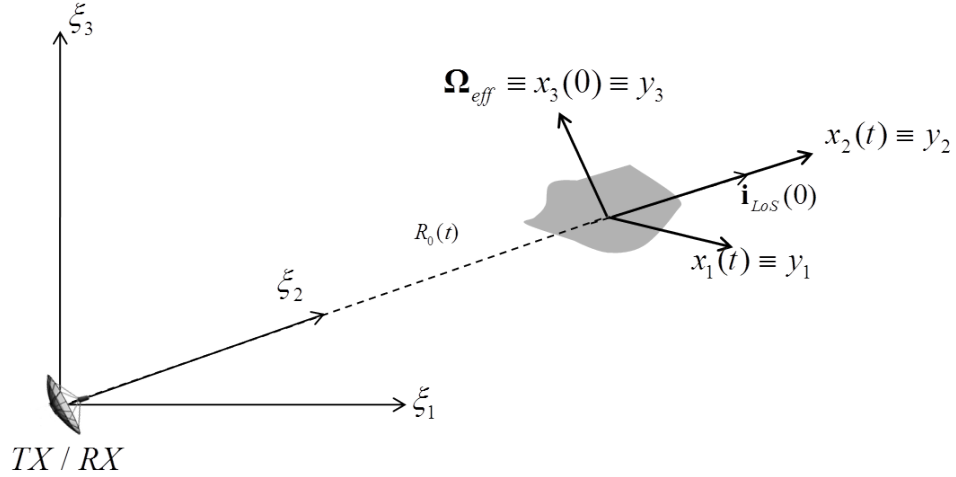
FIGURE 2.1: ISAR Geometry

target can be considered static during a single sweep and the two way delay that the transmitted signal undergoes is constant between two consecutive pulses. Under this assumption the received signal can be expressed as follows:

$$s_R(t_f, t) = \int_V \sigma(\mathbf{y}) s_T\left(t_f - \tau\left(\mathbf{y}, t\right), t\right) d\mathbf{y} \tag{2.1}$$

where $s_T(t_f)$ is the transmitted signal and does not change from pulse to pulse, $\tau\left(\mathbf{y}, t\right) = \frac{2R(\mathbf{y})}{c}$ is the delay time of a scatterer placed in $\mathbf{y}$ with respect to the reference system T_y at slow time t, t_f is the fast time variable, c is the speed of light in a vacuum and $\sigma(\mathbf{y})$ is the target reflectivity function defined in the volume V where the target is.

To obtain high range resolution conventional pulse compression is exploited by means of a matched filter. At the output of the matched filter the baseband signal (i.e., the complex envelope of the signal) in the frequency/slow-time domain, (f, t), can be expressed as:

$$S_R\left(f, t\right) = W\left(f, t\right) \int_V \sigma\left(\mathbf{y}\right) e^{-j2\pi f \tau(\mathbf{y}, f, t)} d\mathbf{y} \tag{2.2}$$

Special attention should be given to the function $W\left(f, t\right)$ that defines the region in the Fourier domain where the signal is defined. For a conventional active radar where the transmitted signal does not change from pulse to pulse it can be written as follows:

$$W\left(f, t\right) = |S_T(f)|^2 rect\left(\frac{t}{T_{obs}}\right) \tag{2.3}$$

In the classical active radar configuration $S_T(f) = rect\left(\frac{f-f_0}{B}\right)$ where f_0 is the carrier frequency and B is the transmitted bandwidth. This is an approximation of a linear frequency modulated signal typically used to obtain fine range resolution. It will be shown that $W(f,t)$ determines the Point Spread Function (PSF) of the ISAR system. By assuming the *straight iso-range approximation* holds the phase term in Eq.(2.2) can be written as follows [11]

$$\phi(\mathbf{y}, f, t) = \frac{4\pi f}{c}(R_0(t) + \mathbf{y} \cdot \mathbf{i}_{LoS}(t)) \tag{2.4}$$

where $R_0(t)$ is the distance between the radar and a reference point on the target at t, $\mathbf{y}$ is the column vector that identify the position of the generic scatterer in the T_y reference system and $\mathbf{i}_{LoS}(t)$ is the unit vector in the direction of the LoS at time t. Assuming that the effective rotation vector is constant during the overall observation time, i.e., $\mathbf{\Omega}_{eff}(t) \approx \mathbf{\Omega}_{eff}$ for $|t| < T_{obs}$, and choosing the axis x_3 so that it is parallel to Ω_{eff}, then the inner product $x_2(\mathbf{y}, t) = \mathbf{y} \cdot \mathbf{i}_{LoS}(t)$ can be expressed in a closed form by solving the differential equation system

$$\dot{\mathbf{x}}(t) = \mathbf{\Omega}_T \times \mathbf{x}(t) \tag{2.5}$$

with the initial condition

$$\mathbf{x}(0) = \mathbf{y} \tag{2.6}$$

The resulting closed form solution is:

$$\mathbf{x}(t) = \mathbf{a} + \mathbf{b}\cos(\Omega_T t) + \frac{\mathbf{c}}{\Omega_T}\sin(\Omega_T t) \tag{2.7}$$

where $\mathbf{a} = \frac{(\mathbf{\Omega}_T \cdot \mathbf{y})}{\Omega_T^2}\mathbf{\Omega}_T$, $\mathbf{b} = \mathbf{y} - \frac{(\mathbf{\Omega}_T \cdot \mathbf{y})}{\Omega_T^2}\mathbf{\Omega}_T$, $\mathbf{c} = \mathbf{\Omega}_T \times \mathbf{y}$

and $\Omega_T = |\mathbf{\Omega}_T|$. $\mathbf{\Omega}_T = (0, \Omega_{T_2}, \Omega_{eff})$ with the described choice of the reference system.

Eq.(2.7) term can be reasonably approximated by its first order Taylor series around $t = 0$ and the results is expressed as follows:

$$\mathbf{x}(t) \cong \mathbf{a} + \mathbf{b} + \mathbf{c}t = \mathbf{y} + \mathbf{c}t \tag{2.8}$$

resulting in:

$$x_2\left(\mathbf{y}, t\right) = y_2 + \Omega_{eff} y_1 t \tag{2.9}$$

with $\Omega_{eff} = |\mathbf{\Omega}_{eff}|$. By substituting Eq.(2.9) in the the received signal, the result is

$$S_R\left(f, t\right) = W\left(f, t\right) \int\limits_V \sigma\left(\mathbf{y}\right) e^{-j\frac{4\pi f}{c}\left(R_0(t) + y_2 + \Omega_{eff} y_1 t\right)} d\mathbf{y} \tag{2.10}$$

The same result can be obtained in a different way considering that the LoS unit vector in the T_y reference system can be expressed as:

$$\mathbf{i}_{LoS}(t) = \begin{bmatrix} sin(\Omega_{eff}t) \\ cos(\Omega_{eff}t) \\ 0 \end{bmatrix} \tag{2.11}$$

and the inner product results in:

$$x_2\left(\mathbf{y}, t\right) = \mathbf{y} \cdot \mathbf{i}_{LoS}(t) = y_2 cos(\Omega_{eff}t) + y_1 sin(\Omega_{eff}t) \tag{2.12}$$

Eq.(2.2) can the be therefore written as:

$$S_R\left(f, t\right) = W\left(f, t\right) \int\limits_{y_1} \int\limits_{y_2} \sigma\left(y_1, y_2\right) e^{-j4\pi\frac{f}{c}\left(R_0(t) + y_2 cos(\Omega_{eff}t) + y_1 sin(\Omega_{eff}t)\right)} dy_1 dy_2$$

$$\tag{2.13}$$

where $\sigma\left(y_1, y_2\right) = \int\limits_{y_3} \sigma(\mathbf{y}) dy_3$ is the projection of the target reflectivity function on the image plane.

Assuming that the phase term due to the translational motion $R_0\left(t\right)$ is perfectly compensated during the ISAR processing, then the motion compensated signal is

$$S_{R_C}\left(Y_1, Y_2\right) = W\left(Y_1, Y_2\right) \int\limits_{y_1} \int\limits_{y_2} f\left(y_1, y_2\right) e^{-j2\pi(y_2 Y_2 + y_1 Y_1)} dy_1 dy_2 \tag{2.14}$$

where Y_1 and Y_2 are the spatial frequencies defined as:

$$\begin{cases} Y_1\left(f, t\right) = \frac{2f}{c} sin(\Omega_{eff}t) \\ Y_2\left(f, t\right) = \frac{2f}{c} cos(\Omega_{eff}t) \end{cases} \tag{2.15}$$
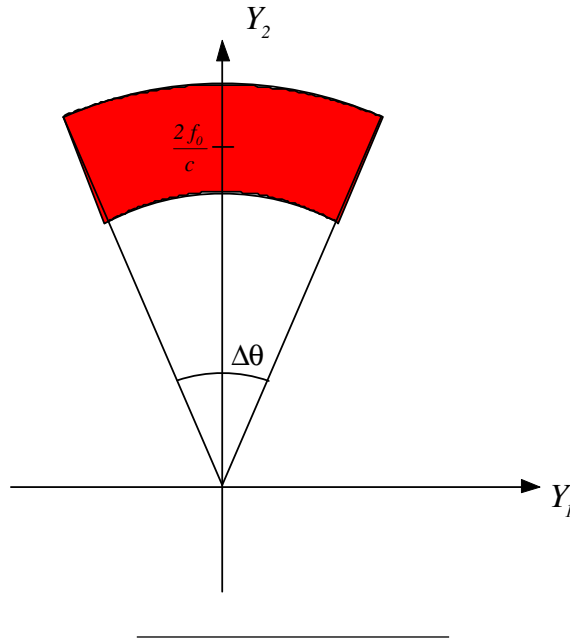
FIGURE 2.2: Spatial frequency domain

From Eq.(2.14) it is obvious that the motion compensated signal is the Fourier transform of the target reflectivity except for the term $W(Y_1, Y_2)$. $W(Y_1, Y_2)$ defines the region in the spatial frequencies domain where the signal is defined , see Fig.2.2.

The Inverse Fourier transform of Eq.(2.14) is the ISAR image which represents an estimate of the target reflectivity function in the range/cross-range domain. By assuming that the target is composed by K of point-like scatterers and neglecting the interactions between the scatterers the target reflectivity function can be written as

$$\sigma\left(y_1, y_2\right) = \sum_{k=1}^{K} \sigma_k \delta\left(y_1 - y_1^{(k)}, y_2 - y_2^{(k)}\right) \qquad (2.16)$$

where $y_1^{(k)}$, $y_2^{(k)}$ and σ_k are the cross-range and the range coordinates and the reflectivity value of the kth scatterer respectively

Eq.(2.14) can be rewritten as follows:

$$S_{R_C}\left(Y_1, Y_2\right) = W\left(Y_1, Y_2\right) \sum_{k=1}^{K} \sigma_k e^{-j2\pi\left(Y_1 y_1^{(k)} + Y_2 y_2^{(k)}\right)} \qquad (2.17)$$

and its Inverse Fourier transform (IFT) is

$$I\left(y_1, y_2\right) = w\left(y_1, y_2\right) \otimes \otimes \sigma\left(y_1, y_2\right) = \sum_{k=1}^{K} \sigma_k w\left(y_1 - y_1^{(k)}, y_2 - y_2^{(k)}\right) \qquad (2.18)$$

where $w(y_1, y_2) = 2D - IFT\left[W(Y_1, Y_2)\right]$.

It is worth pointing out that the domain in which the compensated signal is defined, i.e. $W(Y_1, Y_2)$, is a portion of annulus in the (Y_1, Y_2)

Assuming that the total aspect angle variation $\Delta\Theta = \Omega_{eff}T_{obs}$ is small, the spatial frequencies can be approximated as follows:

$$\begin{cases} Y_1\left(f, t\right) \approx \frac{2\pi f_0}{c}\Omega_{eff}t \\ Y_2\left(f, t\right) \approx \frac{2\pi f}{c} \end{cases} \qquad (2.19)$$

It is worth noting that for Y_1 the frequency f has been substituted by the central frequency f_0, as a result of the approximation of the polar domain by a rectangular window, which intersects the angular sector at the coordinate $Y_2 = \frac{2f_0}{c}$. It should also be noted that this approximation is the one that leads to the minimum error, as it can be inferred by examining Fig.2.3 where the two polar and rectangular domains are represented.

Assuming the approximation in Eq.(2.19), then $W(Y_1, Y_2)$ is approximated by a rectangle in the (Y_1, Y_2) as shown in Fig.2.3. As a consequence the spatial frequencies can be assumed independent variables and the two-dimensional Inverse Fast Fourier Transform (2D-IFFT) can be applied to form the ISAR image.

Eq.2.17 can be rewritten as

$$S_{R_C}\left(f, t\right) = W\left(f, t\right)\sum_{k=1}^{K}\sigma_k e^{-j2\pi\left(f\tau_k + t\nu_k\right)} \qquad (2.20)$$

after a variable change from the spatial frequencies (Y_1, Y_2) to the delay time (τ) and Doppler (ν) coordinates expressed as

$$\begin{cases} \tau = \frac{2y_2}{c} \\ \nu = \frac{2f_0\Omega_{eff}y_1}{c} \end{cases} \qquad (2.21)$$
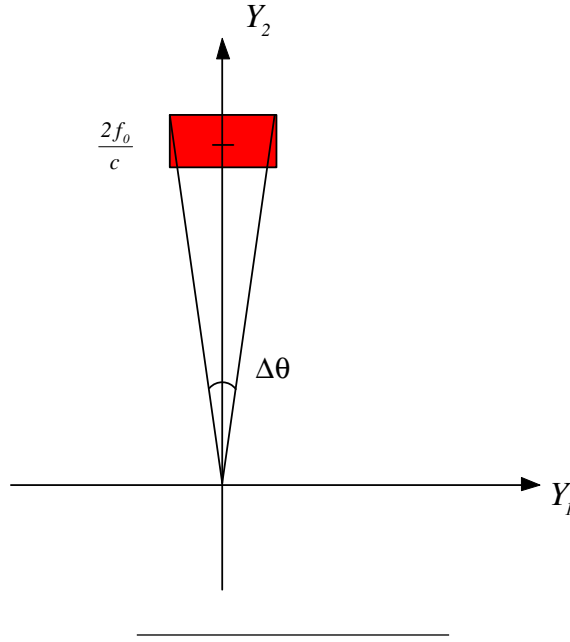
FIGURE 2.3: Approximated spatial frequency domain

The image in the delay time-Doppler frequency domain, $I(\tau, \nu)$, can be obtained via a $2D - IFFT$ of Eq.(2.20)

$$I(\tau, \nu) = w(\tau, \nu) \otimes \otimes \sum_{k=1}^{K} \sigma_k \delta(\tau - \tau_k, \nu - \nu_k) = \sum_{k=1}^{K} \sigma_k w(\tau - \tau_k, \nu - \nu_k) \quad (2.22)$$

Since

$$W(f,t) = rect\left(\frac{f - f_0}{B}\right) rect\left(\frac{t}{T_{obs}}\right) \quad (2.23)$$

then

$$w(\tau, \nu) = BT_{obs} sinc(\tau B) sinc(tT_{obs}) e^{-j2\pi f_0 \tau} \quad (2.24)$$

where $sinc(x) = \frac{sin(\pi x)}{\pi x}$.

Eq.(2.24) is the PSF of the system and can be used to find the resolution in the delay time Doppler dimensions. The resolution in the delay time (Δ_τ) and Doppler (Δ_ν) is defined as the first null of the *sinc* function:

$$\begin{aligned} \Delta_\tau &= \frac{1}{B} \\ \Delta_\nu &= \frac{1}{T_{obs}} \end{aligned} . \quad (2.25)$$

It is worth pointing out that Eq.(2.22) represents the ISAR image in the delay time Doppler domain. To obtain the image of the target in the spatial coordinates range (y_1) cross-range (y_2) a scaling operation is needed. From Eq.(2.21) the relationship between the cross-range and Doppler and between range and delay-time can be obtained

$$
\begin{aligned}
y_1 &= \frac{c}{2f_0\Omega_{eff}}\nu \\
y_2 &= \frac{c}{2}\tau
\end{aligned}
\tag{2.26}
$$

Eq.(2.26) shows that the scaling operation from delay time to range coordinate is straightforward while this is not true for the scaling operation from Doppler frequencies to cross-range coordinates. In fact this coordinates conversion involves the knowledge of the modulus of the effective rotation vector, $\mathbf{\Omega}_{eff}$. Ω_{eff} depends on the motion of the non-cooperative moving target and can not be assumed known in an ISAR scenario.

Another important consideration concerns the definition of the image plane where the target is represented. In Fig.2.1 the reference system T_y has been chosen so that the y_2 axis oriented along the LoS for $t = 0$ and the y_3 axis is parallel to the $\mathbf{\Omega}_{eff}$ vector that produces the aspect angle variation. Since any rotation around the LoS axis does not produce any aspect angle variation, it is quite obvious that $\mathbf{\Omega}_{eff}$ is the projection on the plane orthogonal to the LoS of the total rotation vector $\mathbf{\Omega}_T$. It can be expressed as:

$$
\mathbf{\Omega}_{eff}(t) = \mathbf{y}_2 \times [\mathbf{\Omega}_T(t) \times \mathbf{y}_2]
\tag{2.27}
$$

Therefore the cross-range axis $\mathbf{y_1}$ is

$$
\mathbf{y}_1 = \mathbf{y}_2 \times \mathbf{\Omega}_{eff}
\tag{2.28}
$$

where the dependency on t is dropped out because the image plane can be defined only if $\mathbf{\Omega}_{eff}$ is constant during the observation interval.

It is evident that as it happens for the cross-scaling operation the image plane depends on the unknown quantity $\mathbf{\Omega}_{eff}$ so that the image plane can not be a priori predicted. As it will be clearer at the end of this chapter this is the aspect that distinguish ISAR and SAR where the target motion is known, as well as Ω_{eff}.

Discrete formulation

In a real scenario both the variables in the signal domain (f, t) and in the image domain (τ, ν) are discrete variables. It is therefore important to write eq. (2.20) as a function of the discrete variables defined as:

$$
\begin{aligned}
f &= f_0 + n\Delta_f & n &= -\frac{N}{2}, ..., \frac{N}{2} - 1 \\
\tau &= n_\tau \Delta_\tau & n_\tau &= -\frac{N_\tau}{2}, ..., \frac{N_\tau}{2} - 1 \\
\nu &= m_\nu \Delta_\nu & m_\nu &= -\frac{M_\nu}{2}, ..., \frac{M_\nu}{2} - 1 \\
t &= mT_R & m &= \frac{M}{2} ... \frac{M}{2} - 1
\end{aligned}
\tag{2.29}
$$

Since the relationship between the frequency - slow time, (f, t), and the delay time - Doppler domain, (τ, ν), is given by a Fourier transform the sampling intervals can be expressed as follows:

$$
\begin{aligned}
\Delta_\tau &= \frac{1}{N\Delta_f} = \frac{1}{B} \\
\Delta_\nu &= \frac{1}{MT_R} = \frac{1}{T_{obs}} \\
M_\nu &= M \\
N_\tau &= N
\end{aligned}
\tag{2.30}
$$

The fully discrete signal becomes

$$
S_{R_c}(n, m) = W(n, m) \sum_{k=1}^{K} \sigma_k e^{-j2\pi\left(n\Delta f n_\tau^{(k)}\Delta_\tau + mT_R m_\nu^{(k)}\Delta_\nu\right)}
\tag{2.31}
$$

Considering Eq.(2.30), Eq.(2.32) can be rewritten as

$$
S_R(n, m) = W(n, m) \sum_{k=1}^{K} \sigma_k e^{-j2\pi\left(\frac{nn_\tau^{(k)}}{N} + \frac{mm_\nu^{(k)}}{M}\right)}
\tag{2.32}
$$

Eq.(2.32) can be interpreted as the result of a radar collecting a sample for each transmitted frequency for each sweep.

The data is therefore mapped in a polar grid in the spatial frequencies domain (Y_1, Y_2). The samples are generally not evenly spaced unless the hypothesis of effective rotation vector constant during the observation time, $\Omega_{eff}(t) \approx \Omega_{eff}$,
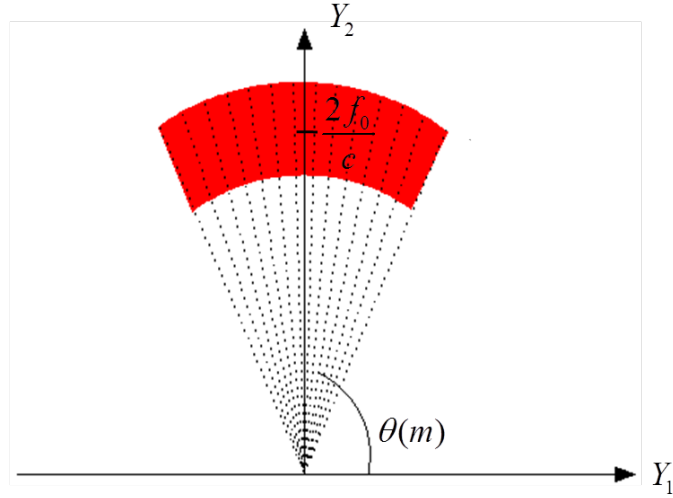
FIGURE 2.4: Discrete spatial frequency domain

holds true. In this case Eq.(2.15) becomes:

$$
\begin{cases}
Y_1(n,m) = \frac{2f_n}{c} sin(\Omega_{eff} m T_R) \\
Y_2(n,m) = \frac{2f_n}{c} cos(\Omega_{eff} m T_R)
\end{cases}
\tag{2.33}
$$

where $f_n = f_0 + n\Delta_f$.

Moreover, if the hypothesis of sufficiently small total aspect angle variation holds true the polar grid becomes a rectangular grid (see Fig.2.5) and 2D-IFFT can be applied to obtain the ISAR image. The rectangular grid is defined as

$$
\begin{cases}
Y_1(n,m) \approx \frac{2\pi f_0}{c} \Omega_{eff} m T_R \\
Y_2(n,m) \approx \frac{2\pi f_n}{c}
\end{cases}
\tag{2.34}
$$

Another important consideration must be drawn about the non-ambiguity region. In fact the sampling interval of the spatial frequencies may produce ambiguity in the ISAR image space if the system parameters are not set properly. In particular the size of the non-ambiguity region in the image domain can be found by means of the Nyquist condition considering the inverse of the sampling interval along the cross-range and range dimension Fig.2.6

$$
\begin{aligned}
D_{y1} &= \frac{1}{\Delta Y_1} = \frac{c}{2f_0 \Omega_{eff} T_R} \\
D_{y2} &= \frac{1}{\Delta Y_2} = \frac{c}{2\Delta_f}
\end{aligned}
\tag{2.35}
$$
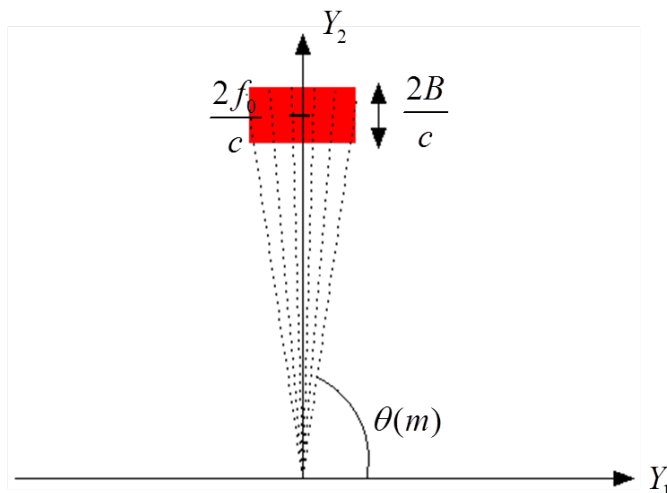
FIGURE 2.5: Approximated discrete spatial frequency domain
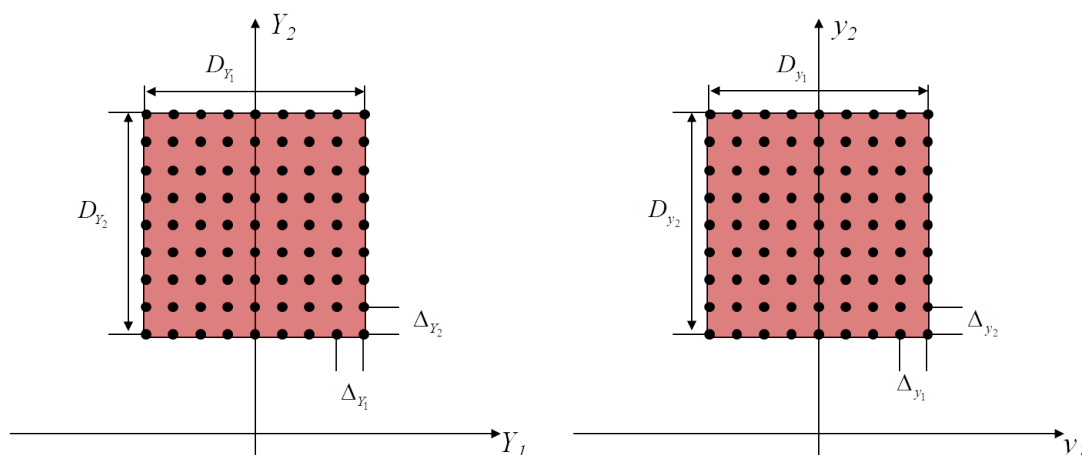
FIGURE 2.6: Non-ambiguity region

In order to avoid ambiguity these are the maximum size of the target. Any target bigger than the non-ambiguity region will be seen as "folded" in the image. It is important to notice that D_{y1} depends on the unknown value of Ω_{eff} so the target size along cross-range dimension is very difficult to be predicted.

In conclusion under the assumptions of straight iso-range approximation and small aspect angle variation, the ISAR processing to obtain high resolution imaging of a non-cooperative moving target is depicted in Fig.2.7. The steps of the ISAR processing are:

- range compression by means of matched filtering
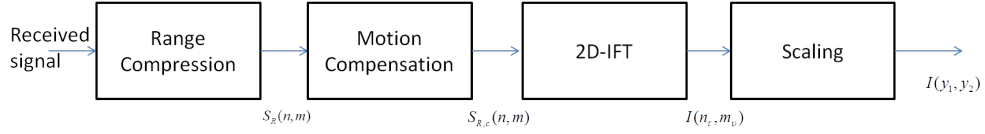
FIGURE 2.7: ISAR image formation processing

- target motion compensation

- 2D-IFFT

- spacial coordinate scaling $(\tau, \nu) -> (y_2, y_1)$

The ISAR processing depicted in Fig.2.7 is the typical Range-Doppler processing of monostatic ISAR systems. In the following section the bistatic case will be described.

2.2.2 Bistatic ISAR

In this section a brief review of the bistatic ISAR configuration will be provided and the differences from the classic monostatic scenario, described in Sect.2.2, will be highlighted. This is important because in a typical multichannel scenario there is only one transmitter and multiple receivers so that the configuration is intrinsically bistatic. An extensive theoretical analysis of the bistatic ISAR is provided in [12].

Consider the bistatic acquisition geometry shown in Fig.2.8. The received signal in the frequency - slow time domain after range compression by means of matched filter can be written as:

$$S_R(f,t) = W(f,t) \int\limits_V \sigma(\mathbf{y}) e^{-j\phi_{BI}(\mathbf{y},f,t)} d\mathbf{y} \tag{2.36}$$

where ϕ_{BI} is the bistatic phase. If the *straight iso-range approximation* holds the phase term can be written as:

$$\phi_{BI}(\mathbf{y},f,t) = \frac{2\pi f}{c} \left[R_{Tx}(t) + R_{Rx}(t) + \mathbf{y} \cdot \left(\mathbf{i}_{LoS_{Tx}}(t) + \mathbf{i}_{LoS_{Ty}}(t) \right) \right] \tag{2.37}$$

where R_{Tx} and R_{Rx} are the distances between the reference point on the target and the transmitter and receiver respectively and $\mathbf{i}_{LoS_{Tx}}(t)$ and $\mathbf{i}_{LoS_{Rx}}(t)$ are the unit
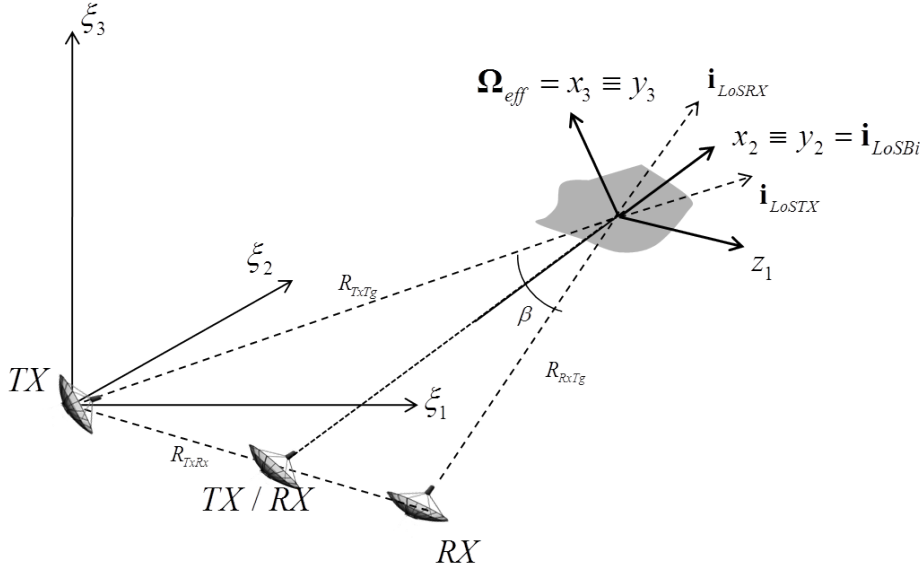
FIGURE 2.8: Bistatic ISAR Geometry

vectors that identify the transmitter and receiver LoS. After some mathematical manipulations the Eq.(2.37) becomes:

$$\phi_{BI}(\mathbf{y}, f, t) = \frac{4\pi f}{c} \left[\frac{R_{Tx}(t) + R_{Rx}(t)}{2} + K_{BI}(t)\, \mathbf{y} \cdot \mathbf{i}_{LoS_{BI}} \right] \qquad (2.38)$$

where

$$K_{BI}(t) = \left| \frac{\mathbf{i}_{Tx}(t) + \mathbf{i}_{Rx}(t)}{2} \right| = cos\left(\frac{\beta(t)}{2} \right) \qquad (2.39)$$

$$\beta(t) = arccos\left[\mathbf{i}_{LoS_{Tx}} \cdot \mathbf{i}_{LoS_{Rx}} \right] \qquad (2.40)$$

$$\mathbf{i}_{LoS_{BI}} = \frac{\mathbf{i}_{LoS_{Tx}} + \mathbf{i}_{LoS_{Rx}}}{|\mathbf{i}_{LoS_{Tx}} + \mathbf{i}_{LoS_{Rx}}|} \qquad (2.41)$$

Eq. (2.39) represents the phase modulation due to the bistatic angle variation $\beta(t)$ expressed in Eq.(2.40). Eq.(2.41) is the LoS of the monostatic configuration equivalent to the real bistatic one. Comparing Eq.(2.4) and Eq.(2.38) it is evident that the phase delay for a bistatic configuration is equivalent to the monostatic case except for the presence of the phase modulation term $K_{BI}(t)$.

In a practical situation, the total aspect angle variation is small (typically a few degrees) so that the bistatic angle can be considered constant during the observation time that is $K_{BI}(t) = K_{BI_0}$. If this assumption does not hold true a distortion

in the system PSF and consequently in the ISAR image is present [12].

When $K(t) = K_0$ the bistatic signal can be treated in the same way of the monostatic signal. The geometry is shown in Fig.2.8 where T_y is the reference system embedded on the target with the $\mathbf{y}_2$ axis oriented along the bistatic LoS at $t = 0$ and T_x is the reference system embedded on the target with the axis x_2 oriented along the LoS at each time instant t. Considering the same mathematical manipulation shown in section2.2 the spatial frequencies can be defined as:

$$\begin{cases} Y_{1_{BI}}(f,t) = \frac{2f}{c} K_{BI_0} sin(\Omega_{eff} t) \\ Y_{2_{BI}}(f,t) = \frac{2f}{c} K_{BI_0} cos(\Omega_{eff} t) \end{cases} \qquad (2.42)$$

Under the assumption of small aspect angle variation, the relation in Eq.(2.42) can be approximated as:

$$\begin{cases} Y_{1_{BI}}(f,t) \approx \frac{2\pi f_0}{c} K_{BI_0} \Omega_{eff} t \\ Y_{2_{BI}}(f,t) \approx \frac{2\pi f}{c} K_{BI_0} \end{cases} \qquad (2.43)$$

In practice, the term K_0 produces a compression in the spatial frequencies domain that corresponds to an expansion in the image domain. The unknown term K_{BI_0} produces therefore an erroneous scaling of the image in both dimension. The estimation of K_{BI_0} is a crucial step for a correct scaling in the image domain.

In conclusion, under certain hypotheses, the bistatic ISAR configuration can be approximated with an equivalent monostatic configuration located halfway between the view angle of the transmitter and the receiver. The imaging processing is the same used for the classical monostatic configuration and the only difference consist in a correction factor in the scaling processing.

2.2.3 Multichannel ISAR signal model

In this section the signal model for a multichannel ISAR system will be provided. This is a generalization of the model in [13] in which the configuration with two orthogonal baselines is presented.

Consider the geometry shown in Fig.2.9 where a two dimensional array illuminates a non-cooperative moving target. The centre of the reference system T_ξ is placed
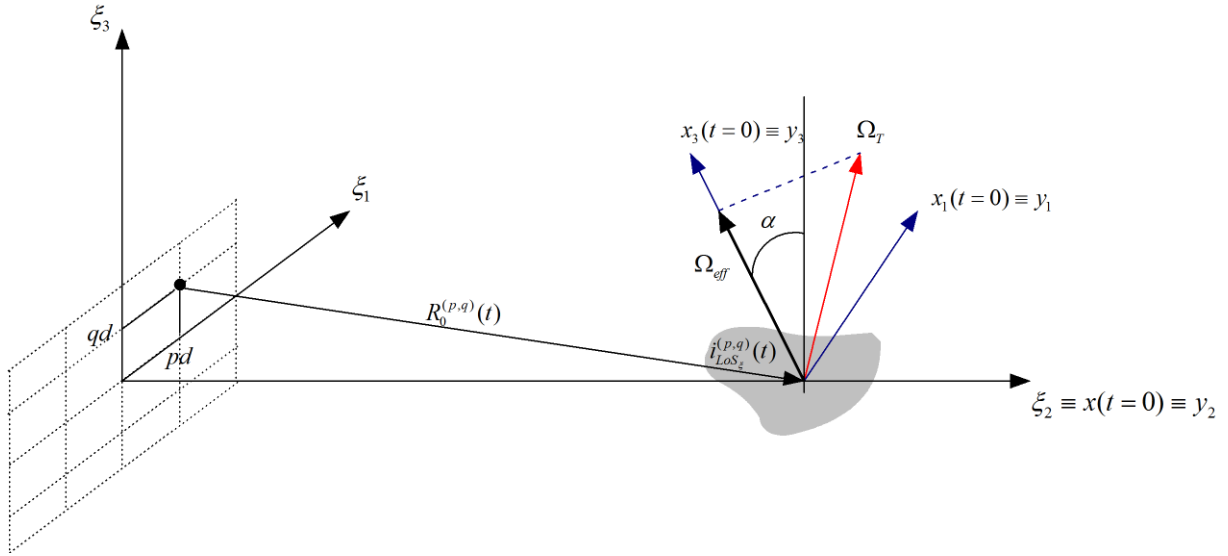
FIGURE 2.9: Multichannel ISAR Geometry

in the phase centre of the transmitter. The reference system T_ξ is oriented so that the axes ξ_2 is parallel to the radar LoS while ξ_1 and ξ_3 correspond to the horizontal and the vertical baseline respectively.

As stated in Sect. 2.2 the target motion can be seen as the superimposition of the translational motion of the reference point $R_0(t)$ and the rotational motion denoted by the rotation vector $\Omega_T(t)$ applied to the reference point. The projection of $\Omega_T(t)$ on the plane orthogonal to the LoS is the effective rotation vector $\Omega_{eff}(t)$. The reference system T_x is embedded on the target with the axes x_2 oriented along the LoS and the axes x_3 oriented along $\Omega_{eff}(t)$. The reference system T_y is embedded on the target, its orientation is fixed and coincides with T_x for $t = 0$. The angle α is the angle between ξ_3 and x_3.

In the considered configuration all the antennas are both transmitter and receivers. It has been demonstrated in Sect.2.2.2 that if only one antenna acts as transmitter and all the others are receivers an equivalent monostatic configuration for each bistatic couple of transmitter and receiver can be considered.

Assuming that the inter-element spacing, d is the same in both the dimensions, the couple (p, q) denotes the array elements placed in $\xi_1 = pd$, $\xi_2 = qd$ where $p = -\frac{P}{2}, ..., \frac{P}{2} - 1$ and $q = -\frac{Q}{2}, ..., \frac{Q}{2} - 1$ are the indexes that identify the element position in the array.

Similarly to what seen in Sect.2.2 the received signal from the generic element (p, q) can be written as:

$$S_R^{(p,q)}(f, t) = \int_V \sigma\left(\mathbf{y}\right)^{(p,q)} e^{-j\frac{4\pi f}{c}\left[R_0^{(p,q)}(t) + \mathbf{y} \cdot \mathbf{i}_{LoS_\xi}^{(p,q)}(t)\right]} d\mathbf{y} W(f, t) \qquad (2.44)$$

Considering an array size much smaller than the radar target distance $R_0(t)$ the reflectivity function can be assumed the same for each element, i.e., $\sigma\left(\mathbf{y}\right)^{(p,q)} = \sigma\left(\mathbf{y}\right)$.

Under the same hypotheses that hold in Sect.2.2 (stright iso range approximation and small aspect angle variation) the position of a scatter in the T_x reference system can be approximated as in Eq.(2.8). The rotation of T_x of an angle θ with respect T_ξ can be defined by a rotation matrix $\mathbf{M}_{\xi x}$:

$$\boldsymbol{M_{\xi x}} = \begin{bmatrix} \cos\alpha & 0 & \sin\alpha \\ 0 & 1 & 0 \\ -\sin\alpha & 0 & \cos\alpha \end{bmatrix} \qquad (2.45)$$

By means of the rotation matrix $\boldsymbol{M_{\xi x}}$, the LoS unit vector $\mathbf{i}_{LoS_x}^{(p,q)}(t)$, expressed with respect to T_x, can be written as the normalized difference between the positions of each sensor and the origin of T_x:

$$\mathbf{i}_{LoS_x}^{(p,q)}(t) = \boldsymbol{M_{\xi x}}\mathbf{i}_{LoS_\xi}^{(p,q)}(t) = \frac{1}{C}\begin{bmatrix} -pd\cos\alpha - qd\sin\alpha \\ R_0(t) \\ pd\sin\alpha - qd\cos\alpha \end{bmatrix} \qquad (2.46)$$

where

$$C = \sqrt{R_0^2(t) + (pd)^2 + (qd)^2} \approx R_0(t) \qquad (2.47)$$

is the normalization factor. The approximation in the right side term can be done because the radar target distance is much bigger than the distance between the generic array element and the array phase centre. Moreover $R_0(t) \approx R_0(0) = R_0$.

From [14] and considering Eq.(2.8)

$$\mathbf{y} \cdot \mathbf{i}_{LoS_\xi}^{(p,q)}(t) = \mathbf{x}(t) \cdot \mathbf{i}_{LoS_x}^{(p,q)}(t) = K_0^{(p,q)} + K_1^{(p,q)}t \qquad (2.48)$$

where

$$K_0^{(p,q)} = y_2 - \frac{d}{R_0} \left[y_1 \left(pcos\alpha + qsin\alpha \right) + y_3 \left(qcos\alpha - psin\alpha \right) \right]$$
$$K_1^{(p,q)} = c_2 - \frac{d}{R_0} \left[c_1 \left(pcos\alpha + qsin\alpha \right) + c_3 \left(qcos\alpha - psin\alpha \right) \right]$$

(2.49)

From Eq.(2.7) $c_2 = \Omega_{eff} y_1$

The ISAR PSF relative to a single scatterer located at $\mathbf{y}^{(}k)$ at the channel (p, q) can obtained after a 2D-IFT of the compensated signal and can then expressed as:

$$I^{(p,q)}(\tau, \nu) = B \cdot T_{obs} \cdot \sigma(y_1^{(k)}, y_2^{(k)}) \cdot e^{j2\pi f_0 \left(\tau - \frac{2}{c} K_0^{(p,q)} \right)} \times$$
$$\text{sinc} \left[T_{obs} \left(\nu + \frac{2f_0}{c} K_1^{(p,q)} \right) \right] \cdot \text{sinc} \left[B \left(\tau - \frac{2}{c} K_0^{(p,q)} \right) \right]$$

(2.50)

It is worth highlighting that under the assumption of array size much smaller than radar-target distance the K_0 and K_1 terms within the sinc functions can be approximated as:

$$K_0^{(p,q)} = y_2$$
$$K_1^{(p,q)} = c_2 = \Omega_{eff} y_1$$

(2.51)

It is obvious that the model presented so far for 2D array is still valid for linear arrays. In particular, the present work focuses on a system with a linear array, which is the case for $q = 0$.

In this case, after the scaling operation shown in Eq.(2.26), the ISAR image at the pth channel can be expressed as:

$$I^{(p)}(y_1, y_2) = B \cdot T_{obs} \cdot \sigma(y_1^{(k)}, y_2^{(k)}) \cdot e^{j \frac{4\pi f_0}{c} \left(y_2 - K_0^{(p)} \right)} \times$$
$$\text{sinc} \left[T_{obs} \left(y_1 + y_1^{(k)} \right) \right] \cdot \text{sinc} \left[B \left(y_2 - y_2^{(k)} \right) \right]$$

(2.52)

In order to obtain an image by processing the images of all the P channels, those images should be summed. The sum can be done only if all the P are in phase, i.e. coherent sum. It is worth pointing out that since the focusing is performed with respect to a single focusing point, the P images are in phase only for this point. So, in order for the sum to be coherent, a bound for the phase difference among the other points of the images should be evaluated in order to find a condition to

meet for coherently sum the images. This condition can be found by imposing an upper bound to the maximum phase difference among the images as:

$$\frac{4\pi}{\lambda}(P-1)\frac{d}{R_0}\left(y_1\cos\alpha - y_3\sin\alpha\right) \leq \frac{\pi}{8} \tag{2.53}$$

That leads to:

$$D_{array} \leq \frac{\lambda R_0}{32\left(y_1\cos\alpha - y_3\sin\alpha\right)} \tag{2.54}$$

where $(y_1\cos\alpha - y_3\sin\alpha)$ is the target size in the ξ_1 dimension. It is quite clear that this condition depends on the array size and the target size along the direction parallel to the array. It is worth pointing out that this method can still be applied when the target size along ξ_1 dimension is bigger than the bound expressed in Eq.(2.54). In this case the the whole region must be split in smaller regions (with dimension lower than the bound in Eq.(2.54)) and the focusing applied on each of this region.

In order to better understand the distortions introduced when the requirement in Eq.(2.54) is not met a closed form of the attenuation term can be evaluated.

Consider the summation along the p channels so that the resulting image can be expressed as

$$\begin{aligned}
I(y_1, y_2) &= \sum_{p=-\frac{P}{2}}^{\frac{P}{2}-1} I^{(p)}(y_1, y_2) \\
&= I^{(0)}(y_1, y_2) \sum_{p=-\frac{P}{2}}^{\frac{P}{2}-1} e^{j\frac{4\pi}{\lambda}\frac{d}{R_0}y_1 p} \\
&= I^{(0)}(y_1, y_2) e^{+j\frac{4\pi}{\lambda}\frac{dPy_1}{2R_0}} \sum_{p=0}^{P-1} e^{j\frac{4\pi}{\lambda}\frac{d}{R_0}y_1 p}
\end{aligned} \tag{2.55}$$

In order to simplify the notation it has been considered the case in which $\alpha = 0$.

After some mathematical manipulations Eq.(2.55) becomes

$$I(y_1, y_2) = I^{(0)}(y_1, y_2)e^{j\frac{2\pi Pd}{\lambda 2R_0}y_1}\frac{\sin\left(\frac{2\pi dy_1 P}{\lambda R_0}\right)}{\sin\left(\frac{2\pi dy_1}{\lambda R_0}\right)} \tag{2.56}$$

The term $J(y_1) = \frac{\sin\left(\frac{2\pi dy_1 P}{\lambda R_0}\right)}{\sin\left(\frac{2\pi dy_1}{\lambda R_0}\right)}$ produces a distortion in the amplitude of the image due to the fact that for cross-range region far away from the focusing point the p images does not sum coherently as explained above.

In order to evaluate the attenuation introduced by the non-coherent summation along the channel dimension the term $J(y_1)$ can be evaluated. In Fig.2.10 the attenuation term $J(y_1)$ is shown for the radar centre-scene distance $R_0 = 5km$ a carrier frequency $f_0 = 10GHZ$ and an interelement distance obtained imposing the condition in Eq.(2.54) with $y_1 = 100m$ so that

$$d = \frac{\lambda R_0}{32y_1(P-1)} \tag{2.57}$$

As it can be noted the condition in Eq.(2.54) is very restrictive leading to a loss of $0.2dB$ within a distance of $100m$ from the focusing point.

In Fig.2.11 the case in which the interelement distance is fixed at $d = \frac{\lambda}{2}$ is shown and the attenuation term for different value of P is represented.

2.3 SAR signal model

In this section a brief review of the Synthetic Aperture Radar (SAR) signal model and SAR image formation algorithms will be provided for both the single channel and the multichannel cases .

2.3.1 Single channel SAR

Consider the Spotlight SAR acquisition geometry shown in Fig.2.12. The radar is mounted on a moving platform and illuminates the target area that remain the
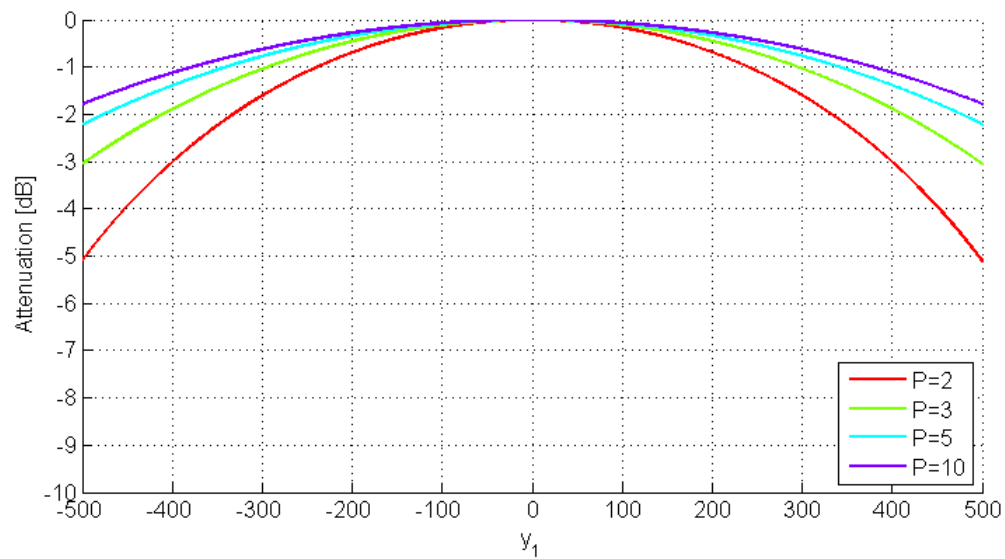
(a)
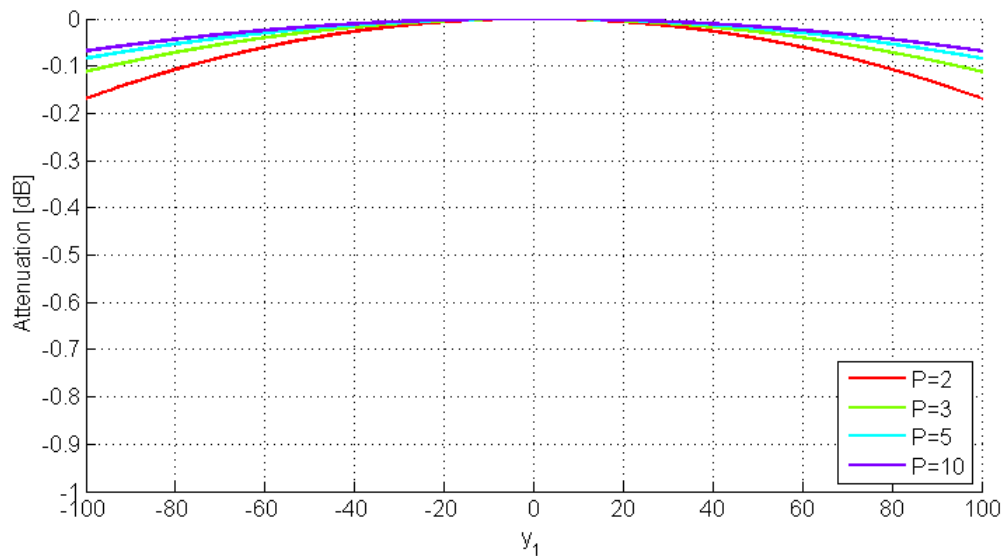
(b)

FIGURE 2.10: Attenuation factor

same for all the observation time since a proper time-varying beampattern steering to focus the transmitted energy on the same spot.

The radar moves with velocity v_p along the trajectory parallel to the cross-range y_1.

It is evident that this geometry is closely related to the ISAR geometry shown in Fig.2.1. In fact in both cases with a proper choice of the reference system it is possible to consider either the radar or the target as fixed and the other moving so that the ISAR and SAR scenario would be completely equivalent to each other.
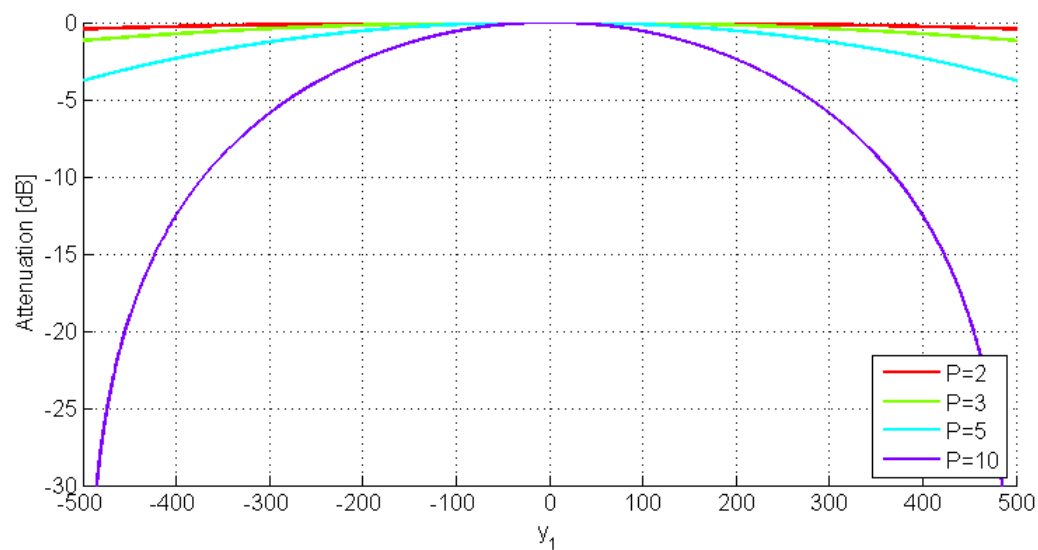
(a)
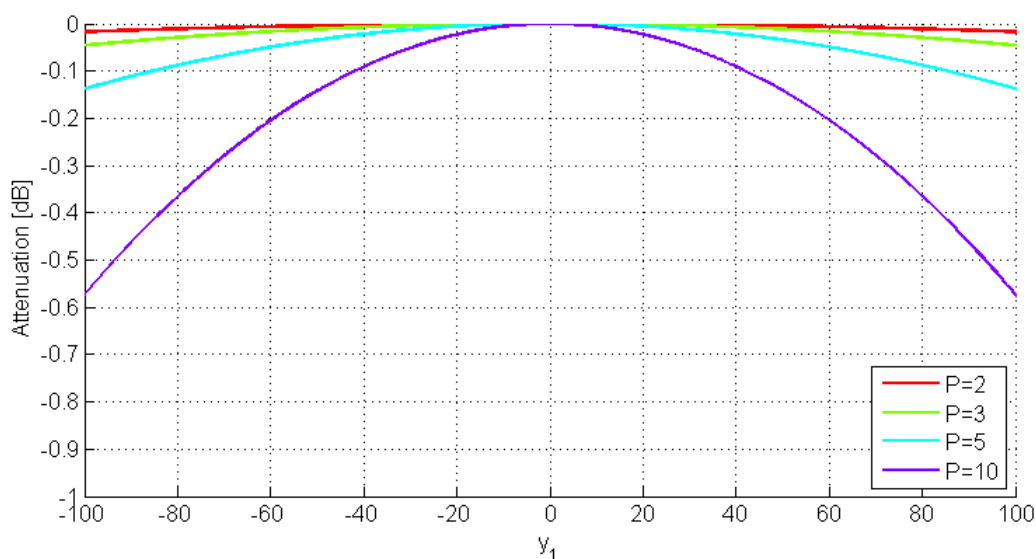
(b)

FIGURE 2.11: Attenuation factor $d = \frac{\lambda}{2}$

The real substantial difference is given by the cooperation of the target. In a SAR scenario the target scene is static or quasi-static and the radar moves along a trajectory that can be assumed a-priori known. So the geometry and kinematic is completely known. For an ISAR system the target is non-cooperative, so the system geometry and kinematic can not be assumed a priori known.

Under the same hypothesis that hold true in the Sect.2.2, i.e., straight iso range approximation and small total aspect angle variation, the received signal is the same of Eq.(2.10) with the only substantial difference that Ω_{eff} is known and can
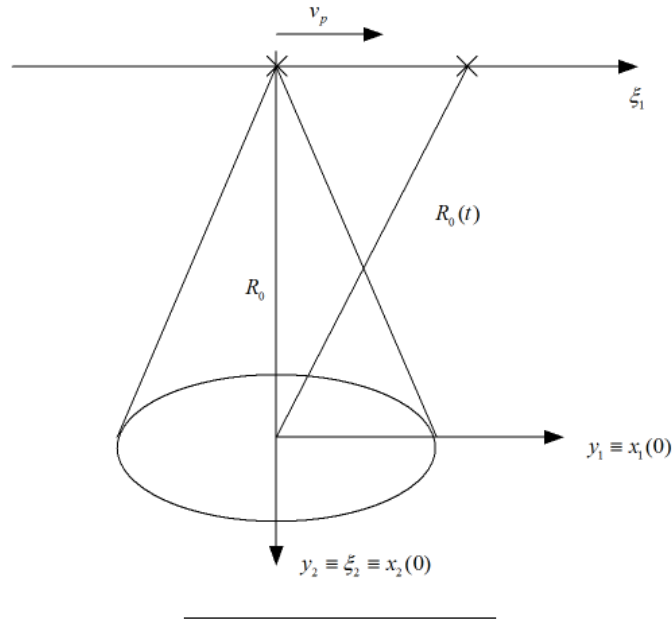
FIGURE 2.12: Single channel SAR geometry

be expressed as follows:

$$\Omega_{eff} = \frac{\Delta\theta}{T_{obs}} = 2atan\left(\frac{v_p T_{obs}}{2R_0}\right) \approx \frac{v_p}{R_0} \tag{2.58}$$

Substituting eq.(2.58) in eq.(2.19) and eq. (2.21) spatial frequencies become

$$\begin{cases} Y_1\left(f,t\right) \approx \frac{2\pi f_0}{c}\frac{v_p}{R_0}t \\ Y_2\left(f,t\right) \approx \frac{2\pi f}{c} \end{cases} \tag{2.59}$$

The expression of the image in the delay time Doppler domain is the Eq.(2.22) and the scaling factors are both a-priori known:

$$\begin{aligned} y_1 &= \frac{cR_0}{2f_0 v_p}\nu \\ y_2 &= \frac{c}{2}\tau \end{aligned} \tag{2.60}$$

The SAR image can then be obtained by means of a 2D-IFT of the received signal after the compensation of the relative motion between radar and target scene.

This algorithm (Fig.2.7) is the commonly known Range Doppler processing, it is the earliest method of imaging and was first implemented in the late 1970's [15]. It is evident from Eq.(2.60), the higher is the aspect angle variation the better are the resolution capabilities of the ISAR/SAR system in the cross-range

dimension. This is in contrast with the hypothesis of small aspect angle variation that makes the approximation in Eq.(2.19) valid. Although this is a problem in the ISAR scenario in a SAR systems the perfect knowledge of the kinematic is exploited to perform an interpolation from the polar grid to a rectangular grid. This is known in literature as *polar format processing*. It was introduced for high resolution spotlight SAR and has been used successfully for a numbers of year. More recently with the improvement of digital signal processing capabilities more precise algorithms have been introduced. These algorithms do not require the straight iso range approximation but they perform wavefront reconstruction with a matched filter (MF). In[16] a survey of some of these techniques is presented. It includes spatial MF interpolation (also known as $\omega - k$ [17] or range migration algorithm [18]), Range Stacking and Time Domain Correlation (TDC). The first algorithm offers the least computational time but requires an interpolation to map the measured data domain to the spatial frequencies domain. It will be used in this work so it is appropriate to remind the fundamental steps.

$\omega - k$

The received signal from a point like scatterer in a SAR system can be written in the frequency slow-time domain, without the application of the staight iso-range approximation:

$$s_R\left(f,t\right) = W(f,t) \int\limits_{y_1}\int\limits_{y_2} \sigma\left(y_1,y_2\right) e^{-j\frac{4\pi f}{c}\sqrt{\left[(R_0+y_2)^2+(y_1-v_pt)^2\right]}} dy_1 dy_2 \qquad (2.61)$$

where (y_1, y_2) are the coordinates of the scatterer.
The Fourier Transform of Eq.(2.61) in the $u = v_p t$ dimension, can be obtained exploiting the principle of stationary phase and the result in the (k, k_u) domain is:

$$S_R\left(f,k_u\right) = W\left(f,k_u\right) \int\limits_{y_1}\int\limits_{y_2} \sigma\left(y_1,y_2\right) e^{-j\sqrt{(4k^2+k_u^2)}(R_0+y_2)-jk_uy_1} dy_1 dy_2 \qquad (2.62)$$

where $k = \frac{2\pi f}{c}$.
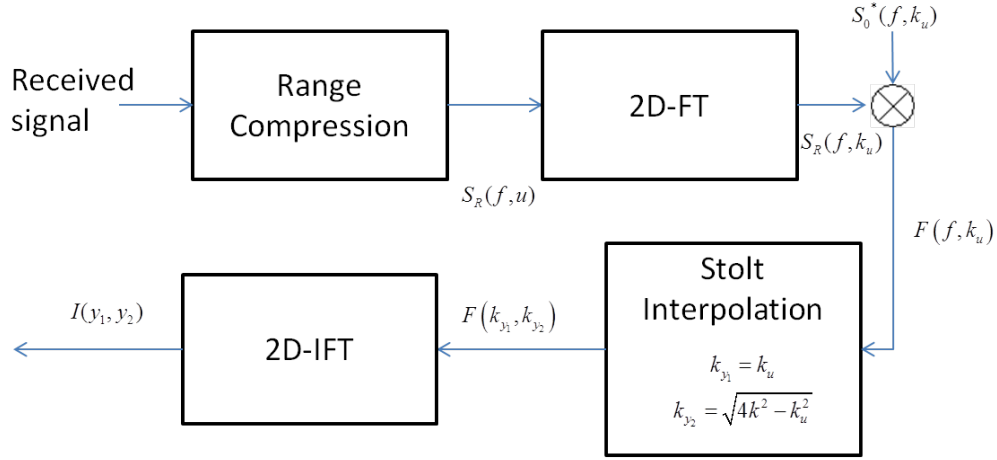
FIGURE 2.13: $\omega - k$ block diagram

Using the relationship between the measured and the spatial frequencies domain,

$$k_{y_2} = \sqrt{4k^2 - k_u^2}$$
$$k_{y_1} = k_u \tag{2.63}$$

Eq. (2.62) can be rewritten as

$$S_R\left(k_{y_2}, k_{y_1}\right) = W\left(k_{y_2}, k_{y_1}\right) \int\limits_{y_1} \int\limits_{y_2} \sigma\left(y_1, y_2\right) e^{-jk_{y_2}(R_0 + y_2) - jk_{y_1} y_1} dy_1 dy_2 \tag{2.64}$$

The MF is the complex conjugate of the signal $S_0\left(k_{y_2}, k_{y_1}\right)$ received from a scatterer placed in the focusing point $(y_1 = 0, y_2 = 0)$ that can be expressed as:

$$S_0\left(k_{y_2}, k_{y_1}\right) = W\left(k_{y_2}, k_{y_1}\right) e^{-jk_{y_2} R_0} \tag{2.65}$$

The output of the matched filter is Fourier to obtain the image.

$$I\left(y_1, y_2\right) = 2D - IFT\left[S_R\left(k_{y_2}, k_{y_1}\right) S_0^*\left(k_{y_2}, k_{y_1}\right)\right] = \sigma\left(y_1, y_2\right) \otimes \otimes w\left(y_1, y_2\right) \tag{2.66}$$

The functional block diagram of the $\omega - k$ image formation algorithms is shown in Fig. 3.2 where the Stolt interpolation step is required to map the signal to a rectangular grid before the 2D-IFFT.

2.3.2 Multichannel SAR

The SAR signal model derived in the previous section will be extended to the multichannel scenario in which the radar is composed by an array of P elements aligned along the flight path. The formulation of the multichannel $\omega - k$ [19] will be recalled.

As stated before, under the assumption of *straight iso-range approximation* and small aspect angle variation the multichannel SAR scenario can be seen as a particular case of the multichannel ISAR described in which all the kinematics are known Sect.2.2.3.

The corresponding ISAR image can be obtained by means of the multichannel Range Doppler algorithm. When these assumptions do not hold other algorithms must be exploited to obtain the SAR image such as multichannel matched filtering [19].

In order to explain how the multichannel MF works consider the multichannel acquisition geometry shown in Fig.2.14. The radar moves with velocity v_p along the trajectory parallel to the cross-range axis y_1. Considering the case in which each array elements transmits and receives. It is quite obvious from Sect.2.2.2 that the more realistic case in which only one elements transmits and all the elements receives can be approximated with the relative equivalent monostatic configuration and so the following model is still valid.

The received signal at the p array element after range compression can be expressed as:

$$s_{R_p}(f,t) = W(f,t) \int\limits_{y_1} \int\limits_{y_2} \sigma(y_1, y_2) e^{-j\frac{4\pi f}{c} R_p(y_1, y_2, t)} dy_1 dy_2 \qquad (2.67)$$

where

$$R_p(y_1, y_2, t) = \sqrt{(R_0 + y_2)^2 + (y_1 - v_p t - pd)^2)} \qquad (2.68)$$

After defining $u = v_p t$ the Fourier transform of eq.(2.67) can be evaluated exploiting the principle of stationary phase and is expressed as:

$$S_{R_p}(f, k_u) = W(f, k_u) \int\limits_{y_1} \int\limits_{y_2} \sigma(y_1, y_2) e^{-j\sqrt{(4k^2 + k_u^2)}(R_0 + y_2) - jk_u(y_1 - pd)} dy_1 dy_2 \quad (2.69)$$

Considering the spatial frequencies as in Eq.(2.63),Eq.(2.70) becomes
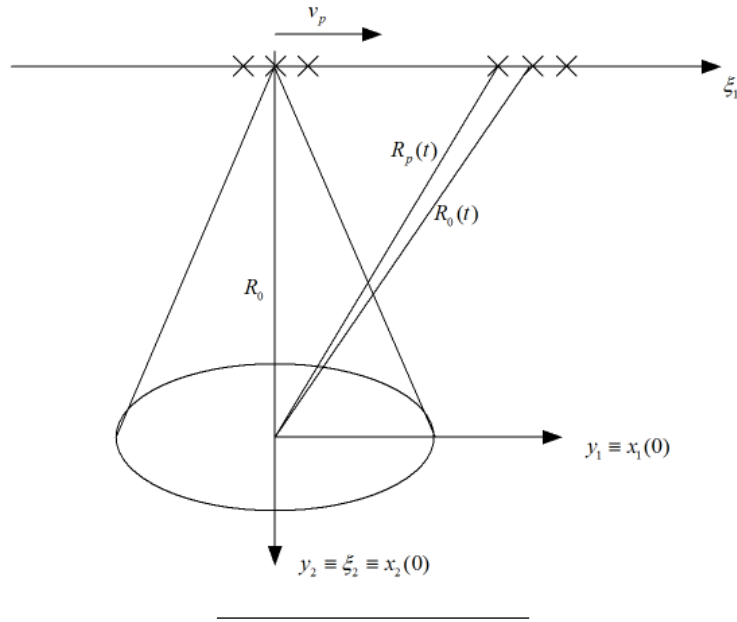
FIGURE 2.14: Multichannel SAR geometry

$$S_{R_p}(f, k_u) = W(f, k_u) \int_{y_1} \int_{y_2} \sigma(y_1, y_2) e^{-jk_{y_2}(R_0 + y_2) - jk_{y_1}(y_1 - pd)} dy_1 dy_2 \qquad (2.70)$$

The MF for the single channel p is the complex conjugate of the signal $S_0(k_{y_1}, k_{y_2})$ received from a scatterer placed in the focusing point $(y_1 = 0, y_2 = 0)$ that can be expressed as:

$$S_{0_p}(k_{y_1}, k_{y_2}) = W(k_{y_1}, k_{y_2}) e^{-jk_{y_2} R_0 - jk_{y_1} pd} \qquad (2.71)$$

and the image at the pth channel can be written as

$$I_p(y_1, y_2) = 2D - IFT \left[S_{R_p}(k_{y_1}, k_{y_2}) S_{0_p}^*(k_{y_1}, k_{y_2}) \right] \qquad (2.72)$$

The multichannel SAR image can the obtained combining the p images as:

$$I(y_1, y_2) = 2D - IFT \left[\sum_p S_{R_p}(k_{y_1}, k_{y_2}) S_{0_p}^*(k_{y_1}, k_{y_2}) \right] \qquad (2.73)$$
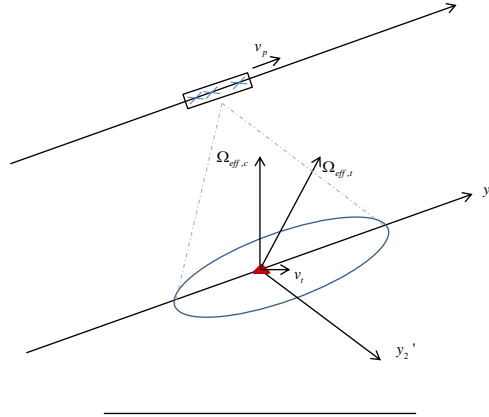
FIGURE 2.15: Acquisition scenario

$$I(y_1, y_2) = \sum_p I_p(y_1, y_2) = 2D - IFT\left[\sum_p S_{R_p}(k_{y_1}, k_{y_2})S_{0_p}^*(k_{y_1}, k_{y_2})\right] \quad (2.74)$$

2.4 Clutter Model

In this section the details about the clutter model exploited in the following will be given.

Consider the acquisition geometry shown in Fig.2.15[1]. A multichannel SAR system illuminates an extended static or quasi static scene in which few moving targets are present. The received signal at the pth sensor can be expressed the superimposition of three contributions:

$$S_p(f, t) = S_{t,p}(f, t) + S_{c,p}(f, t) + N_p(f, t) \quad (2.75)$$

where:

- $S_t(f, t)$ is the moving target contribution

- $S_c(f, t)$ is the static scene contribution

- $N(f, t)$ is the additive noise

[1]In this Figure the axis y_2' represents the ground range coordinates while in this work y_2 denotes the slant range coordinate which is usually referred to as range
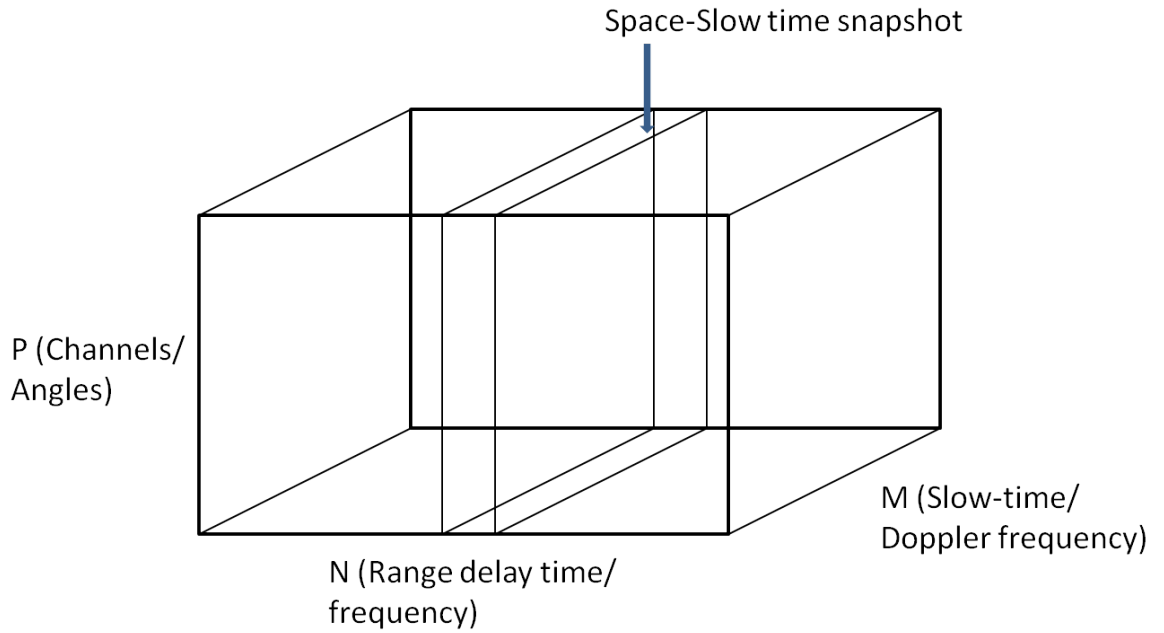
FIGURE 2.16: Data cube

In the problem of imaging of non-cooperative moving targets the return from the static scene is seen as clutter, so, a statistical description is needed in order to define the adaptive processing for clutter suppression.

In order to analyse space-slow time processing algorithms a simple model is sufficient. Considering the discrete version of Eq.(2.76) where the discrete variables are defined in eq. (2.29).

$$S_p(n, m) = S_{t,p}(n, m) + S_{c,p}(n, m) + N_p(n, m) \qquad (2.76)$$

The received signal is commonly represented in a data cube (Fig. 2.16) in which the dimensions represents range (frequency), slow time (Doppler), array element (angle) respectively. All the processing are performed in a space-slow time snapshot.

The received clutter echoes from different resolution cells can then be assumed independent. In the rth range cell the contribution of different scatterers are statistically independent. Since the received echo is the superimposition of a large number of scatterers it is assumed to be Gaussian with assigned correlation properties. To evaluate this correlation properties it can be noted that the values corresponding to the same position at different time instants are supposed to be

correlated with a correlation value depending on the time fluctuation of the observed scene. The hypothesis of stationarity is assumed to be verified during the observation time T_{obs}. Also the values received by two different channels at the same time interval are assumed to be correlated.

In [20] a Gaussian function is taken as mathematical model for both space and time correlation:

$$\rho_s(\Delta_d) = e^{-\frac{\Delta_d^2}{2\sigma_s^2}}$$
$$\rho_t(\Delta_t) = e^{-\frac{\Delta_t^2}{2\sigma_t^2}}$$

(2.77)

Then, considering a generic range cell (or delay time interval), the clutter space-time covariance matrix is calculated as:

$$E\left\{S_{c,i}^*(n_\tau, m)S_{c,k}(n_\tau, l)\right\} = P_c\rho_s\left[(m-l)v_pT_R + (i-k)d\right]\rho_t\left[(m-l)T_R\right] \quad (2.78)$$

where P_c is the clutter power, i and k denote the element indexes and m and l the slow time instants.

Another model for the clutter space-time covariance matrix is given in [21] and is expressed as:

$$E\left\{S_{c,i}(n_\tau, m)S_{c,k}^*(n_\tau, l)\right\} = 2P_cF(i) \otimes sinc\left(\frac{2}{\lambda}\left(d(i-k) + 2v_p(m-l)T_R\right)\right)$$

(2.79)

where $F(i)$ is a function that takes into account the effects of the sensor pattern and the reflectivity pattern of the target.

In the present work the clutter response will be simulated as a complex Gaussian random vector with covariance matrix defined in eq. (2.78) or eq. (2.79). Both models will be used in the simulations.

2.5 Multichannel Simulator

The algorithms that will be proposed in the present work will be tested on simulated data when real data are not available. All the simulations are performed using MATLAB. A block diagram of the simulator is shown in Fig.2.17.
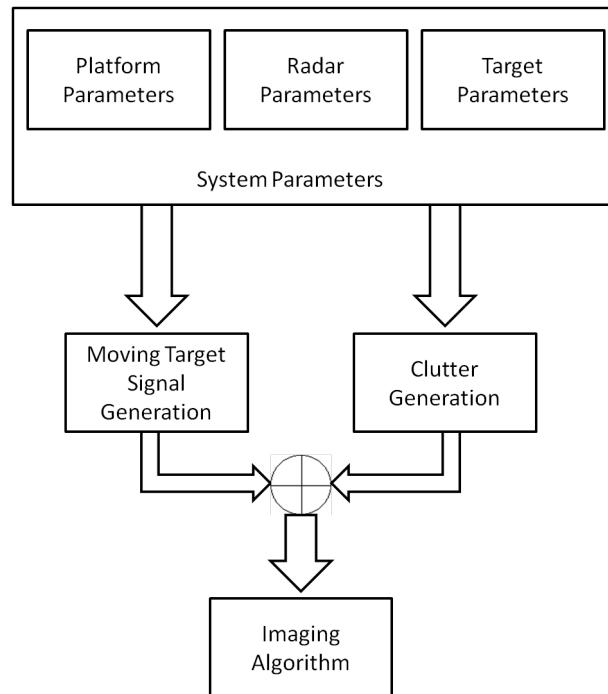
FIGURE 2.17: Simulator block diagram

System parameters

The first block sets up the parameters used to simulate the multichannel SAR system. This parameters can be grouped in the following classes:

- Platform Parameters: define the acquisition scenario setting the platform height (h), the platform velocity v_p and the incident angle θ_{in}

- Radar Parameters: define the radar characteristic setting the number of channels P the carrier frequency, f_0, the bandwidth of the transmitted signal, B, the number of frequency samples, N, the observation time, T_{obs} and the Pulse Repetition Frequency PRF.

- Target Parameters: define the motion of the non-cooperative moving target (velocity v and orientation α, and its reflectivity function for each scatterer $\sigma(y_1^{(k)}, y_2^{(k)})$.

Signal generation

The base band signal after range processing is generated as:

$$S_{t_p}(n, m) = \sum_k \sigma(y_1^{(k)}, y_2^{(k)}) e^{-j\frac{4\pi(f_0 + n\Delta f)}{c} R_{k,p}(mT_R)} \qquad (2.80)$$

where $R_{k,p}(mT_R)$ is the distance between the pth sensor and the kth scatterer.

Clutter Generation

The clutter contribution in the generic range cell (or delay time interval) n_τ with assigned covariance matrix (see Eq.(2.78) and Eq.(2.79)) can be obtained via a linear transformation of a Gaussian random vector with zero mean and Identity covariance matrix $\mathbf{n}$:

$$\mathbf{S}_c(n_\tau) = \mathbf{U}\mathbf{V}^{\frac{1}{2}}\mathbf{n} \qquad (2.81)$$

The matrices $\mathbf{U}$ and $\mathbf{V}$ are obtained via eigen decomposition of the assigned covariance matrix $\mathbf{R}$

$$\mathbf{R}_c = \mathbf{U}\mathbf{V}\mathbf{U}^H \qquad (2.82)$$

where $\mathbf{U}$ is the square matrix formed by the eigenvectors and $\mathbf{V}$ is the diagonal matrix of the eigenvalues.

in this way, the obatined clutter contribution is a zero mean Guassian Vector with covariance matrix $\mathbf{R}_c$

2.6 Conclusion

In this chapter a survey of the signal models that will be exploited in the next chapters has been presented. A brief review of the ISAR signal model has been provided for the monostatic, the bistatic and the multichannel case. Then, a SAR signal modelling has been given starting from an ISAR point of view. The multichannel scenario has been treated as well. Finally a clutter modelling has

been described, since it is fundamental to define the adaptive processing developed in the next chapters.

Chapter 3

High Resolution Imaging of Non-Cooperative targets in SAR images

3.1 Introduction

High resolution ISAR imaging of non-cooperative moving target in single channel SAR images is the core idea of this chapter.

A solution based on the application of ISAR processing will be described. A comprehensive description of the ISAR image formation process will be given. Results of the application of the proposed processing to two real datasets will be provided.

3.2 SAR systems and Moving Targets

Synthetic Aperture Radar (SAR) systems were originally employed in Earth observation applications, such as ocean, land, ice, snow and vegetation monitoring, among others [22], [23], [18]. Nevertheless, the ability to form high resolution images from remote platforms in all day/all weather conditions has also rapidly made SAR systems became very attractive for military and homeland security applications.

In such applications, man-made non-cooperative target imaging becomes the main

interest rather than the observation of natural phenomena.

Nevertheless, many SAR processors, which are designed to form highly focussed images at very high resolution, are based on the assumption that the illuminated area is static during the synthetic aperture formation [18]. As a consequence, standard SAR techniques are typically unable to focus moving targets while forming a focussed image of the static scene, leading to blurred and displaced images of any object that is not static during the synthetic aperture formation.

Many papers in literature deal with the problem of moving targets motion compensation. In [24] an algorithm for moving targets detection in SAR images and estimation of their motions parameters is proposed. In the same paper, however, the authors compensate for the Doppler shift by simply inserting the targets at the estimated position, and without performing phase compensation to eliminate motion induced phase errors. Moreover the algorithm needs of a sequence of SAR images of the same target to properly estimate its motion parameters.

In [25],[26], [27], [28], the authors attempt to compensate the relative motion between the SAR antenna phase center and the moving targets by first estimating target motion parameters and then by using the estimates in phase compensation. These papers, although proposing different methods, are based on the assumption that targets move along rectilinear trajectory with uniformly accelerated motion. In a real scenario however, air and maritime targets undergo translational and angular motions due, for example, to the manoeuvrings or the sea state so that a more proper target motion model should be accounted for.

In [29], [30] more complex target motions are considered, specifically both the papers aim at compensate the translational and rotational target motion. These methods however require the presence of multiple prominent scattering centres on the target that should be tracked across the aperture. In order to properly estimate the translational and rotational motions the authors state that at least 4 scatterers are required for each target. It could be difficult, however, to accurately isolate the received signal of such scatterers because of the target image is defocused and because the target is usually superimpose upon a clutter background.

Inverse Synthetic Aperture Radar (ISAR) has been suggested as another way to look at the problem of forming a synthetic aperture to high resolution images of non-cooperative targets [1],[2]. ISAR techniques do not base their functioning on the assumption that the target is static during the synthetic aperture formation. Conversely, the target motion is crucial for synthetic aperture formation. ISAR
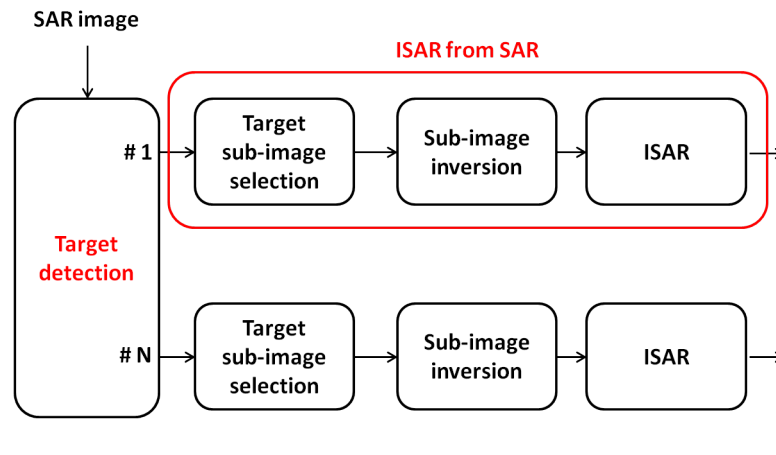
FIGURE 3.1: Block scheme of the detection and refocusing processor

techniques do not requere the knowledge of a priori information about the target's motion, but some other issues must be taken into account in ISAR image formation process. Typical problems are related to the cross-range scaling, the identification of the image plane and fact that the imaging system performance is not entirely predictable. Other image formation constraints may include the image size and the achievable cross-range resolution [1]. Notwithstanding, ISAR imaging provides acceptable solutions when SAR imaging fails, as it will be proven in this chapter on real data.

3.3 Proposed solution

In this work a solution based on the application of the ISAR processing to compensate the unknow part of the relative motion between radar and non-cooperative moving target is proposed. The functional block diagram is shown in Fig.3.1 and it is composed by the following main steps:

- Target Detection. Every target to be refocused must be detected within the SAR image. This is a crucial step because the unknown target motion leads to dispersion of the useful target energy over a wide region. Detection is a critical when dealing with ground target because of strong clutter.

- Target sub-image selection. Once detected every target must be cropped and separated from every contribution due to clutter and other targets. In

this way , a number of sub images equal to the number of detected targets is obtained.

- Sub-image inversion. Since the ISAR processing takes as input raw data, an inversion map from target image to target raw data is mandatory. It is worth highlighting that raw data obtained from the whole SAR image is not a suitable input for the ISAR processing because it usually contains the returns from several moving targets each one with its own motion. ISAR processing must be applied to a single target raw data at each time.

- ISAR processing. It performs motion compensation and image formation

Details about sub-image inversion and ISAR processing will be given in the next sections while the detection will be extensively treated in the next chapters.

3.4 Sub-image inversion

Moving targets are typically displaced and defocused in SAR images because of their relative motion with respect to the scene center. Since man made targets of interests are usually non-cooperative, the use of Non-Cooperative Target Imaging (NCTI) techniques, such as ISAR, becomes mandatory.

As one of the aim of this work is refocusing SAR images of moving targets, the first challenging problem to be tackled in this work is the transformation of the SAR image containing the defocussed targets into raw data. This operation is mandatory since ISAR processors must process images in which only one target is present, in order to estimate its motion and perform the motion compensation. In SAR images usually a number of target is present, each one with its own motion, so that the ISAR processor is not able to properly estimate target motion parameters. So, sub images, each one containing only one target are cut away from the SAR image and then converted to raw data. The following sections address the problem of conversion focusing on two different algorithm, namely the Inverse $\omega - k$ and the Inverse Range Doppler.
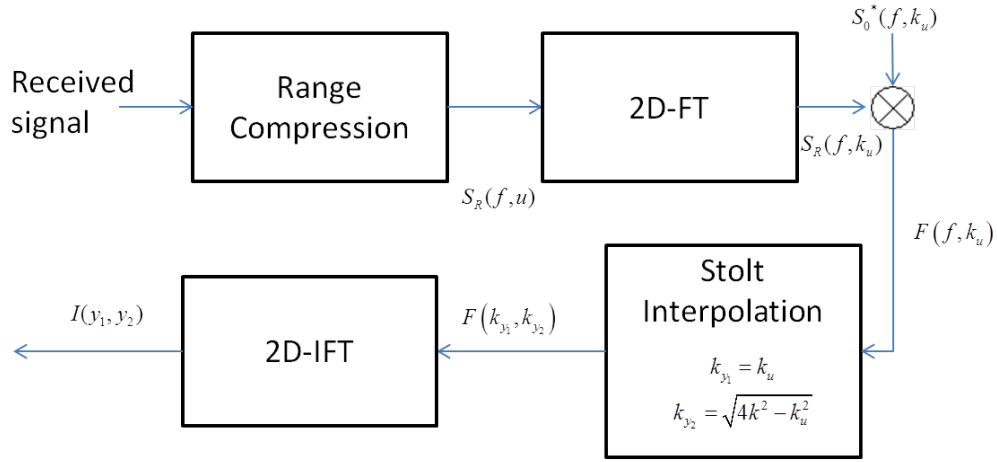
FIGURE 3.2: $\omega - k$ block diagram
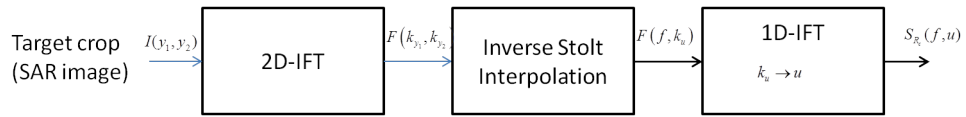
FIGURE 3.3: Inverse $\omega - k$ block diagram

3.4.1 Inverse $\omega - k$

The $\omega-k$ algorithm has been presented in Sect.2.3.1 and the relative block diagram is recalled in Fig.3.2 for the sake of clarity.

The inverse $\omega - k$ algorithm proposed in this work has been obtained by inverting each single step of the direct algorithm, as shown in Fig.3.3. It is worth highlighting that the $\omega - k$ algorithm makes use of an interpolation to obtain very high resolution SAR images. Unfortunately, such an operation on the data makes the $\omega-k$ algorithm not perfectly invertible, which means that some errors or artefacts may appear in the data after this type of inversion.

3.4.2 Inverse Range Doppler

When the total aspect angle variation is not too large and when the effective rotation vector is sufficiently constant during the observation time, the Range Doppler technique represents an accurate and computationally effective tool for SAR/ISAR image reconstruction.

Under these constraints, the polar grid in the spatial frequency domain can be

assumed to be a nearly regularly sampled rectangular grid. Therefore, a two-dimensional Fast Fourier Transform (FFT) can be used to reconstruct the image. In this case the inversion algorithm, namely Inverse Range Doppler (IRD), consists of a Fourier inversion, which is usually implemented via a two-dimensional inverse fast Fourier transform (IFFT).

It is worth pointing out that after the 2D-IFT a new spatial frequency domain must be defined for each SAR sub-image. As the resolution of the whole SAR image and that of the sub-image are equal, the observation time and the bandwidth must be the same. On the other hand, since the number of samples in the cross range and range of the crops are different the PRF and the frequency spacing, Δ_f in the equivalent raw data are different and can be calculated as follows:

$$
\begin{aligned}
PRF_{eq} &= \frac{N}{T_{obs}} \\
\Delta f_{eq} &= \frac{B}{M}
\end{aligned}
\tag{3.1}
$$

where N is the number of samples in the cross-range direction and M is the number of samples in the range direction of each sub-image.

3.5 ISAR processing

The data obtained by inverse Fourier transforming the sub-image is then used as input for the ISAR processor, which provides a well-focussed image of the target. The ISAR processing consists of four steps:

- Motion compensation

- Time window selection

- Image formation

- Cross-Range Scaling

3.5.1 Motion Compensation

The motion compensation (autofocusing) technique adopted here is the Image Contrast Based Autofocus (ICBA) algorithm [31]. The ICBA is a parametric

technique based on the Image Contrast (IC) maximisation.

As it has been shown in Sect.2.2 the received signal can be seen as the superimposition of the contributions due to the K scatterers:

$$S_R(f,t) = W(f,t) \sum_{k=1}^{K} \sigma_k e^{-j \frac{4\pi f}{c} R_k(t)} \tag{3.2}$$

where $R_k(t)$ is the distance between the radar and the kth scatterer. It is worth pointing out that after the SAR processing this distance take into account only the the target motion since the platform motion has been already compensated in the SAR image formation processing. Moreover Eq.(3.2) represents an approximation since the inversion process is not exact (due to the interpolation process).

If the target size is much smaller than the radar target distance the straight-iso range approximation holds and considering the geometry described in Sect.2.2 the residual distance can be approximated as:

$$R_k(t) = R_0(t) + \mathbf{y} \cdot \mathbf{i}_{LoS}(t) \tag{3.3}$$

The autofocus technique aims at removing the term $R_0(t)$ due to the target's residual translational motion. For a relatively short observation time interval T_{obs} and relatively smooth target motions, the radar-target residual distance can be expressed by means of a quadratic form, as

$$R_0(t) = R_0 + v_R t + \frac{a_R}{2} t^2 \tag{3.4}$$

where v_R and a_R are the radial velocity and acceleration of the target, respectively. The estimation of $R_0(t)$ coincides with the estimation of the target radial motion parameters. Let $\mathbf{\Theta} = [v_R, a_R]$ be a vector containing the unknown motion parameters, the radial motion compensation problem can be recast as an optimisation problem where the Image Contrast (IC) is maximised with respect to the unknown vector $\mathbf{\Theta}$, as defined in (3.5)

$$\hat{\mathbf{\Theta}} = \underset{\mathbf{\Theta}}{argmax} \left\{ IC\left(\mathbf{\Theta}\right) \right\} \tag{3.5}$$

where IC is defined as:

$$IC\left(\mathbf{\Theta}\right) = \frac{\sqrt{E\left\{ \left[I\left(\mathbf{\Theta}\right) - E\left[I\left(\mathbf{\Theta}\right) \right] \right]^2 \right\}}}{E\left\{ I\left(\mathbf{\Theta}\right) \right\}} \tag{3.6}$$

and where $E\{\cdot\}$ indicates an average operation, $I(\boldsymbol{\Theta})$ is the ISAR image magnitude after the compensation the target translational motion by using $\boldsymbol{\Theta}$ as focusing parameters. This can be expressed mathematically as:

$$I(\boldsymbol{\Theta}) = \left| 2D - IFT \left[S_R(f,t) \cdot e^{j\frac{4\pi f}{c}R_0(t)} \right] \right| \tag{3.7}$$

3.5.2 Time Window Selection

As stated in Sect.2.2 the RD technique can be successfully applied when the effective rotation vector does not change significantly during the observation time and when the total aspect angle variation is small.

However, the target motion may induce a non-uniform target rotation vector and especially for manoeuvring ships the aspect angle can be too large to properly apply the RD technique. In order to overcome these issues the Coherent Processing Interval (CPI) is controlled via a Time-Windowing approach.

In [32] an automatic selection of the time window is proposed. Specifically, the time window position across the data and its length are automatically chosen in order to obtain one or more images with the highest focus. The criterion used to define the highest focused image is based on the IC (Eq.(3.6)).

Therefore, the optimal position, $\bar{t}$, and length of the time window, Δt are obtained by maximising the IC with respect to the couple $(\bar{t}, \Delta t)$. Therefore, optimisation problem can be formulated as

$$\left(\bar{t}_{opt}, \Delta t_{opt} \right) = \underset{(\bar{t},\Delta t)}{argmax} \left[IC \left(\bar{t}, \Delta t \right) \right] \tag{3.8}$$

It is worth pointing out that a reduction of the CPI leads to a reduction in the cross-range resolution capability.

3.5.3 Image Formation

The image formation is the third step of the ISAR processing and it is based on a Fourier approach (see Sect.2.2).

Range-Doppler images are formed by applying a 2D-FT to the motion compensated data [1],[2]. The Fourier approach can be applied when the total aspect angle

variation is not too large and when the effective rotation vector is sufficiently constant. Under these assumptions the polar grid in the spatial frequency domain can be approximated by an uniformly sampled rectangular grid so that $I(\tau, \nu)$ is the complex valued ISAR image defined as:

$$I(\tau, \nu) = 2D - IFT\{S_{R_C}(f, t)\} \tag{3.9}$$

3.5.4 Cross-Range Scaling

ISAR processing generates two dimensional high resolution images of targets in time delay τ – Doppler domain ν. In order to determine the size of the target, it is preferable to have fully scaled image. The range scaling can be performed by using the well known relationship $y_2 = \frac{c\tau}{2}$. On the other hand, cross range scaling requires the estimation of the modulus of the target effective rotation vector Ω_{eff} (see Eq.(2.60)).

A novel algorithm has been proposed recently to solve this problem [33]. It is based on the assumption of quasi-constant target rotation. When the target rotation vector can be assumed constant within the coherent integration time, the chirp rate produced by the scattering centres can be related to the modulus of the target effective rotation vector by means of an analytically expression. Therefore each scattering centre carries information about the modulus of the target rotation vector through its chirp rate.

When the angular motions are slow and regular during the observation time, the analytical expression of the phase associated with a single scattering centre after motion compensation can be written as:

$$\phi_k(\mathbf{y}_k, f, t) = \left(-\frac{4\pi f}{c}\left[sin(\Omega_{eff}t)y_1^{(k)} + cos(\Omega_{eff}t)y_2^{(k)}\right]\right)rect\left(\frac{t}{T_{obs}}\right) \tag{3.10}$$

Eq.(3.10) can be rewritten considering a second-order Taylor's polynomial approximation as

$$\phi_k(\mathbf{y}_k, f, t) = \left(-\frac{4\pi f}{c}\left[\Omega_{eff}ty_1^{(k)} + y_2^{(k)} - \frac{y_2^{(k)}}{2}\Omega_{eff}^2t^2\right]\right)rect\left(\frac{t}{T_{obs}}\right) \tag{3.11}$$

So after range compression and considering only the kth resolution cell the received signal due to a single ideal scatterer is:

$$S_R(\tau_k, t) = \sigma_k e^{\left(-j\frac{4\pi f_0}{c}y_2^{(k)}\right)} e^{\left[-j\frac{4\pi f_0}{c}\left(y_1^{(k)}\Omega_{eff}t - \frac{y_2^{(k)}}{2}\Omega_{eff}^2 t^2\right)\right]} \tag{3.12}$$

By applying a second order Local Polynomial Fourier Transform (LPFT) [34] a complex 3 variables ISAR image can be obtained in the delay time-Doppler-Chirp Rate domain:

$$S_R(\tau_k, \nu, \mu) = \sigma_k e^{\left(-j\frac{4\pi f_0}{c}y_2^{(k)}\right)} \int_{-\frac{T_{obs}}{2}}^{\frac{T_{obs}}{2}} e^{\left[-j\pi\left(\left(\nu + \frac{2f_0}{c}y_1^{(k)}\Omega_{eff}\right)t + \frac{1}{2}\left(\mu - \frac{2f_0}{c}y_2^{(k)}\Omega_{eff}^2\right)t^2\right)\right]} dt \tag{3.13}$$

From Eq.(3.13) it is possible to estimate Doppler frequency, ν_k, and the chirp rate, μ_k, by maximizing the magnitude of $S_R(\tau_k, \nu, \mu)$ as

$$\begin{bmatrix} \hat{\nu} \\ \hat{\mu} \end{bmatrix} = \underset{(\nu,\mu)}{argmax}\left[S_R\left(\tau_k, \nu, \mu\right)\right] = \begin{bmatrix} -\frac{2f_0}{c}y_1^{(k)}\Omega_{eff} \\ \frac{2f_0}{c}y_2^{(k)}\Omega_{eff}^2 \end{bmatrix} \tag{3.14}$$

As it can be noted from Eq.(3.14) μ and Ω_{eff} are linked by the relation

$$\mu_k = \frac{2f_0}{c}y_2^{(k)}\Omega_{eff}^2 \tag{3.15}$$

that represents the equation of a straight line in variables μ_k and $y_2^{(k)}$.

So an estimate of the chirp rate $\hat{\mu}_k$ can be obtained and by substituting in Eq.(3.15)

$$\hat{\mu}_k = a y_2^{(k)} + \varepsilon_k \tag{3.16}$$

where ε_k is the estimation error and $a = \frac{2f_0}{c}\Omega_{eff}^2$ is the straight line angular coefficient. A number of scattering centres can be extracted from the ISAR image after image segmentation, and an equal number of chirp rate estimates can be produced. Therefore the problem of estimating the modulus of the effective rotation vector can be solved by estimating the straight line angular coefficient a from a set of

observation, $y_2^{(k)}$, and a set of estimates, $\hat{\mu}_k$. A simple solution for this problem can be obtained by using a least square error (LSE) method.

For the sake of clarity the algorithm can be summarised as follows:

- The ISAR image is segmented in order to extract N subimages $I_T^{(n)}(\tau, \nu)$ relative to N scattering centres. Their relative scattering centre location C_n is also calculated.

- Each subimages is inversely Fourier transformed in the Doppler domain in order to obtain N signals $S_{R_C}^{(n)}(\tau, t)$

- The N signals $S_R^{(n)}(\tau, t)$ are then used for the scattering chirp rate estimation by jointly using the 2-LPFT and the IC. Specifically the chirp rate is estimated by maximising the IC value of the image obtained by applying a second order LPFT to the signal $S_R^{(n)}(\tau, t)$.

- The chirp rate and the scattering locations obtained in the previous steps are used for the estimation of the modulus of the effective rotation vector via the Least Square Error (LSE) approach.

3.6 Experimental results

The results provided in this work are obtained by applying the proposed technique to two different datasets. A Cosmo SKYmed data and a Metasensing data.

3.6.1 Cosmo SkyMed Dataset

Dataset descriprion

The Cosmo-SkyMed (CSK) system consists of a constellation of four Low Earth Orbit mid-sized satellites, each equipped with a multi-mode high-resolution Synthetic Aperture Radar (SAR) operating at X-band. The system is completed by a Ground segment which provides the means and resources to manage and control the mission, to receive and process the data acquired by the satellites, and to disseminate and archive the generated products.

	SAR image	
	Istanbul	**Messina**
PRF	3312.72 Hz	2866.97 Hz
B	199.29 MHz	198.41 MHz
T_{obs}	1.5158 s	1.5186
θ_{in}	57	58
Polarisation	HH	HH
Look	right	right
Direction	Desc	Asc

TABLE 3.1: SAR images specifications

In order to ensure many combinations between image size and spatial resolution the system has been designed to operate in different modalities:

- a Spotlight mode providing low spatial resolution (smaller than 1 meter for civilian costumers) and swath size of $10km \times 10km$.

- two Stripmap modes: Himage mode and PingPong mode. Both modes provide spatial resolution of few meters and a swath size of tenth of kms. The PingPong mode implements a strip acquisition by alternating a pair of polarisation across burst.

- two ScanSAR modes providing from medium to coarse spatial resolution over large swath.

The refocussing algorithm has been tested on maritime targets since in the available SAR images some ships were clearly visible and no ground truth was needed to validate the results. Specifically two CSK SAR image have been processed, the first that covers the area of Messina and the latter that covers the area of Istanbul, which have been acquired on April 23, 2008 and on April 14, 2008 respectively. Some specifications of both the SAR images are summarised in Table 3.1, where θ_{in} is the incidence angle. It is worth pointing out that both the CSK SAR image have been obtained by processing the raw data by means of the $\omega - k$ algorithm.

TABLE 3.2: IC values

IC	SAR	ISAR-IRD	ISAR-IOK
Ship #1	6.2912	10.3545	9.8767
Ship #2	4.3425	6.5967	6.0036
Ship #3	6.9902	7.6421	7.0361
Ship #4	5.6503	7.6923	7.9231

Refocussing Results

Results obtained by applying ISAR image processing to SAR data are presented in this subsection. Specifically, the ICBA autofocusing technique is first applied to the entire sub-image data to refocus moving targets with simple motions.

The time windowing technique is then applied to the case of a moving target with complex motions, which cannot simply be refocussed by applying the autofocus technique to the entire data. Finally, cross-range scaling is applied to the refocussed ISAR images to obtain fully scaled ISAR images, which can directly lead to the target size estimation.

As a first case study, we will consider the problem of refocussing targets with simple motions, which usually do not require any time-windowing. These are typical cases where the target's motion is mainly due to its traslational movement, and therefore, the target's rotation vector can be assumed constant during the observation time. Three examples are shown in Figs. 3.4-3.7 that prove the effectiveness of the proposed refocussing algorithm. Specifically, both the refocussed ISAR images obtained by means of the IRD and IOK are shown to demonstrate that both inversion algorithms are effective.

To complete the result analysis, Table 3.2 contains the IC values of the SAR and the ISAR images obtained by using the whole observation time and both the IRD and the IOK techniques for each target.

By observing the results some considerations can be drawn. The proposed ISAR processing is able to produce well focussed radar images of moving targets when it is applied to data obtained by using the IRD or the IOK inversion algorithms. Therefore, there is no evident reason to prefer one inversion algorithm to another one in terms of image contrast (measurable from the image magnitude). Although the difference in terms of IC does not highlight very evident differences in the ISAR image magnitudes (it is also evident from a visual inspection point of view),

phase errors may be present. These errors are introduced by the IRD, because it is an approximated way of inverting the SAR image, or the IOK, because of the application of an interpolation, which is not an invertible operation. It should be said that phase errors introduced by the inversion algorithm may destroy useful information for phase-related applications/post processing, such as interferometry [35], super-resolution [36, 37] and so on.

As already stated, for long recorded data, the target rotation vector may not be constant during the observation time. Therefore, the Range Doppler technique used to form the ISAR images cannot produce well focussed images. This issue can be overcome by using a time windowing technique which involves sub-aperture formation. This technique allows for control of the Coherent Processing Interval (CPI) in order to select a time interval in which the target rotation vector is constant. Differently from the previous results, in the example below the necessity of using a time windowing algorithm is rather evident.

The target is a small manoeuvring target. As it can be noted by observing Fig.3.8-(a)-(b), the ISAR processing applied to the entire CPI is not able to produce well focussed target images. Furthermore, it is quite clear, by observing Fig. 3.8-(a)-(b), that the target experiences an evident yaw motion during the observation time.

By applying the time windowing technique, better image reconstruction can be obtained. Specifically, $T_{win} = 0.2\ s$ and $T_{step} = 0.1\ s$. In Fig. 3.9 several ISAR images of the target are shown that are obtained by using both the IRD and the IOK, each one obtained from a different time interval. By observing Fig. 3.9, it can be noted that the vessel orientation changes slightly from frame to frame.

The target ISAR images obtained by applying the automatic time windowing algorithm described in Sect.3.5.2 are shown in Fig.3.10. The IC values of both the target images are $IC_{IRD} = 8.41$ and $IC_{IOK} = 8.93$, respectively. As it can ben noted, although good images are obtained by manually choosing the window length , better results and better Doppler resolutions are obtained by using the automatic time windowing algorithm.

Fig. 3.11 (a) and (c), Fig. 3.12 (a) and (c), Fig. 3.13 (a) and (c), Fig. 3.14 (a) and (c) show the fully scaled ISAR images of the targets obtained by using both

TABLE 3.3: Estimated length of the vessels

|	IRD	IOK
Ship #1	131 m	124 m
Ship #2	178 m	164 m
Ship #3	139 m	125 m
Ship #4	78 m	67 m

the IRD and the IOK algorithms. Fig. 3.11 (b) and (d), Fig. 3.12 (b) and (d), Fig. 3.13 (b) and (d), Fig. 3.14 (b) and (d) show the estimated chirp rates (red dots) and the regression straight line (in blue), whose slope is proportional to the effective rotation vector modulus square value. As it can be noted, for each target, the chirp rate estimates fit very tightly the LSE straight line.
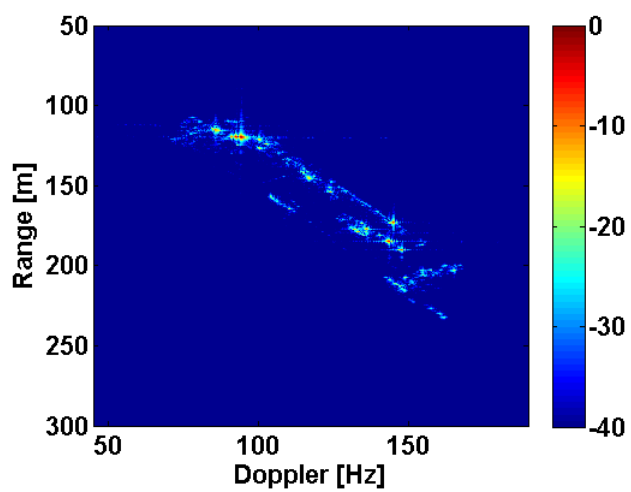
(a)
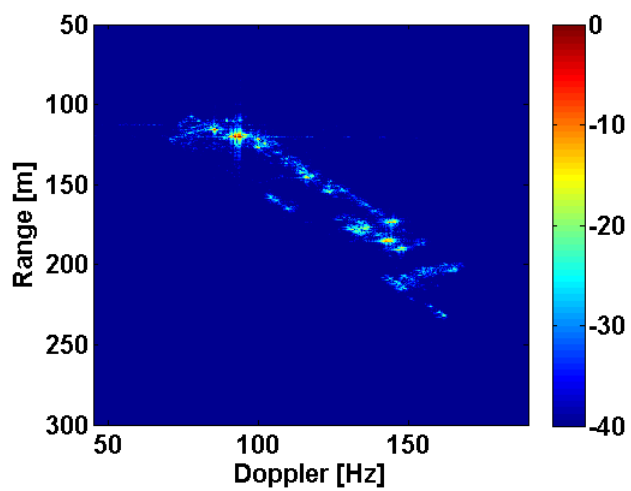
(b)
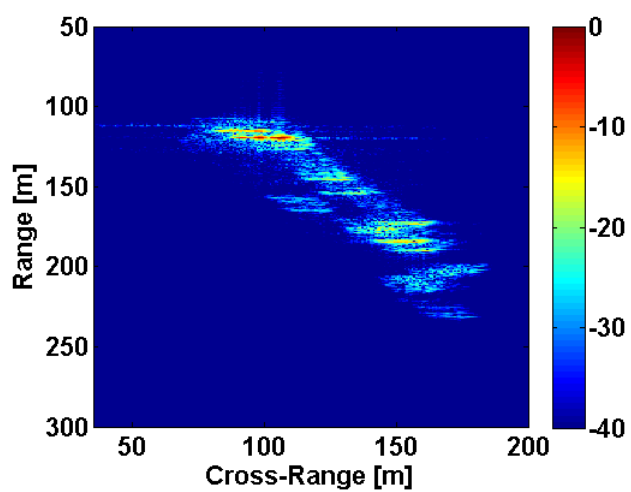
(c)

FIGURE 3.4: ISAR image of ship1 obtained by using the whole observation time and the IRD (a) and the IOK (b) and SAR image of ship 1 (c)

FIGURE 3.5: ISAR image of ship2 obtained by using the whole observation time and the IRD (a) and the IOK (b) and SAR image of ship 2 (c)

(a)
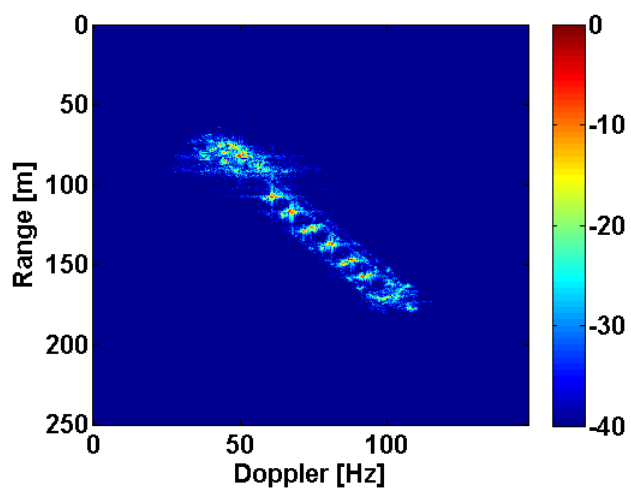
(b)
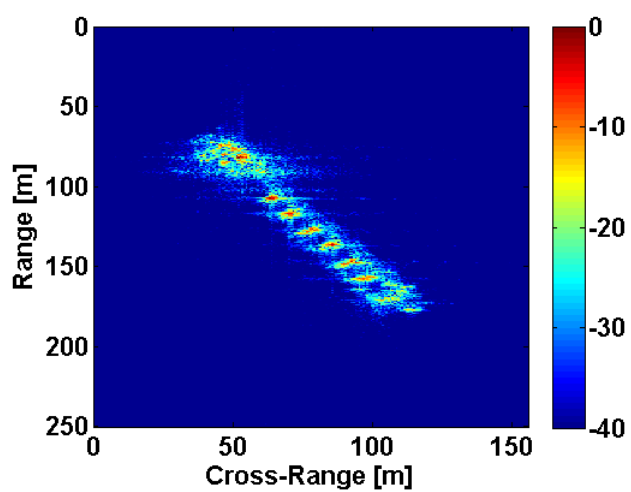
(c)

FIGURE 3.6: ISAR image of ship3 obtained by using the whole observation time and the IRD (a) and the IOK (b) and SAR image of ship 3 (c)
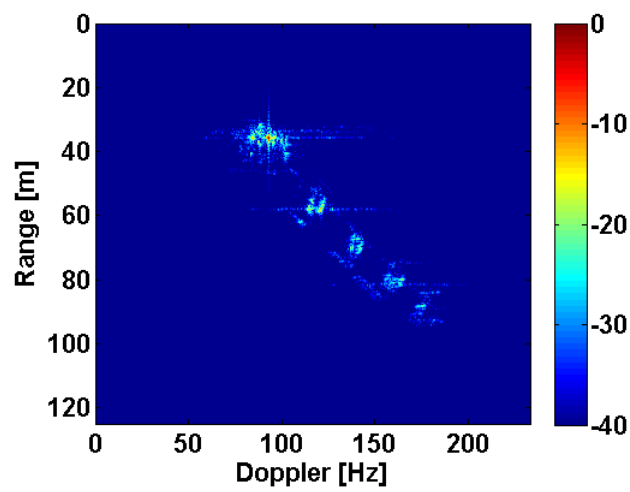
(a)
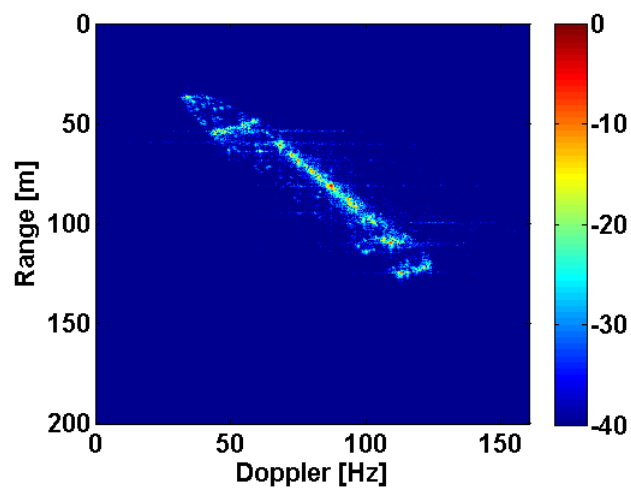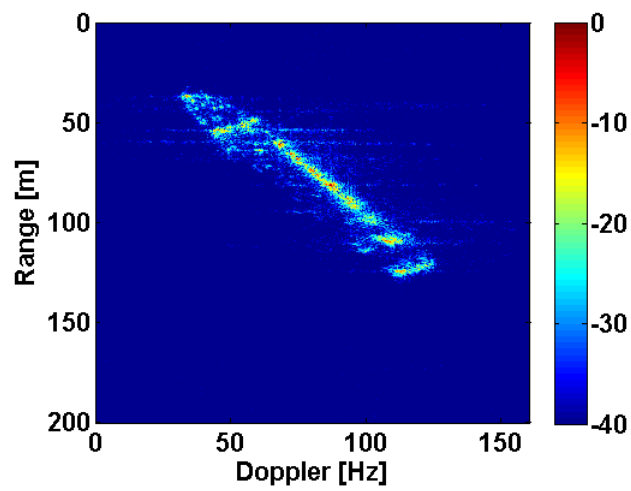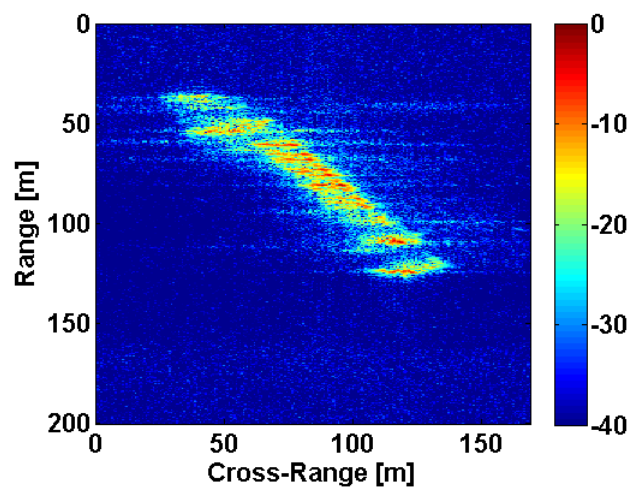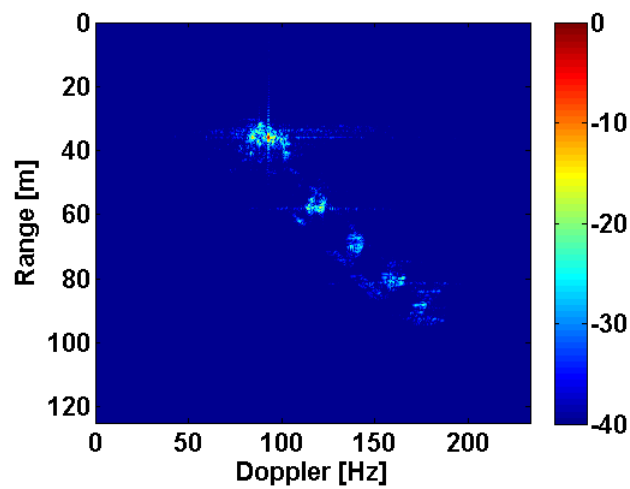

(b)
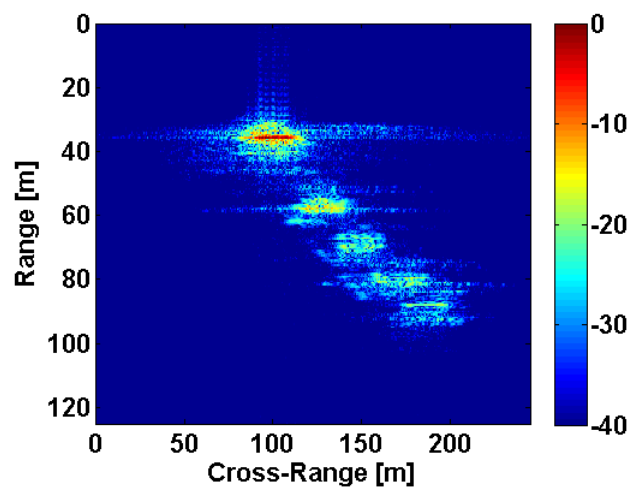
(c)

FIGURE 3.7: ISAR image of ship3 obtained by using the whole observation time and the IRD (a) and the IOK (b) and SAR image of ship 3 (c)
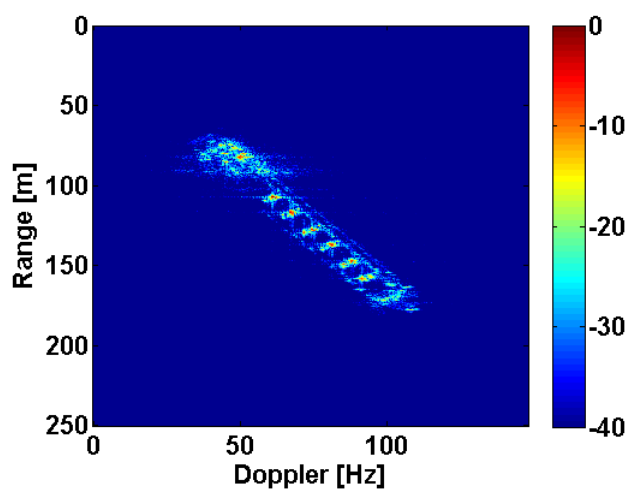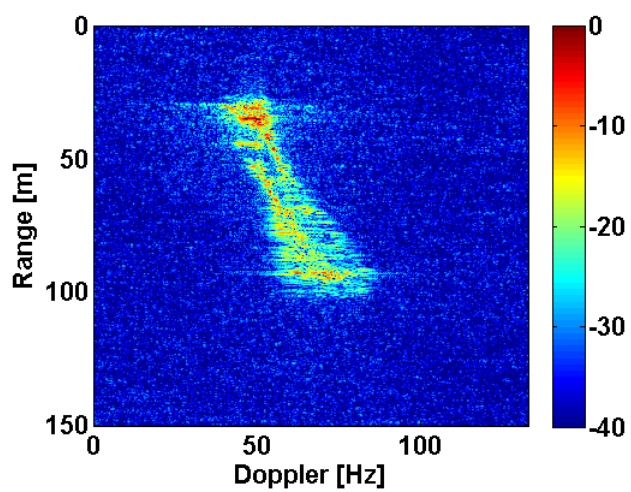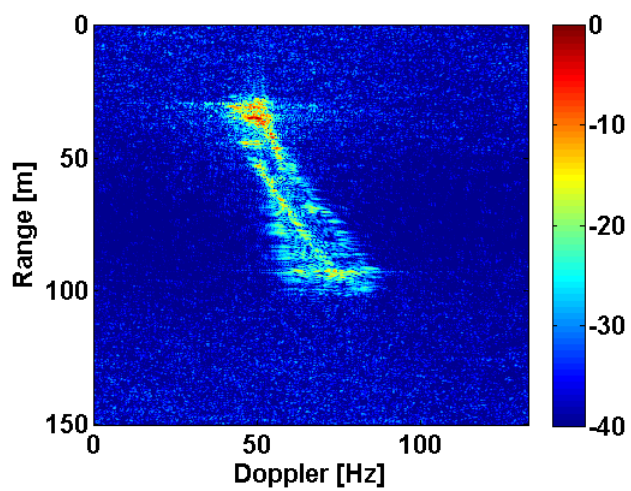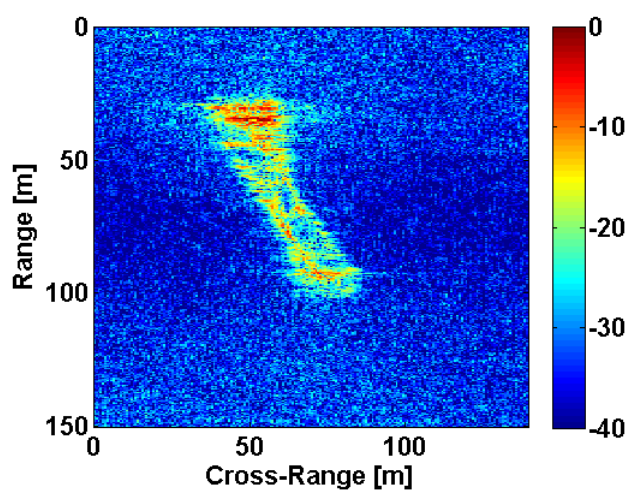
FIGURE 3.8: ISAR image of ship5 obtained by using the whole observation time and the IRD (a) and the IOK (b) and SAR image of ship 5 (c)
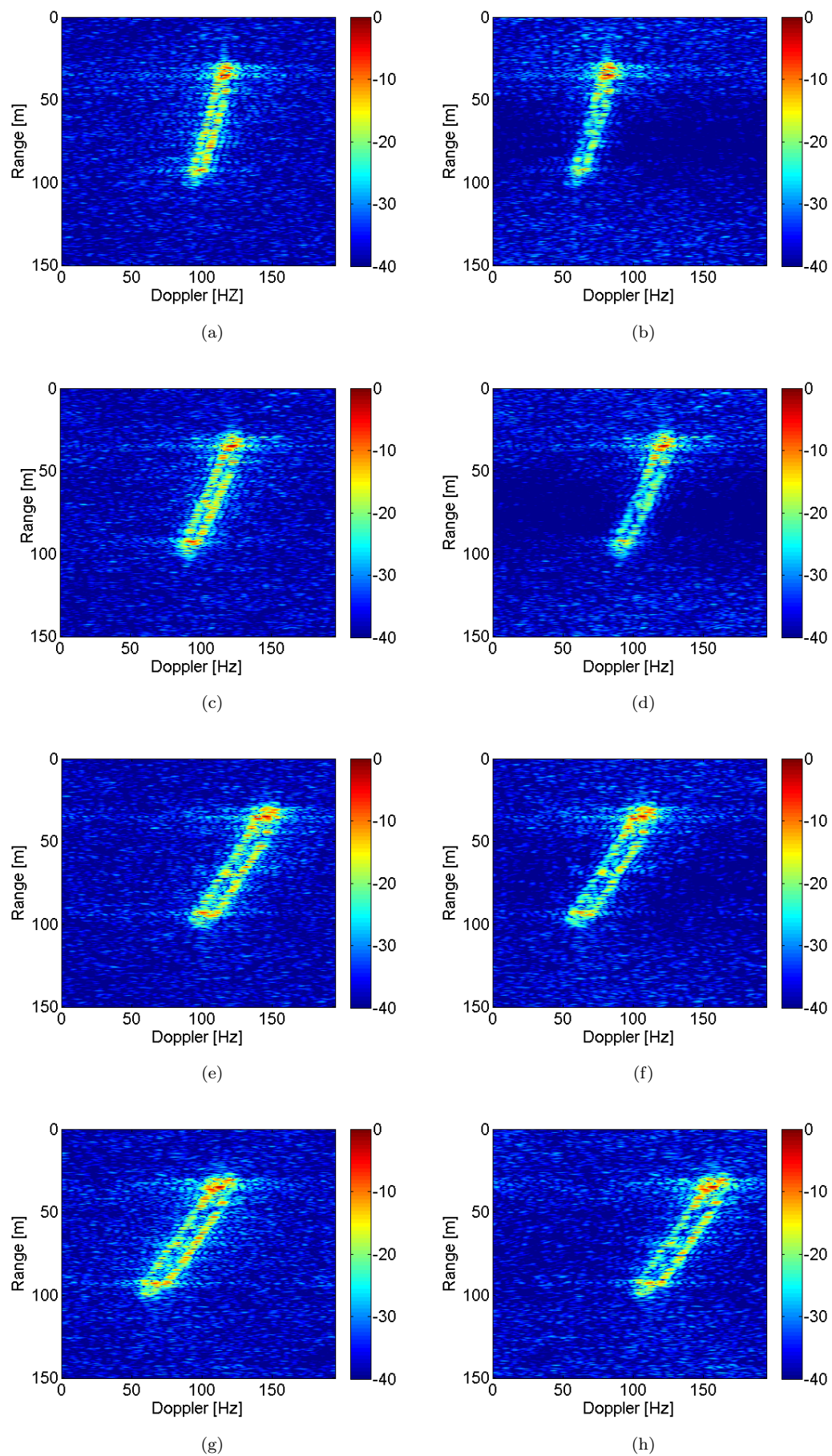
FIGURE 3.9: ISAR image sequences obtained by windowing the data (time sub-apertures) - IRD (a)-(c)-(e)-(g) and IOK (b)-(d)-(f)-(h)
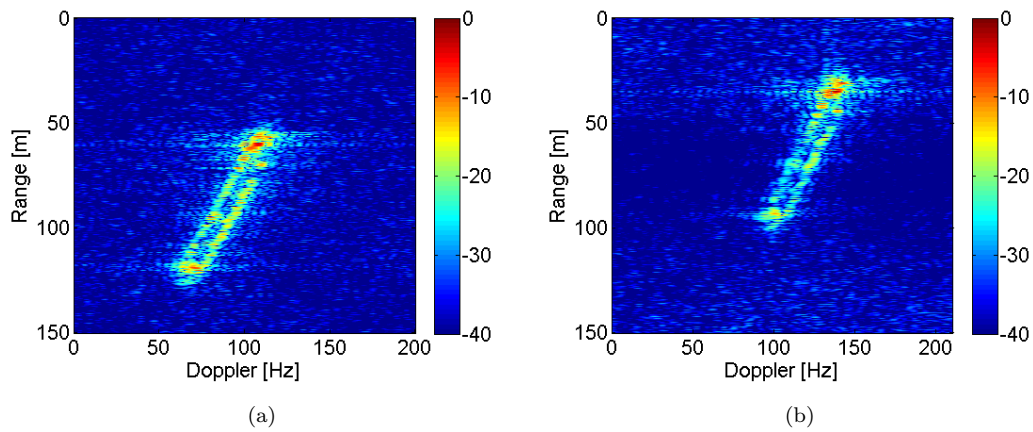
FIGURE 3.10: Most focussed ISAR image obtained by applying the IC based Time-Windowing technique - IRD (a) and IOK (b)
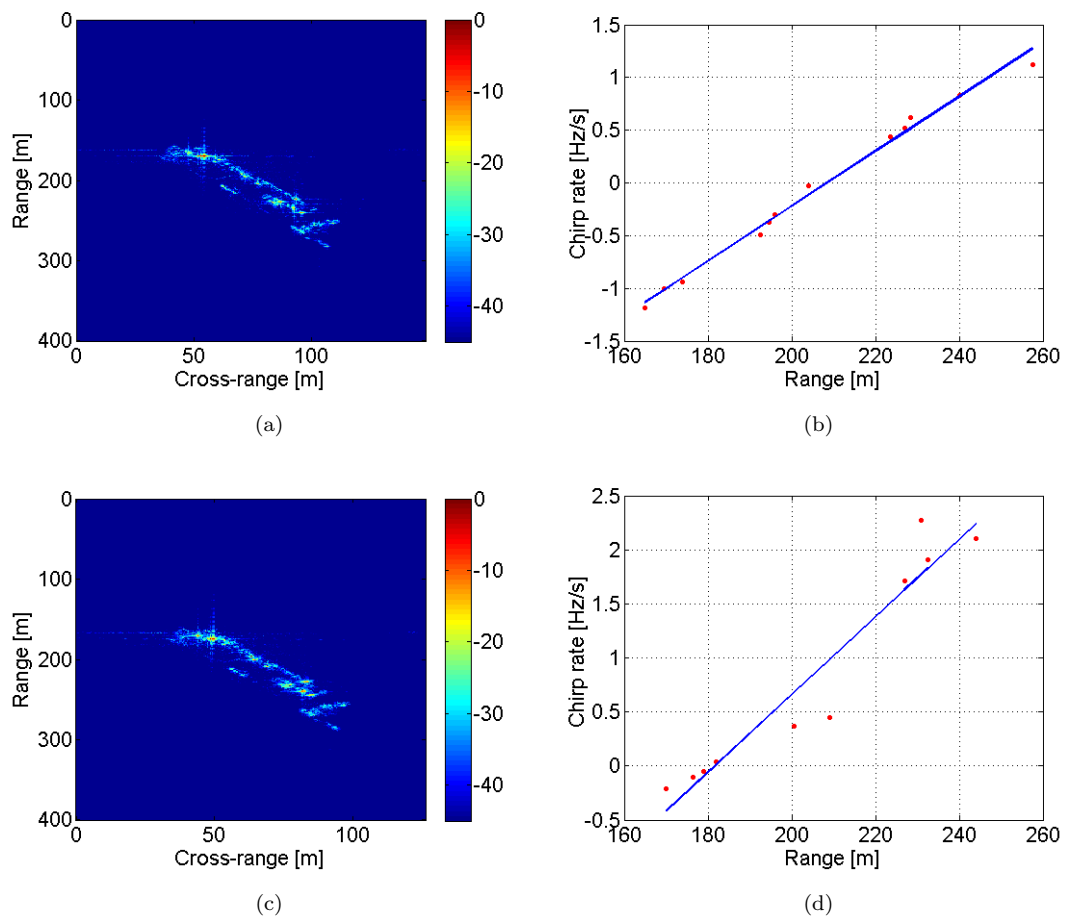
FIGURE 3.11: Fully scaled ISAR images obtained by applying the cross-range scaling technique and chirp rate estimates - IRD (a), (b) and IOK (c), (d)

(a)

(b)

(c)

(d)
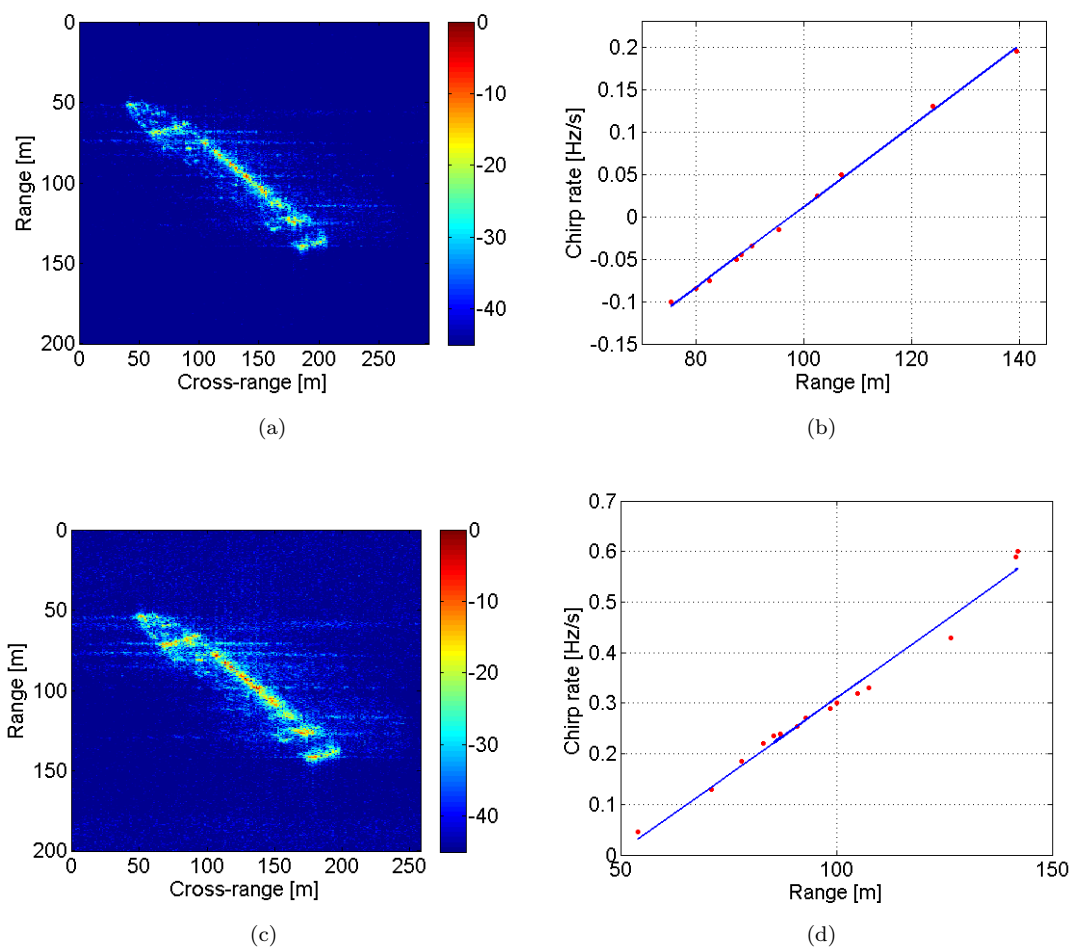
FIGURE 3.12: Fully scaled ISAR images obtained by applying the cross-range scaling technique and chirp rate estimates - IRD (a), (b) and IOK (c), (d)

(a)

(b)

(c)

(d)
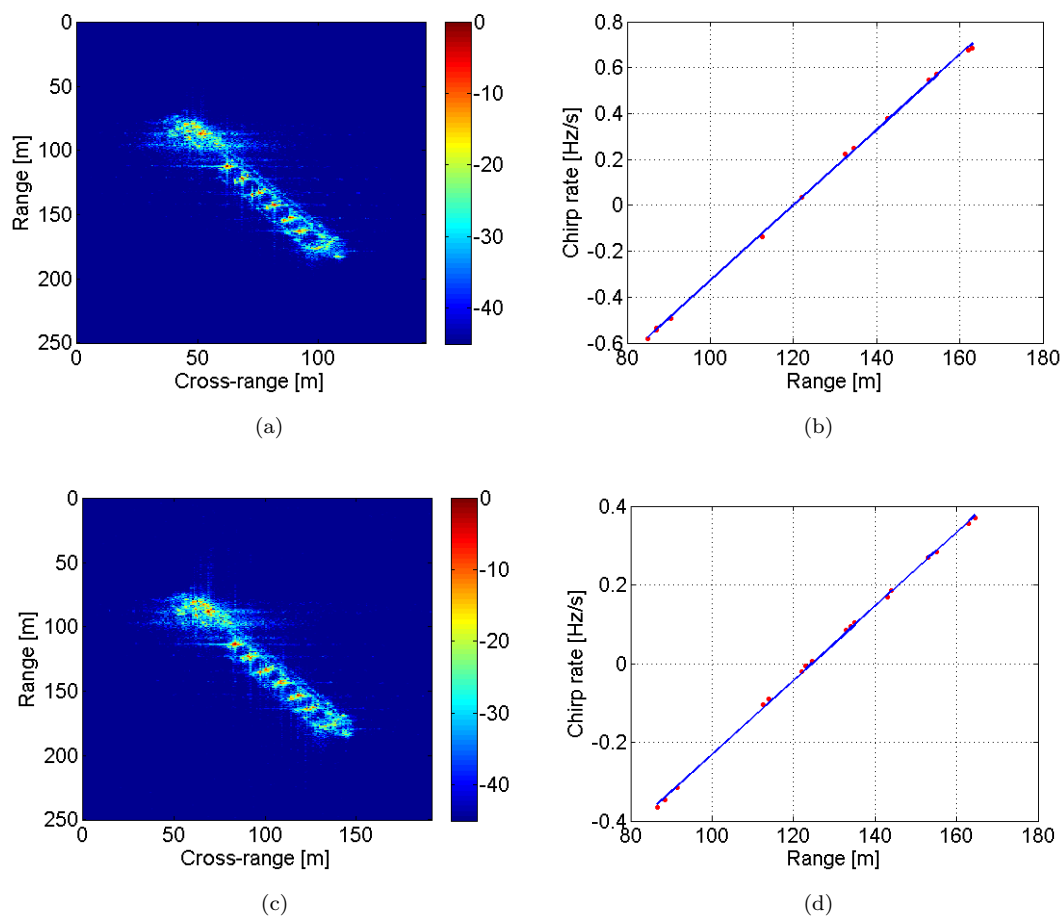
FIGURE 3.13: Fully scaled ISAR images obtained by applying the cross-range scaling technique and chirp rate estimates - IRD (a), (b) and IOK (c), (d)

(a)

(b)

(c)

(d)
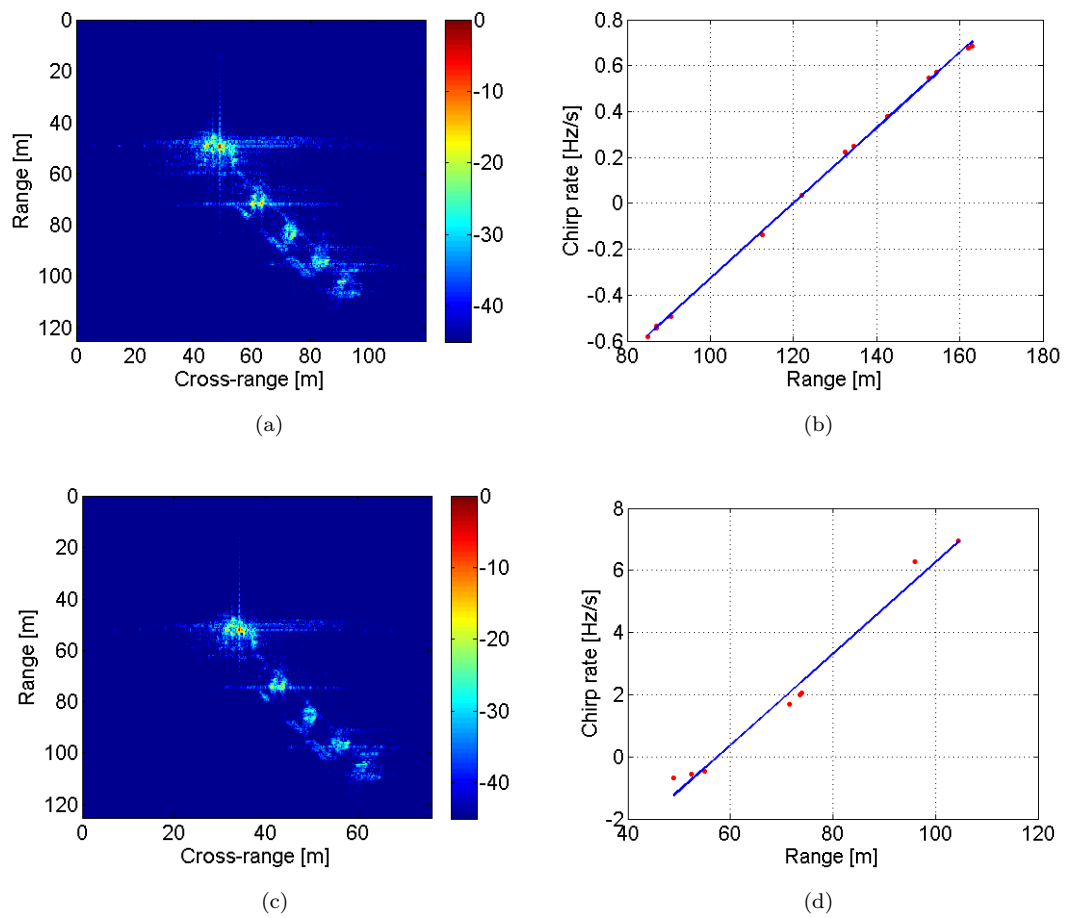
FIGURE 3.14: Fully scaled ISAR images obtained by applying the cross-range scaling technique and chirp rate estimates - IRD (a), (b) and IOK (c), (d)

3.6.2 MetaSensing Dataset

Dataset description

MetaSensing is a remote sensing company located on the site of the European Space Businesspark in Noordwijk, The Netherlands[1]. The airborne FMCW data was collected by MetaSensing over the harbor area of Rotterdam (The Netherlands). An overview of the area imaged is shown in Fig.3.15. MetaSensing dual polarimetric SAR system at X-band was installed on a Cessna 172 (see photo in Fig.3.15) taking off from Rotterdam airport. During the data gathering, the aircraft was flying at an altitude of approximately 1000 meters over the ground at a speed of nearly 50 m/s. The incident angle for the radar antenna is 45º. Data were collected at VV and VH polarization but only VV polarization is used for the present ISAR analysis. The radar central frequency is 9.6 GHz with a transmitted bandwidth 400 MHz. A maneuvering ship is present in the data that appears defocussed in the SAR image.

3.6.3 Refocussing Results

The SAR image of the acquired data is shown in Fig.3.16, where the non-cooperative target is highlighted with a red rectangle.

A zoomed-in version of the target's SAR image is provided in Fig.3.17 to emphasise the defocusing effect of the target's motions. An ISAR image sequence is obtained by applying the proposed technique and shown in Fig.3.19. Three sub-apertures are formed by using the time-windowing approach described in Section 3.5.2. Even though the results are not excellent due to the small size of the target, a significant improvement can still be seen with with respect to the original SAR image.

To strengthen this analysis, the cross-range scaling technique is applied to a refocussed ISAR image. The range/chirp-rate scatterplot is shown in Fig.3.20, whereas the rescaled image is shown in Fig.3.21. It is worth noting that no ground truth is available to compare the cross-range scaling results. Nevertheless, the size of the imaged target seems to be compatible with that in the picture in Fig.3.18.

---

[1]http://www.metasensing.com/

3.7 Conclusion

In this chapter a method to obtain high resolution images of non-cooperative moving targets in SAR images has been presented. It is based on the application of ISAR processing to each target detected in a SAR image. Details about the technique to obtain raw ISAR data from each SAR image crop containing a single target have been given and a description of the ISAR processing provided.

The effectiveness of this method has been tested on two real datasets.

it is worth pointing out that the proposed algorithm relies on the effective target detection within the SAR image. This detection process is straightforward when dealing with maritime target, since the sea clutter is lower than the target return. In this case, a clutter suppression step is not needed. Conversely, when dealing with ground clutter, suppression techniques must be applied since ground clutter return may be so strong to prevent the target detection. The following chapters will investigate this problem and suggest solution based on the exploitation of information from multichannel system.

FIGURE 3.15: Photo of Cessna 172
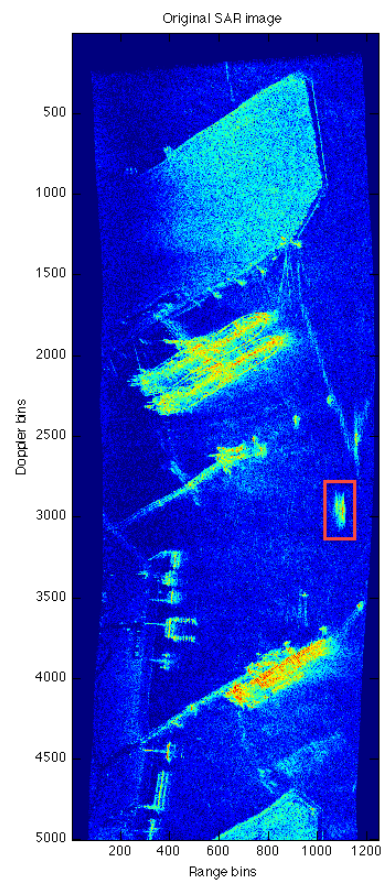
FIGURE 3.16: Original SAR image
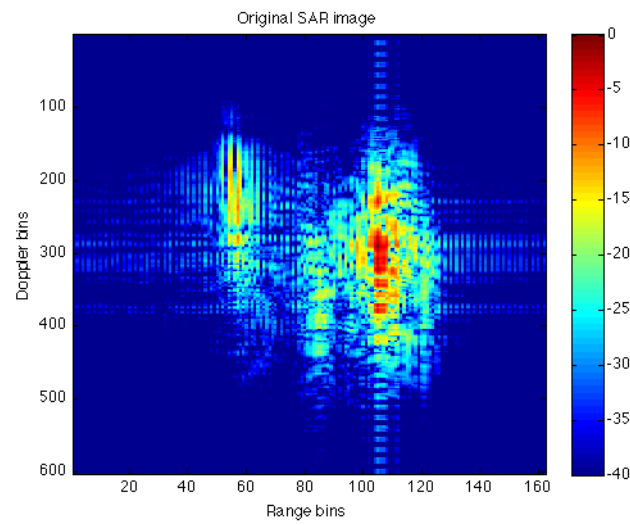
FIGURE 3.17: Original SAR image - Zoom on target
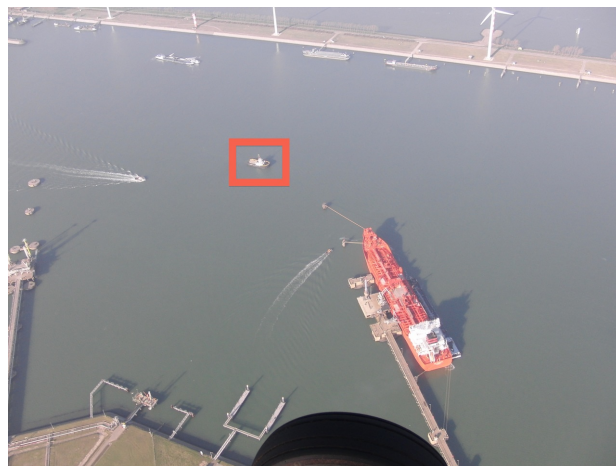
FIGURE 3.18: Photo of the imaged area including the non-cooperative target of interest

(a)

(b)

(c)
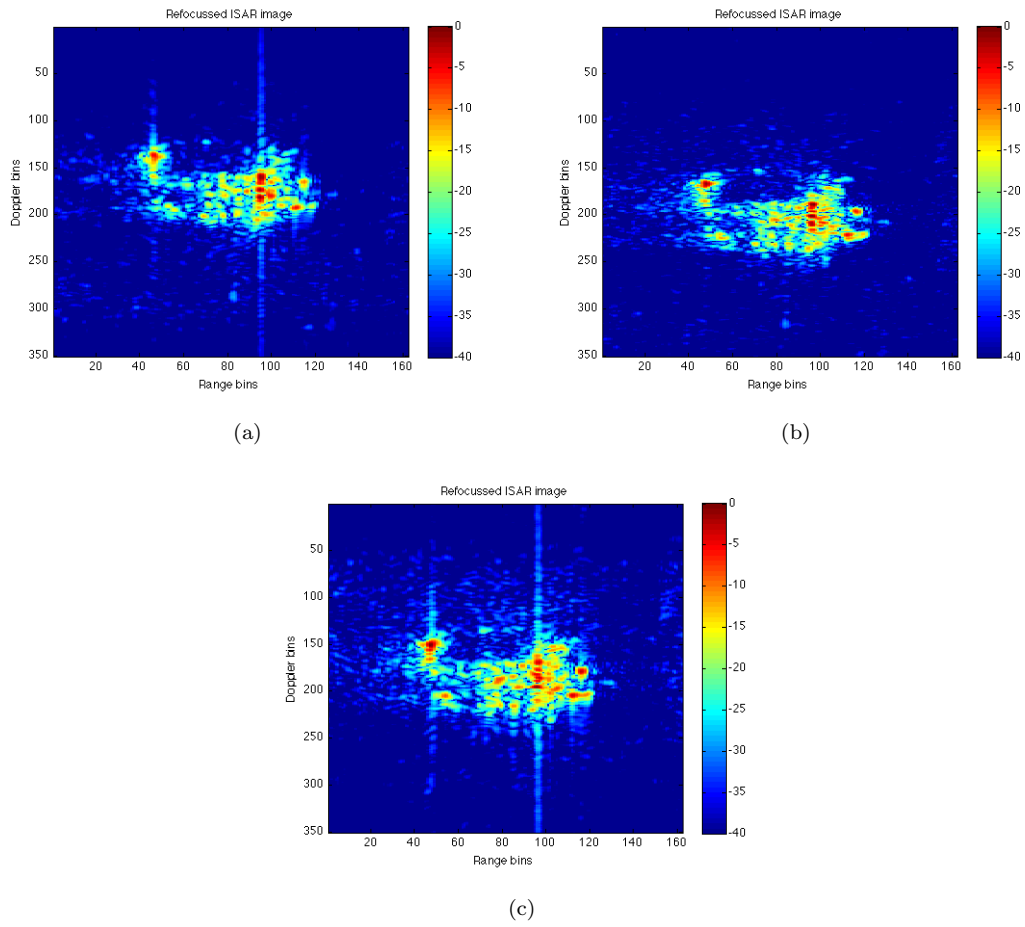
FIGURE 3.19: ISAR image sequence
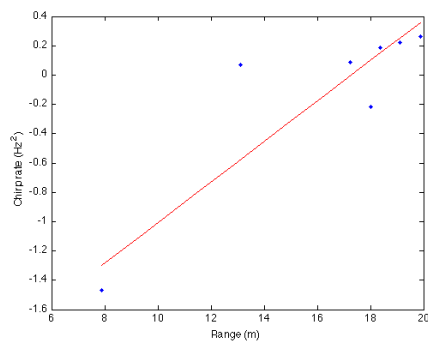
FIGURE 3.20: Range/Chirp-rate scatterplot
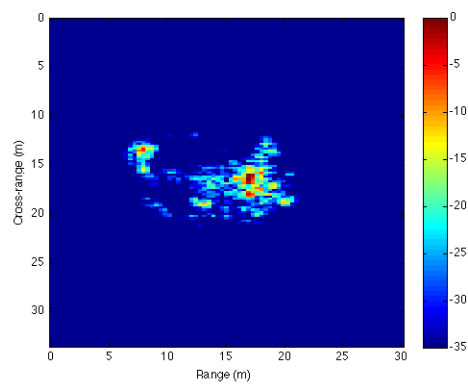
FIGURE 3.21: Range and cross-range scaled ISAR image

Chapter 4

Moving Target Detection Techniques in SAR images

4.1 Introduction

As shown in the previous chapter, SAR systems can be used to produce high resolution images of non-cooperative moving targets by exploiting the ISAR processing techniques. It is worth pointing out that moving targets must firstly be detected before applying the ISAR processing. Although detection can be straightforward when dealing with maritime targets, this is a serious issue when dealing with ground targets. In fact, the unpredictable target motion leads to degradation due to the non-correct functioning of the image formation process. Basically, the range migration through different range resolution cells due to the uncompensated target range motion causes a decrease of the integration time which leads to a loss of resolution and, more important from a detection point of view, to a reduction of the signal-to-clutter power ratio (SCR). Moreover, even in absence of range migration, the useful target energy spreads in a wider region and in a cross-range position that does not correspond to the real target position in the scene.

In this chapter a review of the moving target indication/detection techniques in SAR images will be presented. In particular, techniques that make use of multichannel information will be introduced. These techniques are more effective in case of strong ground clutter in particular for the detection of slow moving targets. A special attention will be given to the Space Time Adaptive Processing because of its characteristics that make it suitable for the purposes of this work.

4.2 Moving target detection techniques for SAR

Different techniques for the detection of moving targets signal in a static scene can be found in literature.

The earliest method that was studied to discriminate moving target signals from the static scene in single channel SAR systems is based on their different location in the Doppler frequency spectrum with respect the static scene spectrum. [38], [39]. This technique is based on the assumption that the radar PRF is high enough to make available a region in Doppler frequency domain not occupied by the static scene spectrum.

This technique can be applied when a single channel is available, but it suffers from some shortcomings. First of all, it requires a high PRF that involves a reduction of the SAR swath and an increase of the dimension of the data to be treated.

Secondly it fails when dealing with the detection of slow moving targets whose Doppler frequency fall completely in the static scene bandwidth.

Other techniques that were proposed in literature for moving target detection with single channel SAR systems are based on change detection from different looks of the same scene at different times [40] or on the application of non-uniform sampling [41]. However the effectiveness of all these methods when dealing with slow moving target is limited in principle because moving targets return cannot be separated from the static scene return in the Doppler domain.

More powerful methodologies to overcome these drawbacks are based on the use of more than one antenna to collect different sets of data of the same scene. The multichannel capability allows for the availability of multiple space samples, i.e.,echoes received from different antenna elements, and time samples , i.e., echoes collected at different time instants. These samples, collected in a data cube Fig.4.2, can be combined to obtain better performance. Along Track Interferometry (ATI), Displaced Phase Centre Array (DPCA), Time-Frequency Transforms (TFT) and Space Time Adaptive processing (STAP) are examples of MTD methods for multichannel SAR systems. Next sections will briefly recall the main feature of the above mentioned techniques.

4.2.1 Displaced Phase Centre Array

The Displaced Phase Centre array is one of the earliest method to perform clutter suppression exploiting multichannel SAR systems. It was conceived in [42] and one of its major application is the JSTARS (Joint Strategic Target Attack Radar Systems) [43],[44],[45],[46]. Details about this technique can be found in [47]. Its functioning is depicted in Fig.4.1.
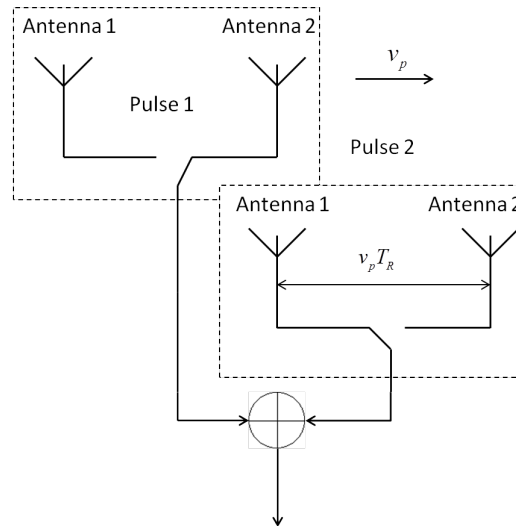
FIGURE 4.1: DPCA

Two identical antennas are aligned along the flight direction and the radar transmits a series of pulses in such a way that the location of the second antenna at the second pulse is the same of the first antenna at the first pulse. This is obtained by properly selecting the system parameters. In particular, the distance between the two antennas must be equal to the distance traveled by the platform in the Pulse Repetition Interval, i.e., $d = v_p T_R$, where v_p is the platform velocity. In this way, the static clutter scene is seen at two different time instants from the same radar location. The clutter is then cancelled by subtracting the echo of the first pulse received by the second antenna from the echo of the second pulse received by the first antenna that is the difference between the data acquired from the same scene at two different time instants. Echoes received from static scene are the same and so they are cancelled after the subtraction. Conversely, echoes from moving targets are different and so they will give a non-zero result from the subtraction. In [9] a theoretical and practical evaluation of this technique has been investigated resulting in a cancellation of the order of $25dB$. In the same paper, a reformulation of the DPCA algorithm as a special case of 2 channel slow time STAP is also

presented resulting in an Adaptive DPCA. It is worth pointing out that the DPCA principle is effective even if the system is undersampled in the spatial domain, i.e., $d > \frac{\lambda}{2}$, or in the time domain, i.e., $PRF < B_D$, (PRF lower than clutter Doppler bandwidth) or both [21].

Limitations of the DPCA approach rely in a loss of receiving aperture due to the need of two antennas, a fixed relation between PRF and v_p, only two spacial degrees of freedon and non adaptivity of the system. The generalization of DPCA for more than two channels is the STAP processing that will be described in the following.

4.2.2 Along Track Interferometry

Similarly to the DPCA, Along-Track Interferometry (ATI) uses two displaced antennas connected to two parallel receiving channels [48], [49],[50]. Two SAR images are generated compensating the time delay between the two azimuth signal by means of two reference signals. The first image is multiplied by the complex conjugate of the second so that the remaining phase is zero for stationary target and non-zero otherwise. ATI-SAR was originally developed to measure the speed of the ocean surface [51], [52].

In order to obtain high phase sensitivity, the two antenna should be widely separated leading to a comb of blind velocities that limits the useful target velocity interval.

A possible variation is to use monopulse techniques to measure the velocity and the Direction of Arrival (DoA) of the moving targets [53], [16]. In [53] the necessity of having more than two channels for MTI task is derived.

4.2.3 Time-Frequency analysis

Time-frequency distributions are an extension of traditional Fourier analysis used to treat time-varying processes.

In [54] a description of a general class of bilinear time-frequency distribution is provided. Among those the Wigner-Vile distribution (WVD) is widely used to perform moving target indication (MTI) since it presents some important features concerning detection and estimation issues [55], [56]. MTI via WVD is based on

the difference between the instantaneous bandwidth of the target and the clutter in the time-frequency domain. It can be demonstrated that while the target bandwidth in the whole observation time depends on the radar target relative motion, the instantaneous bandwidth is proportional to the target size. Therefore the response of a small moving target occupy a large bandwidth during the overall observation interval but its instantaneous bandwidth is considerably smaller. Conversely the instantaneous bandwidth of the clutter response is much larger. This difference allows for the discrimination of the useful energy from the disturbance [57]. It is quite obvious that detection and instantaneous frequency estimation performance depend on the Signal to Clutter Ratio (SCR) value. In [20] and [58] a two step implementation is described. Clutter cancellation is performed first exploiting spatial and temporal information and the output of the cancellation filter is analysed in the time-frequency domain. It is worth pointing out that since WVD is a non-linear transformation undesired cross-products appear when more than one signal is present.

4.2.4   Space Time Adaptive Processing (STAP)

Better performance can be obtained by using more antennas or a phased array antenna, located along the flight direction. The coherent processing of the echoes received from different antenna elements at different times, i.e., a space-time processing, allows for a considerable gain over the conventional processing. This is known as Space Time Adaptive Processing (STAP) and can significantly improve low velocity and small target detection performance in strong clutter environments or in the presence of a strong jamming interference. This technique is widely treated for general airborne radar case [21], [59], [60] but in recent years, with the development of imaging systems with multichannel capabilities, many researchers have studied the applicability of STAP processing in multichannel radar imaging scenario.

In [61], [62] the optimum space-time processing for moving targets detection is analytically derived. The implementation of slow-time STAP in both time and frequency domain is derived and a comparison between the optimal solution and a number of reduced rank filters is provided. These approaches are also known as pre- and post-Doppler STAP.

Other studies in this field have been done in [20] where a comprehensive study of STAP processing combined with a time-frequency analysis in order to obtain an estimation of the target instantaneous phase necessary for the successive formation of the synthetic aperture with respect to the moving target detected is provided. In [63], [64], [65] STAP processing for jammer suppression is widely treated.

4.3 Airborne STAP review

In this section, a review of the Space slow time adaptive processing for airborne radar will be provided.

Consider a radar mounted on an airborne platform that moves along the flight path with velocity v_p. The system is composed by a P channels uniform linear array with inter-element spacing denoted by d. The radar transmits a series of pulses of bandwidth B with pulse repetition frequency PRF. Considering a Coherent Processing Interval (CPI) of T_{obs} the signal received from the P channels is collected and arranged in a data cube as shown in Fig.4.2.

Space-Slow time snapshot

P (Channels/ Angles)

N (Range delay time/ frequency)

M (Slow-time/ Doppler frequency)
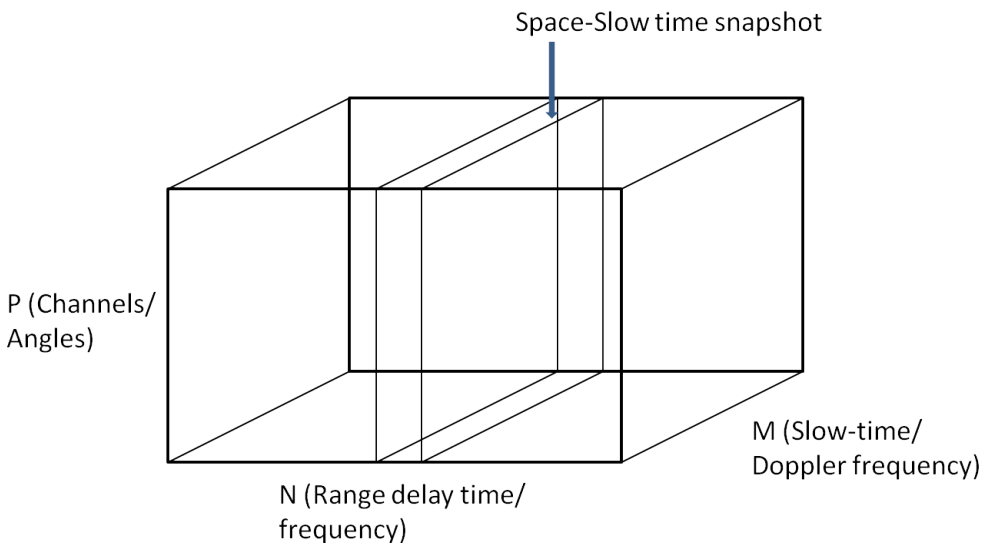
FIGURE 4.2: Data cube

where P is the number of channels and represents the number of spatial Degree of Freedom (DoF), N is the number of range frequencies and M is the number of slow time intervals collected in T_{obs} and represents the number of temporal DoF. Consider a scatterer placed along the DoA denoted by θ. The spatial steering

vector to focus the scatterer can be defined as

$$\mathbf{e}_s\left(\theta\right) = \begin{bmatrix} 1 & e^{-j2\pi F_s} & e^{-j4\pi F_s} & \dots & e^{-j(P-1)2\pi F_s} \end{bmatrix}^T \tag{4.1}$$

where

$$F_s = \frac{d}{\lambda}sin\theta \tag{4.2}$$

is the spatial frequency.

Defining $\mathbf{s}_s\left(n, m\right)$ the data received in the nth frequency bin and relative to the mth pulse, the focused (or steered) output in the direction θ is expressed as

$$y_s\left(\theta, n, m\right) = \mathbf{e}_s\left(\theta\right)^H \mathbf{s}_s\left(n, m\right) \tag{4.3}$$

Considering the temporal dimension it can be noted that each ground patch has a Doppler shift, ν, associated with it that is expressed as:

$$\nu = \frac{2v_p}{\lambda}sin\theta \tag{4.4}$$

Normalizing ν with respect the PRF the normalized Doppler frequency F_D can be defined as

$$F_D = \nu T_R \tag{4.5}$$

Similarly to the spatial case a steering vector can be defined for each normalized Doppler frequency F_D as:

$$\mathbf{e}_t\left(F_D\right) = \begin{bmatrix} 1 & e^{-j2\pi F_D} & e^{-j4\pi F_D} & \dots & e^{-j(M-1)2\pi F_D} \end{bmatrix}^T \tag{4.6}$$

Defining $\mathbf{s}_p(n)$ the data received from the pth channel in the nth frequency bin, the focused output at the generic F_D Doppler frequency can be expressed as:

$$y_{t,p}(F_D, n) = \mathbf{e}_t(F_D)^H \mathbf{s}_p(n) \tag{4.7}$$

From Eq.(4.1) and Eq.(4.6) the space/slow time steering vector can be defined as:

$$\mathbf{e}(\theta, F_D) = \mathbf{e}_s(\theta) \otimes \mathbf{e}_t(F_D) \in \mathbb{C}^{MP \times 1} \tag{4.8}$$

where $\otimes$ denotes the Kronecker product.

In order to apply the space/slow time steering vector to focus a scatterer with DoA equal to θ and Doppler frequency F_D the space-slow time snapshot of the received signal must be rearranged in according to the steering vector construction:

$$\mathbf{s}(n) = \left[\mathbf{s}^T(n, 0), \mathbf{s}^T(n, 1), ..., \mathbf{s}^T(n, M-1)\right]^T \in \mathbb{C}^{MP \times 1} \tag{4.9}$$

According to the definitions in Eq.(4.1) and Eq.(4.6) the focused output for a given pair of DoA and F_D is given by

$$y(\theta, F_D, n) = \mathbf{e}^H(\theta, F_D)\mathbf{s}(n) \tag{4.10}$$

More generally, the steering vector can be replaced with an adaptive weight vector that changes according to a specific criterion

$$y(\theta, F_D, n) = \mathbf{w}^H(\theta, F_D)\mathbf{s}(n) \tag{4.11}$$

The optimum weight vector, $\mathbf{w}$, can be selected with different criteria. For the case treated in this thesis the objective of the space/slow time filtering is to maximize the output signal to interference plus noise ratio (SINR).

Consider a generic received signal backscattered by a target placed in the DoA θ and Doppler frequency F_D of strength σ_T. At the receivers this useful signal is corrupted by an interference component that takes into account clutter, jammer and additive Gaussian noise. In order to simplify the notation, the dependence on (θ, F_D, n) will be dropped in the following. The stacked version of the received signal is expressed as:

$$\mathbf{x} = \sigma_T \mathbf{s}_T + \mathbf{c} \in \mathbb{C}^{MP \times 1} \tag{4.12}$$

The output of the space-slow time adaptive filter is:

$$y = \mathbf{w}^H \left(\sigma_T \mathbf{s}_T + \mathbf{c}\right) = y^{(u)} + y^{(c)} \tag{4.13}$$

The SINR can then be expressed as:

$$SINR = \frac{\left|y^{(u)}\right|^2}{E\left\{\left|y^{(c)}\right|^2\right\}} \tag{4.14}$$

where

$$\left|y^{(u)}\right|^2 = \sigma_T^2 \left|\mathbf{w}^H \mathbf{s}^T\right|^2 \tag{4.15}$$

$$E\left\{\left|y^{(c)}\right|^2\right\} = E\left\{\left|\mathbf{w}^H \mathbf{c}\right|^2\right\} = \mathbf{w}^H \mathbf{R}_c \mathbf{w} \tag{4.16}$$

$\mathbf{R}_c$ represents the space slow time covariance matrix. So SINR is maximum for

$$\mathbf{w}_{opt} = \underset{\mathbf{w}}{argmax} \left\{\frac{\left|\mathbf{w}^H \mathbf{s}_T\right|^2}{\mathbf{w}^H \mathbf{R}_c \mathbf{w}}\right\} \tag{4.17}$$

The solution is found using the Swartz's inequality [66]

$$\mathbf{w}_{opt} = \gamma \mathbf{R}_c^{-1} \mathbf{s}_T \in \mathbb{C}^{MP \times 1} \tag{4.18}$$

where γ is a scalar that does not affect the SINR.

It is quite obvious that this filter is not feasible in practice because it is based on the assumption that both the interference space/slow time covariance matrix, $\mathbf{R}_c$, and the target steering vector, $\mathbf{s}_T$, are a priori known. In a real situation these assumptions do not hold.

Regarding the lack of knowledge of $\mathbf{s}_T$, in practical situations the target steering vector is replaced with a set of test steering vectors pre-computed for each couple (θ, F_D) that must be analysed.

Regarding the lack of knowledge of $\mathbf{R}_c$, a classical approach to overcome this issue is the common known Sample Matrix Inversion (SMI) [67]. It consists of performing a sample matrix estimation of $\mathbf{R}_c$ and using this estimation to obtain the optimum filter. The sample matrix estimation is performed averaging over a number of target free range samples, N_r, (training data) as:

$$\hat{\mathbf{R}}_c = \frac{1}{N_r} \sum_{n_r=1}^{N_r} \mathbf{c}(n_r) \mathbf{c}^H(n_r) \in \mathbb{C}^{PM \times PM} \tag{4.19}$$

A common strategy to select training data is considering data in range cells adjacent to the cell under test excluding a guard interval. The guard interval is needed to select training data without target. In fact if the target contribution is present in the training data, the adaptive filter would consider also the useful signal as a disturbance leading to the target cancellation. It is quite evident that in order to obtain a correct estimation of the space/slow time covariance matrix the statistical property of the disturbance in the training data must be the same of the disturbance in the range cell under test. Since the number of training samples required to obtain a good estimation is of the order of the dimension of $\mathbf{R}_c$ non homogeneity in the training data can be an issue to overcome. It has been demonstrated in [67] that if the training samples are independent and identically distributed a number of $N_r \approx 2PM$ leads to a loss of $3dB$ with respect to the case in which the ideal covariance matrix is assumed known.

Regarding the choice of γ it is evident that this parameter does not affect the SINR at the output of the adaptive filter. However a specific choice of this parameter can impose some specific characteristic at the adaptive filter. For example imposing the square-law output by setting

$$\gamma = \frac{1}{\sqrt{\mathbf{s}_T^H \mathbf{R}_c^{-1} \mathbf{s}_T}} \qquad (4.20)$$

yields to a particular form of the output known as adaptive matched filter (AMF) that exhibits constant false alarm rate (CFAR) properties [68] [69] [70]. Other expression of the SMI filter involving CFAR properties are the generalized likelihood ratio test (GRLT) presented in [69] and the adaptive coherence estimator (ACE) given in [71].
Other possible values of γ can be obtained imposing linear constraints to the maximization of the SINR. These linear constraints are defined as

$$\mathbf{A}^H \mathbf{w} = \mathbf{b} \qquad (4.21)$$

where $\mathbf{A}$ is the constraint matrix and $\mathbf{b}$ is the constraining value.

This formulation of the optimum filter is known in literature as the Linearly Constrained Minimum Variance (LCMV) beamformer [72].

In this case Eq.(4.17) becomes:

$$\mathbf{w}_{LCMV} = \underset{\mathbf{w}}{argmax} \left\{ \frac{\left| \mathbf{w}^H \mathbf{s}_T \right|^2}{\mathbf{w}^H \mathbf{R}_c \mathbf{w}} \right\} \quad \text{subject to} \quad \mathbf{A}^H \mathbf{w} = \mathbf{b} \tag{4.22}$$

resulting in a weightvector expressed as:

$$\mathbf{w}_{LCMV} = \mathbf{R}_c^{-1} \mathbf{A} \left[\mathbf{A}^H \mathbf{R}_c^{-1} \mathbf{A} \right]^{-1} \mathbf{b} \tag{4.23}$$

One of the most common choice of γ is the result of constraining the space/slow time beam pattern to the unity in the steering direction. This leads to the well known Minimum Variance Distortionless Response (MVDR) and is expressed as:

$$\mathbf{w}_{MVDR} = \frac{\mathbf{R}_c^{-1} \mathbf{s}_T}{\mathbf{s}_T^H \mathbf{R}_c^{-1} \mathbf{s}_T} \in \mathbb{C}^{MP \times 1} \tag{4.24}$$

The effectiveness of the combined space/slow time processing with respect the conventional space and slow time beamforming can be explained observing Fig.4.3.
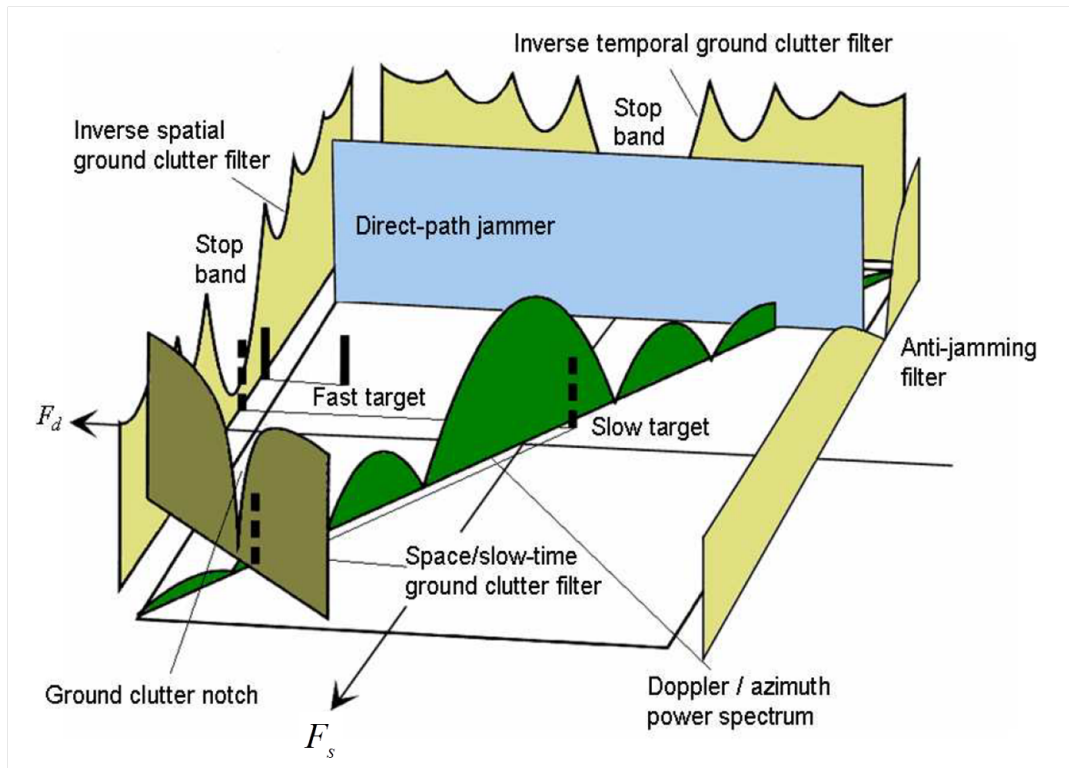

FIGURE 4.3: Principle of space/time filtering

This is a very famous figure and represents the 2D dimensional power spectrum in the spatial frequency/Doppler frequency plane of the received signal in a fixed range bin. In this figure the ground clutter contribution is represented by the clutter ridge. Its slope can be evaluated from Eq.(4.2) and Eq.(4.5) noting the fixed relationship between normalized Doppler frequency and normalized spatial frequency expressed as:

$$F_D = \frac{2v_p T_R}{d} \frac{d}{\lambda} \sin\theta = \beta F_s \qquad (4.25)$$

where $\beta = \frac{2v_p T_R}{\lambda}$

Also two targets with different velocities and a jammer are depicted. It is evident that clutter suppression exploiting only temporal degree of freedom, i.e., classical MTI/MTD represented by inverse temporal ground clutter filter, or only spatial degree of freedom represented the inverse spatial ground clutter filter leads to a broad stop band in the considered dimension that blinds the radar in those interval. It is evident that operating in the whole (F_s, F_D) plane a more effective filtering can be performed so that even slow moving targets can be detected.

4.4 Conclusion

In this chapter a review of moving target indication techniques for SAR application has been provided. In particular, techniques that make use of multichannel information have been presented and their characteristics analysed. Among them special attention has been given to the STAP. STAP processing for classic airborne radar applications has been presented since it is at the basis of the STAP ISAR processing proposed in the next chapter.

Chapter 5

Joint STAP ISAR

5.1 Introduction

In this chapter a technique that combines clutter suppression and ISAR processing
in order to obtain well focused images of extended moving targets is investigated.
The problem will be addressed from the imaging point of view. Two principal
issues will be addressed. The applicability of ISAR processing after clutter miti-
gation first, and then the need of sub-optimal approach due to the difficulties in
the estimation of the clutter space-time covariance matrix will be investigated.

5.2 Optimum Processing

In this section, the optimum clutter suppression and imaging processing will be
described. First of all, the signal model will be recalled and the formulation of the
matching filter processing for cross-range compression will be derived.

Signal Modeling and image formation

Let consider the acquisition geometry shown in Fig.5.1 in which the radar system
observes a moving target within a static background. The total Fourier transform
of the received signal can be expressed as follows:
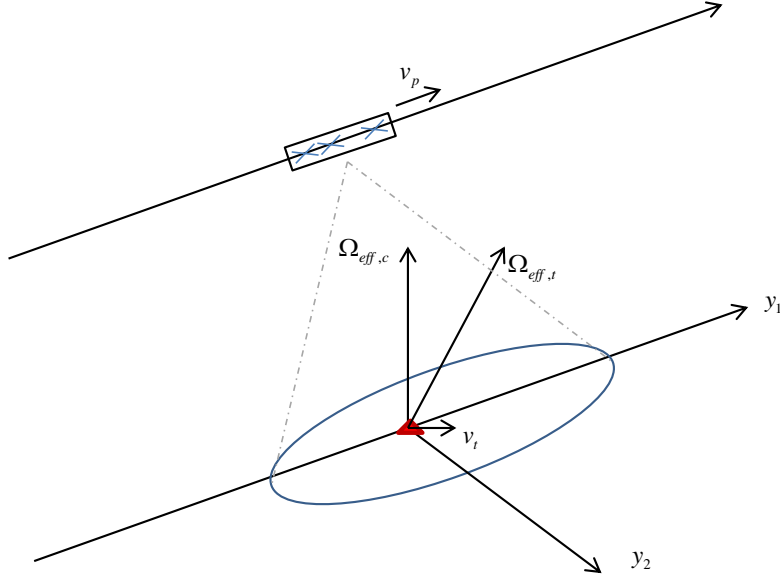
FIGURE 5.1: Acquisition geometry

$$S(f,t) = S_t(f,t) + S_c(f,t) + N(f,t) \tag{5.1}$$

where $S_t(f,t)$ is the contribution due to the moving target, $S_c(f,t)$ is the contribution due to the static scene that in this case is considered clutter and $N(f,t)$ is the additive noise. $f \in \left[f_0 - \frac{B}{2}, f_0 + \frac{B}{2}\right]$ and $t \in \left[\frac{-T_{obs}}{2}, \frac{T_{obs}}{2}\right]$ denote the range frequency and the azimuth slow-time respectively.

A shown in Sect.2.2 under the assumption that the *straight iso range approximation* holds true, the received signal relative to a moving target can be expressed as:

$$S_t(f,t) = e^{-j\frac{4\pi}{\lambda}R_{0t}(t)} \sum_{k=1}^{K} \sigma_k e^{-j\frac{4\pi}{\lambda}\left[y_2^{(k)} + \Omega_{eff,t} y_1^{(k)} t\right]} \tag{5.2}$$

where $R_{0t}(t)$ denotes the position of the reference point on the target at the time t and takes into account the superimposition of the target own motion and the platform motion, k is the scatterer index, $y_1^{(k)}$ and $y_2^{(k)}$ denote the cross-range and the range coordinates of the kth scatterer and $\Omega_{eff,t}$ is the total rotation vector due to the platform and the target motion projected on a plane orthogonal to the LoS.

Considering a target moving on the ground, under the straight iso-range hypothesis, the term $R_{0t}(t)$ can be expressed as:

$$R_{0t}(t) \approx R_0 + v_{t,y_2}t + \frac{(v_p - v_{t,y_1})^2}{2R_0}t^2 \tag{5.3}$$

where R_0 is the distance between the platform and the reference point at $t = 0$, v_p is the platform velocity and v_{t,y_1} and v_{t,y_2} are the target velocity components in the cross-range and range dimension respectively. As stated above, for reasonably small values of observation time it is reasonable to assume that the effective rotation vector is constant.

The received signal from the static scene, i.e., clutter, can be expressed in the same form of Eq.(5.23) with the only difference that the motion parameters are exactly known

$$S_c(f,t) = e^{-j\frac{4\pi}{\lambda}R_{0c}(t)} \iint\limits_{(y_1,y_2)} \sigma(y_1,y_2)e^{-j\frac{4\pi}{\lambda}\left[y_2+\Omega_{eff,c}y_1 t\right]}dy_1 dy_2 \tag{5.4}$$

where
$$R_{0c}(t) = R_0 + \frac{(v_p t)^2}{2R_0} \tag{5.5}$$

and
$$\Omega_{eff,c} = \frac{v_p}{R_0} \tag{5.6}$$

High resolution in range dimension is provided by transmitting wideband signals and matched filtering the received signal. High resolution in azimuth can be obtained by matched filter processing the received signal in the slow time domain. The matched filter in the slow time domain is derived analytically for the case in which the straight iso-range approximation holds true while the general case has been treated in Sect.2.3. High resolution in cross-range dimension is obtained by the convolution between the received signal and a proper reference signal. Consider $S_t(f,t)$ the signal received from a static scatterer placed in the generic position (y_1, y_2) . The output of the matched filter in the slow time domain can be written as:

$$u(f,t) = S_t(f,t) \otimes_t S_{ref}^*(f,t) \tag{5.7}$$

where $S_{ref} = e^{-j\frac{4\pi}{\lambda}R_{0c}(t)}$ is the reference signal.

Eq.(5.7) becomes:

$$u(f,t) = \int_\tau S_t(f,\tau)S_{ref}^*(f,t-\tau)d\tau \tag{5.8}$$

Defining $\alpha = \frac{v_p^2}{2R_0}$ and $i(f,\tau) = \sigma(y_1,y_2)e^{-j\frac{4\pi}{\lambda}\left[y_2+\Omega_{eff,c}y_1 t\right]}$, after some mathematical manipulations Eq.(5.8) can be rewritten as:

$$u(f,t) = e^{-j\frac{4\pi}{\lambda}\alpha t^2}\int_\tau i(f,\tau)e^{j\frac{4\pi}{\lambda}2\alpha t\tau}d\tau \tag{5.9}$$

It is quite evident that the expression within the integral can be seen as an Inverse Fourier Transform (IFT) after defining the Doppler frequency variable as

$$\nu = \frac{4t\alpha}{\lambda} \approx \frac{4t\alpha}{\lambda_0} \tag{5.10}$$

where the approximation is valid under the hypothesis of narrow band system. Under this assumption Eq.(5.10), Eq.(5.9) can be rewritten as

$$u(f,\nu) = K(\nu)\,i(f,\nu) \tag{5.11}$$

where $K(\nu) = e^{-j\frac{\pi\lambda\nu^2}{4\lambda}}$ is a term to be compensated and

$$i(f,\nu) = e^{j\frac{4\pi}{\lambda}y_2}sinc\left(T_{obs}\left(\nu - \frac{2\Omega_{eff,c}}{\lambda_0}y_1\right)\right) \tag{5.12}$$

is the azimuth compressed signal in the range frequency/Doppler frequency domain.

In case of moving targets the azimuth compression can be performed in same way. In this case, the reference signal is $S_{ref}(f,t) = e^{-j\frac{4\pi}{\lambda}R_{0,t}(t)}$. Defining $\alpha_t = \frac{(v_p-v_{t,y_1})^2}{2R_0}$, $i_t(y_1,y_2) = \sigma(y_1,y_2)e^{-j\frac{4\pi}{\lambda}\left[y_2+\Omega_{eff,t}y_1 t\right]}$ With similar mathematical manipulations the output of the matched filter can be expressed as:

$$u(f,t) = e^{-j\frac{4\pi}{\lambda}(v_{y_2}t+\alpha_t t^2)} \int\limits_\tau i(f,\tau) e^{-j\frac{4\pi}{\lambda}(2v_{y_2}\tau-2\alpha_t t\tau)} d\tau \qquad (5.13)$$

that can be seen as an inverse Fourier Transform after defining

$$\nu_t = \frac{4t\alpha_t}{\lambda} \approx \frac{4t\alpha_t}{\lambda_0} \qquad (5.14)$$

So

$$u(f,\nu_t) = K(\nu_t)i(f,\nu_t - \nu_0) \qquad (5.15)$$

where $K(\nu_t)$ is a term to be compensated, $\nu_o = 4\frac{v_{t,y_2}}{\lambda_0}$ is the Doppler centroid that depends on the target radial velocity and

$$i(f,\nu) = e^{j\frac{4\pi}{\lambda}y_2} sinc\left(T_{obs}\left(\nu_t - \frac{2\Omega_{eff,t}}{\lambda_0}y_1\right)\right) \qquad (5.16)$$

It is worth pointing out the difference between ν defined in Eq.(5.10) and ν_t defined in Eq.(5.14). The two expression involves a different sampling rate of the Doppler axis and as a consequence a different Doppler resolution. This is due to the fact that the Doppler resolution (and as a consequence the cross-range resolution) depends on the aspect angle variation between the radar and target. In the case of static target this variation is due to the platform motion only while in case of moving target also the contribution due to the target motion must be taken into account.

It is quite obvious that at this stage the image is obtained after a Fourier transform from range frequency to delay time and after the scaling operation defined in Sect.2.2.

This formulation can be easily extended to a discretized version of the signal in which $S(n,m) = S(n\Delta f, mT_R)$. In this case the matched filter processing can be expressed in terms of a discrete convolution between the received signal and a reference signal as:

$$u(n,m) = S_t(n,m) \otimes_m S_{ref}^*(n,m) \qquad (5.17)$$

where after the same mathematical manipulations seen before, $u(n,m)$ can be written as the discretized version of Eq.(5.11)

$$u(n,m) = u(n\Delta f, m\Delta\nu) \tag{5.18}$$

where $\Delta\nu = \frac{4T_R\alpha}{\lambda}$.

Eq.(5.17) can be written in a vectorial form as:

$$u(n,m) = \mathbf{G}^H(n,m)\mathbf{S}(n) \tag{5.19}$$

where the vectors $\mathbf{G}(n,m)$ and $\mathbf{S}(n)$ are the reference vector and the received signal vector respectively and are defined as:

$$\mathbf{S}(n) = [S(n,0), S(n,1), ..., S(n, M-1)]^T \in \mathbb{C}^{M\times 1} \tag{5.20}$$

$$\mathbf{G}(n,m) = [S_{ref}(n,m), S_{ref}(n,m-1), ..., S_{ref}(n, m-(M-1))]^T \in \mathbb{C}^{M\times 1} \tag{5.21}$$

The multichannel signal model can be easily obtained from the single channel model. For a typical multichannel SAR system, usually one antenna transmits pulses and all antennas receive the echoes reflected by the illuminated scene. For such a multistatic geometry, an equivalent monostatic geometry where each antenna transmits and receives can be adopted to simplify the notation.

The signal received by the pth element can be written as (see Sect.2.2.3):

$$S_{t,p}(f,t) = e^{-j\frac{4\pi}{\lambda}R_{0t,p}(t)} \sum_{k=1}^{K} \sigma_k e^{-j\frac{4\pi}{\lambda}\left[K_{0,k}^{(p)} + K_{1,k}^{(p)}t\right]} \tag{5.22}$$

where the terms $K_0^{(p)}$ and $K_1^{(p)}$ are defined in Eq(2.49).

It is worth pointing out that for array size much smaller than the radar-target distance the LoS is the same for each antenna element and the terms $K_0^{(p)}$ and $K_1^{(p)}$ can be approximated as in Eq.(2.51).

Under this assumption the received signal relative to a moving target, $S_{t,p(f,t)}$, and the static scene $S_{ref}(f,t)$ can be expressed as:

$$S_{t,p}(f,t) = e^{-j\frac{4\pi}{\lambda}R_{0t,p}(t)} \sum_{k=1}^{K} \sigma_k e^{-j\frac{4\pi}{\lambda}\left[y_2^{(k)} + \Omega_{eff,t} y_1^{(k)} t\right]} \tag{5.23}$$

$$S_{c,p}(f,t) = e^{-j\frac{4\pi}{\lambda}R_{0c,p}(t)} \iint\limits_{(y_1,y_2)} \sigma(y_1,y_2) e^{-j\frac{4\pi}{\lambda}\left[y_2 + \Omega_{eff,c} y_1 t\right]} dy_1 dy_2 \tag{5.24}$$

The formulation of the matched filter can be easily extended to the multichannel scenario (see Sect.2.3.2) as:

$$u(n,m) = \sum_{p=1}^{P} u_p(n,m) = \sum_{p=1}^{P} S_p(n,m) \otimes S_{ref,p}(n,m) \tag{5.25}$$

The vectorial form can be easily derived after a stacking operation first along the channel Eq.(5.26)-(5.27) and then along the pulses Eq.(5.28)-(5.29) as:

$$\mathbf{S}(n,m) = \frac{1}{P}\left[S_1(n,m), S_2(n,m), \cdots, S_P(n,m)\right]^T \in C^{P\times1} \tag{5.26}$$

$$\mathbf{S}_{ref}(n,m) = \frac{1}{P}\left[S_{1,ref}(n,m), S_{2,ref}(n,m), \cdots, S_{P,ref}(n,m)\right]^T \in C^{P\times1} \tag{5.27}$$

$$\mathbf{S}(n) = \left[\mathbf{S}^T(n,0), \mathbf{S}^T(n,1), \cdots, \mathbf{S}^T(n,M-1)\right]^T \in C^{MP\times1} \tag{5.28}$$

$$\mathbf{G}(n,m) = \left[\mathbf{S}_{ref}^T(n,m), \mathbf{S}_{ref}^T(n,m-1), \cdots, \mathbf{S}_{ref}^T(n,m-M-1)\right]^T \in C^{MP\times1} \tag{5.29}$$

The output of the matched filter is then expressed as:

$$u(n,m) = \mathbf{G}^H(n,m)\mathbf{S}(n) \tag{5.30}$$

In the case in which the straight iso-range approximation holds true the final image is obtained only Fourier transforming along the range frequency dimension. If the straight iso-range approximation does not hold true the processing in Sect.2.3.2 can be applied. It involves the Stolt Interpolation step at the output of the matched filter.

Slow time STAP

Optimal slow-time STAP involves the replacement of the space-slow time reference vector with a weighvector that maximizes that output SINR as:

$$u(n, m) = \mathbf{W}^H(n, m)\mathbf{S}(n) \tag{5.31}$$

The expression of the of the optimum filter has been derived in the previous section by Sample Matrix Inversion implementation and is expressed as:

$$\mathbf{W}(n, m) = \gamma \hat{\mathbf{R}}_c^{-1}\mathbf{G}(n, m) \in \mathbb{C}^{MP \times 1} \tag{5.32}$$

where $\hat{\mathbf{R}}_c$ is an estimation of the exact space-slow time covariance matrix, $\mathbf{R}_c$, and it is defined as:

$$\hat{\mathbf{R}}_c = \frac{1}{N_r} \sum_{n_r=0}^{N_r-1} \mathbf{Z}(n_r)\mathbf{Z}^H(n_r) \in \mathbb{C}^{MP \times MP} \tag{5.33}$$

and γ is a constant that does not affect the SINR.

The vector $\mathbf{Z}(n_r)$ denotes the target-free data in the n_r^{th} range cell.

It is worth pointing out that the optimum processing in Eq.(5.32) performs both clutter suppression and image formation. In order to obtain well focused images of moving targets, the reference signal vector $\mathbf{G}(n, m)$ must take into account both the platform motion and the target own motion.

It is quite obvious that in a realistic situation this is not possible since no assumptions can be made on the motion of the non-cooperative targets. In this case the image formation becomes a two step process. A first motion compensation is performed in the optimum STAP processing achieving the platform motion compensation. The target own motion is compensated at the output of the STAP filter by applying the ISAR processing Fig.5.2.

The output of the STAP processing is a SAR image in which a number of moving targets can be detected. In order to compensate the motion of these targets, the ISAR processing can be exploited. In order to do this, an image crop should be determined for each target and the ISAR processing applied to each crop. The details of this processing have been provided in Ch.3 and can be summarized as:

1. image crop inversion performed by means of 2D-IFFT

2. target motion compensation by means of ICBA motion estimation

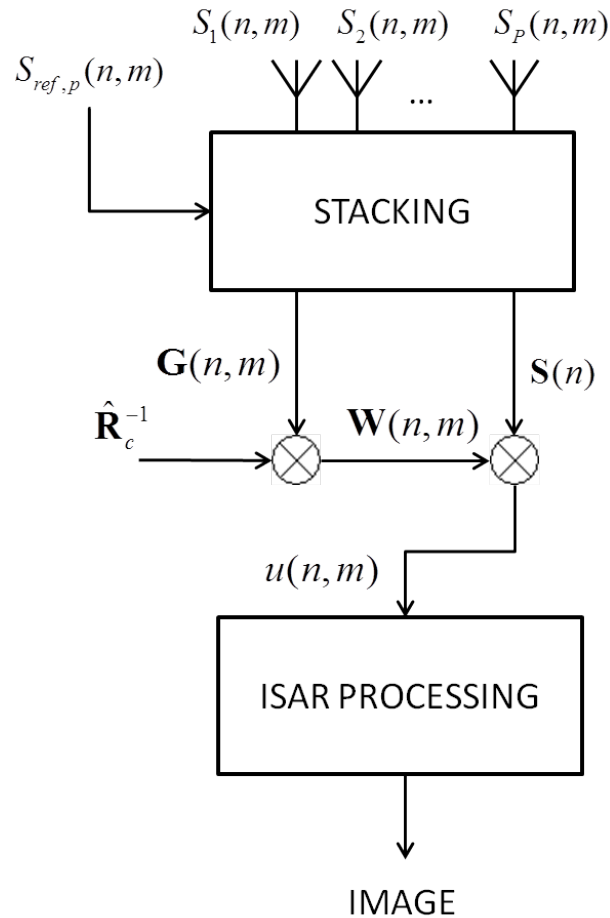3. image formation by means of Range-Doppler technique

FIGURE 5.2: Joint STAP-ISAR processing functional block

The demonstration of the applicability of ISAR processing after STAP clutter suppression is the first aim of this chapter.

Another issue to be addressed concerns the estimation of $\hat{\mathbf{R}}_c$. As stated before in order to obtain an average performance loss of roughly $3dB$ a number of $N_r = 2PM$ target free range cells are needed. With typical values of $PRF = 1KHz$, $T_{obs} = 1s$ and $P = 3$, $N_r = 6000$ range cells are needed. Assuming a range resolution of $0.5m$, this results in an area of homogeneous clutter of $3Km$ in the range dimension.

In the next section a sub-optimum technique to overcome this issue and reduce

the dimensionality of the interference covariance matrix to be estimated will be presented.

5.3 Sub-optimum approach

A reduction in the dimensionality of the space-slow time covariance matrix can be obtained by splitting the filtering operation in Eq.(5.32) in sub-windows as shown in Fig.5.3.
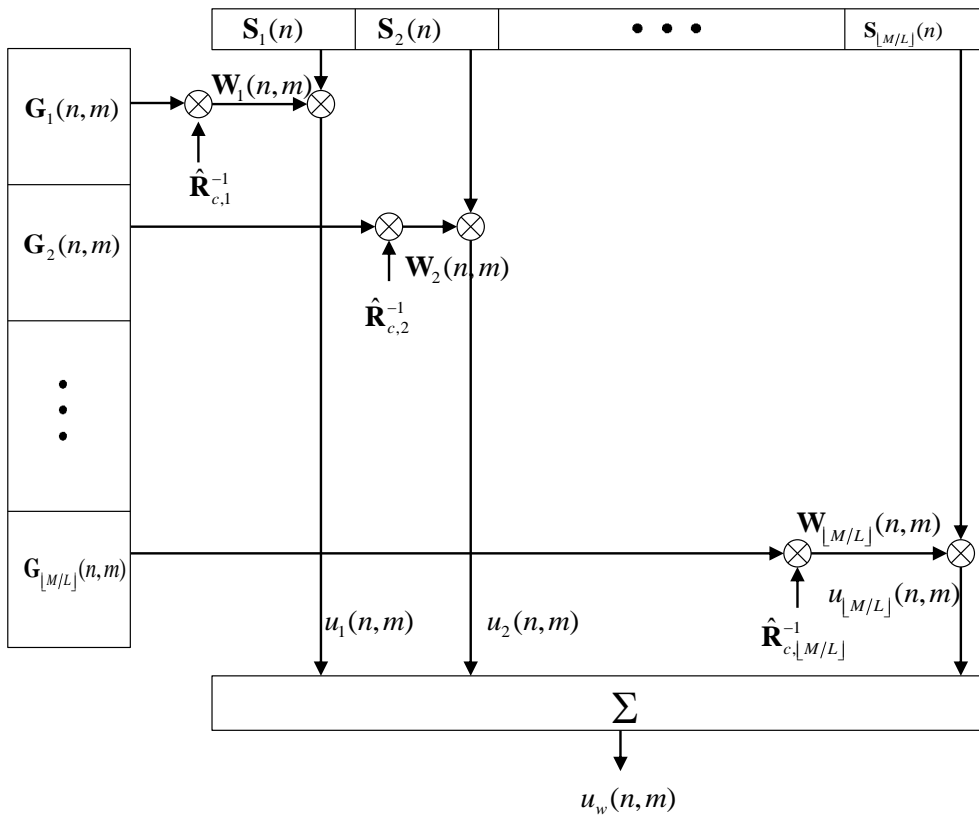

FIGURE 5.3: Sub Optimum approach

This operation consists of applying a windowing operation to the space-slow time data and applying the optimum filter on each window. In this case the dimension of the space-slow time covariance matrix to be estimated is limited by the length of the considered window. It is worth pointing out that the windowing operation does not lead to any losses if only the image formation process is considered, i.e.,

$\mathbf{W}(n, m) = \mathbf{G}(n, m)$.

However, when the weightvector assumes the form of the optimum filter (Eq.(5.32)), the windowing operation consists of considering an approximation of the space-slow time covariance matrix composed by a set of block aligned along the principal diagonal as shown in Fig.5.4.
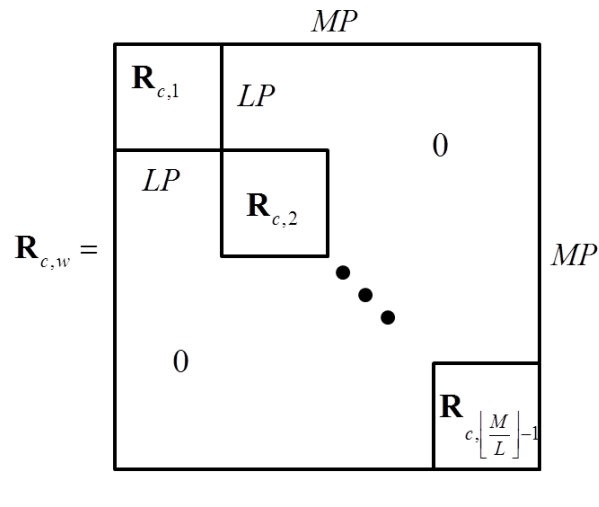

FIGURE 5.4: Covariance matrix approximation

This processing can be formalized as follows. Let i denotes the window index and L the window length, so that the output of the filtering process in the ith window is

$$u_i(n, m) = \mathbf{W}_i^H(n, m)\mathbf{S}_i(n) \tag{5.34}$$

so that the global output of the filtering process is

$$u_w(n, m) = \sum_i u_i(n, m) \tag{5.35}$$

The weightvector in the ith window is expressed as:

$$\mathbf{W}_i(n, m) = \hat{\mathbf{R}}_{c,i}^{-1}\mathbf{G}_i(n, m) \in \mathbb{C}^{LP \times 1} \tag{5.36}$$

where

$$\mathbf{G}_i(n,m) = \begin{bmatrix} \mathbf{S}_{ref}\left(n, m-(i-1)L\right) \\ \mathbf{S}_{ref}\left(n, m-((i-1)L+1)\right) \\ \mathbf{S}_{ref}\left(n, m-((i-1)L+2)\right) \\ \vdots \\ \mathbf{S}_{ref}\left(n, m-((iL-1))\right) \end{bmatrix} \in C^{LP \times 1} \tag{5.37}$$

and

$$\mathbf{S}_i(n) = \begin{bmatrix} \mathbf{S}\left(n, (i-1)L\right) \\ \mathbf{S}\left(n, (i-1)L+1\right) \\ \mathbf{S}\left(n, (i-1)L+2\right) \\ \vdots \\ \mathbf{S}\left(n, iL-1\right) \end{bmatrix} \in C^{LP \times 1} \tag{5.38}$$

The space-slow time disturbance covariance matrix in the ith window, $\hat{\mathbf{R}}_{c,i}$ is estimated as

$$\hat{\mathbf{R}}_{c,i} = \frac{1}{N_r} \sum_{n_r=0}^{N_r-1} \mathbf{Z}_i(n_r)\mathbf{Z}_i^H(n_r) \in \mathbb{C}^{LP \times LP} \tag{5.39}$$

where $\mathbf{Z}_i(n_r)$ is the disturbance in the ith windows and $i = 1, \cdots, \left\lfloor \frac{M}{L} \right\rfloor$.

It is quite obvious that in this case only $N_r = 2LP$ are needed in order to obtain a good estimation of $\hat{\mathbf{R}}_{c,i}$ while limitation on L are due to the distortion introduced by considering the approximation of the space-slow time covariance matrix shown in Fig.5.4.

5.4   Sub-optimum approach - post Doppler processing

A further reduction in the dimensionality of the space-slow time covariance matrix to be estimated can be obtained if processing in the Space Doppler (post Doppler) domain is considered. Details about post-Doppler STAP can be found in [21].
It consists on a Doppler frequency formulation of the optimum processing in Eq.(5.31) as:

$$\tilde{u}(n, m_\nu) = \tilde{\mathbf{W}}^H(n, m_\nu)\tilde{\mathbf{S}}(n) \tag{5.40}$$

where

$$\tilde{\mathbf{W}}(n, m_\nu) = \delta \hat{\mathbf{R}}_{Dc}^{-1} \tilde{\mathbf{G}}(n, m_\nu) \in C^{MP \times 1} \tag{5.41}$$

$$\tilde{\mathbf{G}}(n, m_\nu) = \mathbf{T}\mathbf{G}(n, m) \in C^{MP \times 1} \tag{5.42}$$

$$\tilde{\mathbf{S}}(n) = \mathbf{T}\mathbf{S}(n, m) \in C^{MP \times 1} \tag{5.43}$$

$\mathbf{T}$ denotes the unitary transformation matrix and is the results of the Kronecker product of the time-frequency Fourier transformation matrix, $\mathbf{T}_t$, and the identity matrix of dimension P, $\mathbf{I}_P$. This transformation corresponds to a Fourier transform from the slow-time to the Doppler frequency domain without changing the space dimension.

$$\mathbf{T} = \mathbf{T}_t \otimes \mathbf{I}_P \in C^{MP \times MP} \tag{5.44}$$

The generic element of $\mathbf{T}_t \in C^{M \times M}$ is $t_t(m_\nu, m) = e^{-j2\pi m_\nu \Delta f_d m T_R}$ with $m, m_\nu = [-\frac{M}{2}, \frac{M}{2} - 1]$ and $\Delta f_d = \frac{1}{MT_R}$. $\hat{\mathbf{R}}_{Dc}$ is the estimated interference cross-power spectral matrix and is obtained as:

$$\hat{\mathbf{R}}_{D,c} = \frac{1}{N_r} \sum_{n_r=1}^{N_r} \tilde{\mathbf{Z}}(n_r)\tilde{\mathbf{Z}}^H(n_r) = \frac{1}{N_r} \sum_{n_r=1}^{N_r} \mathbf{T}\mathbf{Z}(n_r)(\mathbf{T}\mathbf{Z}(n_r))^H = \mathbf{T}\hat{\mathbf{R}}_{st}\mathbf{T}^H \in C^{MP \times MP} \tag{5.45}$$

Since $\mathbf{T}$ is a unitary transformation, i.e., $\mathbf{T}\mathbf{T}^H = \mathbf{I}$, it is quite obvious that $u(n, m) = \tilde{u}(n, m_\nu)$.

It can be easily demonstrated that the post-Doppler STAP can be applied also after the blocking operation described in Sect.5.3. In this case the formulation becomes:

$$\tilde{u}_w(n, m_\nu) = \sum_i \tilde{\mathbf{W}}_i^H(n, m_\nu)\tilde{\mathbf{S}}_i(n) \tag{5.46}$$

where

$$\tilde{\mathbf{W}}_i(n, m_\nu) = \hat{\mathbf{R}}_{Dc,i}^{-1} \tilde{\mathbf{G}}_i(n, m_\nu) \in C^{LP \times 1} \tag{5.47}$$

$$\tilde{\mathbf{S}}_i(n) = \mathbf{T}_w \mathbf{S}_i(n, m) \in C^{LP \times 1} \tag{5.48}$$

$$\hat{\mathbf{R}}_{Dc,i} = \mathbf{T}_w \hat{\mathbf{R}}_{c,i} \mathbf{T}_w^H \in C^{LP \times LP} \tag{5.49}$$

$$\tilde{\mathbf{G}}_i(n, m_\nu) = \mathbf{T}_w \mathbf{G}_i(n, m) \in C^{LP \times 1} \tag{5.50}$$

The unitary windowed transformation matrix, $\mathbf{T}_w$, is expressed as:

$$\mathbf{T}_w = \mathbf{T}_{w,t} \otimes \mathbf{I}_P \in C^{LP \times LP} \tag{5.51}$$

where $\mathbf{T}_{w,t} \in \mathbb{C}^{L \times L}$ is time-Doppler frequency Fourier transformation matrix. Its generic element is $t_{w,t}(m_\nu, m) = e^{-j2\pi m_\nu \Delta f_d m T_R}$ with $m, m_\nu = [-\frac{L}{2}, \frac{L}{2} - 1]$ and $\Delta f_d = \frac{1}{LT_R}$. As stated before since $\mathbf{T}_w$ is a unitary transformation, i.e., $\mathbf{T}_w \mathbf{T}_w^H = \mathbf{I}$, it is quite obvious that $u_w(n, m) = \tilde{u}_w(n, m_\nu)$.

Furthermore, issues concerning the number of samples required to obtain a good statistical estimation of the covariance matrices and the performance degradation caused by the *blocking* approximation to the overall covariance matrix remains the same described in the previous section.

Nevertheless, a further reduction in the dimension of data can be obtained by selecting a subset of rows corresponding to the Doppler frequencies where the target is present from the matrix $\mathbf{T}_{w,t}$. This approach is similar to the JDL (Joint Domain Localised) processing [73] where the reduction is performed also considering the angle beams corresponding to the angle regions where the target is present. However, due to the small number of channels being considered and hence the consequent poor angular resolution this approach is not applicable. The processing is the same as described above, after the substitution of $\mathbf{T}_{w,t}$ with the reduced version $\widetilde{\mathbf{T}}_{w,t} \in C^{L_f \times L}$ as shown in Fig.5.5 (L_f is the number of selected frequencies). It is worth pointing out that in this case the equivalence $\tilde{u}(n, m_\nu) = u(n, m)$ is no longer valid since the reduced matrix $\widetilde{\mathbf{T}}_{w,t}$ is no longer unitary and a further distortion in the image is introduced. In this case a good performance in the estimation of the disturbance space-slow time covariance matrix can be obtained with $N_r = 2L_f P$ training range cells.

Obviously, the position of the target in the space-Doppler cannot be assumed a priori known and so a sliding window search process can be applied to test different frequency windows. So the step to be performed are

1. Choice of the size of Doppler frequencies to be processed, L_f. The choice is based on the number of available training data

2. Set a number of Doppler bins of interest and for each bin select a number of L_f Doppler bins around it. Use this set of Doppler frequencies to form the transformation matrix $\tilde{\mathbf{T}}_w$

$$\mathbf{T}_{w,t} = \quad \boxed{\begin{array}{c} \overset{L}{} \\ \tilde{\mathbf{T}}_{t,w} \qquad L_f \\ \end{array}} \quad L$$
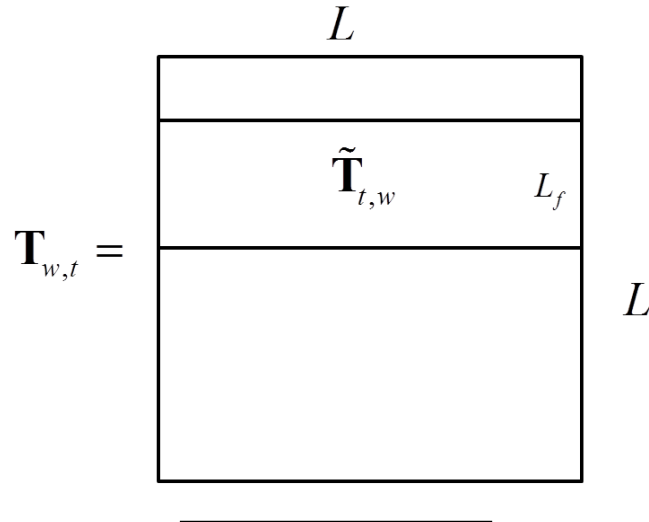
FIGURE 5.5: Reduced Doppler Transformation

3. Transform the data vector and the reference vector (Eq.(5.48)) (5.50)

4. Estimate the cross-power spectral matrix and and obtain the weightvector

5.5 Simulation results

In this section the proposed processing will be tested on simulated data. Details about the simulator set up are provided in Sect.2.5.

The useful signal is the response from an extended non-cooperative moving target which consists of 35 point scatterers that define an aeroplane shape (Fig.5.6). This particular shape is suitable to appreciate the imaging performances of the system.

The clutter is generated as explained in Sect.2.5. The covariance model in Eq.(2.78) has been used to generate the interference because it allows for an easier selection of the space-time correlation proprieties. The time correlation coefficient has been chosen to be high enough in order to simulate clutter that is static or quasi static in the observation time. The spacial correlation has been chosen to obtain a clutter Doppler bandwidth sufficiently large to mask the target return along the Doppler dimension. In fact, it is known in literature that higher spatial correlation involves narrower Doppler occupation [21].

The performance will be measured in term of image contrast (IC) and by using the Signal to Disturbance Ratio (SDR). The image contrast is defined in Eq.(3.6)
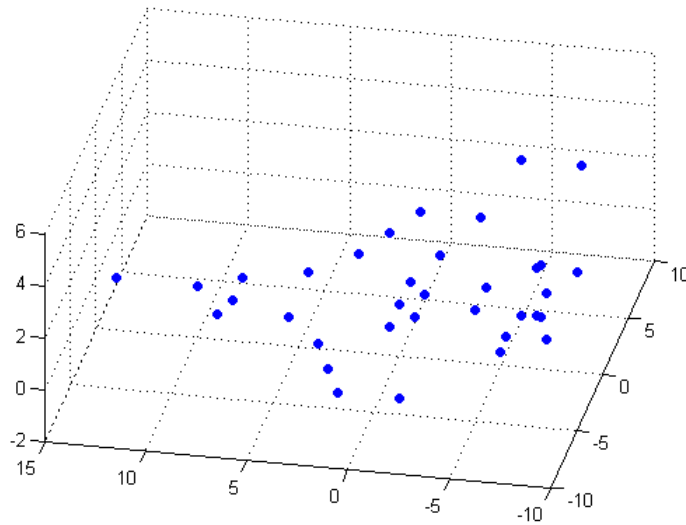
FIGURE 5.6: Target Model

while the SDR is defined as:

$$SDR = 10 \log_{10} \left[\frac{E_I}{E_{I_{diff}}} \right] \tag{5.52}$$

where E_I is the energy of the reference image (without clutter) and $E_{I_{diff}}$ is the energy of the difference between the filtered image (clutter suppressed) and the reference image.

The system and target parameters used in the simulation are summarized in Tab.5.1 and Tab.5.2.

v_p	platform velocity	$200m/s$
h	platform height	$4000m$
θ_{in}	incidence angle	$45°$
f_0	carrier frequency	$10GHz$
B	signal bandwidth	$300MHz$
T_{obs}	observation time	$1s$
PRF	pulse repetition frequency	$1KHz$
d	elements interspace	$0.015m$
SCR	signal to clutter ratio	$-30dB$
P	Number of channels	3

TABLE 5.1: System Parameters

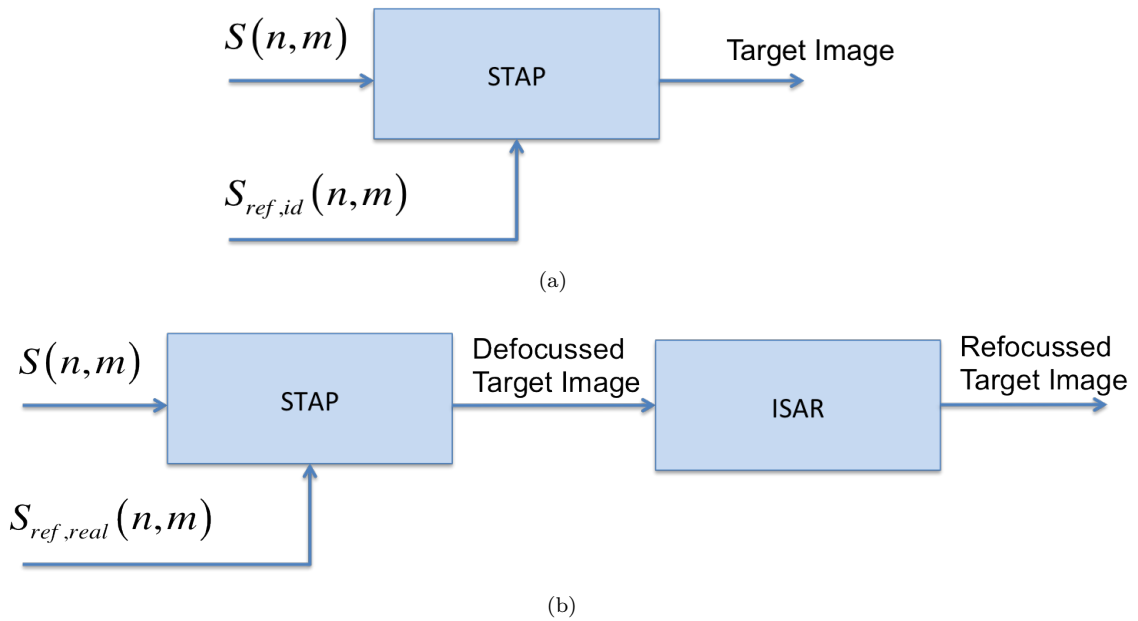| v_t	target velocity	$18m/s$	A_{pitch}	Pitch Amplitude	1°
θ_t	target orientation	$-30°$	T_{pitch}	Pitch Period	$10s$
A_{roll}	Roll Amplitude	2°	A_{yaw}	Yaw Amplitude	1.5°
T_{roll}	Roll Period	$8s$	T_{yaw}	Roll Period	$9s$

TABLE 5.2: Target Parameters

(a)

(b)

FIGURE 5.7: STAP ideal case (a), realistic case (b)

5.5.1 Comparison between ideal and realistic case

In this section the results of clutter suppression and image formation are shown in the ideal case and in the realistic case.

The *ideal case* (Fig.6.4 (a)) is defined as the case in which the target motion is known and the reference signal takes into account both the target and the platform motions. It is obvious that this is an unrealistic situation but it can be considered as a benchmark for the *realistic case* (Fig.6.4 (b)). In the *realistic case* only the platform motion is known and used to obtain the reference signal and the unknown part of the relative radar-target motion is compensated by means of the ISAR processing applied at the output of the STAP processing.

In this case no covariance matrix estimation is performed and the exact one is used to obtain the optimum filter. As stated before the output of the ideal case is a well focused image of the target since the azimuth matched filter takes into account the total relative motion between radar and target.
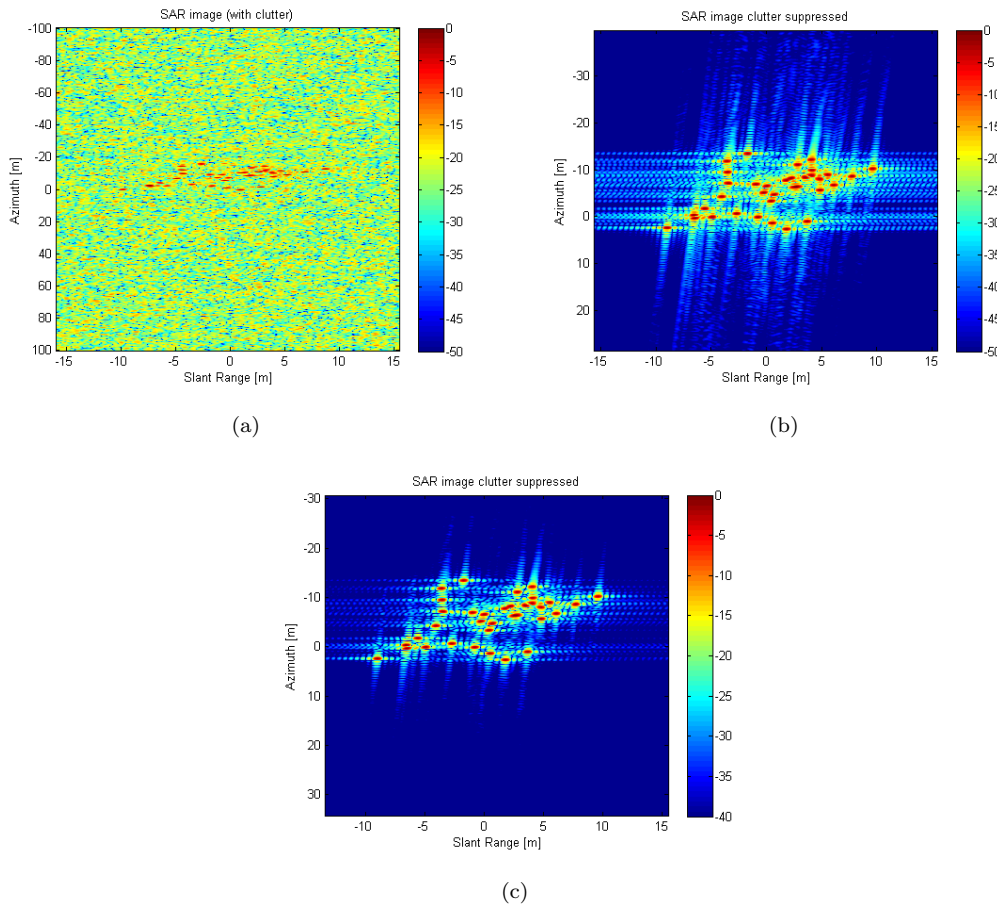
FIGURE 5.8: STAP ideal case: image without clutter suppression (a), image
with clutter suppression (b), without clutter (c)

Fig.5.8(a) shows the image obtained with the matched filter that takes into ac-
count both the target and the platform motion without clutter suppression, i.e.,
$\mathbf{W}(n, m) = \mathbf{G}(n, m)$. The clutter suppression is performed to obtain the image
in Fig.5.8(b), i.e., $\mathbf{W}(n, m) = \mathbf{R}_c^{-1}\mathbf{G}(n, m)$, while Fig.5.8(c) shows the image ob-
tained from a clutter free data, via the ideal matched filter. As it can be seen, due
to the low SCR, the target in Fig.5.8(a) is almost completely masked. However,
the target can still be seen as the ideal matched filter provide an high integration
gain focusing the energy in the scatterers locations. The comparison between the
clutter free image in Fig.5.8(c) and the image obtained after clutter suppression
Fig.5.8(b) shows that the proposed method performs really good.

The realistic case results are shown in Fig.5.9. In particular, Fig.5.9 shows the
SAR image in presence of strong clutter without clutter suppression. As no a
priori information are known about the target motion and due to low SCR, the
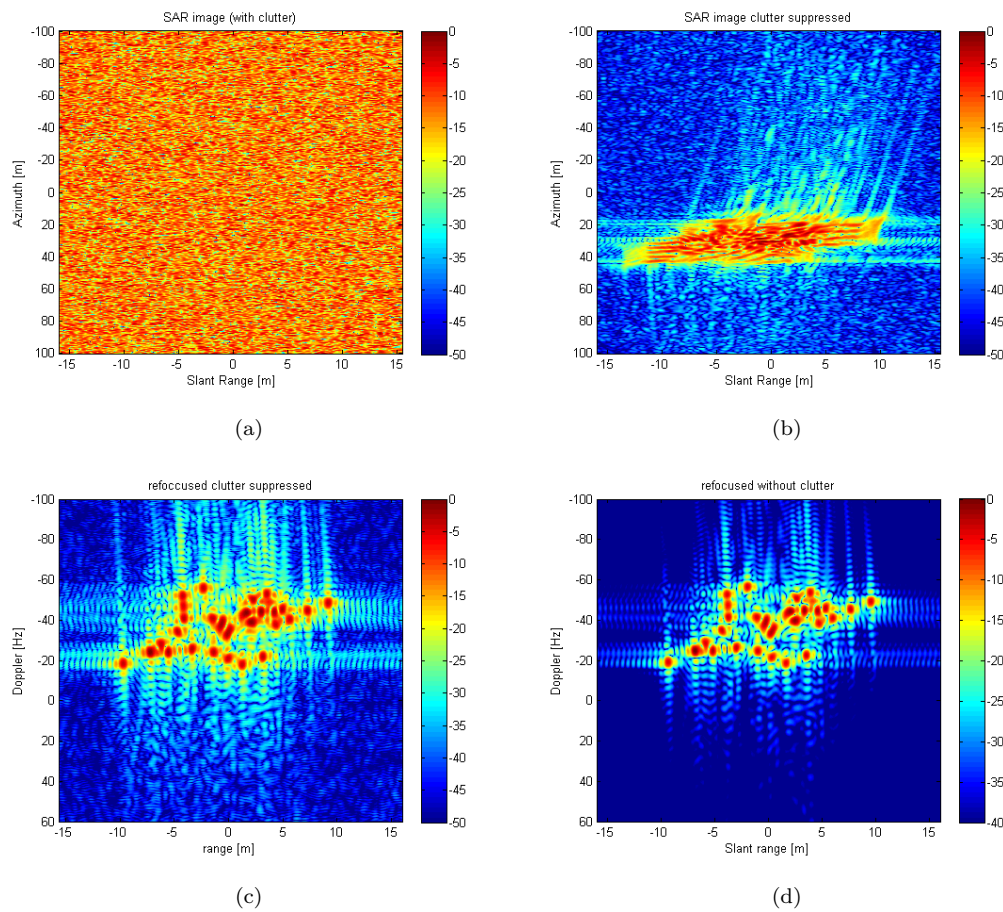target is completely masked by the clutter. In fact, in this case, the target energy

FIGURE 5.9: STAP real case: image without clutter suppression (a), image with clutter suppression (b), refocused after clutter suppression (c), refocused without clutter (d)

is spread over a wider region because of the mismatching between the reference signal used by the matched filter filter and the received signal.

Fig.5.9(b) shows the SAR image after clutter suppression. It can be easily noticed that the target is detectable but the image is defocussed due to the fact that the target own motion is not compensated. The results of ISAR processing is shown in Fig.5.9(c) in which the improvement is evident also from a visual point of view. A comparison of Fig.5.9(c) with the image obtained form a clutter free data (Fig.5.9(d)) shows that the proposed method performs very well even when the target motion is unknown. As it can be noticed, Fig.5.9(d) shows some losses with respect the image in Fig.5.8(d). These losses are present in the image obtained from the clutter free data (without clutter suppression) and they are due to the fact the the inversion in the ISAR processing is performed by means of a 2D-IFT that is not the optimum inversion. These losses are evident from a visual point of view and can be quantified by means of the IC values. For the image shown in

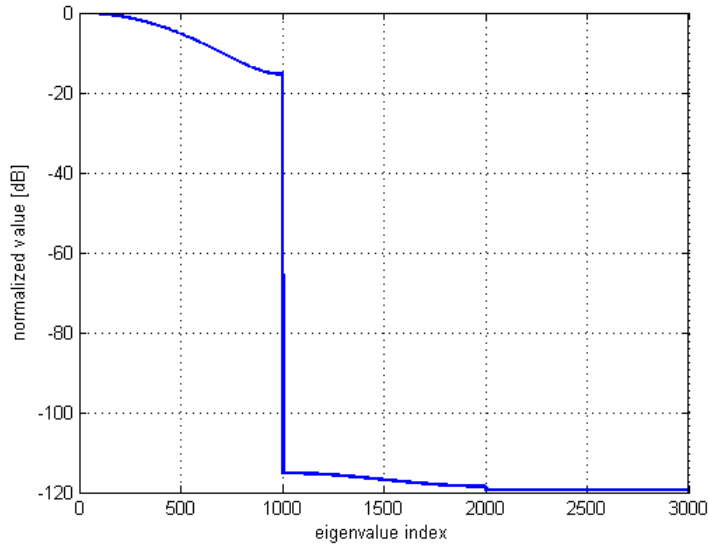Fig.5.8(d) $IC = 9.87$ while for the image shown in Fig.5.9(d) $IC = 7.84$.

FIGURE 5.10: Eigenspectrum of the space-slow time covariance matrix

In Fig.5.10 the eigenspectrum of the space slow time covariance matrix $\mathbf{R}_c$ is shown. The eigenspectrum contains the rank-ordered eigenvalues of $\mathbf{R}_c$ and it allows for an analysis of the disturbances. The eigenvalues distribution exhibits clearly how much the angle-Doppler space is occupied by the interference and how much is left for the useful signal. In particular the number of interference eigenvalues gives an indication of the number of degrees of freedom of the interference scenario. Any interference rejection operation should have at least this number of degrees of freedom. From Fig.5.10 is clear that the clutter occupies only a subspace of dimension M. This is consistent with [61] in which is demonstrated that for each Doppler cell the clutter energy is contained in a one dimensional subspace.

5.5.2 Sub-optimum approaches

A sub-optimum algorithm, which involves a windowing operation, has been proposed in Sect.5.3. In this section the results obtained by means of this approach will be shown and the distortions due to the approximation will be discussed.

The results for different value of the window length, L, are shown in Fig.5.11-5.14. In each of the above mentioned figures, the image before (a) and after refocussing (b) are shown.
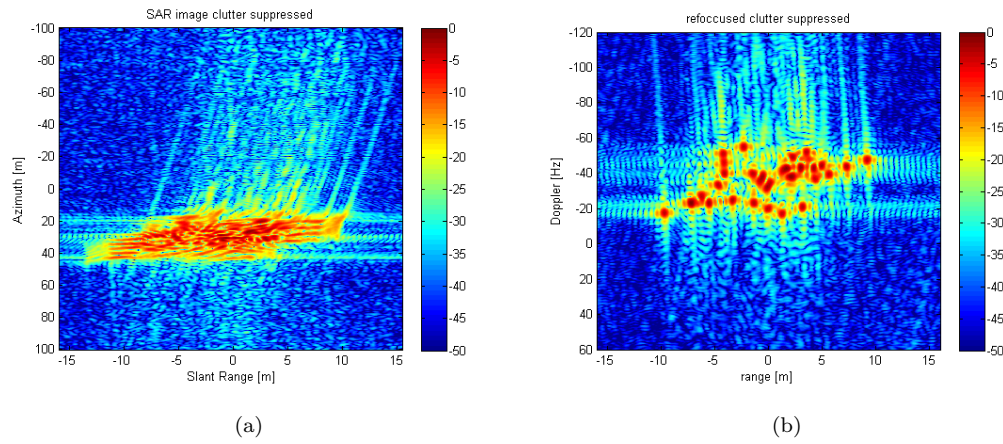
FIGURE 5.11: STAP sub-optimum before L=100 ISAR processing (a), after ISAR processing (b)
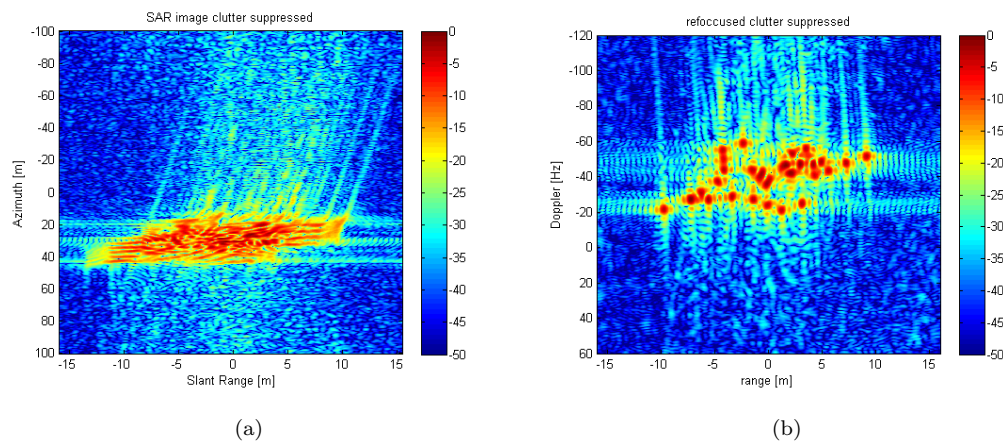
FIGURE 5.12: STAP sub-optimum before L=50 ISAR processing (a), after ISAR processing (b)
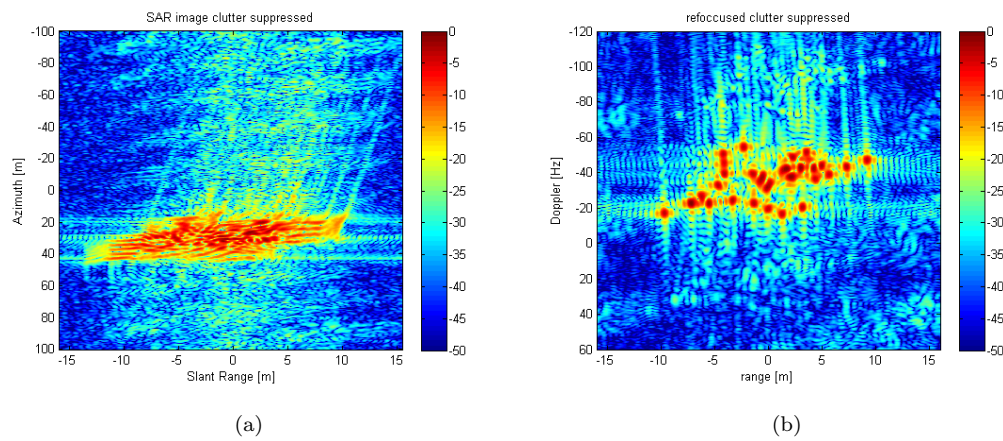
FIGURE 5.13: STAP sub-optimum before L=20 ISAR processing (a), after ISAR processing (b)
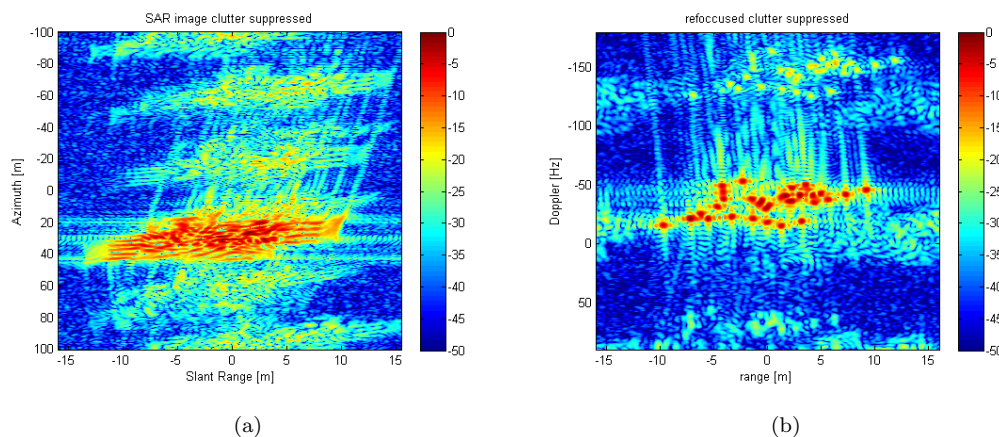
FIGURE 5.14: STAP sub-optimum L=10 before ISAR processing (a), after ISAR processing (b)

As it can be easily noticed, the refocusing performs well and the target energy is refocussed in the scatterers locations, for each of the considered value of L. Notwithstanding, as L decreases (and so the quantity of training data needed), distortions in the image occur. In particular, it has been shown in Fig.5.16 that when the windowing operation is performed, some regions of the interference covariance matrix are not used for clutter suppression so that this error produces a distortion in the image. As L decreases, the error exhibits a periodic behaviour which is likely to be associated to the specific pattern of the error in the considered covariance matrix with respect the exact one.
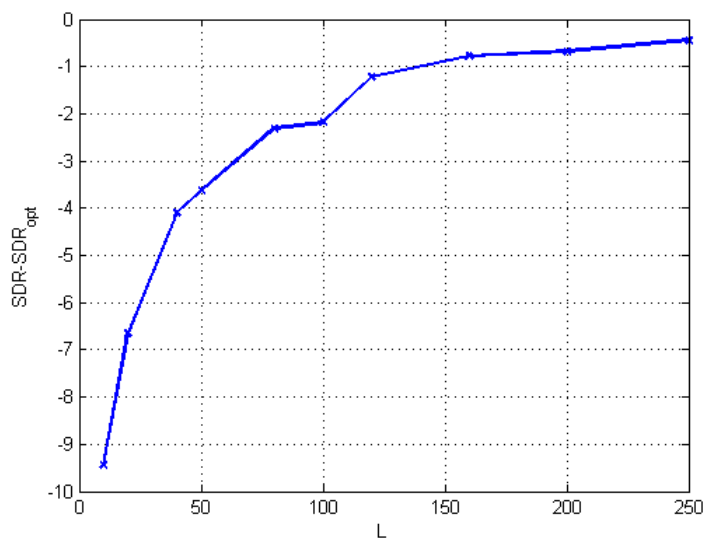

FIGURE 5.15: SDR loss with respect the window length L

In Fig.5.15 the loss with respect the SDR in the case of optimal processing is shown for different values of the window length L. As it can be seen, the distortion in the final image becomes stronger as the windows length decreases.

In order to reduce this distortion a different choice of the pattern must be considered. The easiest way to do this is to consider windows with a fixed percentage of overlap. In this case the considered space slow time covariance matrix is depicted in Fig.5.4 while in Fig.5.16 the results with different values of overlap for the case $L = 10$ are shown.
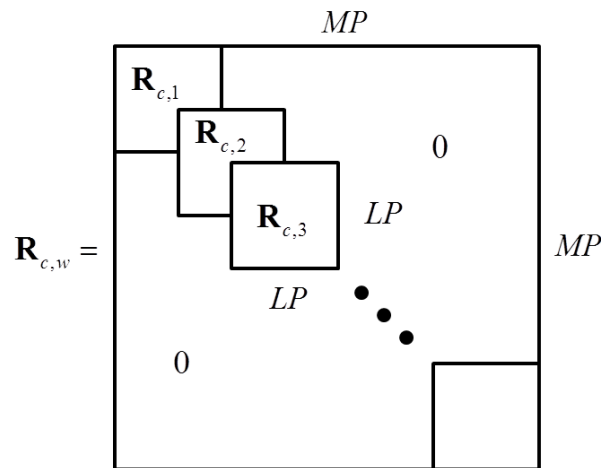

FIGURE 5.16: Covariance matrix approximation with overlap

As it can be seen, introducing the overlap, the periodic disturbance can be reduced or completely eliminated. It is quite obvious that the bigger the overlap is the bigger the increase in the computational time is.
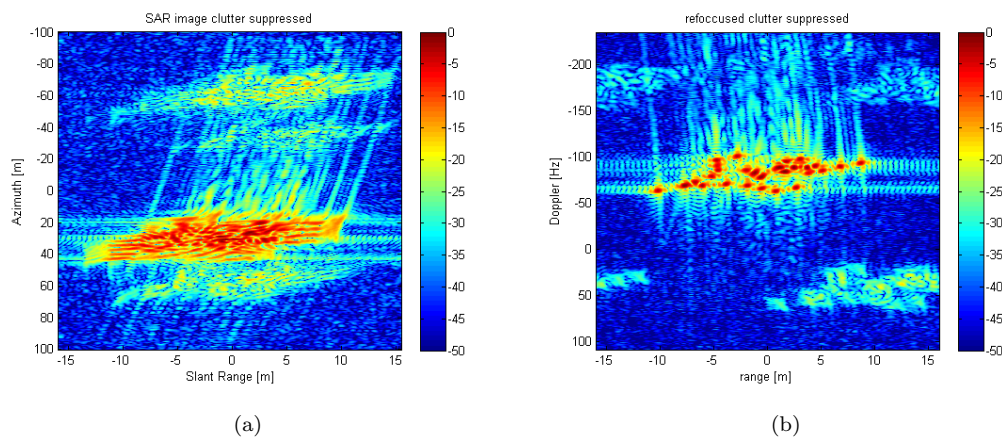

(a) (b)

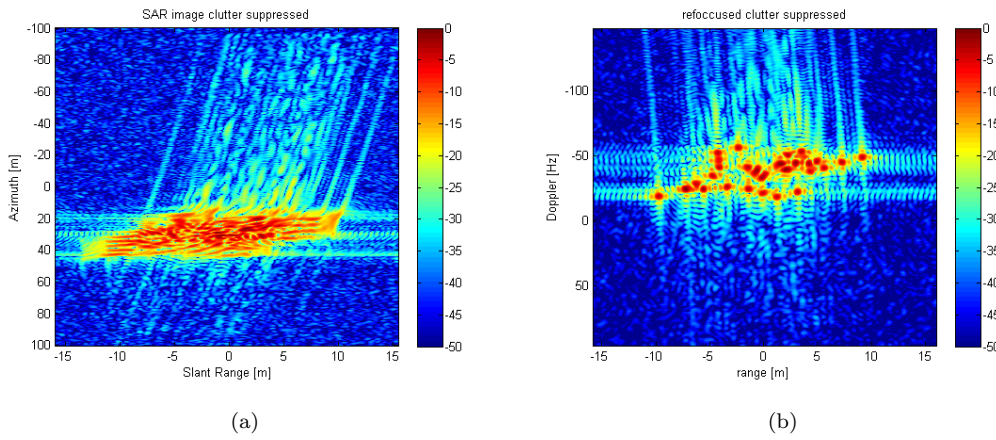FIGURE 5.17: STAP sub-optimum L=10 Overlap=5 before ISAR (a) after ISAR (b)

FIGURE 5.18: STAP sub-optimum L=10 Overlap=9 before ISAR (a) after ISAR (b)

Results with two different values of overlap are shown in Fig.5.17 and Fig.5.18. The window length is $L = 10$. As it can be easily noted with an overlap value of 5 pulses the periodic distortions are reduced with respect the case without overlap shown in Fig.5.14, while for overlap value equal to 9 pulses the distortions completely disappear. As stated before, the overlap involves an increase of the computational time.

In Fig.5.19 the eigenspectra of the ith sub-block of the space-slow time covariance matrix are shown. As it can be noted by comparing Fig.5.19 with Fig.5.10, the shape of the eigenspectrum of the whole covariance matrix has the same shape of the eigenspectrum of the generic sub-block. This is quite obvious because the windowing operation involves a subsampling in the Doppler domain and hence a subsampling of the Doppler-angle spectrum.

In Fig.5.21 a result obtained applying the sub-optimum processing described in Sect.5.4 is shown. In this case the window length is $L = 100$ pulses while the Doppler frequency windows considered is $L_f = 20$. As it can be easily noted, the processing performs well leading to a detectable defocused version of the target image before applying the ISAR refocussing process (Fig.5.21(a)) and a good ISAR image after refocussing process (Fig.5.21(b)). Moreover, applying the Doppler window a reduction in the dimensionality of the covariance matrix to be estimated is obtained.
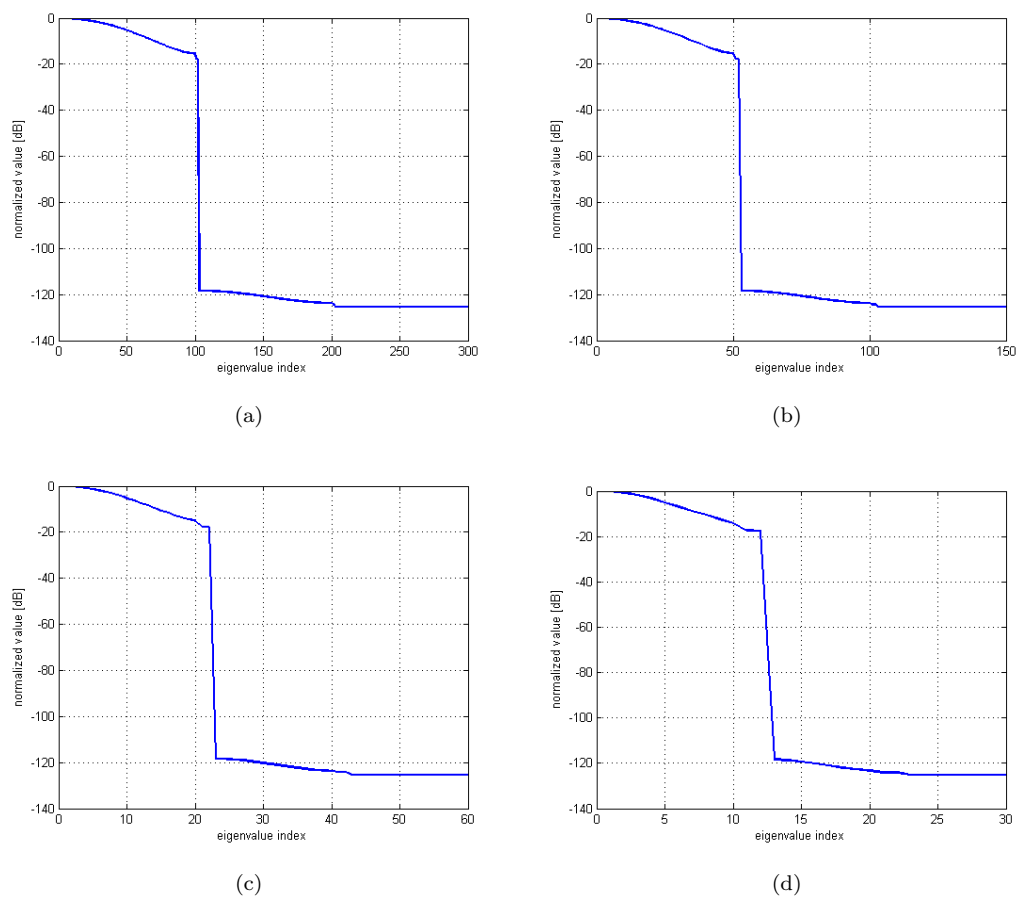
FIGURE 5.19: Eigenspectrum of the sub-block space-slow time covariance matrix L=100(a), L=50(b), L=20(c), L=10(d)
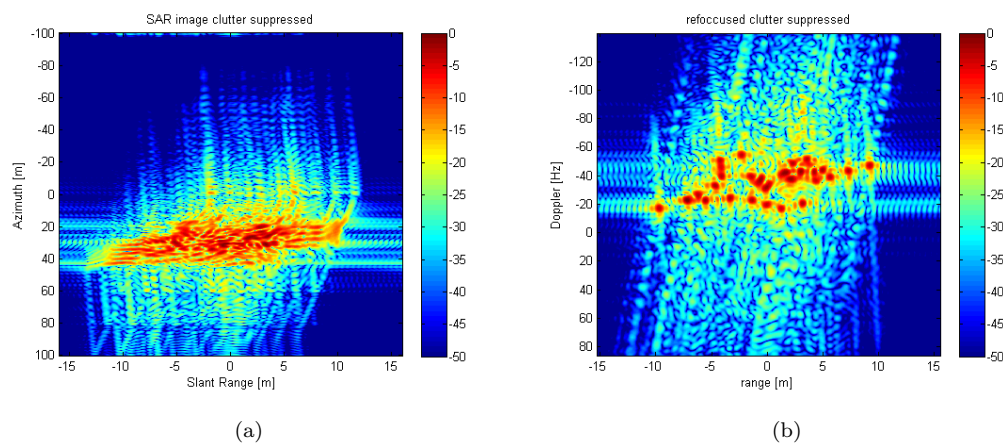

FIGURE 5.20: STAP sub-optimum post Doppler $L = 100$, $L_f = 20$

5.5.3 Realistic training

In the previous section results are obtained by considering the exact space-slow time covariance matrix $\mathbf{R}_c$ (or in case of sub-optimum processing the exact sub-block $\mathbf{R}_{c,i}$). In this section some comments about estimation via training data will be given.

The estimation process is expressed as:

$$\hat{\mathbf{R}}_c = \frac{1}{N_r} \sum_{n_r=0}^{N_r-1} \mathbf{Z}(n_r)\mathbf{Z}^H(n_r) \in \mathbb{C}^{MP \times MP} \tag{5.53}$$

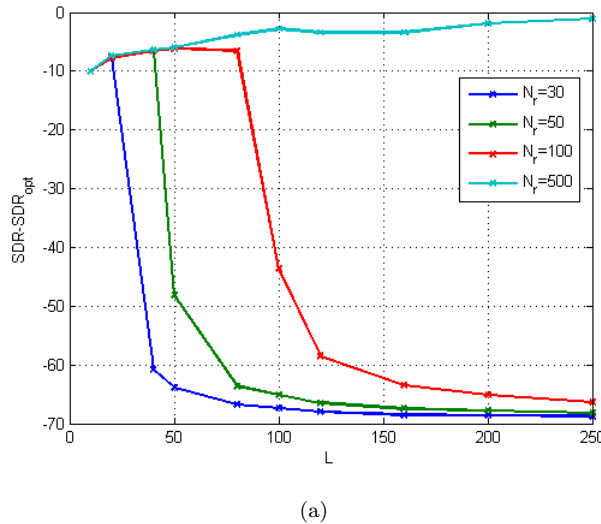where $\mathbf{Z}(n_r)$ are realizations of the interferer.

(a)

FIGURE 5.21: SDR loss with respect L for different value of N_r

In Fig.5.21 the SDR loss is shown with respect the windows length L and the number of training data N_r. As it can be noted, good performance can be obtained with a number of training data lower than the theoretical bound $N_r = 2LP$. This is due to the fact that in order to obtain a good estimation of the interference covariance matrix only a number of training data equal to the number of significant eigenvalues is needed. The values of N_r that allow for good clutter cancellation are consistent with the number of significant eigenvalues shown in the eigenspectra in Fig.5.19. It is quite obvious that better performances are obtained for larger values of the window length L until the number of training data N_r is sufficient to obtain a good estimation of the relative block of the covariance matrix.

In Fig.5.22 the SDR loss for different values of N_r is shown in for the two sub optimum approach described above. In both cases the windows length is $L = 100$. The blue curve corresponds to the sub-obtimum approach described in Sect.5.3 while the red curve refers to the sub-optimum approach described in Sect.5.4 for $L_f = 20$. It is quite obvious the for the second process a smaller value of training data are sufficient to obtain good performances. This is because in the second case a smaller space-slow time covariance matrix must be estimated. The eigenspectrum of the disturbance space-slow time covariance matrix is shown in Fig.5.23. It is evident the reduction of the disturbance degrees of freedom that involves the reduction of the training data support.
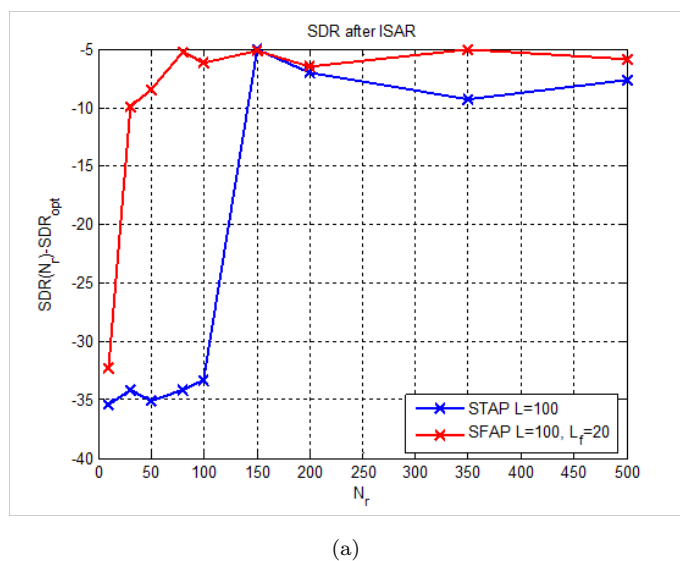

(a)

FIGURE 5.22: SDR loss with respect N_r for the two sub-optimum approaches

All these comments are valid in case of homogeneous clutter. This means that the training data on which the estimation is performed are independent and identically distributed target-free data with the same statistics of the disturbance in the cell under test. Frequently, the training data can be subject to contamination by other moving target or clutter with different statistical properties with respect the disturbance in the region under test. This can lead to losses in the clutter cancellation performance as shown in Fig.5.24.

In Fig.5.24 the performance losses with respect the amount of non-homogeneous clutter in the training data is shown for different degrees of spatial and temporal non-homogeneity. This performances are evaluated considering a window length $L = 100$. The number of homogeneous clutter realization (with $\sigma_{t,1}^2$ and $\sigma_{s,1}^2$) is $N_r = 200$ that is sufficient to obtain a good estimation of $\mathbf{R}_{c,i}$ for the considered window length. This training set is contaminated by non-homogeneity by
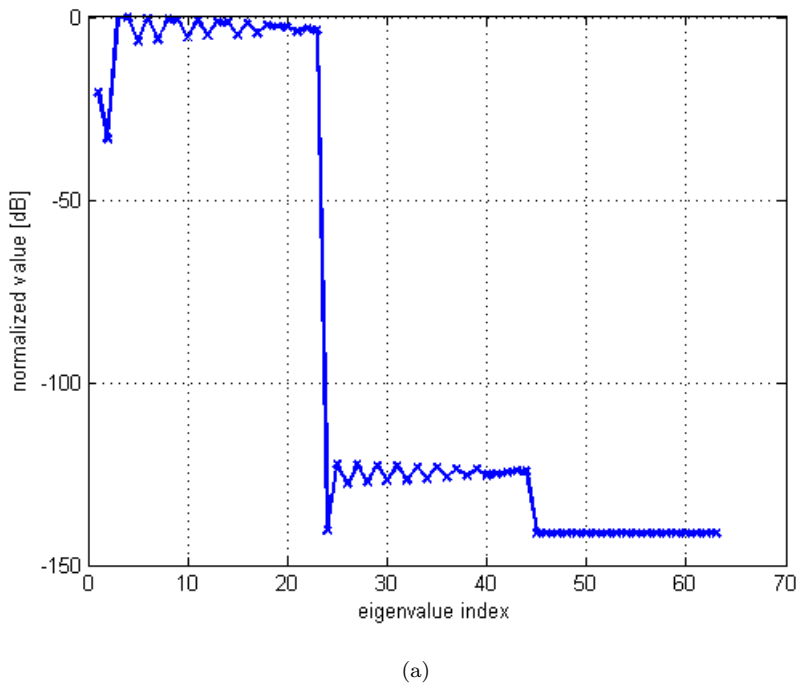
(a)

FIGURE 5.23: Eigenspectrum $L = 100$, $L_f = 20$

considering in the average process a number N_{r2} of disturbance realizations with different statistical properties ($\sigma_{t,2}^2$ and $\sigma_{s,2}^2$). The figure shows the performance losses increasing the amount of non-homogeneous data with different values of non-homogeneity $r = \left(\frac{\sigma_{t/s,1}^2}{\sigma_{t/s,2}^2}\right)$. In Fig.5.24(a) the losses with respect different values of temporal correlation is shown while in Fig.5.24(b) the losses with respect to different values of temporal correlation are shown. As it can be noted by considering disturbance with lower temporal correlation property a performance degradation is evident. This is due to the fact that in this case not only stationary scene is considered to estimate the space-slow time covariance matrix and hence also moving targets are cancelled.

5.6 Conclusion

In this chapter the problem of moving target detection in strong clutter has been investigated. A processing that combines STAP and ISAR processing has been developed. The formulation of the optimum and sub-optimum processing has been derived. The effectiveness of the proposed techniques has been proved on simulated data.
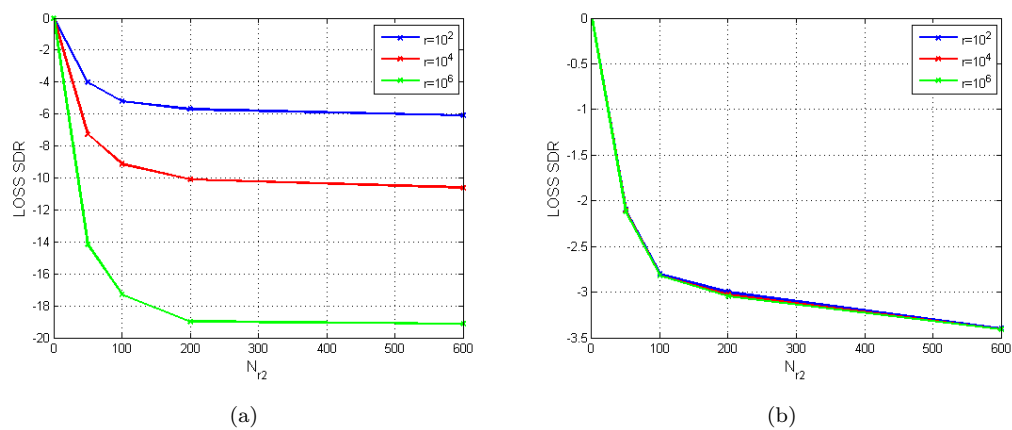
(a)

(b)

FIGURE 5.24: SDR loss with non-homogeneity in the training data in time (a) and space (b)

Chapter 6

Space Doppler Adaptive Processing

6.1 Introduction

In this chapter a modified version of the classical STAP described in the previous chapter is presented. This is derived from the Range Doppler image formation algorithm and works in the Space Doppler domain. In the following, it will be addressed as Space Doppler Adaptive Processing (SDAP).

The theoretical formulation will be derived both for optimum and sub-optimum processing. It will be combined with the ISAR processing in order to obtain well focused images of non-cooperative moving targets embedded in strong clutter environments. The effectiveness of the proposed processor will be proved on simulated data. A comparison with the STAP-ISAR processing described in the previous chapter will be presented.

6.2 Jonit SDAP-ISAR Optimum Processing

In this section the formulation of the optimum SDAP will be presented. The combination with the ISAR processing to obtain high resolution images of non-cooperative moving targets will be investigated.

Signal Modelling and image formation

Let consider the same acquisition geometry shown in Fig.5.1. The expression of the received signal is the same of the previous chapter and will be recalled here for the sake of clarity. The total Fourier transform of the received signal is

$$S(f,t) = S_t(f,t) + S_c(f,t) + N(f,t) \tag{6.1}$$

where the three components represent the target contribution, $S_t(f,t)$, the clutter contribution due to the static scene, $S_c(f,t)$ and the additive Gaussian noise, $N(f,t)$, respectively. The target and clutter contributions can be expressed as:

$$S_t(f,t) = e^{-j\frac{4\pi}{\lambda}R_{0t}(t)} \sum_{k=1}^{K} \sigma_k e^{-j\frac{4\pi}{\lambda}\left[y_2^{(k)} + \Omega_{eff,t}y_1^{(k)}t\right]} \tag{6.2}$$

$$S_c(f,t) = e^{-j\frac{4\pi}{\lambda}R_{0c}(t)} \iint_{(y_1,y_2)} \sigma(y_1,y_2) e^{-j\frac{4\pi}{\lambda}\left[y_2 + \Omega_{eff,c}y_1 t\right]} dy_1 dy_2 \tag{6.3}$$

These expressions are valid in case of *straight iso-range approximation*. It is worth pointing out that since the proposed SDAP is based on the range Doppler image formation algorithm, the straight iso-range approximation is mandatory to apply this processing.

High resolution in range dimension is obtained by transmitting wideband signals and matched filtering the received signal. High resolution in azimuth con be obtained by applying the range Doppler processing described in Sect.2.2. Considering $S_t(f,t)$ the signal received from a static scatterer placed in the generic position (y_1,y_2), the range Doppler processing can be expressed as:

$$u_D(f,\nu) = FT_t\left\{S_t(f,t)S_{ref}^*(f,t)\right\} \tag{6.4}$$

where $FT_t\{\}$ is the Fourier Transform along the slow time dimension t.

Eq.(6.4) can be expressed in terms of convolution in the Doppler frequency domain as:

$$u_D(f, \nu) = \tilde{S}_{ref}(f, -\nu) \otimes \tilde{S}_t(f, \nu) \tag{6.5}$$

where

$$\tilde{S}_t(f, \nu) = FT_t \{S(f, t)\} \tag{6.6}$$

and

$$\tilde{S}_{ref}(f, \nu) = FT_t \{S_{ref}(f, t)\} \tag{6.7}$$

are the Fourier transformed received signal and reference signal along the slow time dimension respectively.

It is evident from Eq.(6.5) that the range Doppler image formation processing can be seen as a matched filtering in the frequency Doppler domain.

This formulation can be easily extended to a discretized version of the signal in which $S(n, m) = S(n\Delta f, mT_R)$. In this case the range Doppler image formation processing can be expressed as:

$$u_D(n, m_\nu) = DFT_m \left\{ S_t(n, m) S_{ref}^*(n, m) \right\} \tag{6.8}$$

or in term of Doppler matched filtering as

$$u_D(n, m_\nu) = \tilde{S}_t(n, m_\nu) \otimes_{m_\nu} \tilde{S}_{ref}(n, -m_\nu) \tag{6.9}$$

where

$$\tilde{S}_t(n, m_\nu) = DFT_m \{S_t(n, m)\} \tag{6.10}$$

$$\tilde{S}_{ref}(n, m_\nu) = DFT_m \{S_{ref}(n, m)\} \tag{6.11}$$

and $\otimes_{m_\nu}$ denotes the discrete convolution along the m_ν dimension and DFT_m is the Discrete Fourier Transform along the discretized slow time dimension.

The matched filtering operation in Eq.(6.9) can be expressed in a vectorial form

after defining the signal vector, i.e., $\tilde{\mathbf{S}}(n)$, and the reference vector, i.e., $\tilde{\mathbf{G}}_D(n, m_\nu)$, as

$$\tilde{\mathbf{S}}(n) = \left[\tilde{S}(n,0), \tilde{S}(n,1), ..., \tilde{S}(n, M-1)\right]^T \in \mathbb{C}^{M \times 1} \tag{6.12}$$

$$\tilde{\mathbf{G}}_D(n, m_\nu) = \left[\tilde{S}_{ref}(n, m_\nu), \tilde{S}_{ref}(n, m_\nu - 1), ..., \tilde{S}_{ref}(n, m_\nu - (M-1))\right]^T \in \mathbb{C}^{M \times 1} \tag{6.13}$$

so that

$$u_D(n, m_\nu) = \tilde{\mathbf{G}}_D^H(n, m_\nu)\tilde{\mathbf{S}}(n) \tag{6.14}$$

This processing can be easily extended to the multichannel scenario. The signal model has been derived in the previous chapters.

The formulation of the multichannel Ranged Doppler (see Sect.2.2.3) can be expressed as:

$$u_D(n, m_\nu) = \sum_{p=1}^{P} u_{D,p}(n, m_\nu) = \sum_{p=1}^{P} \tilde{S}_{t,p}(n, m_\nu) \otimes_{m_\nu} \tilde{S}_{ref,p}(n, -m_\nu) \tag{6.15}$$

Eq.(6.15) can be expressed in a vectorial form after performing a stacking operation first along the channel dimension Eq.(6.16)-(6.17) and along the Doppler frequency dimension Eq.(6.18)-(6.19) as

$$\tilde{\mathbf{S}}(n, m_\nu) = \frac{1}{P}\left[\tilde{S}_1(n, m_\nu), \tilde{S}_2(n, m_\nu), ..., \tilde{S}_P(n, m_\nu)\right]^T \in \mathbb{C}^{P \times 1} \tag{6.16}$$

$$\tilde{\mathbf{S}}_{ref}(n, m_\nu) = \frac{1}{P}\left[\tilde{S}_{ref,1}(n, m_\nu), \tilde{S}_{ref,2}(n, m_\nu), ..., \tilde{S}_{ref,P}(n, m_\nu)\right]^T \in \mathbb{C}^{P \times 1} \tag{6.17}$$

$$\tilde{\mathbf{S}}(n) = \left[\tilde{\mathbf{S}}(n,0), \tilde{\mathbf{S}}(n,1), ..., \tilde{\mathbf{S}}(n, M-1)\right]^T \in \mathbb{C}^{MP \times 1} \tag{6.18}$$

$$\tilde{\mathbf{G}}_D(n, m_\nu) = \left[\tilde{\mathbf{S}}_{ref}(n, m_\nu), \tilde{\mathbf{S}}_{ref}(n, m_\nu - 1), ..., \tilde{\mathbf{S}}_{ref}(n, m_\nu - (M-1))\right]^T \in \mathbb{C}^{MP \times 1} \tag{6.19}$$

The output of the Doppler matched filter is then expressed as:

$$u_D(n, m_\nu) = \tilde{\mathbf{G}}_D^H(n, m_\nu)\tilde{\mathbf{S}}(n) \tag{6.20}$$

It is worth highlighting that in order to apply this image formation processing the straight iso-range approximation must hold true. Moreover in order to properly obtain the multichannel image the sum along the spacial dimension must be performed (Eq.(6.15)). In order avoid distortions in the resulting image this must be a coherent sum leading to limitation in the array and in the imaging area size. This limitations have been analysed in Sect.2.2.3 deriving the condition that must be met to properly process multichannel data via Range Doppler based processing expressed in Eq.2.54.

At this stage, to obtain the final image a Fourier transform along the range frequency dimension is performed.

SDAP ISAR

Optimum Space Doppler Adaptive Processing involves the replacement of the space-Doppler reference vector with the weightvector that maximizes the output SINR as:

$$u_D(n, m_\nu) = \tilde{\mathbf{W}}_D^H(n, m_\nu)\tilde{\mathbf{S}}(n) \tag{6.21}$$

The expression of the optimum filter has been derived in the previous chapter. The sample matrix inversion implementation is expressed as:

$$\tilde{\mathbf{W}}_D(n, m_\nu) = \gamma \hat{\mathbf{R}}_{Dc}^{-1}\tilde{\mathbf{G}}_D(n, m_\nu) \tag{6.22}$$

where γ is a scalar that does not affect the SINR at the output of the optimum filter and $\hat{\mathbf{R}}_{Dc}$ is the estimation of the interference cross-power spectral matrix $\mathbf{R}_{Dc}$ and it is obtained by averaging along N_r target free range cells of training data as

$$\hat{\mathbf{R}}_{Dc} = \frac{1}{N_r} \sum_{n_r=0}^{N_r-1} \tilde{\mathbf{Z}}(n_r)\tilde{\mathbf{Z}}^H(n_r) \in \mathbb{C}^{MP \times MP} \tag{6.23}$$

The vector $\tilde{\mathbf{Z}}(n_r)$ denotes the target-free data in the nth range cell in the Space-Doppler frequency domain.

It is worth pointing out that the optimum processing in Eq.(6.22) performs both

clutter suppression and image formation by means of range Doppler processing. As stated in the previous chapter, in order to obtain a well focused image of the non-cooperative moving target the reference vector $\tilde{\mathbf{G}}_D(n, m_\nu)$ must compensate both platform and target own motion. Obviously this is not a realistic situation since the target is non-cooperative. So, a first motion compensation is performed in the SDAP processing considering only the known part of the relative radar target motion while high resolution image of non-cooperative target is obtained by applying the ISAR processing at the output of the space Doppler adaptive processing. As stated before ISAR processing must be applied separately at each target detected after clutter mitigation. The fundamental steps can be recalled here and they are:

1. image crop inversion via 2D-IFFT

2. target motion compensation by means of ICBA motion estimation

3. image formation via Range-Doppler technique

The functional block is depicted in Fig.6.1.

It is worth pointing out that the issues concerning the estimation of the cross-power spectral matrix are the same seen in the previous chapter for the estimation of the space-slow time covariance matrix. Theoretically, $N_r = 2PM$ target free range cells are needed to obtain an average performance loss of $3dB$ in the estimation of R_{Dc}. As stated in the previous chapter sub-optimum approaches are needed to overcome the statistical issues

6.3 Sub-Optimum approach

The reduction in the dimensionality of the cross-power spectral matrix can be obtained by splitting the filtering operation in Eq.(6.22) in sub-windows as shown in Fig.6.2.

This operation consists of splitting the Doppler dimension in sub-windows of length L and applying a reduced dimension SDAP in each sub-block. The reduction in the dimensionality of the cross-power spectral matrix to be estimated is given by the

$$\tilde{S}_1(n,m_\nu) \quad \tilde{S}_2(n,m_\nu) \quad \tilde{S}_P(n,m_\nu)$$
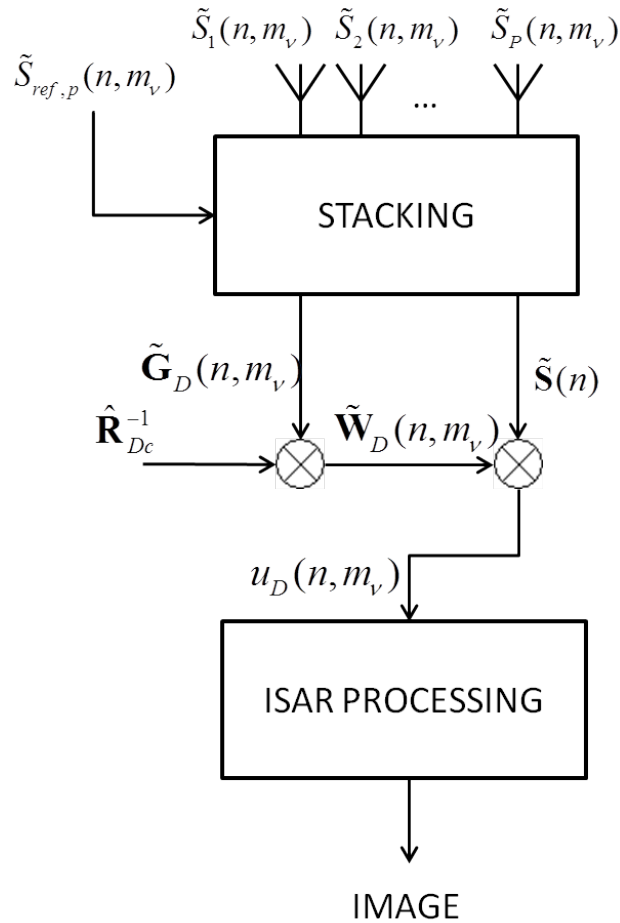
$$\tilde{S}_{ref,p}(n,m_\nu)$$

FIGURE 6.1: Optimum SDAP ISAR functional block

length of the considered sub-window. It is worth pointing out that, as stated in the previous chapter, this windowing operation does not involves any losses if only the Doppler matched filtering operation is performed, i.e., $\tilde{\mathbf{W}}(n,m_\nu) = \tilde{\mathbf{G}}_D(n,m_\nu)$. However when the clutter mitigation is performed and the weighvector assumes the structure in Eq.(6.22), the windowing operation involves an approximation in the considered cross-power spectral matrix, i.e., $R_{Dc,w}$, with respect the ideal one R_{Dc}. This approximation consists of considering only a set of block of the overall cross-power spectral matrix aligned along the principal diagonal as shown in Fig.6.3.

This sub-optimum processing can be formalized as follows. Let i denotes the window index and L the window length. The output of the filtering operation in the ith sub-block is:
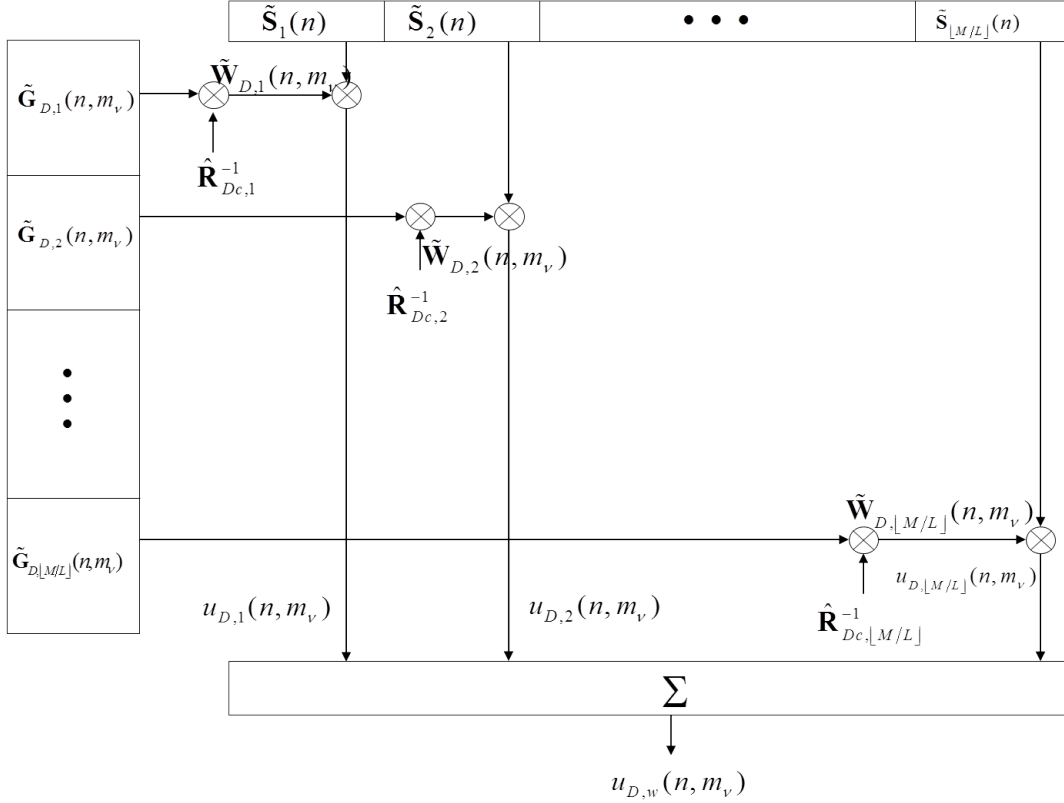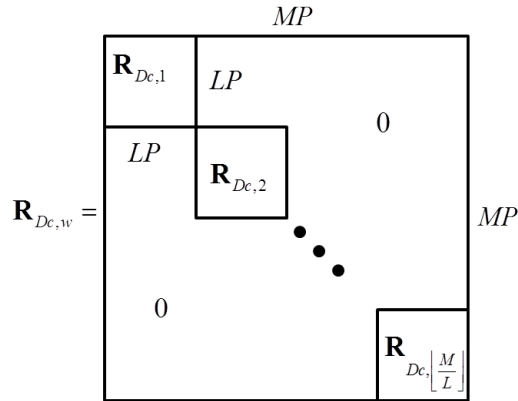
FIGURE 6.2: Sub-optimum Optimum SDAP ISAR functional block

FIGURE 6.3: Approximated corss-power spectral matrix

$$u_{D,i}(n, m_\nu) = \tilde{\mathbf{W}}_{D,i}^H(n, m_\nu)\tilde{\mathbf{S}}_i(n) \tag{6.24}$$

where $\tilde{\mathbf{W}}_{D,i}(n, m_\nu)$ and $\tilde{\mathbf{S}}_i(n)$ are the weightvector and the signal vector with respect the ith block. The global output of the sub-optimum SDAP filtering process is

$$u_{D,w}(n, m_\nu) = \sum_i u_{D,i}(n, m_\nu) \tag{6.25}$$

The weightvector in the ith window is expressed as:

$$\tilde{\mathbf{W}}_{D,i}(n, m_\nu) = \hat{\mathbf{R}}_{Dc,i}^{-1} \tilde{\mathbf{G}}_{D,i}(n, m_\nu) \tag{6.26}$$

where

$$\tilde{\mathbf{G}}_{D,i}(n, m_\nu) = \begin{bmatrix} \tilde{\mathbf{S}}_{ref}(n, m_\nu - (i-1)L) \\ \tilde{\mathbf{S}}_{ref}(n, m_\nu - ((i-1)L+1)) \\ \tilde{\mathbf{S}}_{ref}(n, m_\nu - ((i-1)L+2)) \\ \vdots \\ \tilde{\mathbf{S}}_{ref}(n, m_\nu - ((iL-1))) \end{bmatrix} \in C^{LP \times 1} \tag{6.27}$$

and

$$\tilde{\mathbf{S}}_i(n) = \begin{bmatrix} \tilde{\mathbf{S}}(n, (i-1)L) \\ \tilde{\mathbf{S}}(n, (i-1)L+1) \\ \tilde{\mathbf{S}}(n, (i-1)L+2) \\ \vdots \\ \tilde{\mathbf{S}}(n, iL-1) \end{bmatrix} \in C^{LP \times 1} \tag{6.28}$$

The cross-power spectral matrix in the ith window, $\hat{\mathbf{R}}_{Dc,i}$, is estimated as

$$\hat{\mathbf{R}}_{Dc,i} = \frac{1}{N_r} \sum_{n_r=0}^{N_r-1} \tilde{\mathbf{Z}}_i(n_r) \tilde{\mathbf{Z}}_i^H(n_r) \in \mathbb{C}^{LP \times LP} \tag{6.29}$$

Since the dimension of the matrix to be estimated is reduced a reduced number of training range cells are needed. In fact to obtain a performance loss of $3dB$ only $N_r = 2LP$ target free range cells are needed. It is quite obvious that the windowing operation may introduce some distortion in the resulting image since an approximated cross-power spectral matrix is used. In the next section simulated data will be used to analyse the performance of both optimum and sub-optimum

processing and to make a comparison with the STAP ISAR processing described in the previous chapter.

6.4 Simulation results

In this section the proposed processing will be tested on simulated data. Details about the simulator set up have been provided in Sect.5.5. The simulated scenario is the same described in the previous chapter. This allows for a comparison between the two proposed processings, i.e., STAP ISAR and SDAP ISAR, in the same conditions. The system and target parameters are summarized in Tab.5.1,5.2. The target is the same used in the previous chapter, Fig.5.6, and the clutter correlation parameters are the same.

6.4.1 Comparison between ideal case and realistic case

In this section the results of clutter suppression and image formation are shown in both ideal case and realistic case. The *ideal case* (Fig.6.4(a)) is defined as the case in which the reference vector takes into account both the target and the platform motions. As stated before, this unrealistic situation gives a benchmark for the *realistic case* (Fig.Fig.6.4(b)) in which only the platform motion is known and used to form the reference signal vector. In this case the unknown part of the relative platform-target motion is compensated by means of the ISAR processing.

Fig.6.5(a) shows the image obtained by applying the Range Doppler processing after the compensation of the total radar-target motion without clutter suppression, i.e., $\tilde{\mathbf{W}}(n, m_\nu) = \tilde{\mathbf{G}}_D(n, m_\nu)$. The image after clutter suppression (and ideal motion compensation), i.e., $\tilde{\mathbf{W}}(n, m_\nu) = \hat{\mathbf{R}}_{Dc}\tilde{\mathbf{G}}_D(n, m_\nu)$, is shown in Fig.6.5(b), while Fig.6.5(c) shows the image obtained from a clutter free data. As it can be noted in Fig.6.5(a), due to the low SCR, the clutter completely masks the target. A comparison between the clutter free image in Fig.6.5(c) and the clutter suppressed image Fig.6.5(b) results shows that the proposed algorithm performs really good leading to a well focused image of the target.

Fig.6.6 shows the results in the realistic case scenario. In particular, in Fig.6.6(a) the SAR image without clutter suppression is shown. It is quite obvious that also
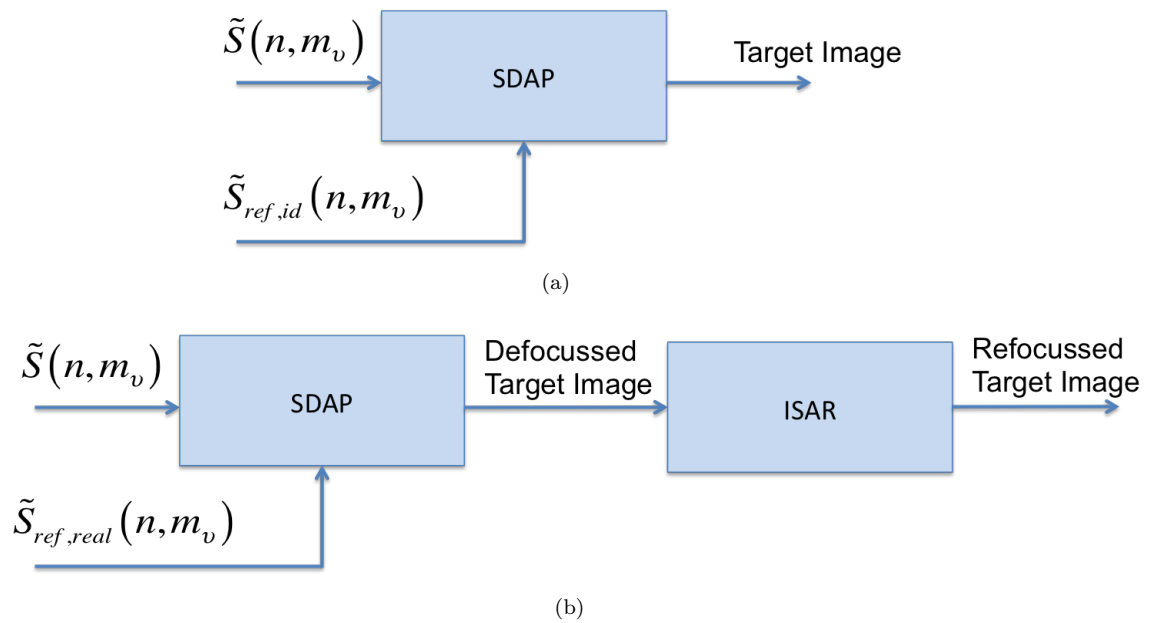
(a)

(b)

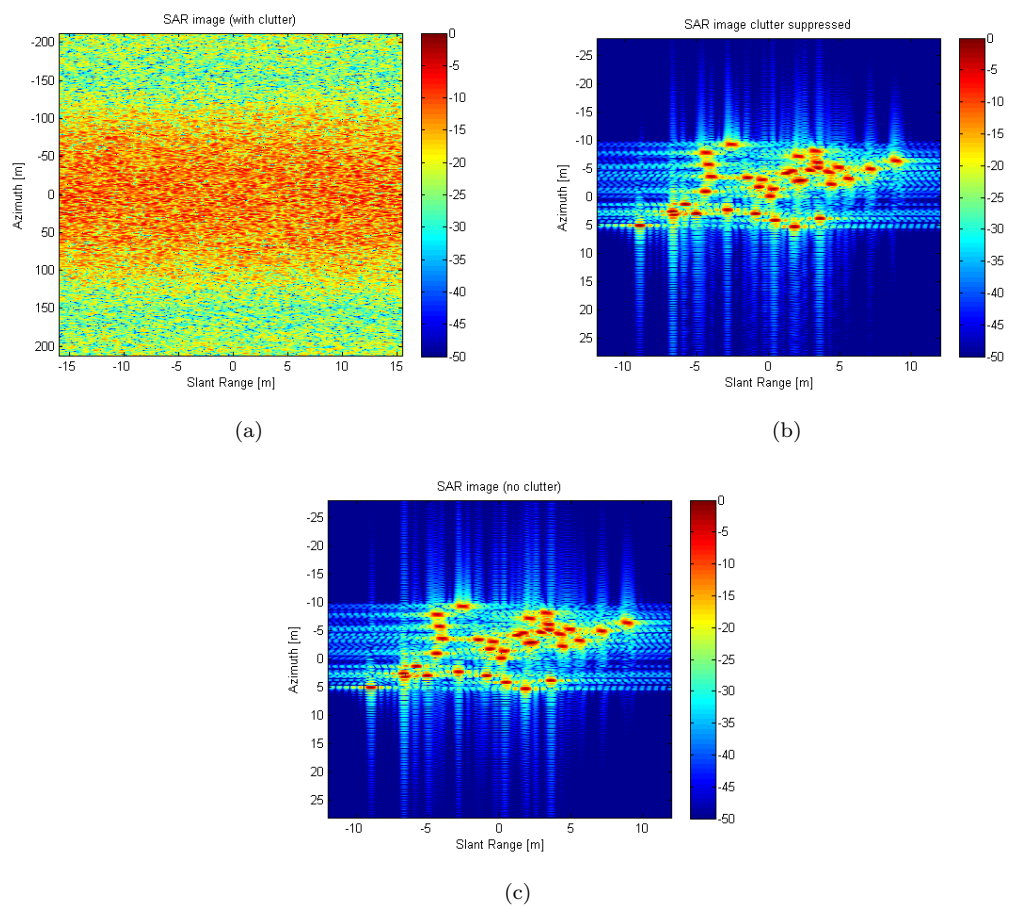FIGURE 6.4: SDAP ideal case (a), realistic case (b)

(a)

(b)

(c)

FIGURE 6.5: SDAP ideal case: image without clutter suppression (a), image with clutter suppression (b), without clutter (c)
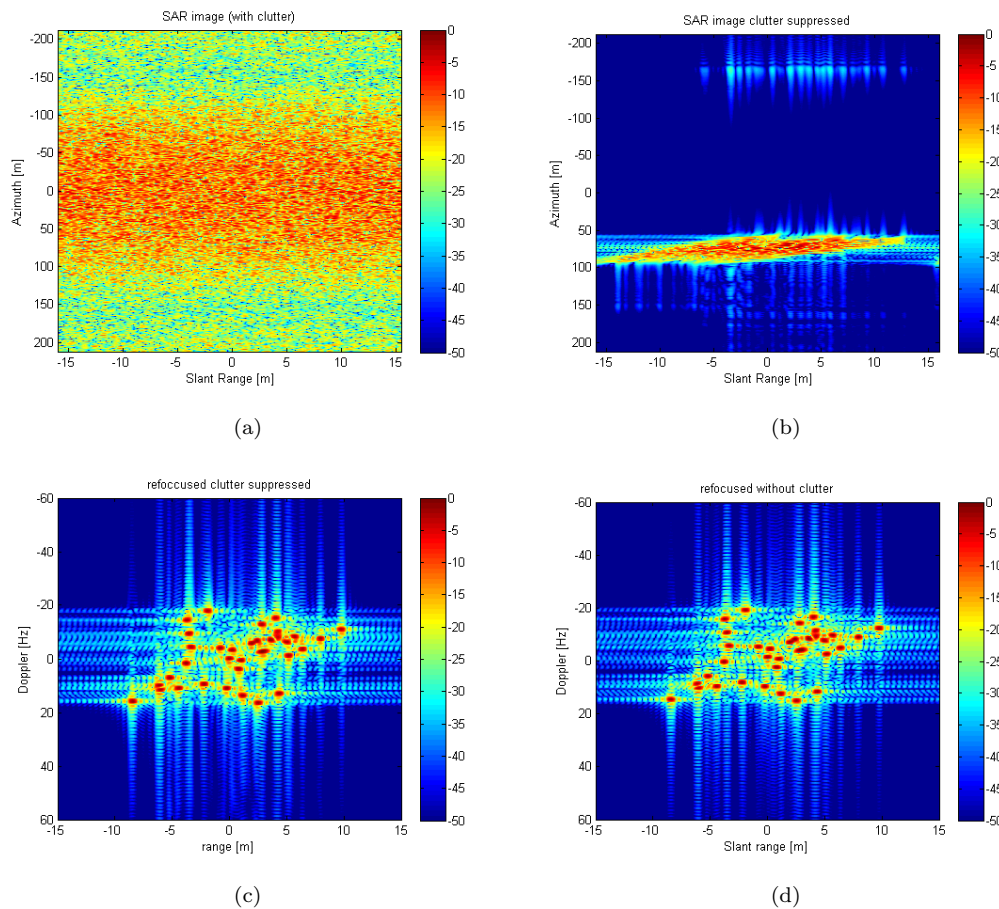
FIGURE 6.6: SDAP real case: image without clutter suppression (a), image with clutter suppression (b), refocused after clutter suppression (c), refocused without clutter (d)

in this case the target is completely masked by the strong clutter. Fig.6.6(b) shows the SAR image after clutter suppression. It can be easily noted that in this case the target is visible but the image is defocused because only the platform motion is considered in the motion compensation. The results after applying the ISAR processing is shown in Fig.6.6(c), in which the improvement in the image focus is very evident also from a visual point of view. A comparison between Fig.6.6(c) and the ISAR image obtained from the clutter free data shown in Fig.6.6(d) shows that he proposed method performs very well also in case of unknown target motion.

6.4.2 Sub-Optimum Approach

In this section the results obtained by means of the sub-optimum processing described in Sect.6.3 are shown.

The sub-optimum processing involves a windowing operation. Results obtained with different values of the window length, L, are in Fig.6.7-6.10. In each case the image before (a) and after the ISAR refocusing process (b) are shown.

As it can be noted, the sub optimum process performs quite well. Notwithstanding, with small values of L some distorion are introduced. This is due to the approximation of the cross-power spectral matrix depicted in Fig.6.3. The loss in the signal to disturbance ratio with respect the optimum case is shown in Fig.6.11. It is worth pointing out that with $L = 10$ samples the loss is roughly $4dB$.
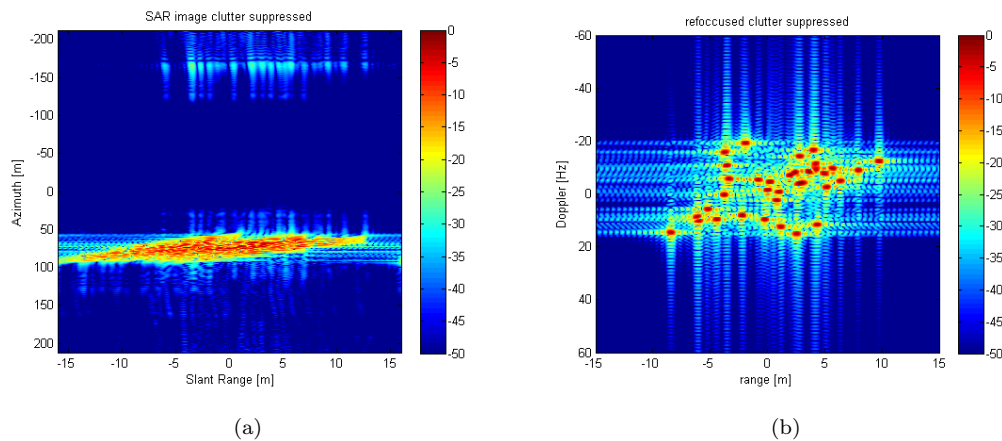

(a)   (b)

FIGURE 6.7: SDAP sub-optimum before L=100 ISAR processing (a), after ISAR processing (b)
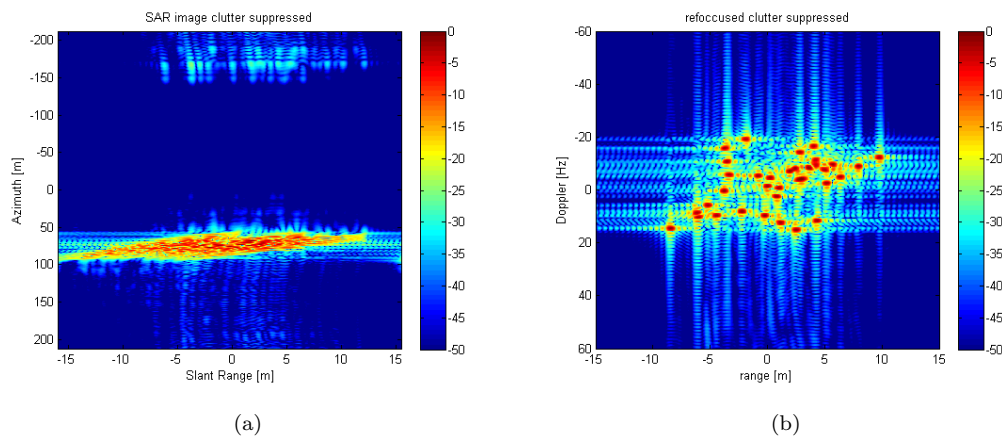

(a)   (b)

FIGURE 6.8: SDAP sub-optimum before L=50 ISAR processing (a), after ISAR processing (b)

All these results have been obtained considering the ideal cross-power spectral matrix, $\mathbf{R}_{Dc}$, (or in the case of sub optimum processing the exact sub-block $\mathbf{R}_{Dc,i}$. No estimation is performed. In the next section results obtained using the estimated $\hat{\mathbf{R}}_{Dc,i}$ via a more realistic training strategy will be shown.
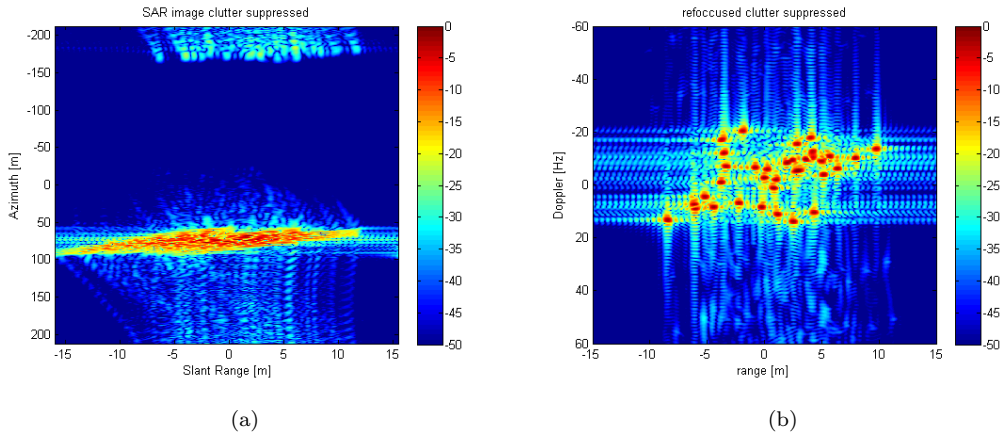
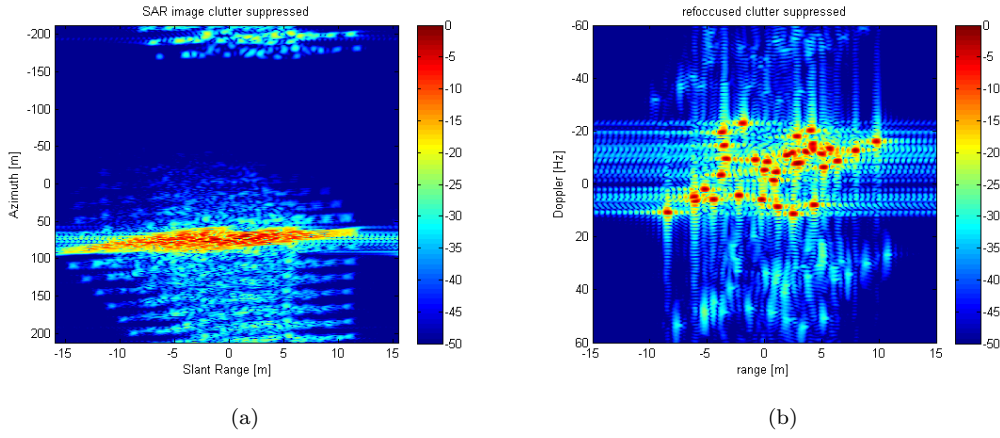FIGURE 6.9: SDAP sub-optimum before L=20 ISAR processing (a), after ISAR processing (b)

FIGURE 6.10: SDAP sub-optimum L=10 before ISAR processing (a), after ISAR processing (b)

6.4.3 Realistic Training

In this section, results considering the cross-power spectral matrix estimation process will be given.

The estimation process is expressed as:

$$\hat{\mathbf{R}}_{Dc} = \frac{1}{N_r} \sum_{n_r=0}^{N_r-1} \tilde{\mathbf{Z}}(n_r)\tilde{\mathbf{Z}}^H(n_r) \in \mathbb{C}^{MP \times MP} \tag{6.30}$$

where the vector $\tilde{\mathbf{Z}}(n_r)$ denotes the target-free data in the nth range cell in the Space-Doppler frequency domain.
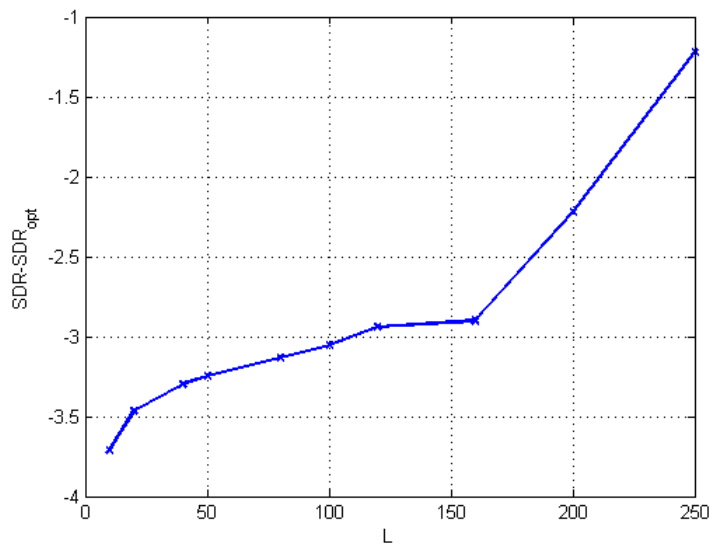
FIGURE 6.11: SDR loss with respect the window length L

In Fig.6.12 the SDR loss with respect to different values of the window length, L, for different number of training range cells, N_r, is shown. As it can be noted, good results are obtained with a number of training range cells lower than the theoretical one, i.e., $N_r = 2LP$. This is due to the fact that the limitation in the training data required is imposed by the number of significant eigenvalues in the cross-power spectral matrix. It is evident that better performances are obtained for larger values of L. However, when the number of available training data, N_r, does not allows for a good estimation of relative blocks of the cross-power spectral matrix, the losses with respect to the optimum case rapidly increases.

6.4.4   Comparison between STAP-ISAR and SDAP-ISAR

In this section,the SDAP ISAR processing presented in this chapter and the STAP ISAR porcessing presented in the previous chapter will be compared.

The most important difference regards the applicability of the two methods. In fact, the STAP processing is based on the matched filter image formation algorithm. This method can be applied also when the straight iso-range approximation does not hold true and the total aspect angle variation is large. Conversely, in order
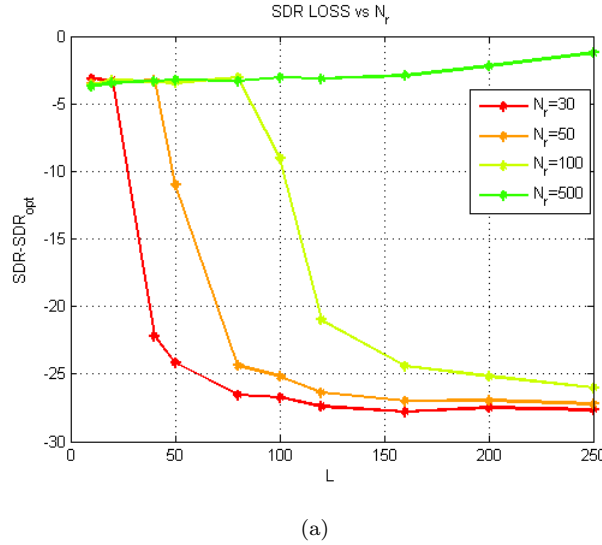
(a)

FIGURE 6.12: SDR loss with respect L for different value of N_r

to apply the SDAP processing, which is based on the range Doppler image formation algorithm, all the requirements of the range Doppler, i.e., straight iso-range approximation and small aspect angle variation, should be met. In particular, in order to obtain well focused images via Range Doppler processing applied to the signal acquired by a multichannel system, it has been demonstrated that the imaging area and the array dimension must meet the requirement expressed in Eq.(2.54), and recalled here for the sake of clarity

$$D_{array} \leq \frac{\lambda R_0}{32 \left(y_1 \cos \alpha - y_3 \sin \alpha \right)} \tag{6.31}$$

Furthermore, the range Doppler processing produces SAR images with poor resolution with respect matched filtering based approaches (see Sect.2.3).

The second difference to analyse is in the image formation processing. It is quite evident by a comparison between the results obtained with the two image formation algorithms that the cross-range (Doppler) axis presents a different scaling. It can be demonstrated that a scaling factor exists between the scaling of the Cross-Range axis of the two presented algorithms. It is worth pointing out that the scaling factor can be derived only when both the imaging algorithms can be applied. This means that the scenario must comply requirements needed for the application of the range Doppler processing It can be noted that these requirements are mandatory also to obtain a closed form for the image PSF obtained via

matched filtering. In fact, as stated before, when the straight iso-range approximation does not hold true the processing described in Sect.5.2 becomes the $\omega - k$ described in Sect.2.3. In this case the PSF is space variant and no closed form can be easily derived.

Consider the SDAP processing. In this case the Doppler spacing $\Delta \nu_{SD}$ and the Doppler non-ambiguous, $D\nu$, region can be expressed as:

$$\Delta \nu_{SD} = \frac{1}{T_{obs}} \tag{6.32}$$

$$D\nu_{SD} = \frac{1}{T_R} \tag{6.33}$$

In the STAP processing the Doppler spacing, $\Delta \nu_{ST}$ and the Doppler non-ambiguous region $D\nu$, can be derived from Eq.(5.14) and is expressed as:

$$\Delta \nu_{ST} = \frac{4T_R \alpha}{\lambda_0} \tag{6.34}$$

$$D\nu_{ST} = \frac{4T_{obs} \alpha}{\lambda_0} \tag{6.35}$$

The scaling factor, χ, between the images obtained via the two methods can be defined as:

$$\chi = \frac{\Delta \nu_{ST}}{\Delta \nu_{SD}} = \frac{D\nu_{ST}}{D\nu_{SD}} \tag{6.36}$$

Considering the parameters used in the simulations, Eq.(6.36) $\chi = 0.47$. This is coherent with the image shown in Sect.5.5 in which a compression factor of about a 2 is evident with the respect the images shown in Sect.6.4.

Another important difference is the fact that the back projection operation from the image domain to the data domain in the SDAP-ISAR, which is mandatory for the application of the ISAR refocusing, is performed without any approximation. In fact, the 2D-IFT represents the exact inversion of the range Doppler image formation technique. As a consequence no distortions are introduced by the image

inversion processing as it is evident by comparing the image obtained in the ideal case Fig.6.5 with respect to the ISAR image obtained in the realistic case Fig.6.6[1]. As stated in the previous chapter, this is not true in case of STAP-ISAR processing because the inversion by means of 2D-IFT is not the exact one and leads to distortion in the final refocussed image.

Moreover, a comparison between the two sub-optimum approaches results shows that the approximation of the cross-power spectral matrix in the SDAP processing produces less distortions in the final image with respect to the approximation of the space-time covariance matrix in the sub-optimum STAP processing. This can be noted by comparing the results shown in Sect.6.4.2 and Sect.5.5.2 and the SDR loss graphs in Fig.6.11 and Fig.5.15.

6.5   Conclusion

In this chapter a Space Doppler Adaptive Processing (SDAP) for clutter suppression and imaging has been presented. This processing has been combined with ISAR technique to obtain high resolution images of non-cooperative moving targets within SAR images.
The presented processing has been derived from the Range Doppler image technique and its effectiveness has been proven on simulated data. It has been proven that under the hypothesis that make this processing applicable hold true it works better than the joint STAP ISAR processing presented in the previous chapter.

---

[1]It is evident also in case of clutter-free data

Chapter 7

Real data analysis

7.1 Introduction

In this chapter the SDAP processing previously described will be tested on real data. The data have been provided by Metasensing[1] and consist of the data acquired by a two channels SAR system. As it will be explained in the following the system set up is not optimal for the application of the algorithms described in the previous chapters, so some preliminary operations are needed to arrange the data in a manner that allows for the proposed processing to be applied.

In Sect.7.3 the multichannel range Doppler processing to obtain the SAR image will be tested and some conclusions will be drawn.

In Sect.7.4 the SDAP-ISAR processing will be applied exploiting the two available channels. In Sect.7.4.3 a method to synthesize three virtual channels will be presented. The SDAP-ISAR processing will be then applied to the three channels data and compared to the results obtained with the two real channels data.

7.2 Dataset description

The available dataset has been provided by Metasensing. A measure campaign has been conducted within the activities of the NATO SET 196. The campaign took place on the 5th June 2013 close to Teuge airport (NL). The platform used is a 208 Grand Caravan from Paracentrum Teuge (PH-SWP). The radar mounted on

---

[1]www.metasensing.com

the platform is a dual channel FMCW SAR system. A summary of the measures campaign conducted by Metasensing can be found in [74], [75] and [76]. Details about the functioning of the FMCW system can be found in [77] while some signal processing aspects are treated in [78] and [79].

The acquisitions have been performed by flying over a highway in proximity of Teuge airport. The highway was perpendicular to the flight trajectory.

The acquisition parameters are summarized in Tab.7.1;

Platform	208 Grand Caravan from Paracentrum Teuge (PH-SWP)
Look angle	55°
Flight Altitude	$1200m$
Velocity	$180km/h$
Mean Range	$2km$
Swath	$1km$

TABLE 7.1: Acquisition Parameters

The radar parameters are listed in Tab.7.2 while the antennas specification are in Tab.7.3

Center Frequency	$9.6GHz$
TX Bandwidth	$120MHz$
PRF	$5kHz$
ADC sampling frequency	25MHz

TABLE 7.2: Radar Parameters

Fig.7.1 shows the transmitter (a) and receiver (b) antennas respectively. The set up of the platform is shown in Fig.7.2 while a picture of the area under test is shown in Fig.7.3.

It is quite obvious that the measure set up described above is not optimal for the testing of the proposed method. The principal shortcomings are

- Small bandwidth ($B = 120MHz$). This involves a slant-range range resolution $\Delta_{y_2} = 1.25m$. This is poor resolution especially when dealing with ground target.

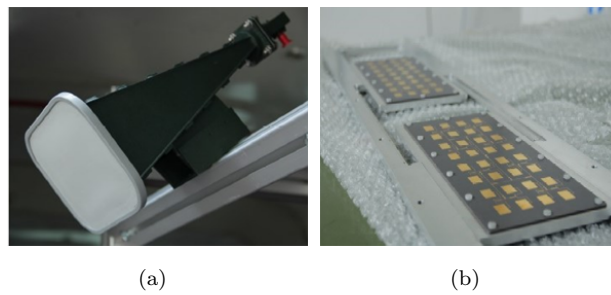| TX: horn	
Gain	$19.6dB$
Antenna Aperture ($3dB$)	elevation $20°$
	azimuth $20°$
RX: microstrip patch	
Gain	$21.4dB$
Antenna Aperture ($3dB$)	elevation $22°$
	azimuth $7.5°$
Baseline	$15cm$

TABLE 7.3: Antennas parameters

(a)   (b)

FIGURE 7.1: TX antenna (a) RX Antennas (b)

FIGURE 7.2: Platform set up

- Baseline $d > \frac{\lambda}{2}$. This is a problem from a beamforming point of view but also for the multichannel Range Doppler image formation process.

- Only two channels resulting in a small number of spatial degrees of freedom.

FIGURE 7.3: Multichannel Range Doppler image results

- Highway parallel to the range dimension. This involves a difficult estimation of the interference space/slow time covariance matrix.

All these issues will be analysed in the following.

7.3 Multichannel Range Doppler image formation

In this section the performance of the multichannel Range Doppler image formation processing will be discussed. In particular the condition on the array size derived in Sect.2.2.3 will be analysed. The condition is here recalled for the sake of clarity

$$D_{array} \leq \frac{\lambda R_0}{32 \left(y_1 \cos \alpha - y_3 \sin \alpha \right)} \tag{7.1}$$

As it has been explained in the Ch.2 this condition involves that the P images obtained by processing the data collected by the P different channels sum coherently so that no distortion are introduced by the multichannel imaging processing.

It is worth pointing out that since in a SAR scenario $\alpha = 0$ (see Fig.2.9), Eq.(7.1) imposes a direct relationship between the image cross-range and the array size. The available data were acquired by a two channels SAR system with baseline $d = 15cm \approx 5\lambda$. It is quite clear that such a distance is quite large and considering the cross-range y_1 imaging area the array size, D_{array} does not meet the condition in Eq.(7.1). In fact, considering the system parameters listed in Tab.7.3, the cross range imaging size can be roughly evaluated considering receiver antenna beamwidth as

$$D_{y_1} \approx R_0 \theta_{az} = 262m \tag{7.2}$$

The results of the imaging processing are shown in Fig.7.4. In Fig.7.4 (a) and (b) the images obtained by applying the range Doppler processing on data acquired by channel 1 and channel 2 respectively are shown. In Fig.7.5 the image obtained by applying multichannel range Doppler is shown. As can be noted the distortions due to the above mentioned effects are evident. The array size is too large and the summation is coherent only in a small cross-range region.

In order to reduce the baseline between the two antennas, the first N_d samples are discarded in the channel 1 data and the last N_d samples are discarded in the channel 2 data (see Fig.7.6). In this way the equivalent baseline, d_{eq} between the two channels becomes
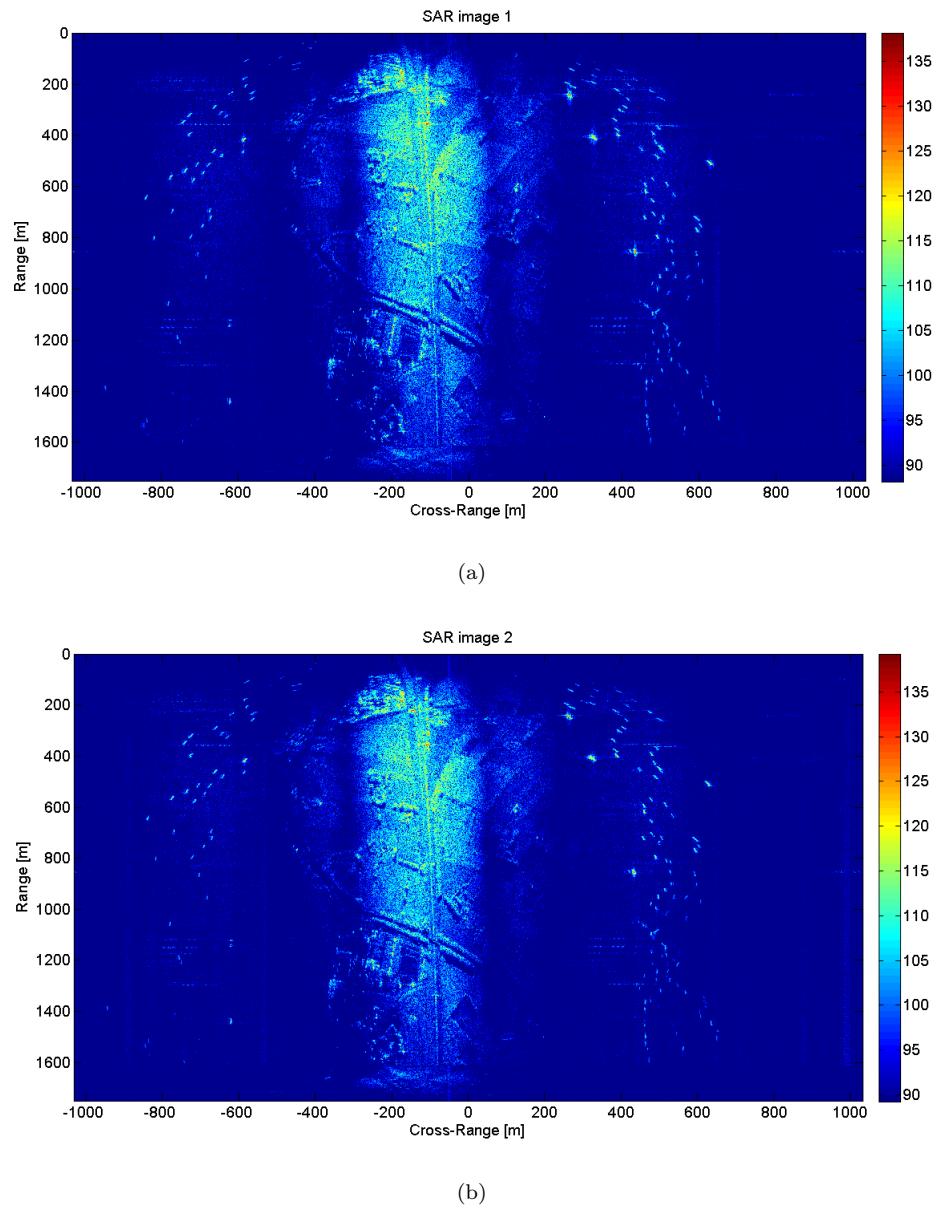
(a)

(b)

FIGURE 7.4: Range Doppler image results (a) channel 1, (b) channel 2

$$d_{eq} = d - N_d v_p T_R \qquad (7.3)$$

The reduction in the inter-element distance is depicted in Fig.7.6.

It is quite obvious that in this case the acquisitions are no longer contemporary. This is not an issue for the image formation processing but it can affect the performances when clutter suppression is performed.
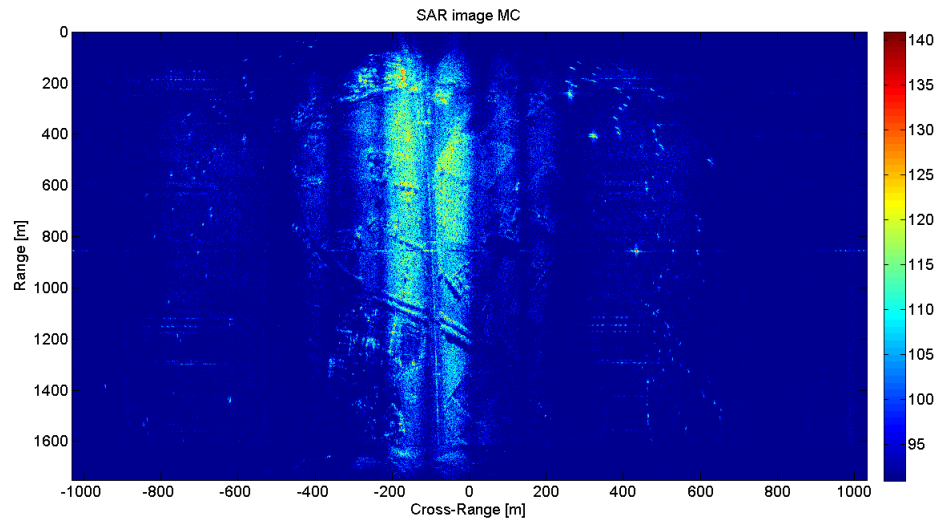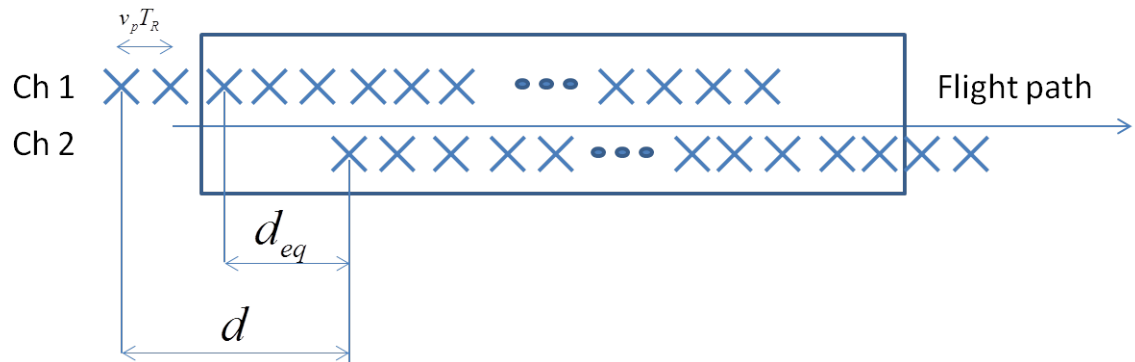
FIGURE 7.5: Multichannel Range Doppler image results

FIGURE 7.6: baseline reduction

Results with different values of discarded data, N_d, are shown in Fig.7.7 - 7.10. Considering the system parameters described in Sect.7.2 ($d = 15cm$, $v_p = 45m/s$) the configuration in which the elements are as close as possible is obtained with $N_d = 17$.

It is evident by observing Fig.7.7 - 7.10 that the closer the antenna elements are the larger the undistorted imaging region is. This is coherent with the relationship evaluated in Sect.2.2.3. The attenuation term is depicted in Fig.7.11 for different values of N_d.
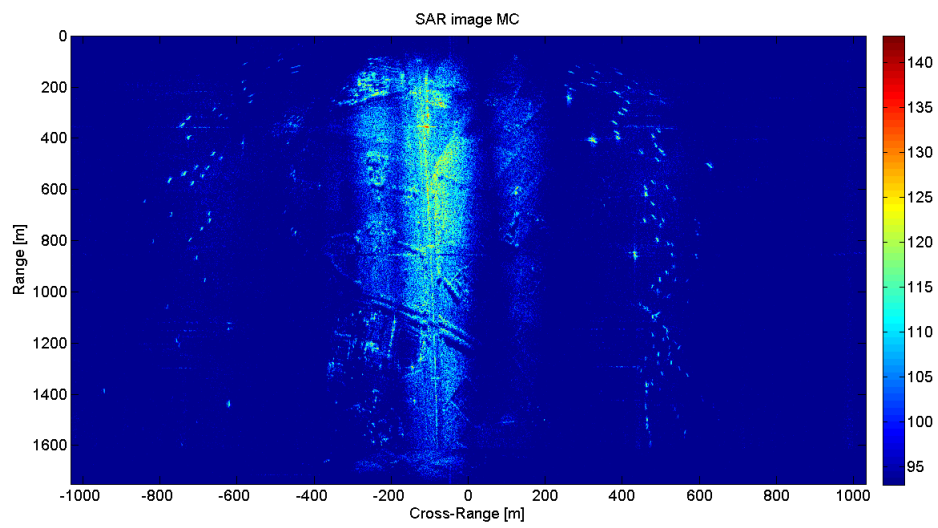
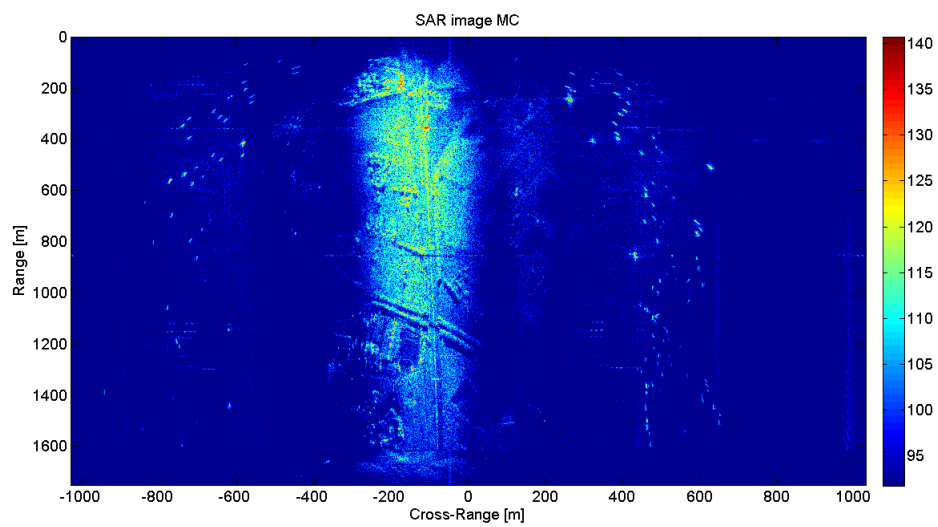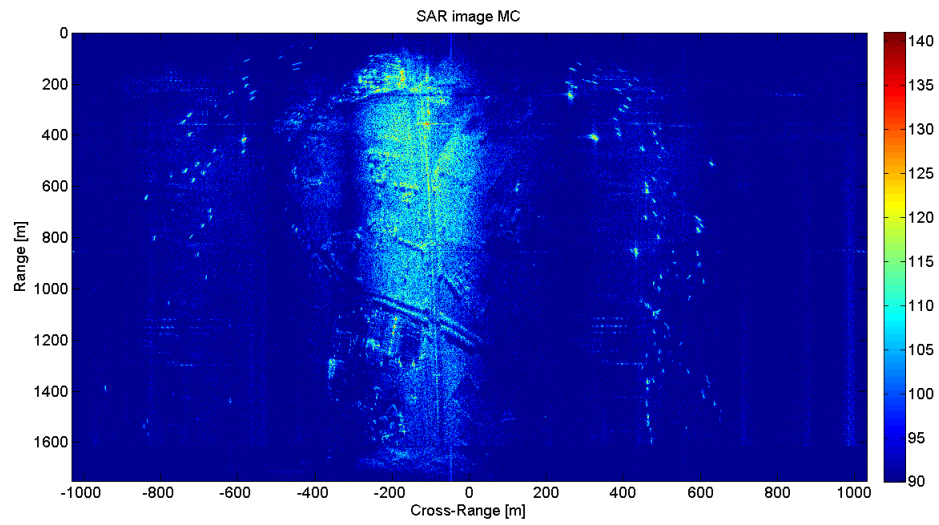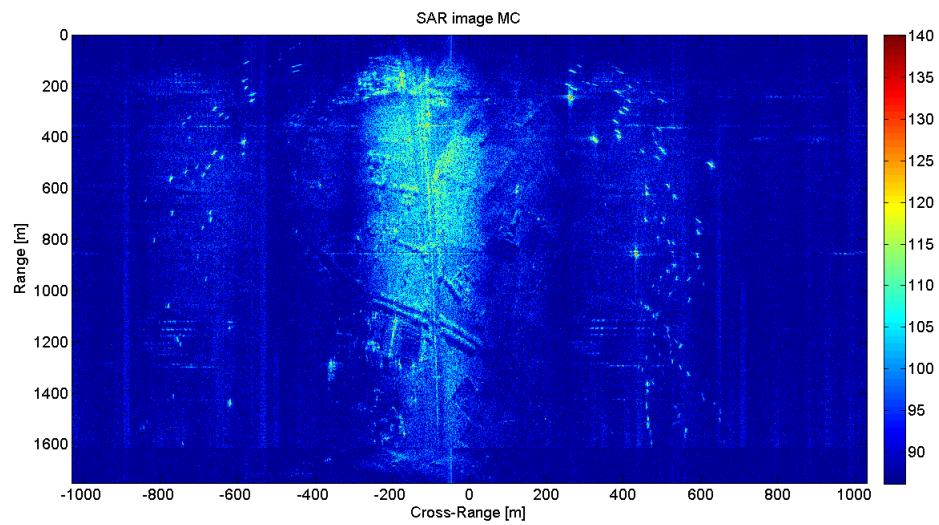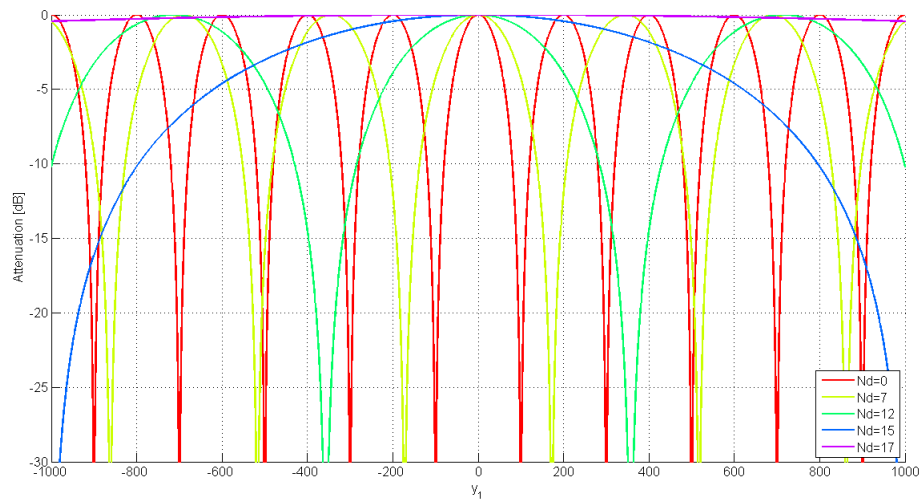FIGURE 7.7: Multichannel Range Doppler image results $N_d = 7$
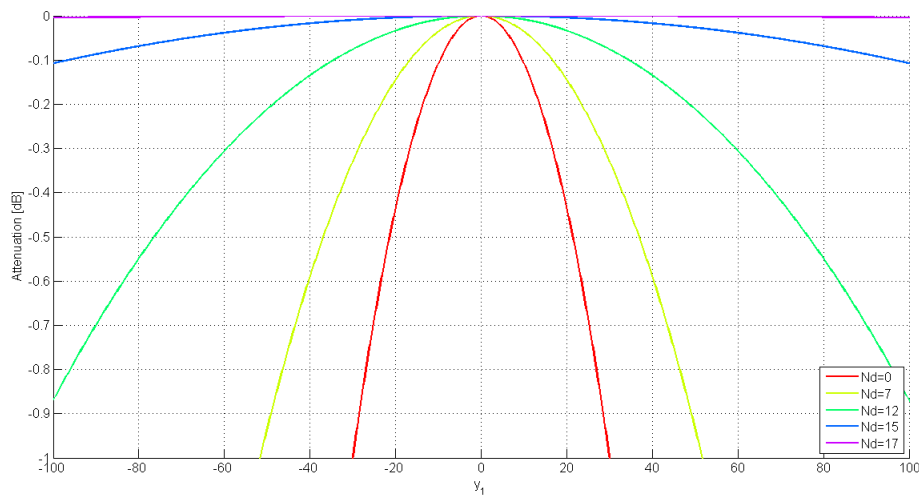

FIGURE 7.8: Multichannel Range Doppler image results $N_d = 12$

FIGURE 7.9: Multichannel Range Doppler image results $N_d = 15$

FIGURE 7.10: Multichannel Range Doppler image results $N_d = 17$

(a)

(b)

FIGURE 7.11: attenuation term with respect N_d

7.4   Clutter suppression and imaging

In this section the results of the application of SDAP ISAR processing described in Ch.6 will be presented.

As stated in the previous section, some preliminary operations on the available data are needed before applying the clutter suppression and the imaging processing. Specifically, the actual baseline, $d = 15cm$, is an issue not only for the multichannel Range Doppler imaging processing, as discussed in the previous section, but also from a spacial filtering point of view. In fact, $d > \frac{\lambda}{2}$ involves a spatial undersampling that affects the performances of the SDAP processing. A solution to this issue has been presented in the previous section, and it consists of discarding of the first N_d samples from the data acquired by the first channel and the last N_d samples acquired by the second channel (see Fig.7.6). However, it is worth pointing out that after this preprocessing the data acquired by the two channels are no longer contemporary. Although this is not an issue in the multichannel Range Doppler processing, a time decorrelation is introduced which can affect the performance of the SDAP processing. Nevertheless, it is worth noting that the system PRF is very high, i.e., $PRF = 5kHz$, and for such an high PRF the scene can be considered static within the N_d pulses.

Another shortcoming is due to the observed scene. As can be noted, an highway is present in the scene and is oriented along the range direction. This involves the presence of a number of moving targets along all the range dimension of the image. It is quite obvious that, in this particular situation, the estimation of the space-slow time covariance matrix of the disturbance becomes a difficult task because of the lack of the availability of target-free range cells. However, the SCR is very low because the clutter region is significantly larger than the targets region, so that the estimation can be reasonably performed.

It is worth pointing out that in order to evaluate the performances of the proposed clutter suppression and imaging process, a ground truth would be necessary. This would allow for a comprehensive performance evaluation. Unfortunately the ground truth is not available.

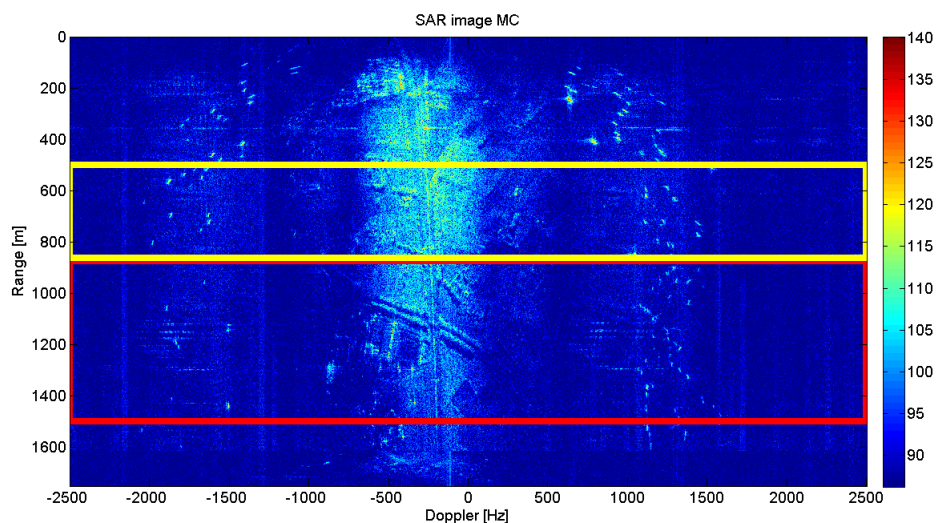In Fig.7.12 the region under test and the training region are highlighted.

FIGURE 7.12: SAR image with region under test (red box) and training range cells (yellow box)

The region under test is within the red box while the training range cells exploited to perform the estimation of the disturbance space-slow time covariance matrix are in the yellow box.

It is evident that moving targets are presents in both the regions as stated before, so that the estimation of the clutter covariance matrix will be affected.

Three cases situation will be analysed.

In the first case the proposed SDAP ISAR processing will be applied on the data collected by the two channels after applying the baseline reduction described above. As it will be evident after the analysis of the results, in this scenario, the clutter suppression seems to work properly. However, since the ground truth is not available it is very difficult to asses the correct functioning of the proposed processing. In fact, all the moving targets appear outside of the clutter Doppler bandwidth. The clutter seems to be properly cancelled, but it is very hard to state if some of the moving targets within the clutter bandwidth are cancelled as well. Moreover, since it is reasonable to assume that the targets in the scene are cars moving along the highway, it is reasonable to state that they are moving with more or less the same velocity in the two direction. This involves that the resulting SAR image presents moving targets with Doppler frequency with absolute values close to each other and sign depending on their heading.

In order to better evaluate the functioning of the proposed processing a case in which the presence of some targets in the clutter Doppler bandwidth must be simulated. This is easily obtained performing a sub-sampling in the slow time dimension (in addition to the baseline reduction) as shown in Fig.7.13.
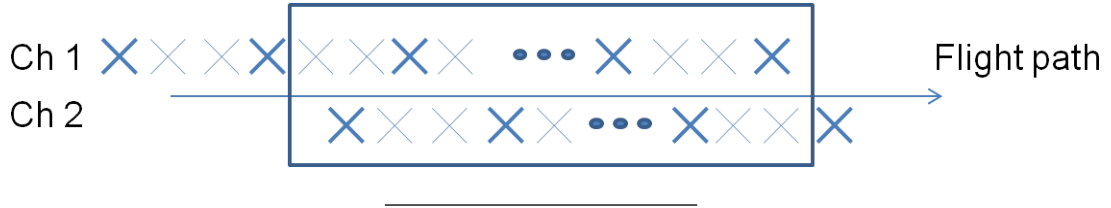

FIGURE 7.13: baseline reduction and subsampling

A subsampling factor value of 3, $sf = 3$, has been chosen. In this way the equivalent PRF is obtained as

$$PRF_{eq} = \frac{PRF}{3} = 1.67 kHz \tag{7.4}$$

A fixed relationship between the Doppler frequency of a target in the image obtained considering the data without subsampling and the Doppler frequency of the same target in the image obtained by processing the data with PRF_{eq} exists and can be exploited to verify if some moving targets are cancelled by the clutter suppression process. The relationship between the target Doppler frequency before and after the subsampling can be derived by considering Fig.7.14.

Specifically, a target with Doppler frequency $|f_D| < \frac{PRF_{eq}}{2}$ will appear in the same Doppler position within the images obtained by processing the data with the two PRF values. On the other hand, a target with Doppler frequency $\frac{PRF_{eq}}{2} < |f_D| < \frac{PRF}{2}$ will be wrapped in the image obtained by processing the data with PRF_{eq}. In this case the target will appear in a Doppler position that can be expressed as

$$f_{D_{eq}} = -sgn\left(f_D\right) PRF_{eq} + f_D \tag{7.5}$$

It is worth point out that the case in which $|f_{D_{eq}}| > \frac{PRF_{eq}}{2}$ can occur. In this case a second wrap occurs and Eq.7.5 can be used iteratively until the condition $|f_{D_{eq}}| < \frac{PRF_{eq}}{2}$ is verified.

In this way, a pseudo ground truth is created and used to verify the effectiveness of the proposed algorithm. Moreover, the subsampling operation involves a reduction

of the data to be processed allowing for the processing of larger windows of data without increasing the computation time. It is quite obvious that the larger the window of data processed is the finer the image resolution in the Cross-Range (Doppler) dimension is.
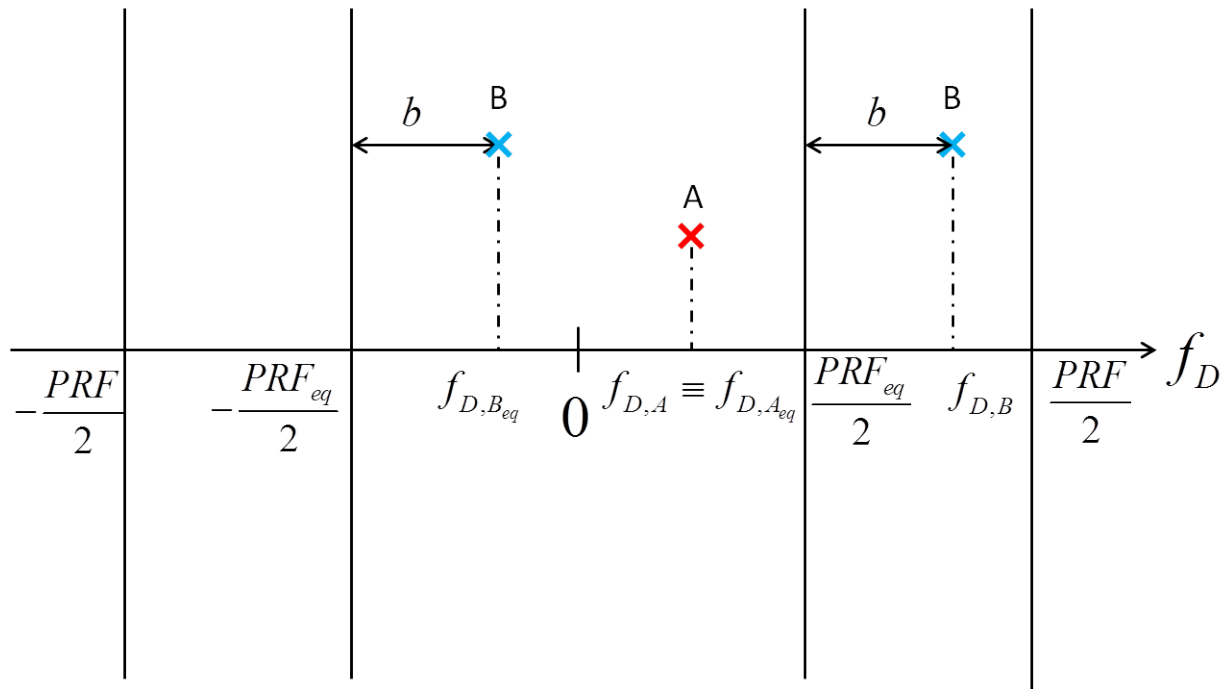

FIGURE 7.14: Doppler mapping

In the third scenario, a 3 channels system will be synthesized by exploiting the high PRF of the system. The data acquired by the first channel will be exploited and three adjacent samples will be treated as acquired by an equivalent three channels system with baseline $d_{virt} = v_p T_R$, as shown in Fig.7.15.
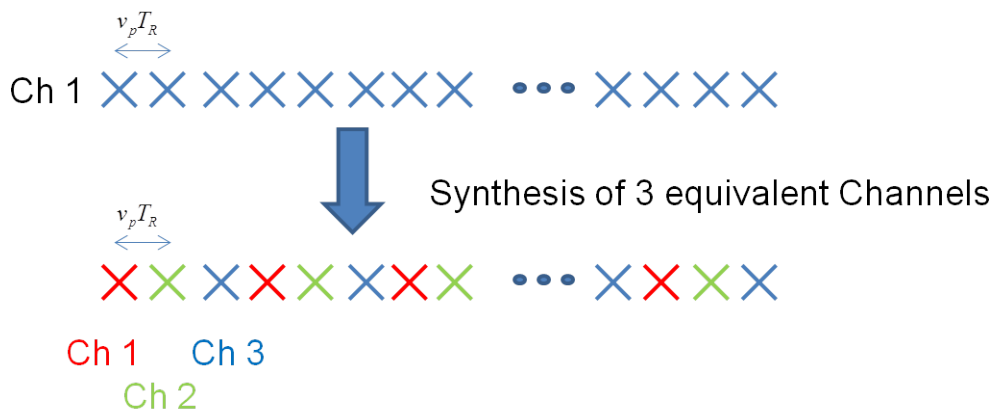

FIGURE 7.15: Virtual Channels

v_p	Platform Velocity	$45m/s$
f_0	Carrier Frequency	$9.6GHz$
B	TX bandwidth	$120MHz$
T_{obs}	Observation Time	$0.2s$
PRF	Pulse Repetition Frequency	$5kHz$
N_d	Discarded Pulses	17
L	Windows Length	32

TABLE 7.4: Case 1 - Parameters

7.4.1 Case study 1

As stated before, in the first case study the SDAP processing is applied to the data acquired by the two real channels. The baseline reduction is performed in order to obtain an undistorted SAR image by exploiting the proposed multichannel Range Doppler image formation processing. An amount of data corresponding to an observation time $T_{obs} = 0.2s$ is used. This small value of observation time allows for the processing of an amount of data that can be easily processed with a general purpose PC. In Fact, with $PRF = 5kHz$ larger T_{obs} correspond to large amounts of data that cannot be treated.

The sub-optimum SDAP processing described in Sect.6.3 is applied with window length $L = 32$ samples.

The system parameters are summarized in Tab.7.4.

In Fig.7.16 the images of the region under test without clutter suppression (a) and with clutter suppression (b) are shown.

As can be noted after a visual inspection the proposed SDAP processing performs the clutter cancellation very well. However, as stated before, it is not possible to asses the correct functioning of the method because of the lack of the ground truth. In fact, by observing Fig.7.16, it seems that there are no slow moving targets that fall within the clutter Doppler bandwidth. In this case, a simple Doppler low pass filter would be enough to cancel the clutter return from the image.

Two crops cut from the images shown in Fig.7.16 are shown in Fig.7.17 and 7.18. In Fig.7.17 (a) and 7.18 (a) the image without clutter suppression is shown while in
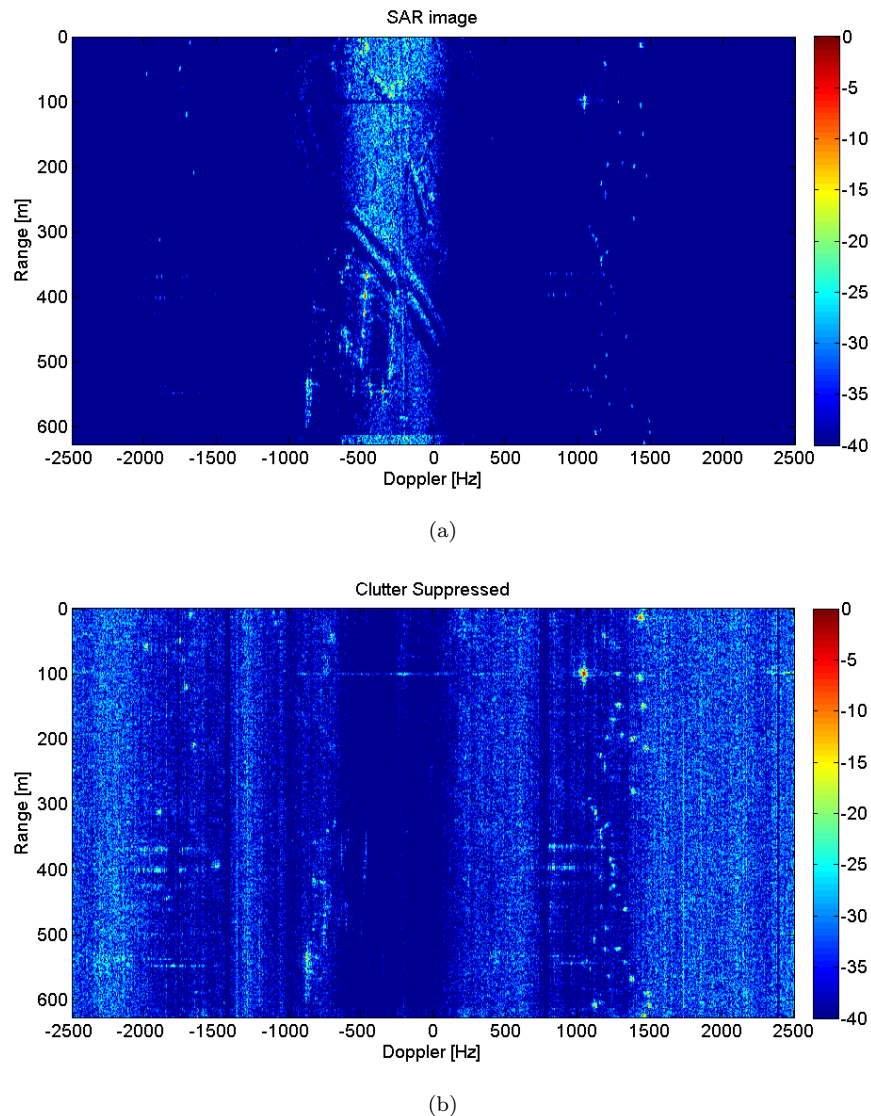
FIGURE 7.16: SAR image (a) and clutter suppressed SAR image (b)

Fig.7.17 (b) and 7.18 (b) the output of the clutter suppression processing is shown. As can be noted, the moving targets are present after the clutter suppression.

Moreover, the image after clutter suppression seems to be more noisy but this is only a visualization issue. In fact, both the images are normalized with respect their maximum value and a dynamic of $40dB$ is represented. Since the image after clutter mitigation presents a lower peak value than the SAR image (because of the cancellation of the static scene) more noise is visible within the $40dB$ dynamic in Fig.7.16 and 7.17 (b) with respect Fig.7.16 and 7.16 (a).

As stated before no conclusions can be drawn by observing these results because all the moving targets seem to be outside of the clutter Doppler bandwidth.
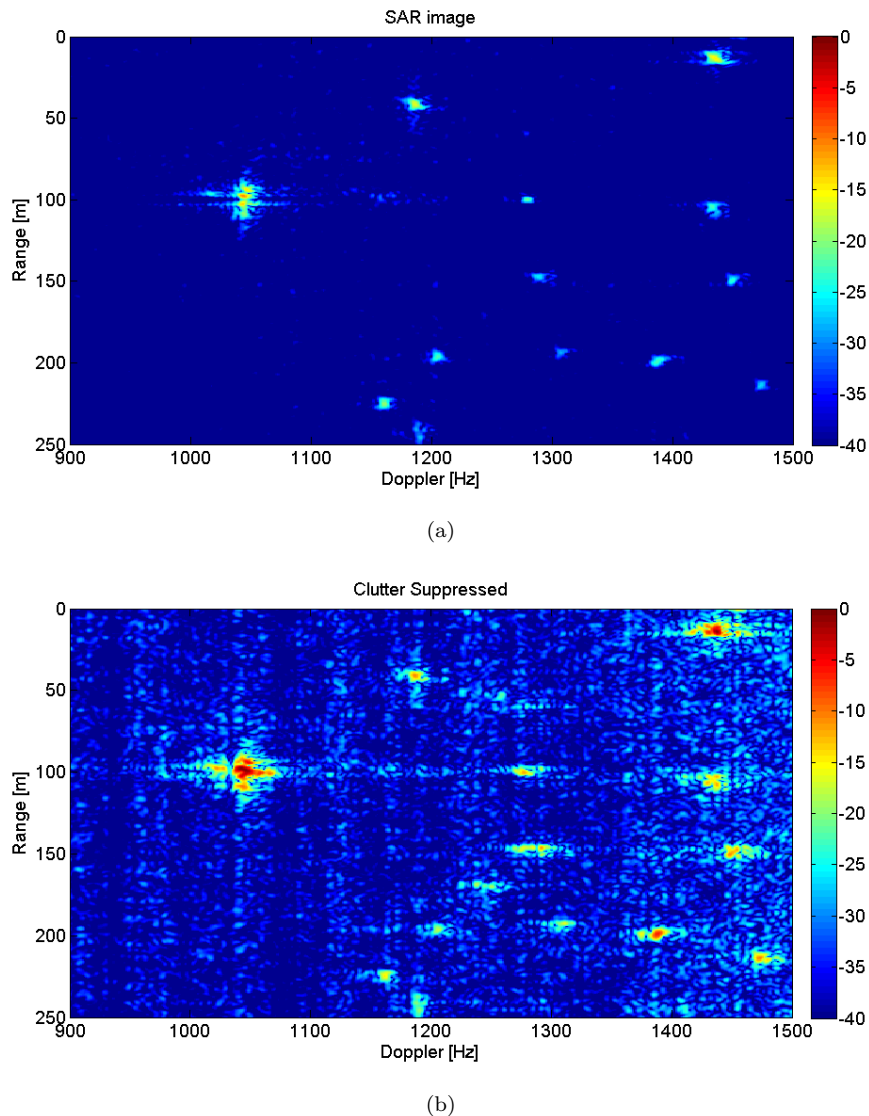
(a)

(b)

FIGURE 7.17: Detail 2: SAR image (a) and Clutter suppressed SAR image (b)

An other issue regards the application of the ISAR refocussing processing. In Fig.7.19 and Fig.7.20 two target crops are shown before (a) and after the ISAR processing (b). As can be noted, the improvement in the image focus is almost irrelevant. This is due to the fact that with the considered CPI the defocussing effect introduced by the uncompensated target own motion is negligible and the ISAR processing does not lead to any significant improvement. However, a little improvement in the image focus is present and can be measured by exploiting the IC values before and after the application of the ISAR processing that are summarized in Tab.7.5.
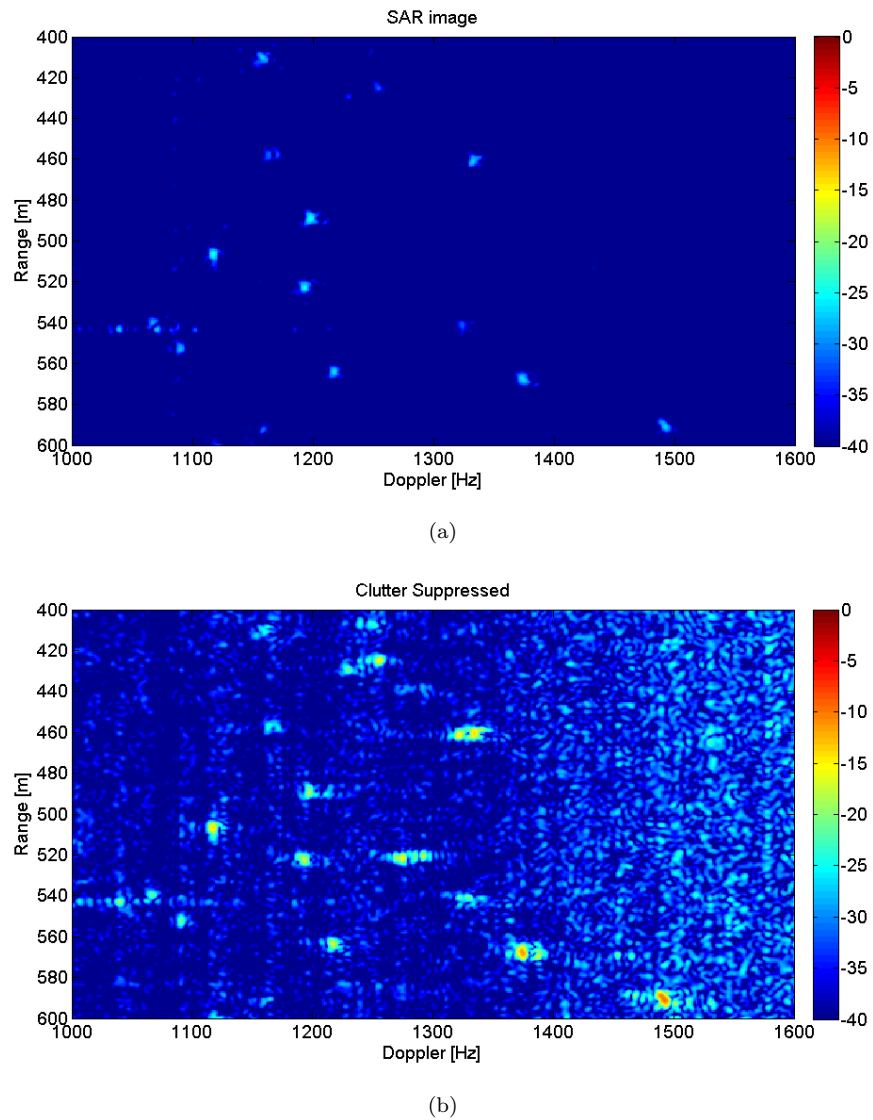
(a)

(b)

FIGURE 7.18: Detail 2: SAR image (a) and Clutter suppressed SAR image (b)

	IC SAR	IC ISAR
Crop 1	9.943	11.819
Crop 2	5.945	7.995

TABLE 7.5: Case study 1: IC values
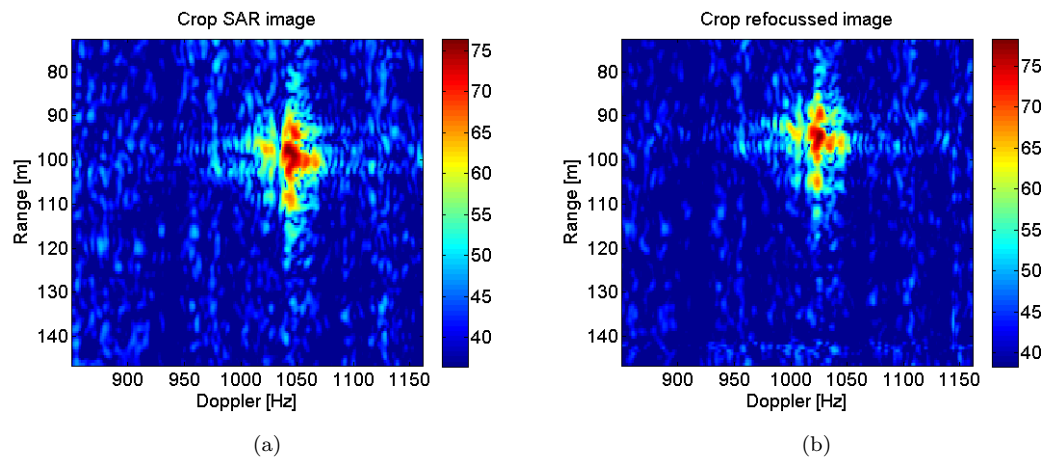
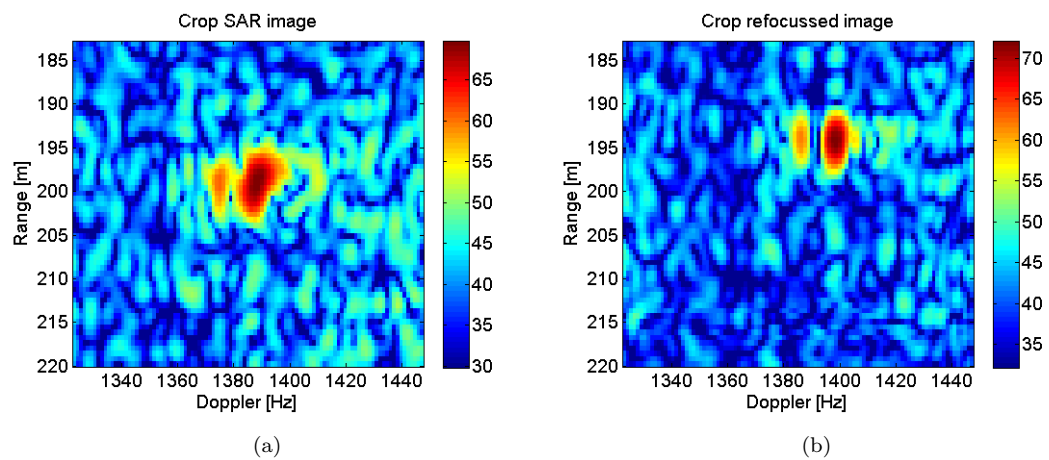FIGURE 7.19: Crop 1: original SAR image (a) refocussed image (b)

FIGURE 7.20: Crop 2: original SAR image (a) refocussed image (b)

v_p	Platform Velocity	$45m/s$
f_0	Carrier Frequency	$9.6GHz$
B	TX bandwidth	$120MHz$
T_{obs}	Observation Time	$0.6s$
PRF	Pulse Repetition Frequency	$1.67kHz$
N_d	Discarded Pulses	5
L	Windows Length	16

TABLE 7.6: Case 2 - Parameters

7.4.2 Case study 2

In this section the second case study is analysed. As stated before, the second case study is obtained applying a subsampling operation to the acquired data along the slow time dimension. In this way a data reduction is obtained allowing for the processing of a larger CPI and, more important, the presence of moving targets within the clutter Doppler bandwidth is imposed. A subsampling factor $sf = 3$ has been chosen. The system parameters of the case study 2 are summarized in Tab.7.6.

The SAR image obtained by processing the subsampled data is shown in Fig.7.21. The region under test and the training range cells are in the red and the yellow box respectively. By comparing Fig.7.21 and Fig.7.12 it is evident that the moving targets that appear clearly visible in the image with full PRF are wrapped within the clutter Doppler bandwidth in the image with the reduced PRF.

The SAR images of the region under test without clutter suppression and with clutter suppression are shown in Fig.7.22 (a) and (b) respectively. It is quite evident that in this case some of the targets fall in the clutter Doppler bandwidth. This is due to the subsampling process as explained before. Moreover, as can be noted after a visual inspection, clutter suppression seems to work properly and a lot of targets that are masked under the static scene in Fig.7.22 become clearly visible in Fig.7.22 (b). In order to better appreciate the moving target detection improvement, three sub-regions are represented in Fig.7.23, Fig.7.28 and Fig.7.32.

In Fig.7.23 the SAR image of the sub-region 1 without application of the clutter mitigation processing (a) and with the application of the clutter mitigation
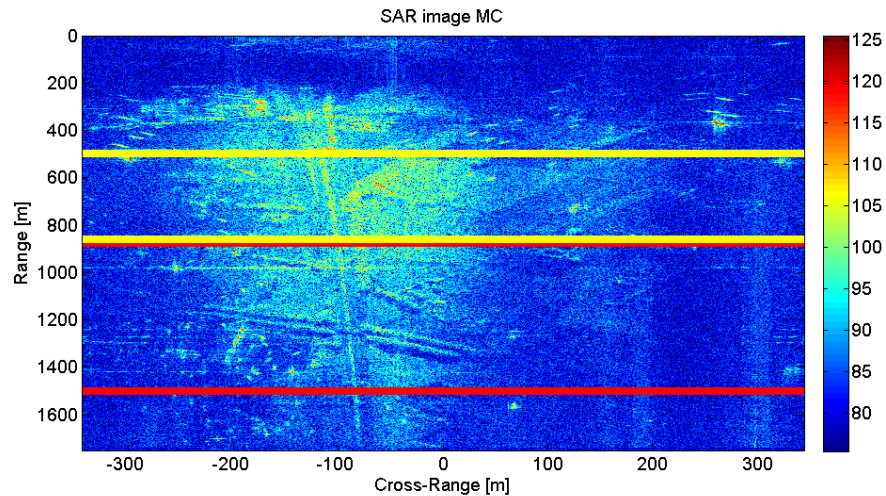
FIGURE 7.21: SAR image obtained processing subsampled data

processing (b) are shown. Moreover, the portion of the image obtained by processing the data without subsampling, $PRF = 5kHz$, in which the same targets are present is shown in Fig.7.23 (c). This last image represents the Doppler region that in the image obtained by processing the subsampled data is folded within the clutter Doppler bandwidth. As a consequence, it provides a pseudo ground truth that can be exploited to verify the effectiveness of the proposed method.

The Doppler frequencies of every visible target in the pseudo ground truth image (Fig.7.23 (c)) are listed in Tab.7.7 with the relative Doppler frequency evaluated considering the sub-sampling operation. The range coordinates are listed as well in order to locate the target within Fig.7.23 (b) and (c).

As can be noted six target out of fourteen are cancelled.

It is worth pointing out that the target that can be clearly seen in Fig.7.23 (b) with coordinates range and Doppler coordinates, $Range = 55m$ and $f_D = -310Hz$ respectively, does not appear in Fig.7.23 (c). This is not an artefact introduced by the processing but a target that in the pseudo ground truth image has coordinates equal to $Range = 55m$ and $f_D = -1976Hz$ and results folded in the right position.

In Fig.7.24-7.27 the results of the application of the ISAR processing are shown. Specifically, four targets are selected (Target n. 1,2,5,6) and for each of them the SAR image (a) and the refocussed ISAR image (b) are shown. The defocussing effect due to the uncompensated target own motion is evident by observing the target SAR images while the improvement in the image focus obtained by applying
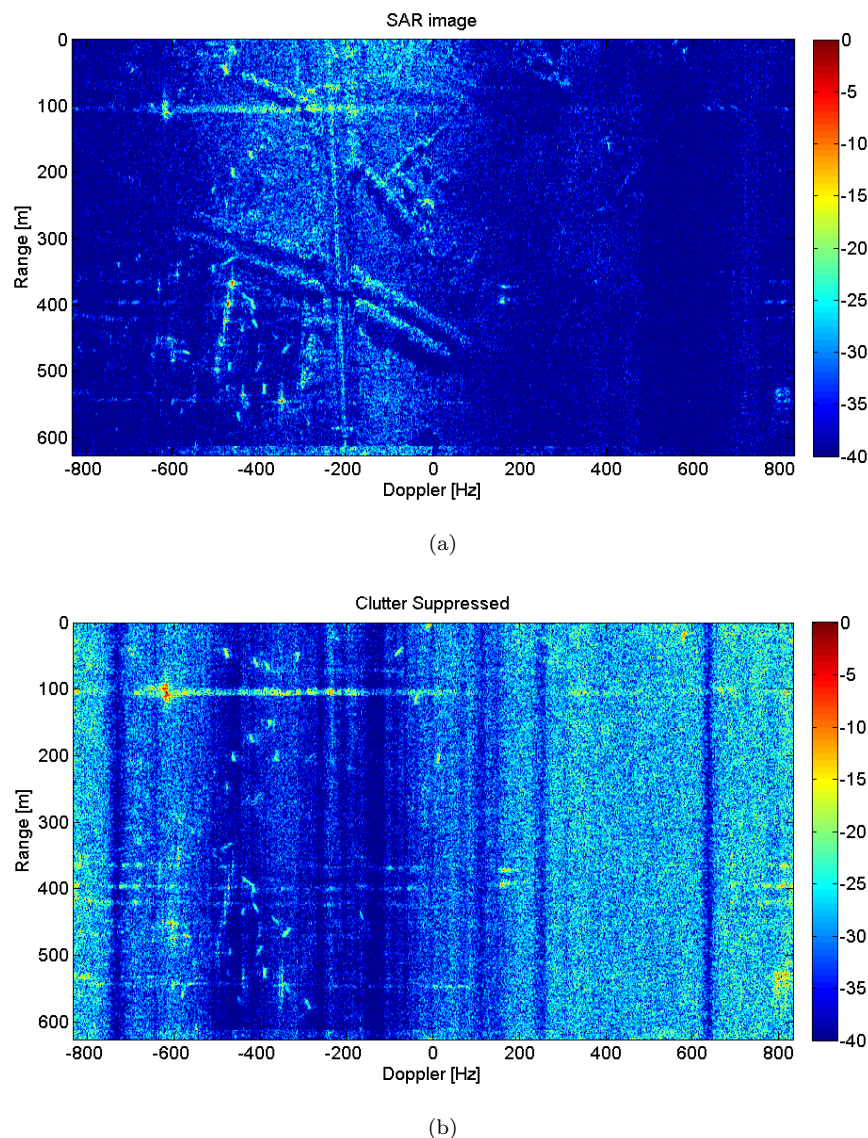
(a)

(b)

FIGURE 7.22: SAR image (a) and Clutter suppressed SAR image (b)

the ISAR autofocusing process can be clearly noticed by visual inspection of the results shown.

In order to better evaluate the performance of the refocussing process the IC values before and after the autofocusing are listed in Tab.7.8 for all the targets detected in Fig.7.23 (b). The improvement in the image quality is evident.

The same analysis is performed in two other sub-regions of the scene under test. In Fig.7.28 sub-region two is shown. The SAR images without clutter suppression and with clutter suppression are shown in Fig.7.28 (a) and (b) respectively. The pseudo ground truth obtained by forming the SAR image from the data without sub-sampling is shown in Fig.7.28 (c).

Target N.	f_D [Hz] $(PRF = 5kHz)$	f_D [Hz] $(PRF = 1.67kHz)$	Range [m]	Missing targets
1	1187	-479	40	
2	1257	-409	58	
3	1284	-382	65	
4	1047	-619	103	
5	1288	-378	147	
6	1250	-416	172	
7	1203	-463	197	
8	1305	-361	199	
9	1383	-283	204	X
10	1158	-504	227	X
11	1440	-227	24	X
12	1437	-230	110	X
13	1474	-193	220	X
14	1384	-283	282	X

TABLE 7.7: Sub-region 1: Pseudo ground truth comparison

Target N.	IC SAR	IC ISAR
1	2.673	10.174
2	1.472	4.84
3	0.83	3.344
4	2.80	5.326
5	1.345	3.698
6	1.161	4.165
7	1.879	6.502
8	1.072	4.92

TABLE 7.8: Sub-region 1: IC values before and after ISAR processing

Also in this case the improvement in the detection capability results evident from the visual inspection. The results of the comparison between the pseudo ground truth and the clutter suppressed image are listed in Tab.7.9. Also in this case a couple of targets out of thirteen are cancelled. It is worth pointing out that this second sub-region is farther from the training range cells than the sub-region 1 so the estimation of the space-slow time covariance matrix could be less accurate for

this region with respect sub-region 1.

Target N.	f_D [Hz] $(PRF = 5kHz)$	f_D [Hz] $(PRF = 1.67Kz)$	Range [m]	Missing targets
1	1255	-412	395	
2	1165	-502	419	X
3	1257	-410	427	
4	1301	-366	445	
5	1332	-355	465	
6	1268	-399	489	
7	1198	-469	498	
8	1117	-550	510	
9	1281	-386	524	
10	1667	-600	543	X
11	1329	-338	546	
12	1090	-577	558	
13	1379	-288	573	

TABLE 7.9: Sub-region 2: Pseudo ground truth comparison

The IC values for each target before and after the application of ISAR processing are listed in Tab.7.10. The improvement in the image focus is evident for all the considered targets. Three of them (specifically target number 1,4, and 6) are shown in Fig.7.45 - 7.47.

Similarly for the sub-region three in Fig.7.32 the SAR image without clutter suppression (a), the SAR image with clutter mitigation (b) and the pseudo ground truth (c) are shown. Also in this case targets that are completely masked under the static clutter in Fig.7.32 (a) become clearly visible in Fig.7.32 (b).

The results of the comparison between the pseudo ground truth and the clutter suppressed image are listed in Tab.7.11. In this case no targets are missing.

The results of the ISAR refocusing process applied to target number 2 and 4 are shown in Fig.7.33 and Fig.7.34 while the image contrast values for all the detected target in this sub-region are listed in Tab.7.12. Also in this last case the focus improvement is evident. For target number 3 the ISAR processing fails because this target results distorted by a strong interference as it is evident from Fig.7.32 (b)

Target N.	IC SAR	IC ISAR
1	1.475	4.935
3	1.812	5.560
4		
5	1.856	7.673
6	1.455	4.694
7	1.028	3.703
9	1.615	6.327
10		
11		
12	0.882	2.755
13	1.426	5.774

TABLE 7.10: Sub-region 2: IC values before and after ISAR processing

Target N.	f_D [Hz] $(PRF = 5kHz)$	f_D [Hz] $(PRF = 5Kz)$	Range [m]	Missing targets
1	-1674	-7	3	
2	-1750	-85	43	
3	-1708	-43	122	
4	-1655	-12	205	

TABLE 7.11: Sub-region 3: Pseudo ground truth comparison

Target N.	IC SAR	IC ISAR
1	2.105	5.805
2	2.343	6.728
3	Fail	
4	1.915	5.087

TABLE 7.12: Sub-region 3: IC values before and after ISAR processing

A final test has been conducted applying a CFAR detector (available in the lab and not implemented by the author) to the data before and after the clutter suppression. Details can be found in [80], [81] and [82].

The detection results are shown in Fig.7.35.

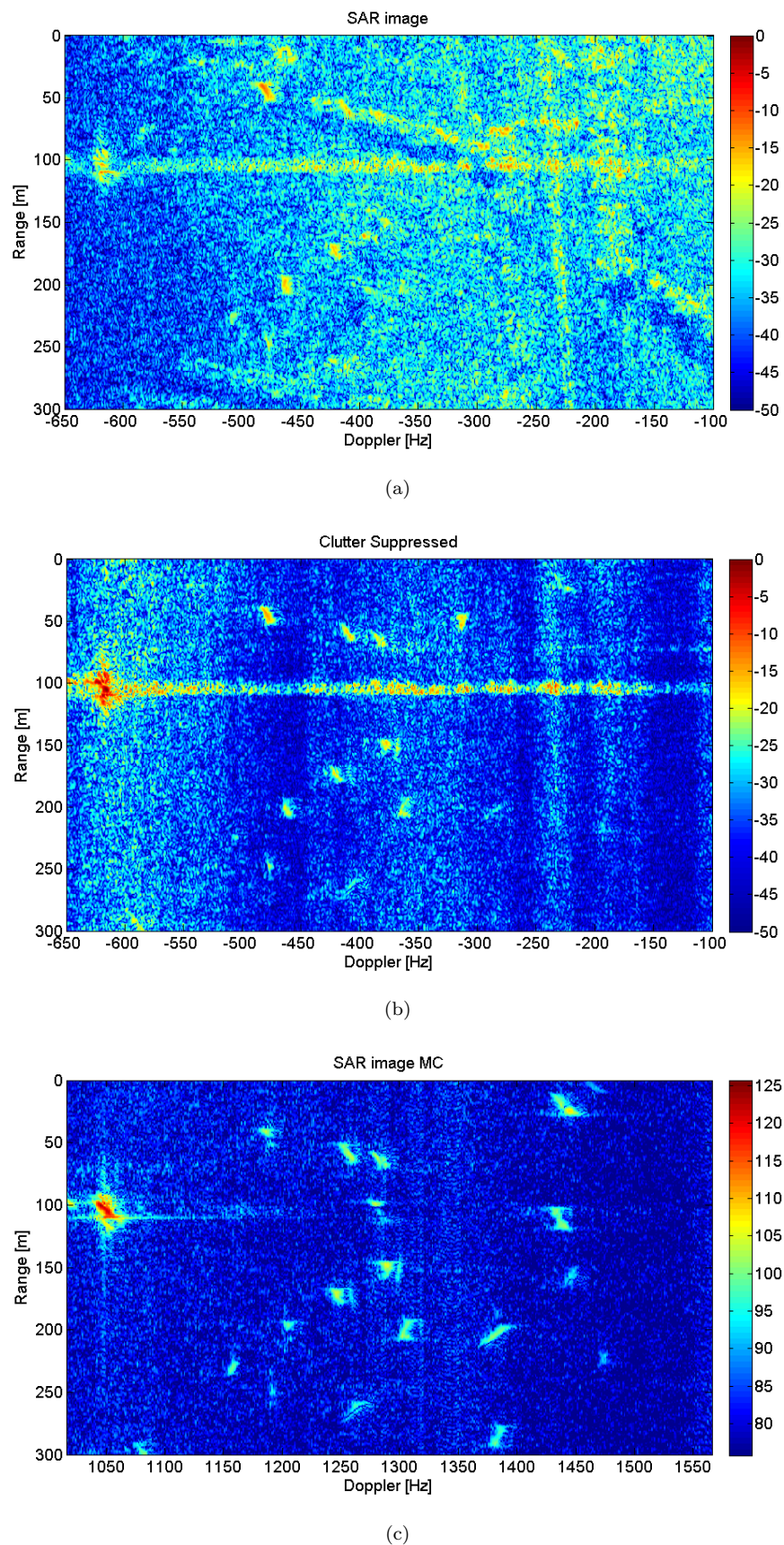The improvement in the target detection performances is very evident.

(a)

(b)

(c)

FIGURE 7.23: Sub-image 1: SAR image (a) Clutter suppressed SAR image (b) Pseudo ground truth (c)
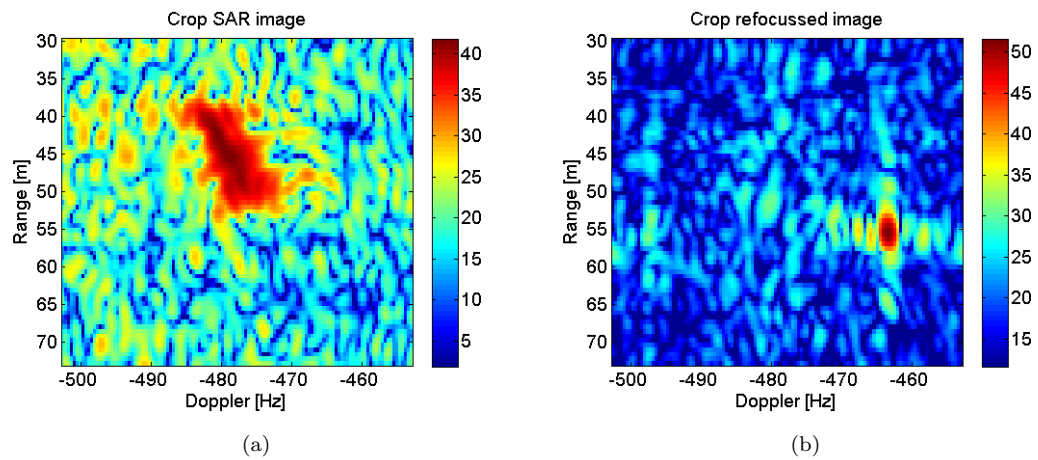
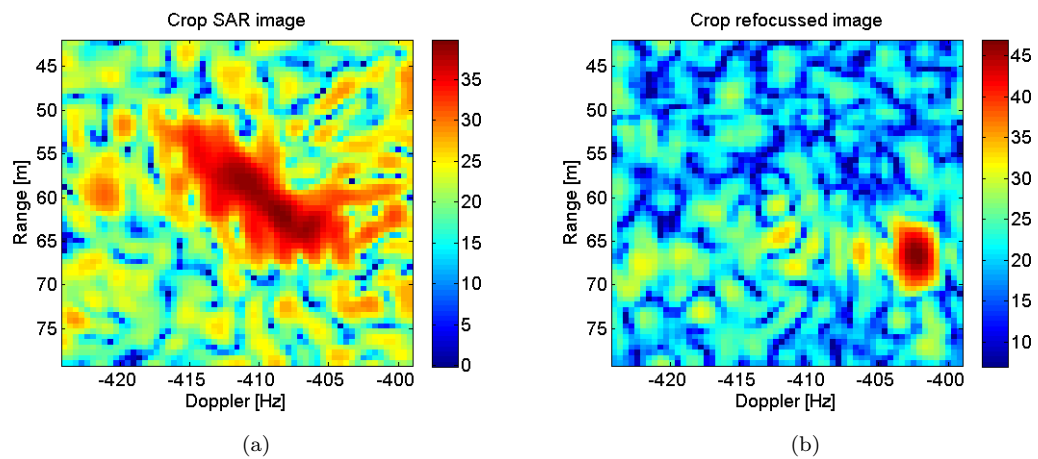FIGURE 7.24: Sub-region 1 - Crop 1: original SAR image (a) refocussed image (b)

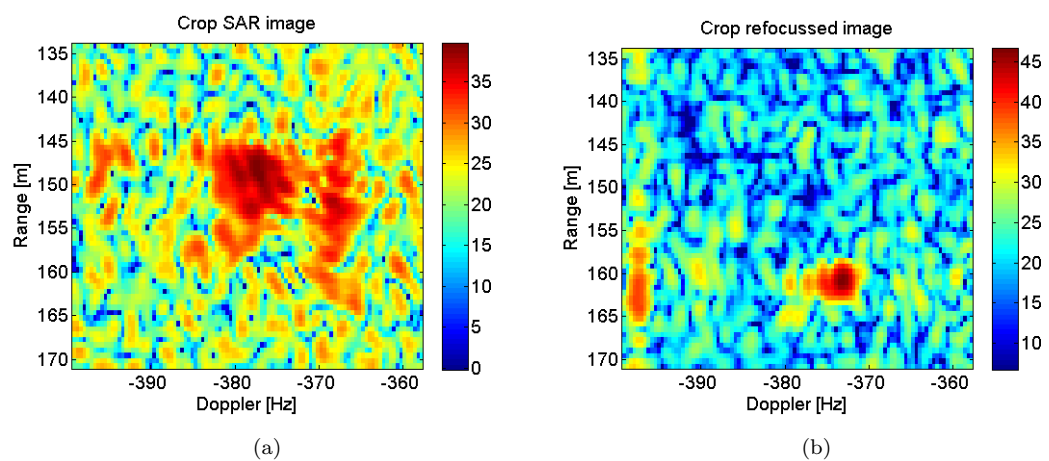FIGURE 7.25: Sub-region 1 - Crop 2: original SAR image (a) refocussed image (b)

FIGURE 7.26: Sub-region 1 - Crop 5: original SAR image (a) refocussed image (b)
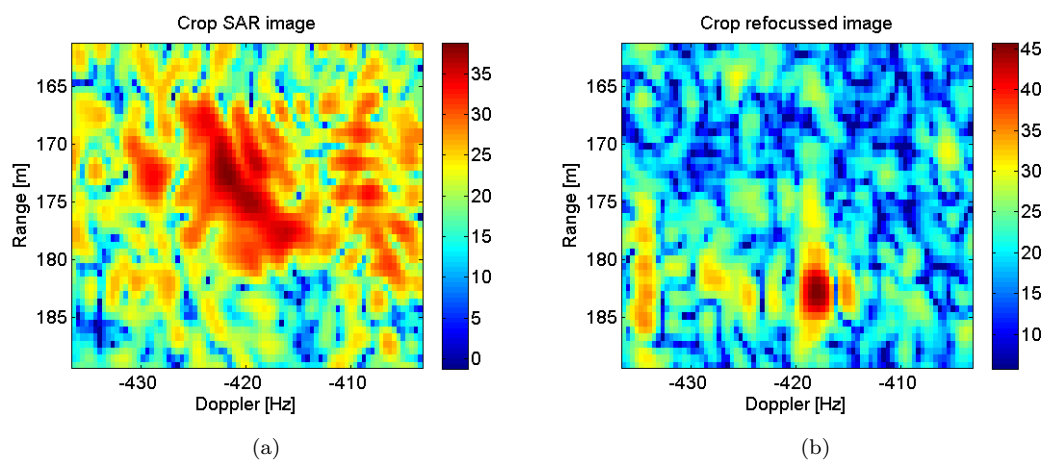
FIGURE 7.27: Sub-region 1 - Crop 6: original SAR image (a) refocussed image (b)
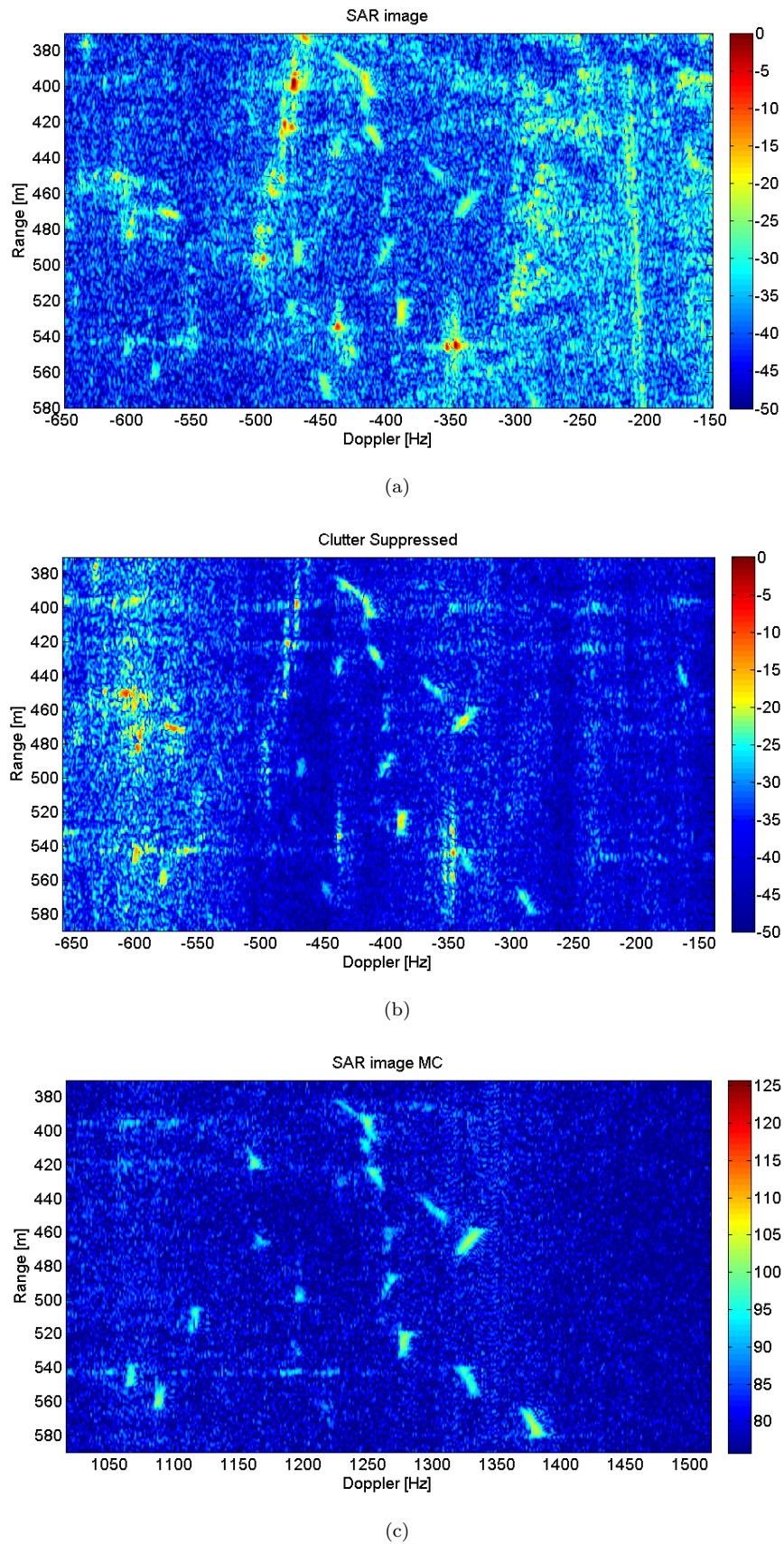
SAR image

(a)

Clutter Suppressed

(b)

SAR image MC

(c)

FIGURE 7.28: Sub-image 2: SAR image (a) Clutter suppressed SAR image (b) Pseudo ground truth (c)
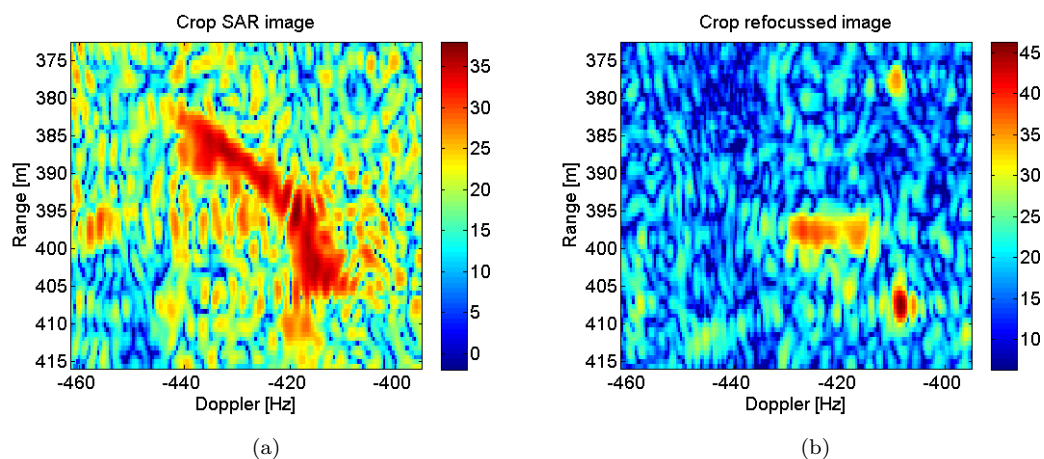
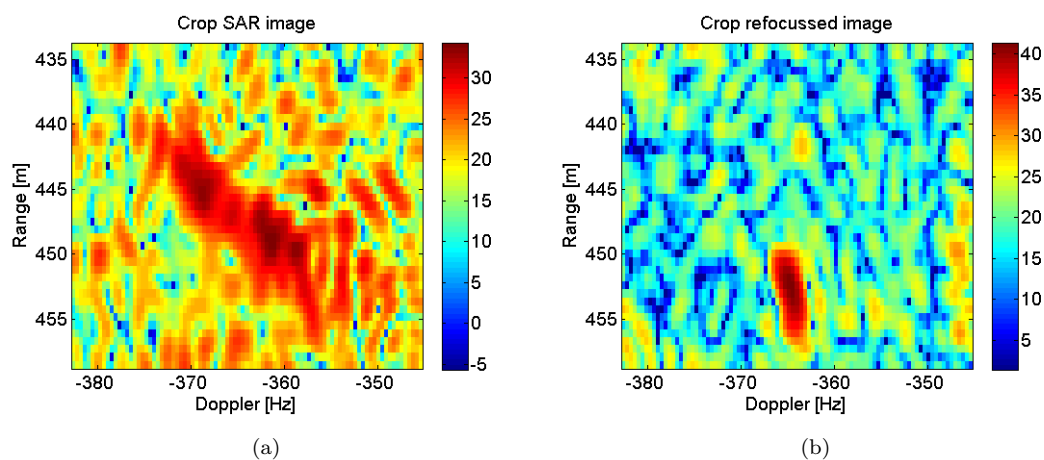FIGURE 7.29: Sub-region 2 - Crop 1: original SAR image (a) refocussed image (b)

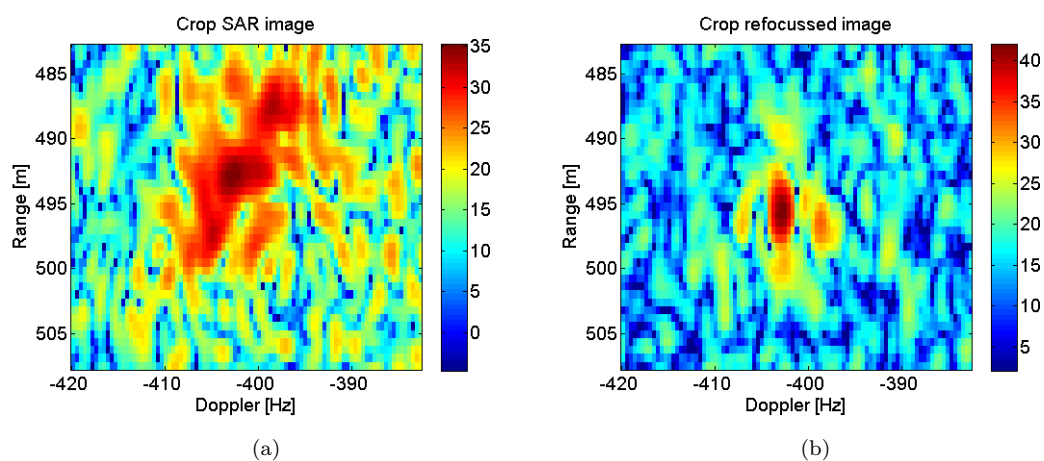FIGURE 7.30: Sub-region 2 - Crop 4: original SAR image (a) refocussed image (b)

FIGURE 7.31: Sub-region 2 - Crop 6: original SAR image (a) refocussed image (b)
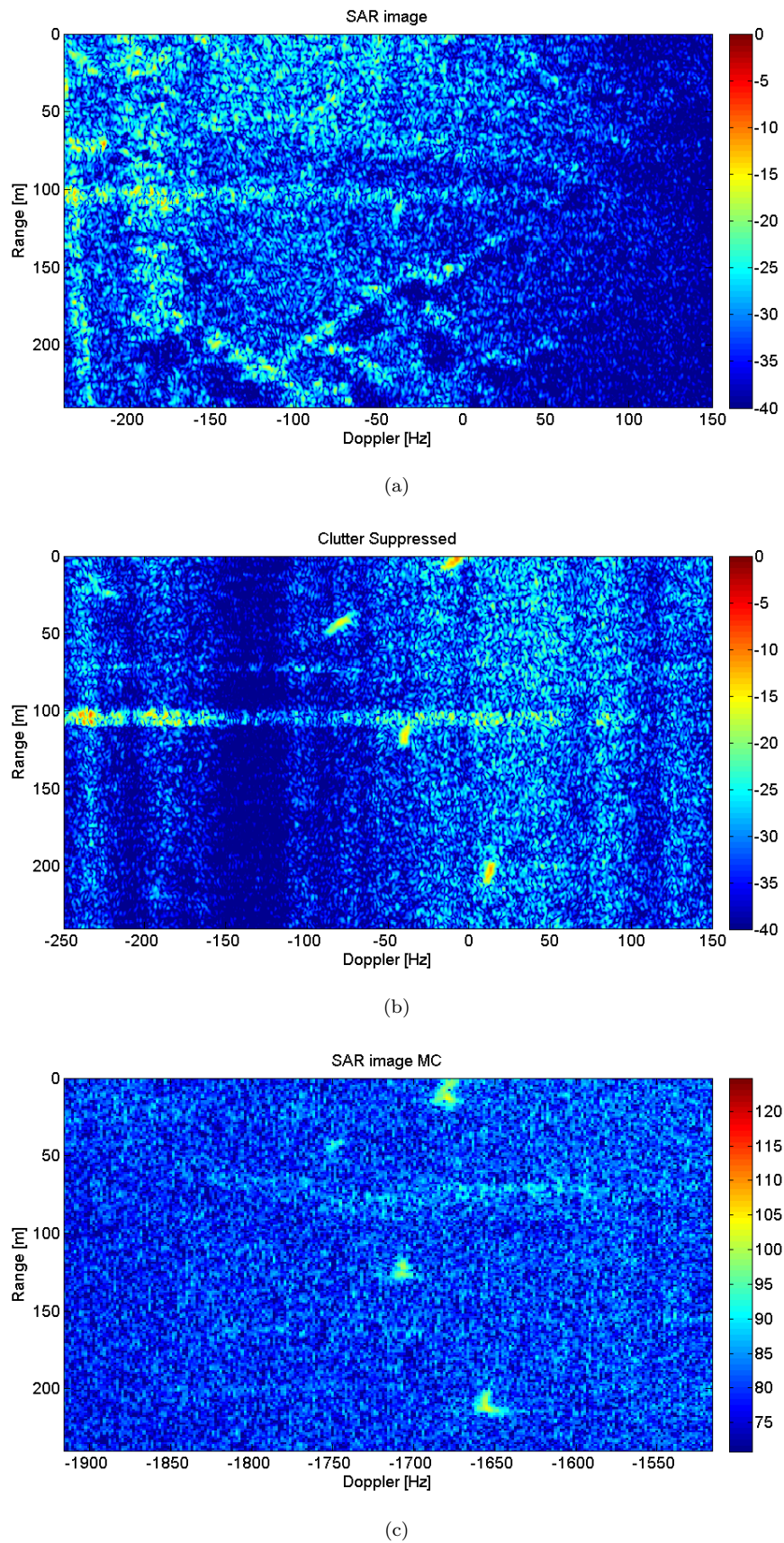
(a)

(b)

(c)

FIGURE 7.32: Sub-image 3: SAR image (a) Clutter suppressed SAR image (b) Pseudo ground truth (c)
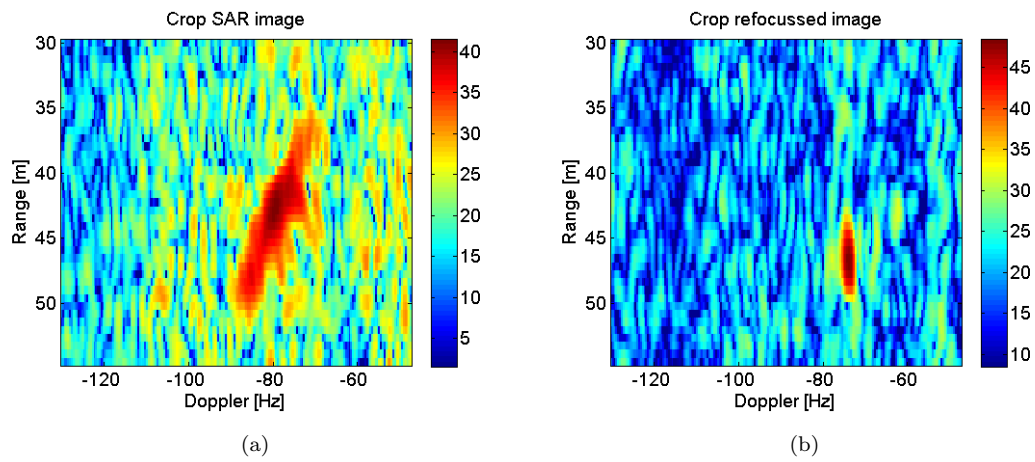
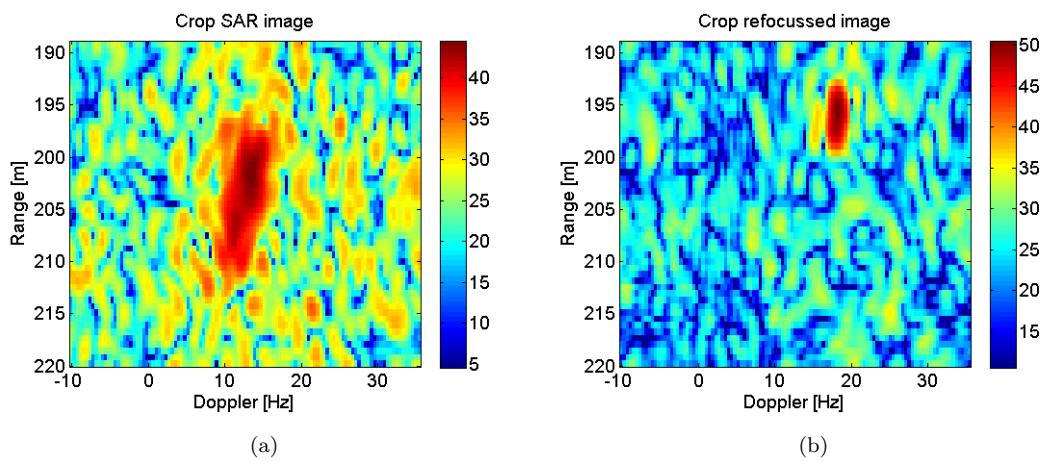FIGURE 7.33: Sub-region 3 - Crop 4: original SAR image (a) refocussed image (b)

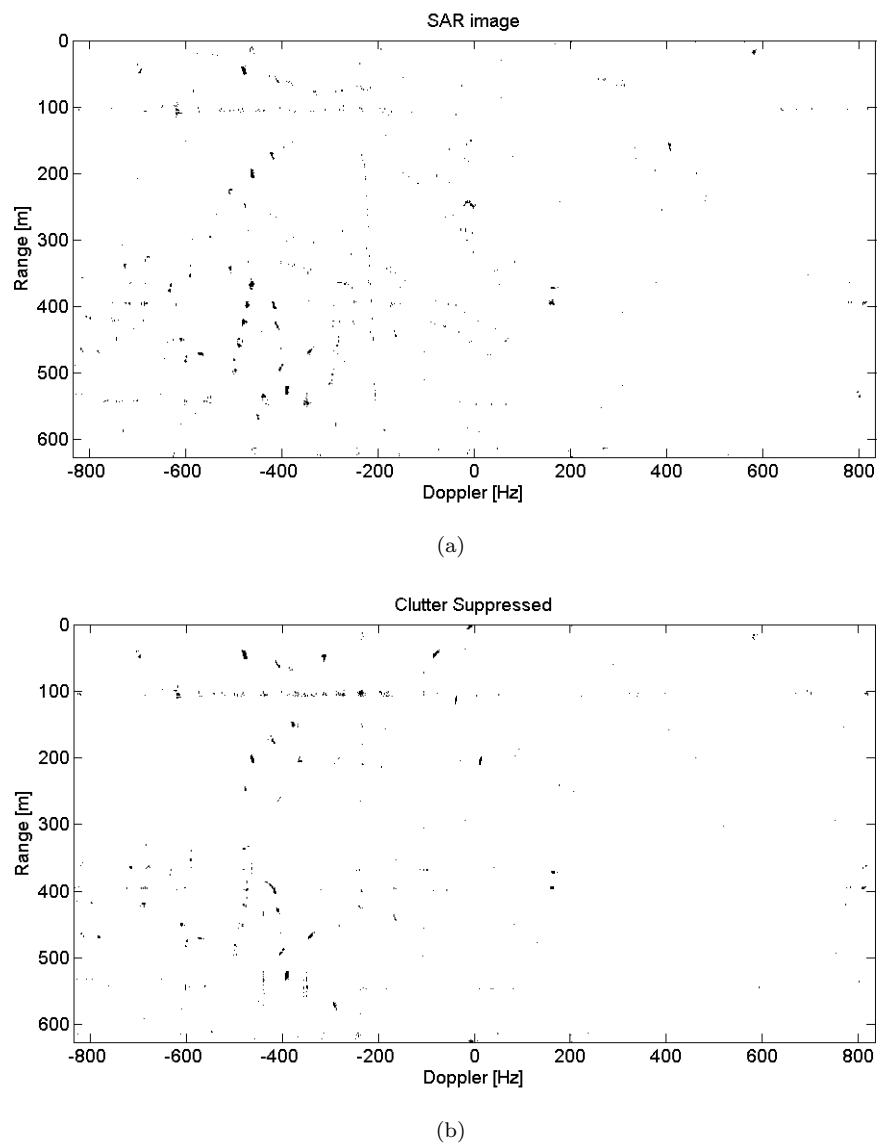FIGURE 7.34: Sub-region 3 - Crop 6: original SAR image (a) refocussed image (b)

FIGURE 7.35: Detection results: original SAR image (a) clutter suppressed image (b)

7.4.3 Case study 3

In this section the third case study is analysed.

As stated before, the third case study consists on the synthesis of an equivalent three channel system exploring the high PRF of the acquired data. In this case, the signal acquired by one of the two real channels is used. The three equivalent channels are obtained considering three consecutive pulses as they would have been acquired by a three channels system. This is depicted in Fig.7.15.

It is quite obvious that the equivalent three channels system considered is only an approximation of a real three channels system. In fact, in a real three channels system the signal is acquired at the same time by the three channels. In the approximation used here, the signal is acquired by the second and third channels two and three pulses later with respect the first one respectively. This introduces a decorrelation along the channels.

It is worth pointing out that also the baseline reduction described in the previous section introduces a decorrelation between the signal acquired by the two channels. In that case, the decorrelation is larger with respect the decorrelation introduced in the third case study because the time distance between the data acquired by the two channels is larger.

Moreover, in this third case only the data acquired by one real channel is considered. As a consequence, this allows for overcoming of all the calibration issues between the two different receiver chains.

In conclusion, better results are expected in this third case with respect to the case 2 for the following three reasons

1. Three equivalent channels are considered so one more spatial degree of freedom with respect case two can be exploited

2. Less time decorrelation introduced. The time delay between the signal acquired by the three channels is T_R while in the case two the time distance between the signal acquired by the two channels is $N_d T_R$

3. No calibration issues since the signal is acquired by the same real channel

The system parameters are listed in Tab.7.13.

v_p	Platform Velocity	$45m/s$
f_0	Carrier Frequency	$9.6GHz$
B	TX bandwidth	$120MHz$
T_{obs}	Observation Time	$0.6s$
PRF_{eq}	Pulse Repetition Frequency	$1.67kHz$
d_{virt}	baseline	$v_pT_R = 9mm$
L	Windows Length	16

TABLE 7.13: Case 3 - Parameters

The region under test and the training range cells are the same shown in Fig.7.21.

The SAR images of the region under test without clutter clutter suppression and with clutter suppression are shown in Fig.7.36 (a) and Fig.7.36 (b) respectively. As can be noted the clutter mitigation process seems to work very well. In order to better appreciate the performances the three sub-regions analysed in the previous section will be shown.

In Fig.7.37 the first sub-region is depicted. The SAR image is shown in Fig7.37 (a) while the image after clutter suppression and the relative pseudo ground truth are shown in Fig7.37 (b) and (c) respectively. The range and Doppler position of the targets in the scene are the same summarized in Tab.7.7 with the difference that in this third case no targets are missing.

In order to evaluate the performance of the ISAR refocussing process the IC values of the target images before and after the refocusing process are listed in Tab.7.14. Some targets (specifically target number 1, 2, 5, 6, 13 and 14) are shown in Fig.7.38 - 7.43. The SAR image (a) and the ISAR image (b) are shown.

The sub-region 2 is shown in Fig.7.44. The SAR image, the clutter suppressed image and the pseudo ground truth are shown in Fig.7.44 (a), (b) and (c) respectively. The range and Doppler position of each target are listed in Tab.7.9. In the third case study only the target number 2 is missing. The SAR (a) and ISAR (b) images of targets number 1, 5, and 6 are shown in Fig.7.45 - 7.45 and the IC values of all the target detected in the sub region are listed in Tab.7.15. As can be noted the ISAR processing fails in some cases.

Sub-region 3 is shown in Fig.7.48. In this case the four considered targets fall within the null of the filter and they are cancelled.
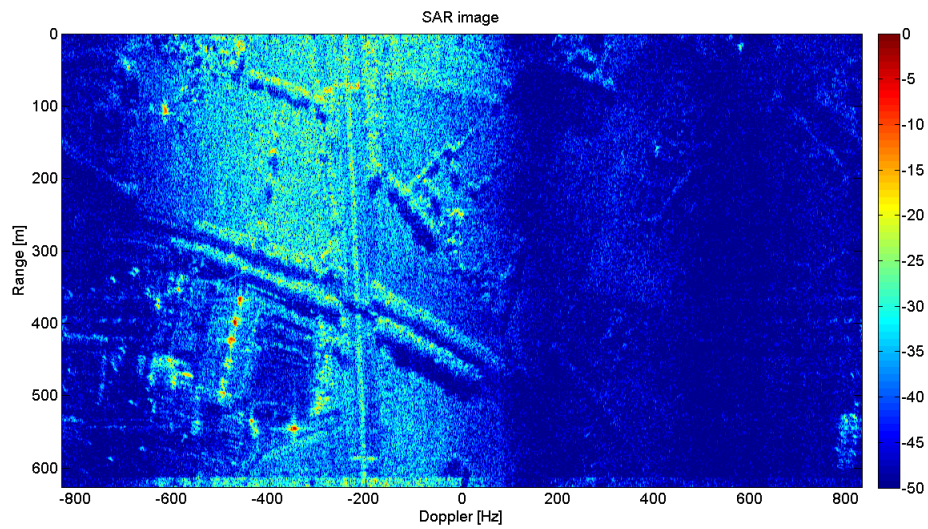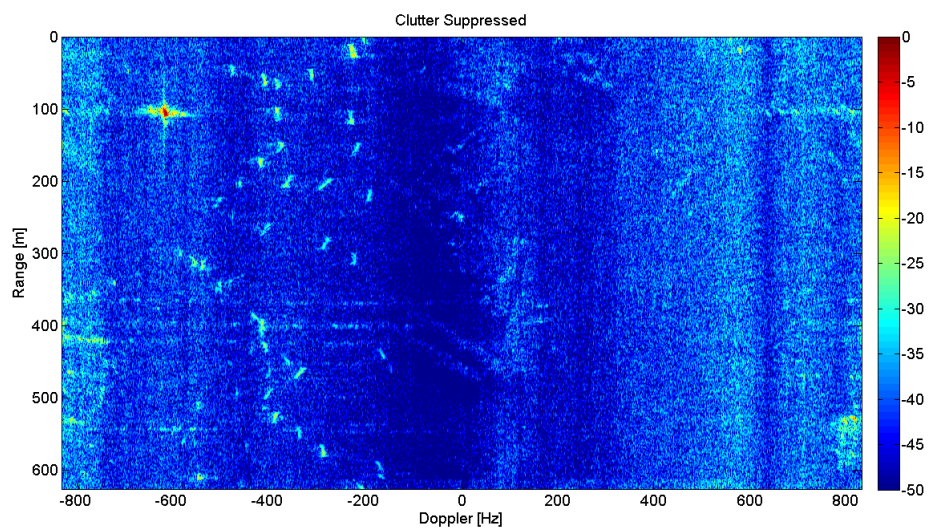
FIGURE 7.36: SAR image (a) and Clutter suppressed SAR image (b)

The results of the detection with the CFAR detector are shown in Fig.7.49.

Target N.	IC SAR	IC ISAR
1	1.519	5.649
2	1.935	4.619
3	1.766	4.238
4	6.053	13.799
5	1.655	4.685
6	1.915	6.205
7	1.96	2.853
8	1.52	3.44
9	9.968	3.41
10	1.676	7.309
11	2.573	6.699
12	1.748	5.359
13	1.622	7.589
14	1.254	6.021

TABLE 7.14: Sub-region 1: IC values before and after ISAR processing

Target N.	IC SAR	IC ISAR
1	2.059	7.263
3	1.7	5.158
4		
5	1.789	7.795
6	1.311	4.37
7		
8	1.405	5.628
9	1.405	5.628
10		
11	0.434	3.253
12		
13	2.215	7.976

TABLE 7.15: Sub-region 2: IC values before and after ISAR processing
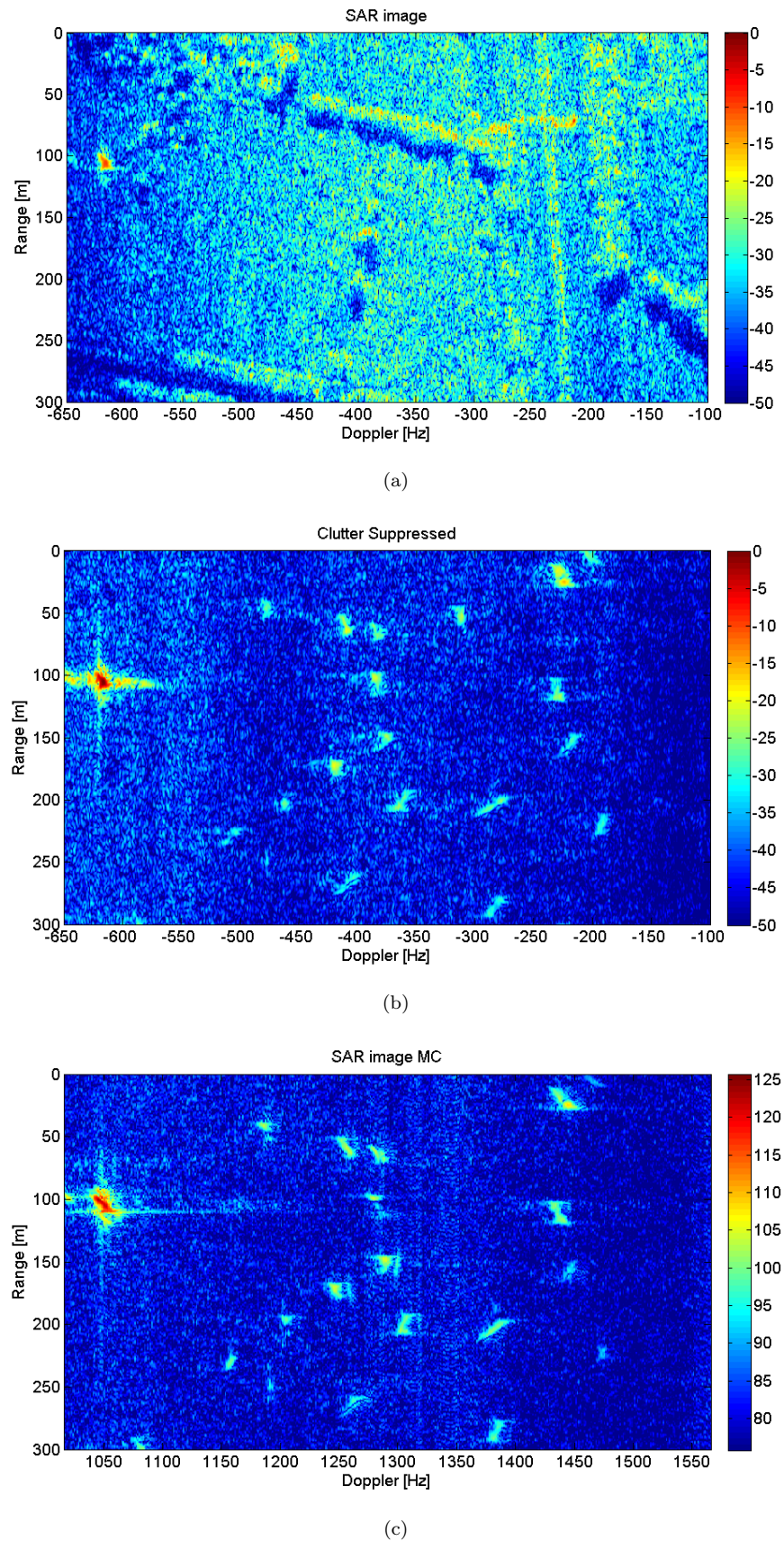
(a)

(b)

(c)

FIGURE 7.37: Sub-image 1: SAR image (a) Clutter suppressed SAR image (b)
Pseudo ground truth (c)

FIGURE 7.38: Sub-region 1 - Crop 1: original SAR image (a) refocussed image (b)

FIGURE 7.39: Sub-region 1 - Crop 2: original SAR image (a) refocussed image (b)

FIGURE 7.40: Sub-region 1 - Crop 5: original SAR image (a) refocussed image (b)

FIGURE 7.41: Sub-region 1 - Crop 6: original SAR image (a) refocussed image (b)
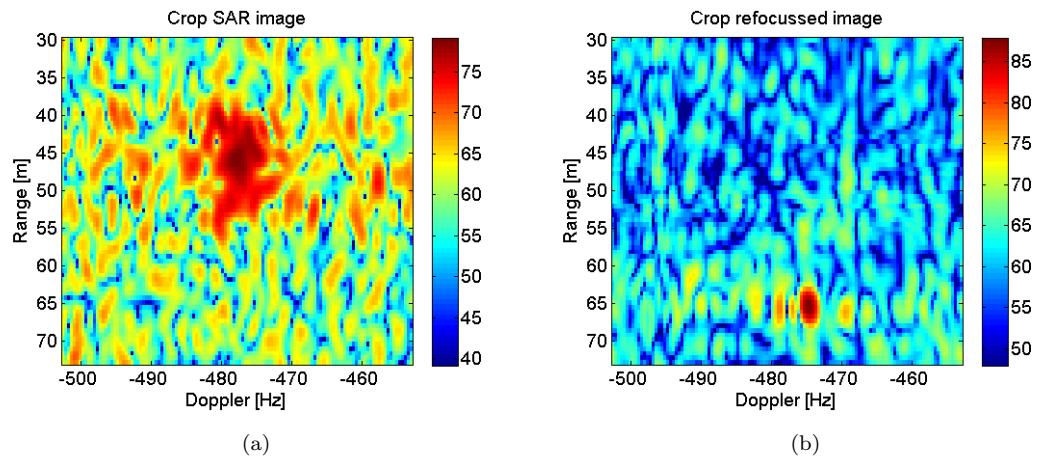

FIGURE 7.42: Sub-region 1 - Crop 13: original SAR image (a) refocussed image (b)

FIGURE 7.43: Sub-region 1 - Crop 14: original SAR image (a) refocussed image (b)

SAR image

(a)

Clutter Suppressed

(b)

SAR image MC

(c)
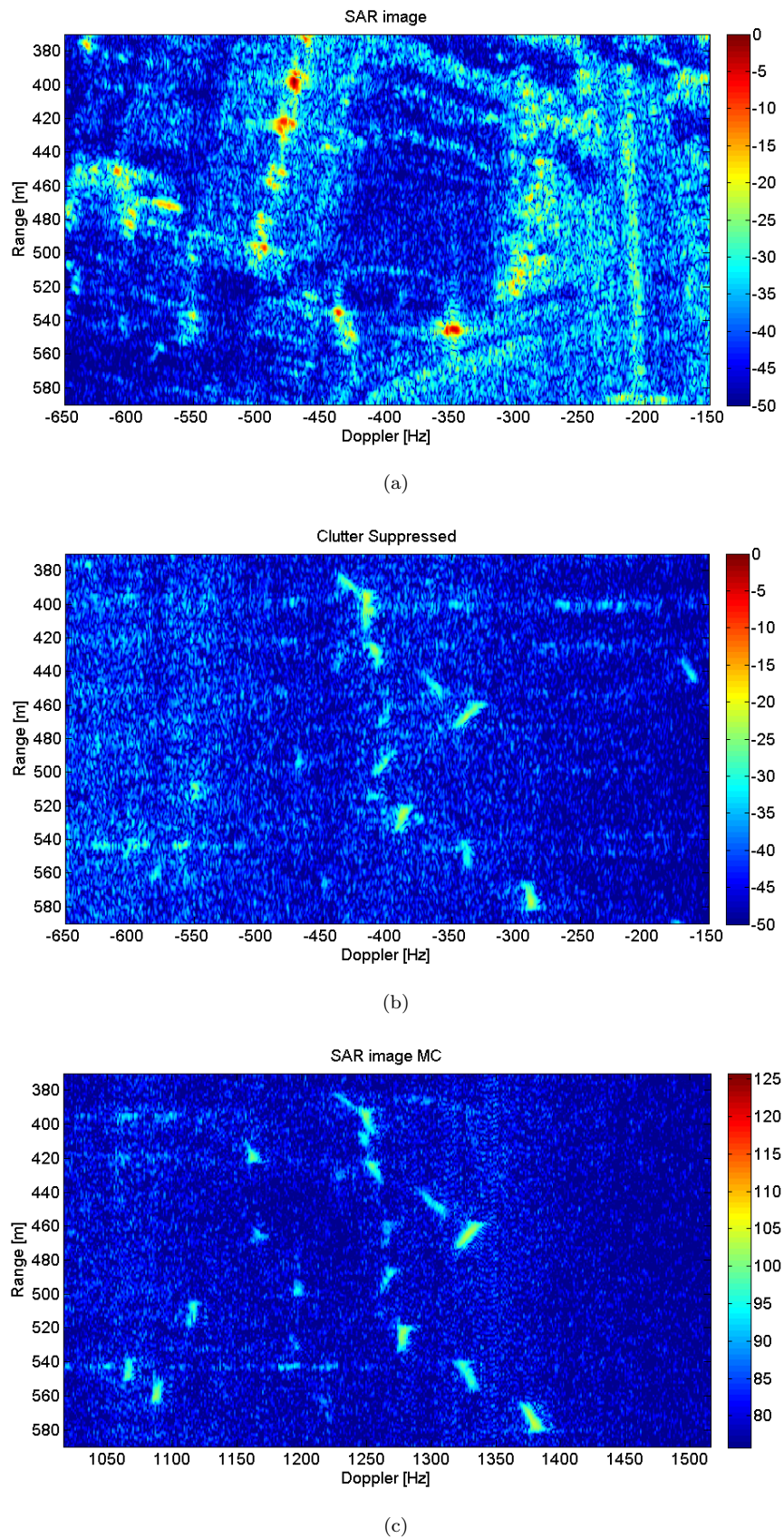
FIGURE 7.44: Sub-image 2: SAR image (a) Clutter suppressed SAR image (b) Pseudo ground truth (c)
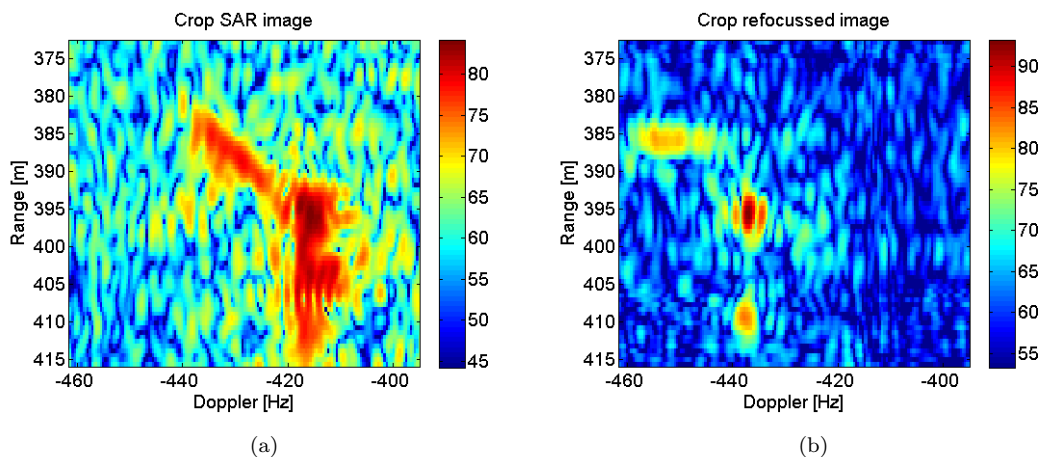
FIGURE 7.45: Sub-region 2 - Crop 1: original SAR image (a) refocussed image (b)
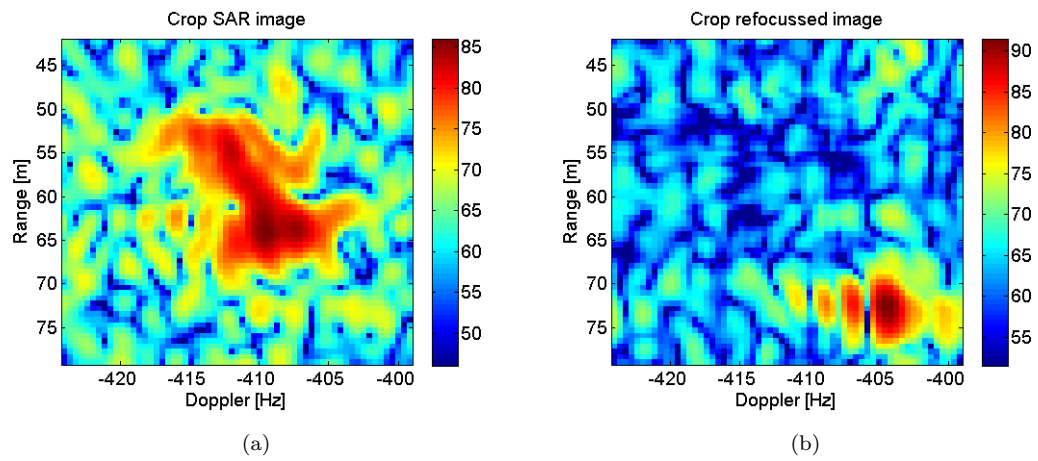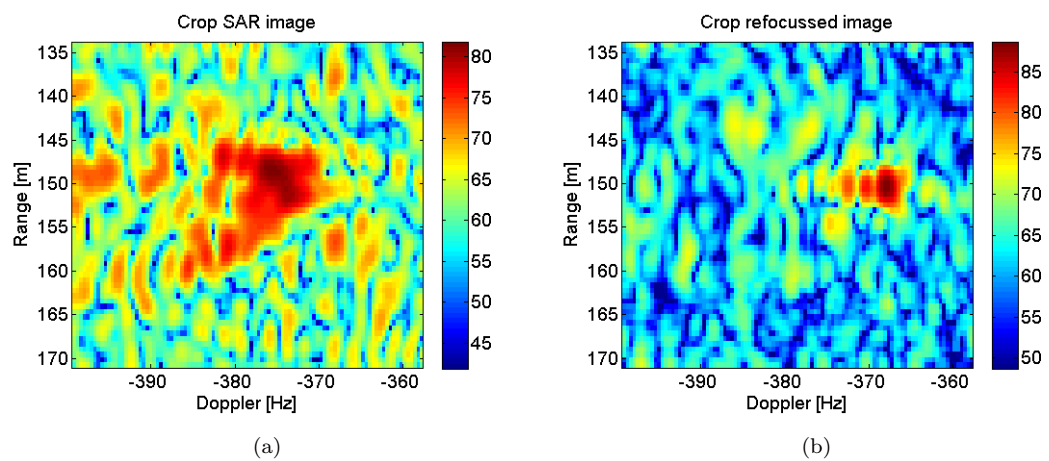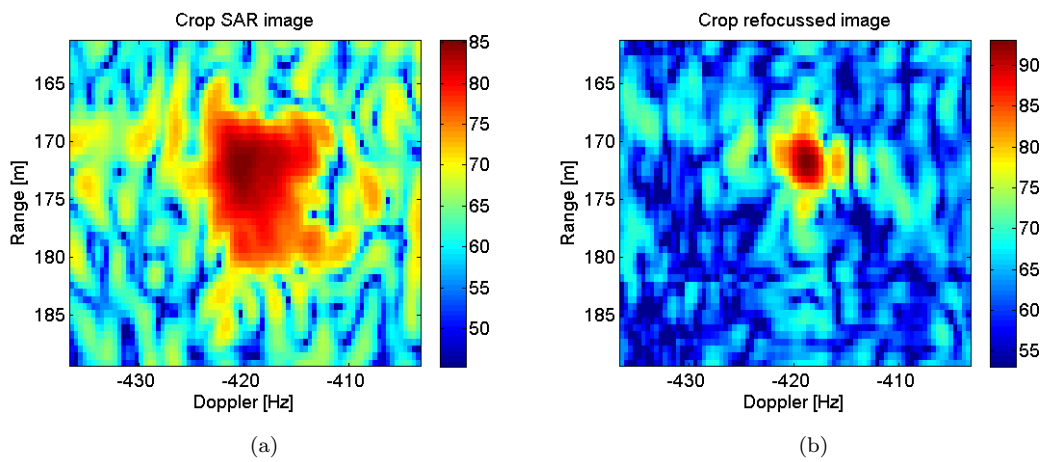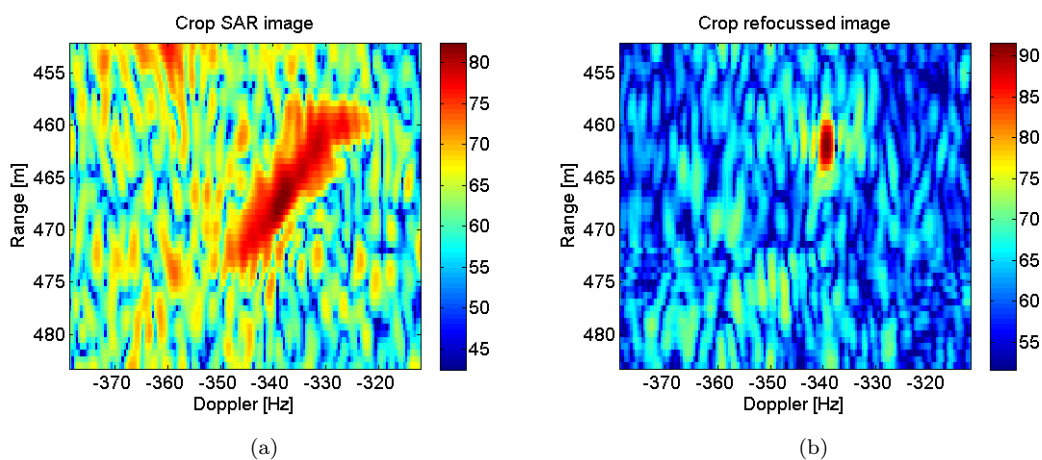

FIGURE 7.46: Sub-region 2 - Crop 5: original SAR image (a) refocussed image (b)
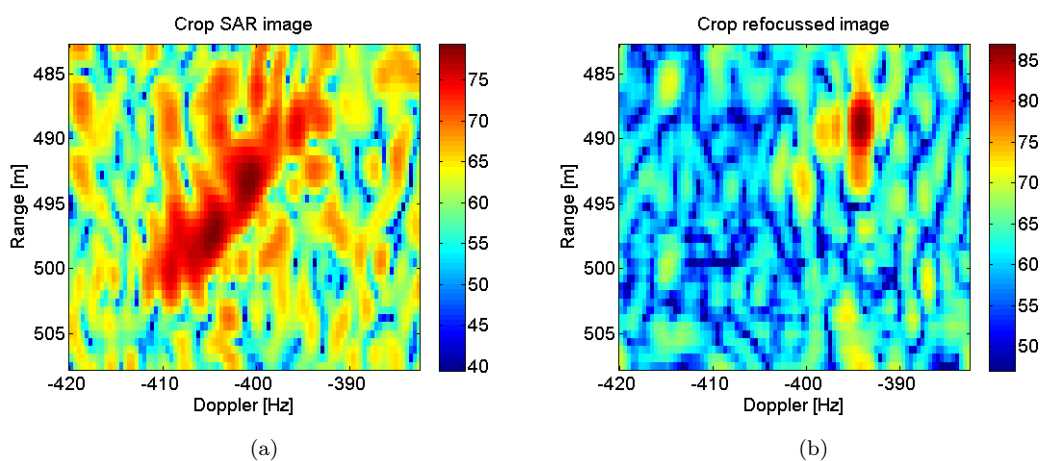
FIGURE 7.47: Sub-region 2 - Crop 6: original SAR image (a) refocussed image (b)
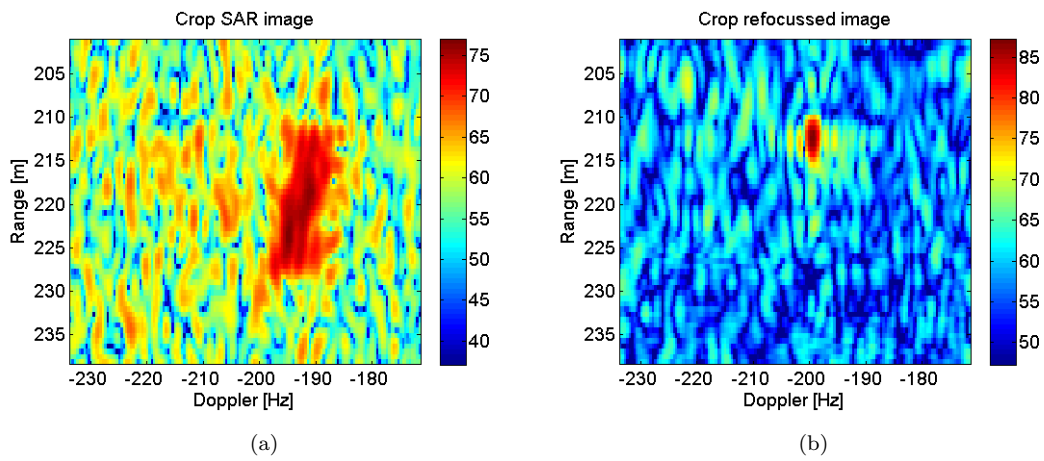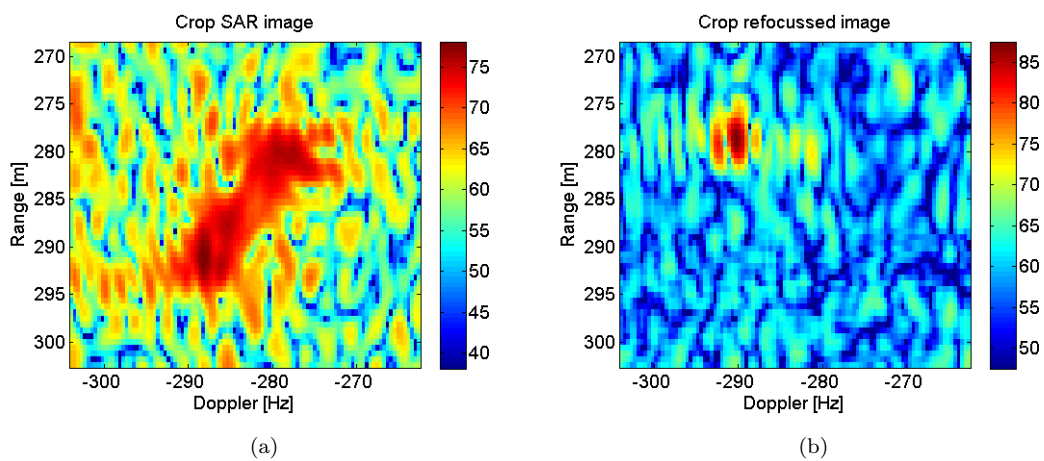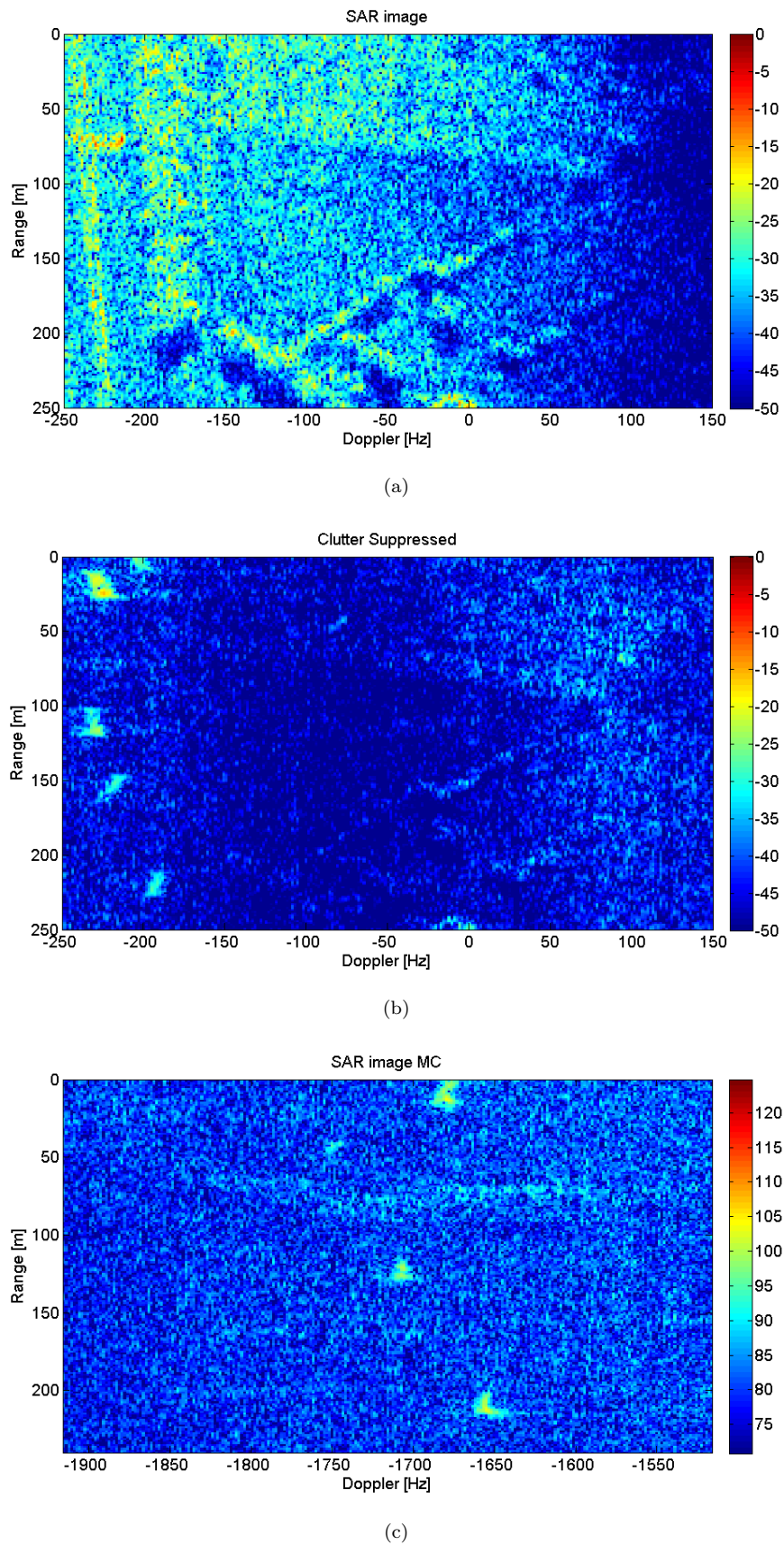
FIGURE 7.48: Sub-image 3: SAR image (a) Clutter suppressed SAR image (b) Pseudo ground truth (c)
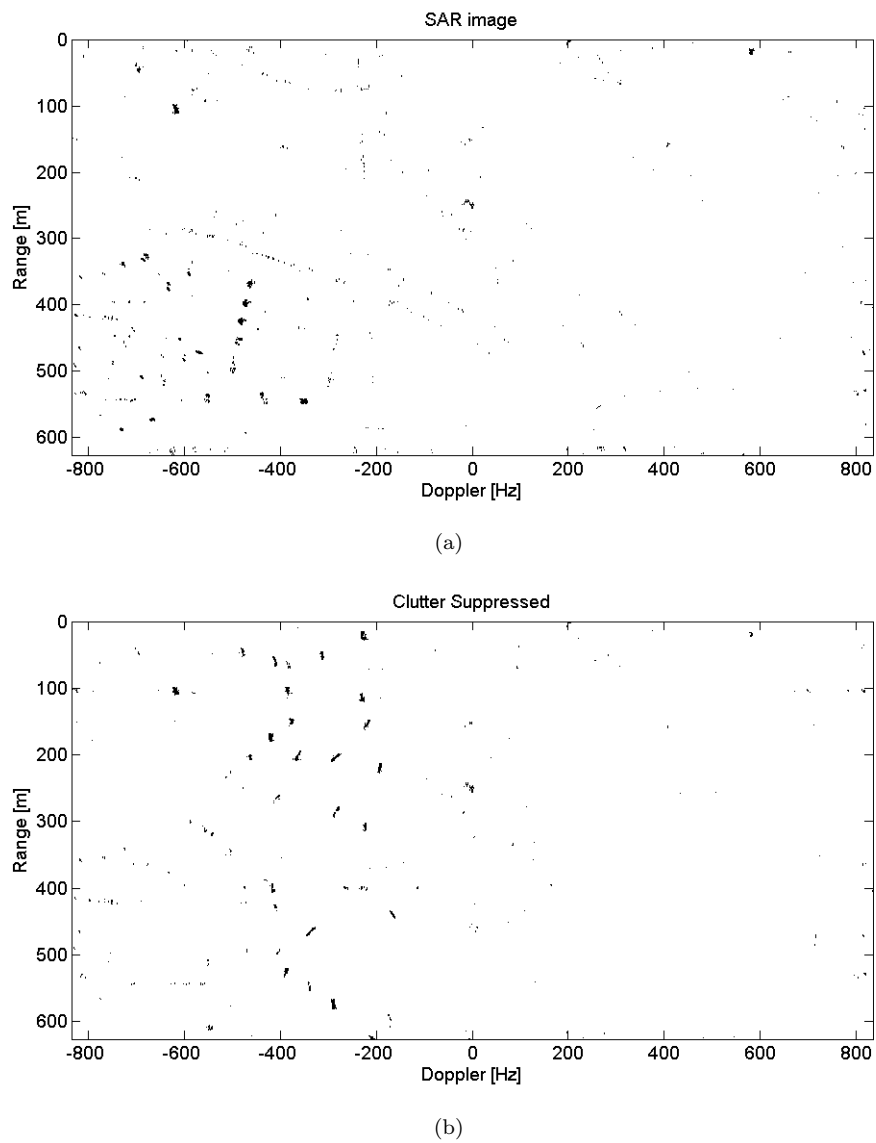
FIGURE 7.49: Detection results: original SAR image (a) clutter suppressed image (b)

7.5 Conclusion

In this chapter the proposed SDAP-ISAR processing was tested on a real dataset. The dataset description was provided and some issues relative to the measurement set up were described. Solution to these issues were proposed. The performances of the multichannel Range Doppler image formation algorithm were analysed. Then three case studies were analysed to asses the correct functioning of the clutter mitigation and imaging processing. The effectiveness of the proposed processing was proven and performance evaluation was performed.

Chapter 8

Conclusion

In this thesis the problem of the imaging of non-cooperative moving targets within SAR images has been addressed. The proposed solution is based on the applicability of the ISAR processing to compensate the unknown part of the relative radar-target motion. The applicability of ISAR processing to refocus moving targets within conventional single channel SAR images has been investigated first.

It is worth pointing out that in order to apply ISAR processing, each target to be refocussed must be detected first. This is a critical aspect especially in case of ground target. In fact, ground clutter can be much stronger than the target return and can completely mask the target of interest.
In order to overcome this issue multichannel information has been exploited. In fact, spatial degrees of freedom can be used as well as the temporal degrees of freedom to mitigate the static clutter making improving detection capabilities.

A review of the ISAR and SAR signal modelling in the monostatic, bistatic and multistatic cases has been presented. A multichannel formulation of the commonly used (especially in ISAR imaging) Range Doppler image formation algorithm has been derived and its limitations have been analysed. A statistical description of the static ground clutter has been presented in order to develop a multichannel simulator to test the proposed algorithms. A review of MTI/MTD techniques for SAR has been provided with particular attention to the STAP techniques. Then, joint STAP-ISAR processing has been formalized and presented. Optimal and sub optimal approaches have been developed and tested on simulated data. An exhaustive performance analysis has been performed.

Starting from the proposed multichannel Range Doppler a different algorithm has been presented named Space Doppler Adaptive Processing. Also in this case both optimal and sub optimal approaches have been formalized and tested on simulated data. A combined SDAP-ISAR processing has been proposed as a complete processing chain to perform clutter suppression and imaging of non-cooperative moving targets in strong clutter scenario. A comparison between STAP-ISAR and SDAP-ISAR has been provided highlighting pros and contra of both the processing chains.

In the final part of this thesis real data analysis has been performed exploiting a multichannel dataset provided by Metasensing within the activities of the NATO-SET 196. The performances of the multichannel Range Doppler image formation algorithm have been analysed first. Then the SDAP-ISAR processing has been applied to obtain well focused images of non-cooperative moving targets. Results have demonstrated the effectiveness of the proposed processing chain and its applicability in real systems for surveillance purposes.

The main future direction will involve the reduction of the computational cost and the overcome of statistical issues due to the need of the disturbance covariance matrix estimation. Reduced rank techniques could be studied and applied to modify the proposed algorithms leading to near or better performances with respect their full rank counterpart with a reduced computational load. Making the processing chain fully automatic avoiding the need of external inputs can be another aspect to investigate.

Bibliography

[1] Dale A. Ausherman, Adam Kozma, Jack L. Walker, Harrison M. Jones, and Enrico C. Poggio. Developments in radar imaging. *Aerospace and Electronic Systems, IEEE Transactions on*, AES-20(4):363–400, 1984. ISSN 0018-9251. doi: 10.1109/TAES.1984.4502060.

[2] Jack L. Walker. Range-doppler imaging of rotating objects. *Aerospace and Electronic Systems, IEEE Transactions on*, AES-16(1):23–52, 1980. ISSN 0018-9251. doi: 10.1109/TAES.1980.308875.

[3] N. J S Stacy, D. P. Badger, A.S. Goh, M. Preiss, and M. L. Williams. The dsto ingara airbone x-band sar polarimetric upgrade: first results. In *Geoscience and Remote Sensing Symposium, 2003. IGARSS '03. Proceedings. 2003 IEEE International*, volume 7, pages 4474–4476 vol.7, 2003. doi: 10.1109/IGARSS. 2003.1295551.

[4] G. Albarel, J.S. Tanner, and Manfred Uhlmann. The trinational amsar programme: Car active antenna architecture. In *Radar 97 (Conf. Publ. No. 449)*, pages 344–347, 1997. doi: 10.1049/cp:19971692.

[5] J. H G Ender, P. Berens, A.R. Brenner, L. Rossing, and U. Skupin. Multichannel sar/mti system development at fgan: from aer to pamir. In *Geoscience and Remote Sensing Symposium, 2002. IGARSS '02. 2002 IEEE International*, volume 3, pages 1697–1701 vol.3, 2002. doi: 10.1109/IGARSS. 2002.1026225.

[6] J. H G Ender and A.R. Brenner. Pamir - a wideband phased array sar/mti system. *Radar, Sonar and Navigation, IEE Proceedings -*, 150(3):165–172, 2003. ISSN 1350-2395. doi: 10.1049/ip-rsn:20030445.

[7] T.J. Nohara, P. Weber, A. Premji, and C. Livingstone. Sar-gmti processing with canada's radarsat 2 satellite. In *Adaptive Systems for Signal Processing,*

Communications, and Control Symposium 2000. AS-SPCC. The IEEE 2000, pages 379–384, 2000. doi: 10.1109/ASSPCC.2000.882504.

[8] A. Roth. Terrasar-x: a new perspective for scientific use of high resolution spaceborne sar data. In *Remote Sensing and Data Fusion over Urban Areas, 2003. 2nd GRSS/ISPRS Joint Workshop on*, pages 4–7, 2003. doi: 10.1109/DFUA.2003.1219947.

[9] D. J. Coe and R.G. White. Moving target detection in sar imagery: experimental results. In *Radar Conference, 1995., Record of the IEEE 1995 International*, pages 644–649, 1995. doi: 10.1109/RADAR.1995.522625.

[10] C. Kopp. *F-111 upgrade options*. Australian Aviation, 1997. URL http://f-111.net/CarloKopp/F-111_Upgrade_Option_Pt_3.htm.

[11] F. Berizzi and G. Corsini. Autofocusing of inverse synthetic aperture radar images using contrast optimization. *Aerospace and Electronic Systems, IEEE Transactions on*, 32(3):1185–1191, 1996. ISSN 0018-9251. doi: 10.1109/7.532282.

[12] M. Martorella, J. Palmer, J. Homer, B. Littleton, and I.D. Longstaff. On bistatic inverse synthetic aperture radar. *Aerospace and Electronic Systems, IEEE Transactions on*, 43(3):1125–1134, 2007. ISSN 0018-9251. doi: 10.1109/TAES.2007.4383602.

[13] N. Battisti and M. Martorella. Intereferometric phase and target motion estimation for accurate 3d reflectivity reconstruction in isar systems. In *Radar Conference, 2010 IEEE*, pages 108–112, 2010. doi: 10.1109/RADAR.2010.5494644.

[14] F. Berizzi and M. Diani. Target angular motion effects on isar imaging. *Radar, Sonar and Navigation, IEE Proceedings -*, 144(2):87–95, 1997. ISSN 1350-2395. doi: 10.1049/ip-rsn:19970965.

[15] William M. Brown and R.J. Fredricks. Range-doppler imaging with motion through resolution cells. *Aerospace and Electronic Systems, IEEE Transactions on*, AES-5(1):98–102, 1969. ISSN 0018-9251. doi: 10.1109/TAES.1969.309826.

[16] M. Soumekh. *Synthetic Aperture Radar Signal Processing with MATLAB Algorithms*. Wiley-Interscience publication. Wiley, 1999. ISBN 9780471297062.

[17] I.G. Cumming and F.H.C. Wong. *Digital Signal Processing of Synthetic Aperture Radar Data: Algorithms and Implementation.* Artech House signal processing library. Artech House, Incorporated, 2005. ISBN 9781580530583. URL http://books.google.it/books?id=e9xxQgAACAAJ.

[18] W.G. Carrara, R.S. Goodman, and R.M. Majewski. *Spotlight Synthetic Aperture Radar: Signal Processing Algorithms.* Artech House signal processing library. Artech House, Incorporated, 1995. ISBN 9780890067284. URL http://books.google.it/books?id=uztiQgAACAAJ.

[19] Luke Rosenberg and Douglas Andrew Gray. Multichannel sar imaging using wavefront reconstruction. In *International Radar Symposium (2004: Warsaw, Poland)*, 2004.

[20] S. Barbarossa and Alfonso Farina. Space-time-frequency processing of synthetic aperture radar signals. *Aerospace and Electronic Systems, IEEE Transactions on*, 30(2):341–358, 1994. ISSN 0018-9251. doi: 10.1109/7.272259.

[21] R. Klemm, Institution of Engineering, and Technology. *Principles of Space-Time Adaptive Processing, 3rd Edition.* IET radar, sonar, navigation and avionics series. Institution of Engineering and Technology, 2006. ISBN 9780863415661. URL http://books.google.it/books?id=z6ICP3PtYi0C.

[22] F.T. Ulaby, R.K. Moore, and A.K. Fung. *Microwave Remote Sensing: Radar remote sensing and surface scattering and emission theory.* Remote Sensing. Addison-Wesley Publishing Company, Advanced Book Program/World Science Division, 1981. ISBN 9780201107609. URL http://books.google.it/books?id=ms8PAQAAIAAJ.

[23] J. C. Curlander. *Synthetic Aperture Radar: Systems and Signal Processing.* Wiley, 1991.

[24] M. Kirscht. Detection and imaging of arbitrarily moving targets with single-channel sar. *Radar, Sonar and Navigation, IEE Proceedings -*, 150(1):7–11, 2003. ISSN 1350-2395. doi: 10.1049/ip-rsn:20030076.

[25] R.P. Perry, R.C. DiPietro, and R. Fante. Sar imaging of moving targets. *Aerospace and Electronic Systems, IEEE Transactions on*, 35(1):188–200, 1999. ISSN 0018-9251. doi: 10.1109/7.745691.

[26] Shengqi Zhu, Guisheng Liao, Yi Qu, Zhengguang Zhou, and Xiangyang Liu. Ground moving targets imaging algorithm for synthetic aperture radar. *Geoscience and Remote Sensing, IEEE Transactions on*, 49(1):462–477, 2011. ISSN 0196-2892. doi: 10.1109/TGRS.2010.2053848.

[27] F. Zhou, R. Wu, M. Xing, and Z. Bao. Approach for single channel sar ground moving target imaging and motion parameter estimation. *Radar, Sonar Navigation, IET*, 1(1):59–66, 2007. ISSN 1751-8784. doi: 10.1049/iet-rsn:20060040.

[28] I. Djurovic, T. Thayaparan, and L.J. Stankovic. Sar imaging of moving targets using polynomial fourier transform. *Signal Processing, IET*, 2(3):237–246, 2008. ISSN 1751-9675. doi: 10.1049/iet-spr:20070114.

[29] S. Werness, M.A. Stuff, and J.R. Fienup. Two-dimensional imaging of moving targets in sar data. In *Signals, Systems and Computers, 1990 Conference Record Twenty-Fourth Asilomar Conference on*, volume 1, pages 16–, 1990. doi: 10.1109/ACSSC.1990.523292.

[30] S.A.S. Werness, W.G. Carrara, L.S. Joyce, and D.B. Franczak. Moving target imaging algorithm for sar data. *Aerospace and Electronic Systems, IEEE Transactions on*, 26(1):57–67, 1990. ISSN 0018-9251. doi: 10.1109/7.53413.

[31] M. Martorella, F. Berizzi, and B. Haywood. Contrast maximisation based technique for 2-d isar autofocusing. *Radar, Sonar and Navigation, IEE Proceedings -*, 152(4):253–262, 2005. ISSN 1350-2395. doi: 10.1049/ip-rsn:20045123.

[32] M. Martorella and F. Berizzi. Time windowing for highly focused isar image reconstruction. *Aerospace and Electronic Systems, IEEE Transactions on*, 41 (3):992–1007, 2005. ISSN 0018-9251. doi: 10.1109/TAES.2005.1541444.

[33] M. Martorella. Novel approach for isar image cross-range scaling. *Aerospace and Electronic Systems, IEEE Transactions on*, 44(1):281–294, 2008. ISSN 0018-9251. doi: 10.1109/TAES.2008.4517004.

[34] Xiumei Li, Guoan Bi, and Yingtuo Ju. Quantitative snr analysis for isar imaging using lpft. *Aerospace and Electronic Systems, IEEE Transactions on*, 45(3):1241–1248, 2009. ISSN 0018-9251. doi: 10.1109/TAES.2009.5259197.

[35] M. Martorella N. Battisti. Interferometric phase and target motion estimation for accurate 3D reflectivity in ISAR system. pages 108–112. IEEE Radar Conference 2010, 2010.

[36] M. Martorella, N. Acito, and F. Berizzi. Statistical clean technique for isar imaging. *IEEE Tr. on Geoscience and Remote Sensing*, 45(11):3552–3560, 2007.

[37] J. Tsao and B.D. Steinberg. Reduction of sidelobe and speckle artifacts in microwave imaging: The CLEAN technique. *IEEE Tr. on Antennas and Propagation*, 36:543–556, 1988.

[38] E. D'Addio, M. Di Bisceglie, and S. Bottalico. Detection of moving objects with airborne {SAR}. *Signal Processing*, 36(2):149 – 162, 1994. ISSN 0165-1684. doi: http://dx.doi.org/10.1016/0165-1684(94)90204-6. URL http://www.sciencedirect.com/science/article/pii/0165168494902046.

[39] R.K. Raney. Synthetic aperture imaging radar and moving targets. *Aerospace and Electronic Systems, IEEE Transactions on*, AES-7(3):499–505, 1971. ISSN 0018-9251. doi: 10.1109/TAES.1971.310292.

[40] R.G. White. Change detection in sar imagery. In *Synthetic Aperture Radar, IEE Colloquium on*, pages 5/1–5/3, 1989.

[41] J. A. Legg, A. G. Bolton, and D. A. Gray. Sar moving target detection using a non-uniform prf. In *European SAR conference*, pages 423–426, 1996. doi: 10.1049/cp:19971666.

[42] Jr. Dickey, F.R., M. Labitt, and F.M. Staudaher. Development of airborne moving target radar for long range surveillance. *Aerospace and Electronic Systems, IEEE Transactions on*, 27(6):959–972, 1991. ISSN 0018-9251. doi: 10.1109/7.104273.

[43] H. Shnitkin. Joint stars phased array radar antenna. In *Aerospace and Electronics Conference, 1994. NAECON 1994., Proceedings of the IEEE 1994 National*, pages 142–150 vol.1, 1994. doi: 10.1109/NAECON.1994.333005.

[44] H. Shnitkin. Joint stars phased array radar antenna. In *Antennas and Propagation Society International Symposium, 1994. AP-S. Digest*, volume 2, pages 856–859 vol.2, 1994. doi: 10.1109/APS.1994.407930.

[45] H. Shnitkin. Joint stars phased array radar antenna. *Aerospace and Electronic Systems Magazine, IEEE*, 9(10):34–40, 1994. ISSN 0885-8985. doi: 10.1109/ 62.318882.

[46] H. Shnitkin. Unique joint stars phased-array antenna. In *Antennas and Propagation Society International Symposium, 1990. AP-S. Merging Technologies for the 90's. Digest.*, pages 678–681 vol.2, 1990. doi: 10.1109/APS.1990. 115200.

[47] M. Skolnik. *Radar Handbook, Third Edition*. Electronics electrical engineering. McGraw-Hill Education, 2008. ISBN 9780071485470. URL http: //books.google.it/books?id=76uF2Xebm-gC.

[48] V. Pascazio, G. Schirinzi, and A. Farina. Moving target detection by along-track interferometry. In *Geoscience and Remote Sensing Symposium, 2001. IGARSS '01. IEEE 2001 International*, volume 7, pages 3024–3026 vol.7, 2001. doi: 10.1109/IGARSS.2001.978242.

[49] C. Gierull. Moving target detection by along-track sar interferometry. In *DREO Technical Report*, 2002. doi: 10.1109/IGARSS.2001.978242.

[50] E. Chapin and C.W. Chen. Along-track interferometry for ground moving target indication. *Aerospace and Electronic Systems Magazine, IEEE*, 23(6): 19–24, 2008. ISSN 0885-8985. doi: 10.1109/MAES.2008.4558004.

[51] Mingquan Bao, C. Bruning, and W. Alpers. Simulation of ocean waves imaging by an along-track interferometric synthetic aperture radar. *Geoscience and Remote Sensing, IEEE Transactions on*, 35(3):618–631, 1997. ISSN 0196-2892. doi: 10.1109/36.581977.

[52] Bertrand Chapron, Fabrice Collard, and Fabrice Ardhuin. Direct measurements of ocean surface velocity from space: Interpretation and validation. *Journal of Geophysical Research: Oceans*, 110(C7):n/a–n/a, 2005. ISSN 2156-2202. doi: 10.1029/2004JC002809. URL http://dx.doi.org/10.1029/ 2004JC002809.

[53] H. M. J.. Cantalloube. Moving target indication (mti) using multi-channel along-track interferometer in x-band and antenna with wide illumination pattern in ku-band. In *European SAR conferencel*, pages 213–216, 1995. doi: 10.1109/RADAR.1995.522625.

[54] L. Cohen. Time-frequency distributions-a review. *Proceedings of the IEEE*, 77(7):941–981, 1989. ISSN 0018-9219. doi: 10.1109/5.30749.

[55] W. Rieck. Time-frequency distribution of multichannel sar-data for autofocusing of moving targets. In *Radar 97 (Conf. Publ. No. 449)*, pages 224–228, 1997. doi: 10.1049/cp:19971666.

[56] W. Rieck. Sar imaging of moving targets: Application of time-frequency distribution for single and multichannel data. In *European SAR conference*, pages 431–434–228, 1996. doi: 10.1049/cp:19971666.

[57] S. Barbarossa and A. Zanalda. A combined wigner-ville and hough transform for cross-terms suppression and optimal detection and parameter estimation. In *Acoustics, Speech, and Signal Processing, 1992. ICASSP-92., 1992 IEEE International Conference on*, volume 5, pages 173–176 vol.5, 1992. doi: 10. 1109/ICASSP.1992.226630.

[58] P. Lombardo. Estimation of target motion parameters from dual-channel sar echoes via time-frequency analysis. In *Radar Conference, 1997., IEEE National*, pages 13–18, 1997. doi: 10.1109/NRC.1997.588100.

[59] J.R. Guerci. *Space-time Adaptive Processing for Radar*. Artech House radar library. Artech House, 2003. ISBN 9781580536998. URL http://books. google.it/books?id=cmdI8pvOdqAC.

[60] James Ward. *Space-Time Adaptive Processing for Airborne Radar*. MASSACHUSETTS INST OF TECH LEXINGTON LINCOLN LAB, 1994. URL http://www.dtic.mil/cgi-bin/GetTRDoc?Location=U2&doc= GetTRDoc.pdf&AD=ADA293032.

[61] J.H.G. Ender. Space-time adaptive processing for synthetic aperture radar. In *Space-Time Adaptive Processing (Ref. No. 1998/241), IEE Colloquium on*, pages 6/1 –618, apr 1998. doi: 10.1049/ic:19980244.

[62] J. H G Ender. Space-time processing for multichannel synthetic aperture radar. *Electronics Communication Engineering Journal*, 11(1):29–38, 1999. ISSN 0954-0695. doi: 10.1049/ecej:19990106.

[63] L. Rosenberg, M. Trinkle, and D. Gray. Fast-time stap performance in pre and post range processing adaption as applied to multichannel sar. In *Radar*

Symposium, 2006. IRS 2006. International, pages 1 –4, may 2006. doi: 10.
1109/IRS.2006.4338136.

[64] L. Rosenberg and D. Gray. Robust interference suppression for multichannel
sar. In *Signal Processing and Its Applications, 2005. Proceedings of the Eighth
International Symposium on*, volume 2, pages 883 – 886, 28-31, 2005. doi:
10.1109/ISSPA.2005.1581080.

[65] L. Rosenberg and D. Gray. Anti-jamming techniques for multichannel sar
imaging. *Radar, Sonar and Navigation, IEE Proceedings -*, 153(3):234 – 242,
june 2006. ISSN 1350-2395.

[66] W.L. Melvin. A stap overview. *Aerospace and Electronic Systems Magazine,
IEEE*, 19(1):19–35, 2004. ISSN 0885-8985. doi: 10.1109/MAES.2004.1263229.

[67] I.S. Reed, J.D. Mallett, and L.E. Brennan. Rapid convergence rate in adaptive
arrays. *Aerospace and Electronic Systems, IEEE Transactions on*, AES-10(6):
853–863, 1974. ISSN 0018-9251. doi: 10.1109/TAES.1974.307893.

[68] F.C. Robey, D.R. Fuhrmann, E.J. Kelly, and R. Nitzberg. A cfar adaptive
matched filter detector. *Aerospace and Electronic Systems, IEEE Transactions on*, 28(1):208–216, 1992. ISSN 0018-9251. doi: 10.1109/7.135446.

[69] E.J. Hendon and Irving S. Reed. A new cfar sidelobe canceler algorithm
for radar. *Aerospace and Electronic Systems, IEEE Transactions on*, 26(5):
792–803, 1990. ISSN 0018-9251. doi: 10.1109/7.102714.

[70] E.J. Kelly. An adaptive detection algorithm. *Aerospace and Electronic Systems, IEEE Transactions on*, AES-22(2):115–127, 1986. ISSN 0018-9251. doi:
10.1109/TAES.1986.310745.

[71] S. Kraut, L.L. Scharf, and L.T. McWhorter. Adaptive subspace detectors.
Signal Processing, IEEE Transactions on, 49(1):1–16, 2001. ISSN 1053-587X.
doi: 10.1109/78.890324.

[72] Harry L Van Trees. Optimum array processing (detection, estimation, and
modulation theory, part iv). *Wiley-Interscience, Mar*, (50):100, 2002.

[73] H. Wang and L. Cai. A localized adaptive mtd processor. *Aerospace and
Electronic Systems, IEEE Transactions on*, 27(3):532–539, 1991. ISSN 0018-
9251. doi: 10.1109/7.81435.

[74] C. Trampuz, A. Meta, A. Coccia, and E. Imbembo. Metasensing - the advanced solution for commercial and scientific sar imaging. In *Advances in Radar and Remote Sensing (TyWRRS), 2012 Tyrrhenian Workshop on*, pages 326–329, 2012. doi: 10.1109/TyWRRS.2012.6381150.

[75] Adriano Meta. Metasensing compact, high resolution interferometric sar sensor for commercial and scientific applications. In *Synthetic Aperture Radar (EUSAR), 2010 8th European Conference on*, pages 1–4, 2010.

[76] Adriano Meta, Ernesto Imbembo, Christian Trampuz, Alex Coccia, and Giulio De Luca. A selection of metasensing airborne campaigns at l-, x- and kuband. In *Synthetic Aperture Radar, 2012. EUSAR. 9th European Conference on*, pages 414–417, 2012.

[77] A. Meta, J. J M De Wit, and P. Hoogeboom. Development of a high resolution airborne millimeter wave fm-cw sar. In *Radar Conference, 2004. EURAD. First European*, pages 209–212, 2004.

[78] A. Meta and P. Hoogeboom. Development of signal processing algorithms for high resolution airborne millimeter wave fmcw sar. In *Radar Conference, 2005 IEEE International*, pages 326–331, 2005. doi: 10.1109/RADAR.2005. 1435845.

[79] A. Meta and P. Hoogeboom. High resolution airborne fm-cw sar: digital signal processing aspects. In *Geoscience and Remote Sensing Symposium, 2003. IGARSS '03. Proceedings. 2003 IEEE International*, volume 6, pages 4074–4076 vol.6, 2003. doi: 10.1109/IGARSS.2003.1295366.

[80] G.B. Goldstein. False alarm regulation in log normal and weibull clutter. *IEEE Transactions on Aerospace and Electronic Systems*, 9(1):260 – 278, January 1973.

[81] H.M. Finn, editor. *Adaptative detection in clutter*, volume 22, 1966. National Electronics Conference.

[82] H.M. Finn and R. S. Johnson. Adaptive detection mode with threshold control as a function of spatially sampled clutter level estimates. *RCA*, 29:414 – 464, September 1968.